Asphalt pavement performance under complex service conditions
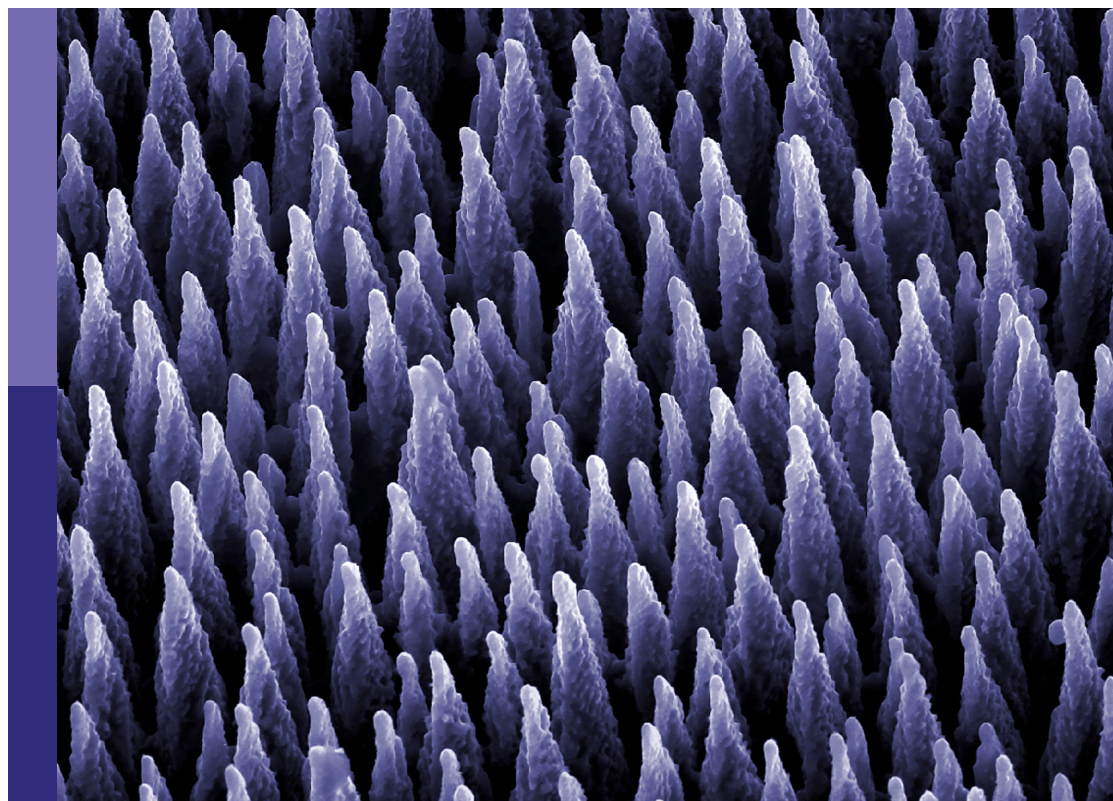
Edited by
Leilei Chen, Nicholas Thom and Linglin Li

Generative AI statement
Any alternative text (Alt text) provided alongside figures in the articles in this ebook has been generated by Frontiers with the support of artificial intelligence and reasonable efforts have been made to ensure accuracy, including review by the authors wherever possible. If you identify any issues, please contact us.

About Frontiers

Frontiers is more than just an open access publisher of scholarly articles: it is a pioneering approach to the world of academia, radically improving the way scholarly research is managed. The grand vision of Frontiers is a world where all people have an equal opportunity to seek, share and generate knowledge. Frontiers provides immediate and permanent online open access to all its publications, but this alone is not enough to realize our grand goals.

Frontiers journal series

The Frontiers journal series is a multi-tier and interdisciplinary set of open-access, online journals, promising a paradigm shift from the current review, selection and dissemination processes in academic publishing. All Frontiers journals are driven by researchers for researchers; therefore, they constitute a service to the scholarly community. At the same time, the *Frontiers journal series* operates on a revolutionary invention, the tiered publishing system, initially addressing specific communities of scholars, and gradually climbing up to broader public understanding, thus serving the interests of the lay society, too.

Dedication to quality

Each Frontiers article is a landmark of the highest quality, thanks to genuinely collaborative interactions between authors and review editors, who include some of the world's best academicians. Research must be certified by peers before entering a stream of knowledge that may eventually reach the public - and shape society; therefore, Frontiers only applies the most rigorous and unbiased reviews. Frontiers revolutionizes research publishing by freely delivering the most outstanding research, evaluated with no bias from both the academic and social point of view. By applying the most advanced information technologies, Frontiers is catapulting scholarly publishing into a new generation.

What are Frontiers Research Topics?

Frontiers Research Topics are very popular trademarks of the *Frontiers journals series*: they are collections of at least ten articles, all centered on a particular subject. With their unique mix of varied contributions from Original Research to Review Articles, Frontiers Research Topics unify the most influential researchers, the latest key findings and historical advances in a hot research area.

Find out more on how to host your own Frontiers Research Topic or contribute to one as an author by contacting the Frontiers editorial office: frontiersin.org/about/contact

Asphalt pavement performance under complex service conditions

Topic editors

Leilei Chen — Southeast University, China
Nicholas Thom — University of Nottingham, United Kingdom
Linglin Li — Hefei University of Technology, China

Table of contents

Check for updates

Editorial: Asphalt pavement performance under complex service conditions

Leilei Chen[1]*, Xinyuan Zhao[1], Linglin Li[2,3] and Chenchen Zhang[4]

[1]Intelligent Transportation System Research Center, Southeast University, Nanjing, China, [2]Nottingham Transportation Engineering Centre, Faculty of Engineering, University of Nottingham, Nottingham, United Kingdom, [3]School of Automotive and Transportation Engineering, Hefei University of Technology, Hefei, China, [4]Anhui Water Conservancy Technical College, Hefei, China

Editorial on the Research Topic
Asphalt pavement performance under complex service conditions

Asphalt pavements often deteriorate under complex service conditions, as evidenced by reduced mechanical integrity, weakened interfacial bonding, and the emergence of secondary damage. These issues can significantly escalate maintenance costs and undermine operational safety and efficiency. While recent technological advances have improved the durability of asphalt materials, the combined effects of moisture, temperature variations, and traffic loading continue to present substantial challenges to long-term performance. Therefore, the development of advanced testing and characterization methods tailored to these multifactorial service conditions is essential to uncovering failure mechanisms and extending the service life of asphalt pavements.

"Frontiers in Materials" is an internationally recognized, high-visibility journal dedicated to publishing rigorously peer-reviewed studies that cover a wide spectrum of Research Topic in materials science and engineering. The Research Topic "Asphalt Pavement Performance under Complex Service Conditions" highlights recent advances and emerging technologies related to asphalt pavements. Specifically, this Research Topic addresses the multiscale investigation of asphalt pavement materials, performance evaluation under complex service conditions, and maintenance materials and schemes.

1. Multiscale investigation of asphalt materials: As a typical multiphase composite material, asphalt materials exhibit scale-dependent mechanical properties. Integrating investigations on these materials across multiple scales can provide valuable insights and explanations into their failure mechanisms. At the microscopic scale, the physical, chemical, and mechanical properties of the asphalt binder are governed by interactions among molecules of varying polarity and size. The effects of Sasobit and Evotherm warm mix agents on Karamay 90# asphalt and Tahe 90# asphalt in Xinjiang were evaluated by using Fourier transform infrared (FTIR) and molecular dynamics simulations. The results showed that Sasobit has good compatibility with Karamay 90# asphalt, while Evotherm has a good modification effect on Tahe 90# asphalt (Hu et al.). Rheological and microscale chemical indicators were proposed to evaluate the extent of aging of polymer-modified asphalt binder, including the complex shear modulus $|G^*|$ at 52°C, the derivative of

creep compliance J' at $-18°C$, and the carbonyl index I_{CA} (Chen et al.). At the mesoscopic scale, the adhesive property between aggregates and bitumen directly affects the performance of the asphalt mixture. The surface roughness, chemical composition, and surface adhesion properties of limestone were better than those of diabase, which resulted in limestone fine aggregate showing better adhesion performance with bitumen than diabase fine aggregate. It was recommended that diabase coarse aggregate and limestone fine aggregate be used to improve the asphalt-aggregate interface (Zeng et al.). In addition, an innovative asphalt mixture design method based on the binder film thickness (BFT) was developed, which, compared with the conventional Marshall and Superpave methods, may achieve superior rutting resistance and balanced durability while reducing binder content (Khan et al.). At the macroscopic scale, a new method of mineral aggregate gradation optimization based on the fuzzy analytic hierarchy process and a comprehensive evaluation method was proposed to obtain the optimal gradation for road performance (Zhu et al.). Polyacrylamide (PAM) can significantly enhance the mechanical properties of cement-stabilized construction waste slurry under varying moisture contents. An optimal PAM content of approximately 0.5% improves unconfined compressive strength, elastic modulus, and shear strength, and provides valuable insights for waste slurry resource utilization (Guo et al.). Overall, by integrating microscopic, mesoscopic, and macroscopic investigations, multiscale research not only deepens the fundamental understanding of the physical, chemical, and mechanical behaviors of asphalt materials but also provides practical guidance for material modification and mixture design, thereby improving pavement performance and durability.

2. Performance evaluation under complex service conditions: The effective determination of the working stress and service performance of asphalt pavements under complex service conditions is fundamental to analyzing their failure mechanism. The incorporation of recycled concrete aggregate (RCA) and freeze-thaw cycles was found to have a significant impact on the fatigue performance of asphalt concrete, where increasing freeze-thaw cycles accelerate fatigue damage, while an appropriate amount of recycled aggregate content was observed to mitigate strength loss and enhance durability under coupled environmental and mechanical loading conditions (Yan et al.). Salt erosion markedly deteriorated the mechanical strength and drying shrinkage resistance of cement-stabilized macadam. As salt solution concentration increased, the cement-stabilized macadam transitioned from shrinkage to expansion, thereby causing arching distress (Wang et al.). Furthermore, the temperature-load coupling effect had a significant influence on the permanent deformation behavior of steel-concrete composite beam bridge deck pavement, in which thermal stress and repeated loading jointly accelerate rutting development, thereby compromising structural durability and service performance (Yang et al.). In summary, the coupled effects of environmental and mechanical factors exert a critical influence on asphalt pavement performance and should be thoroughly addressed in durability-oriented pavement design.

3. Maintenance materials and schemes: For maintenance materials, SBS/CR-modified asphalt binder with C9 petroleum resin exhibited superior rheological properties and 3D printability, which enhanced its adaptability as a crack-filling material by providing improved deformation resistance at high temperatures and flexibility at low temperatures (Niu et al.). Regarding intelligent maintenance, a pavement dynamic monitoring data processing approach based on wavelet decomposition and reconfiguration was proposed, which effectively filters noise and enhances feature extraction, thereby improving the accuracy and reliability of pavement condition evaluation (Shang et al.). Overall, advances in maintenance material development and intelligent monitoring technologies offer promising approaches to improving the effectiveness, reliability, and efficiency of asphalt pavement maintenance.

A total of eleven manuscripts were submitted for possible publication in this Research Topic. Each manuscript underwent a rigorous, fair, and anonymous peer-review process. The quality and originality of every study were thoroughly evaluated. Ultimately, all eleven research articles were accepted for publication.

Our editorial team members sincerely acknowledge the reviewers for their professional and dedicated support and extend our gratitude to all contributing authors for their valuable efforts. We are also deeply appreciative of the editorial and support teams of Frontiers in Materials.

Author contributions

LC: Conceptualization, Writing – original draft. XZ: Writing – original draft. LL: Writing – review and editing. CZ: Writing – review and editing.

Funding

Conflict of interest

The authors declare that the research was conducted in the absence of any commercial or financial relationships that could be construed as a potential conflict of interest.

Generative AI statement

The author(s) declare that no Generative AI was used in the creation of this manuscript.

Any alternative text (alt text) provided alongside figures in this article has been generated by Frontiers with the support of artificial intelligence and reasonable efforts have been made to ensure accuracy, including review by the authors wherever possible. If you identify any issues, please contact us.

Publisher's note

All claims expressed in this article are solely those of the authors and do not necessarily represent those of their affiliated organizations, or those of the publisher, the editors and the reviewers. Any product that may be evaluated in this article, or claim that may be made by its manufacturer, is not guaranteed or endorsed by the publisher.

Pavement dynamic monitoring data processing based on wavelet decomposition and reconfiguration methods

Shujie Shang[1], Ming Liang[2]*, Hao Wang[1], Yuepeng Jiao[2], Zhaoxin Liu[1], Congwei Bi[3], Fei Xu[4], Runzhi Zhang[3], Hongjie Li[3], Yongfeng Zhao[3] and Zhanyong Yao[2]

[1]Shandong High-Speed Infrastructure Construction Co., Ltd., Jinan, China, [2]School of Qilu Transportation, Shandong University, Jinan, China, [3]Shandong Hi-Speed Jiwei Expressway Co., Ltd., Jinan, China, [4]School of Safety Engineering and Emergency Management, Shijiazhuang Tiedao University, Jinan, China

Early damage to asphalt pavements generally occurs due to the increasing traffic flow and the loads of vehicles, coupled with alternating high- and low-temperature cycles, freeze−thaw cycles, ultraviolet radiation, and other harsh environments. Several types of distress, such as rutting, cracking, and other damage, deteriorate the serviceability of asphalt pavements and shorten the road service life. Thus, the long-term structural mechanical response of asphalt pavements under the influence of loads and the environment is crucial data for the road sector, which provides guidance about road maintenance. Effectively processing the pavement dynamic monitoring data is a prerequisite to obtain the dynamic response of asphalt pavement structures. However, the dynamic monitoring data of pavements are often characterized by transient weak signals with strong noises, making it challenging to extract their essential characteristics. In this study, wavelet decomposition and reconstruction methods were applied to reduce the noise of pavement dynamic response data. The parameters of the signal-to-noise ratio (SNR) and root mean square error (RMSE) were introduced to compare and analyze the effect of the decomposition of two different wavelet functions: the symlet (sym) wavelet function and the Daubechies (db) wavelet function. The results showed that both the sym and db wavelet functions can effectively obtain the average similarity information and the detailed information of the dynamic response signals of the pavement, the SNR after the sym wavelet fixed-threshold denoising process is relatively higher, and the RMSE is smaller than that of the db wavelet. Thus, wavelet transformation exhibits good localization properties in both the time and frequency domains for processing pavement dynamic monitoring data, making it a suitable approach for handling massive pavement dynamic monitoring data.

KEYWORDS

asphalt pavement, pavement dynamic response, signal processing, wavelet decomposition and reconfiguration, monitor

1 Introduction

The increasing demand for fast and convenient transportation has resulted in the need for intelligent road infrastructure. This infrastructure heavily relies on the application of digital transport systems and road monitoring information support (Wang and Wang, 2019). Previous studies have mainly relied on macroscopic road surface investigations and non-destructive testing techniques to evaluate asphalt pavement performance. However, asphalt pavements are subjected to various factors, such as external loads, temperature, and humidity. To monitor the dynamic response and internal environmental information of pavement structures, researchers have used fiber-optic grating sensors and resistance-type sensors, enabling the monitoring of pavement dynamics and environmental changes. This information helps us in the understanding of the relationship between load and pavement performance, providing valuable insights about road maintenance (Liu and Qin, 1998).

Mechanical parameters, including stress and strain, are essential for the pavement design, according to the Chinese Specifications for Design of Highway Asphalt Pavement (Ministry of Transport of the People's Republic of China, 2017; Li and Ji, 2019). Researchers have attempted to obtain the mechanical response of asphalt pavement interlayers. Embedded sensors in layered structures have proven effective in monitoring these parameters and capturing their dynamic response. For example, Guan and Zhuang (2012) measured road strain–stress signals using asphalt strain gauges and earth pressure boxes, analyzing the dynamic strain and compressive stress in different layers. Liu and Li (2017) collected asphalt pavement strain data using I-beam strain sensors and developed software for post-processing. Yang and Wang (2010) investigated the dynamic strain response of asphalt layers under heavy loads and temperature effects. Wei and Wang (2009) measured strain data under different loads and analyzed the response using resistance strain sensors. Several other studies have also explored strain sensor arrangements and have developed monitoring systems for asphalt pavements (Tan and Li, 2017; Cornaggia et al., 2022).

Various signal processing techniques have been utilized in pavement research studies. For instance, Hui et al. (2023) and Hui and Yu (2023) used fast Fourier transform (FFT) to analyze acoustic emission signals and characterize asphalt damage patterns. Jiang and Nie (2015) applied wavelet decomposition and reconstruction filtering to reduce vibration noise in the output signal of a fiber-optic gyroscope. Wavelet-based methods have also been utilized in pavement identification, adhesion coefficient estimation, and crack detection (Sun et al., 2011; Golestani et al., 2013; Devi et al., 2022). However, previous studies have lacked effective preprocessing, real-time analysis, and feature extraction methods for handling large-scale pavement monitoring data. Accurate processing of dynamic monitoring data is crucial for the understanding of the dynamic response of asphalt pavements, as road dynamic signals are weak and transient and often accompanied by significant noise. In this context, traditional Fourier filtering techniques are not suitable due to the non-smooth nature of the signals. Wavelet transformation emerges as a suitable approach for processing extensive monitoring data in asphalt pavements.

Symmetrical wavelets, also known as orthogonal wavelets or biorthogonal wavelets, are a class of wavelet functions that exhibit symmetry properties (Powers, 2022). Unlike other types of wavelets, symmetrical wavelets possess both symmetry and anti-symmetry characteristics (Gossler et al., 2022). These wavelets are designed to

have equal energy distribution in their positive and negative frequency components (Banerjee and Bhowmik, 2022). The key characteristic of symmetrical wavelets is their ability to provide a balanced representation of both high-frequency and low-frequency components of a signal (Bairwa and Rathod, 2022). This property makes them particularly useful for analyzing signals with symmetric properties or those that require a balanced representation of positive and negative values. In practical terms, the use of symmetrical wavelets in signal processing allows for an accurate and stable analysis of signals, as they can capture both fine details and global trends in a signal (Ghobber and Mejjaoli, 2023). They are commonly utilized in various applications, including image processing, audio and speech analysis, data compression, and time–frequency analysis. The symmetric properties of these wavelets enable efficient filtering of signals, noise reduction, feature extraction, and decomposition of signals into different frequency components. They provide a versatile tool for analyzing and processing signals in both the time and frequency domains (Ke et al., 2023). In the context of pavement engineering and maintenance, the application of symmetrical wavelets in signal processing can help extract meaningful information from dynamic response signals obtained from field testing (Janani et al., 2022). Through symmetrical wavelet analysis, the method proposed in this study can effectively remove noise and enhance the accuracy and clarity of the pavement's dynamic behavior representation, enabling a better understanding of its performance and facilitating decision-making in pavement engineering practices (Mallat, 1989; Zeng, 2007; Qin, 2014; Shao and Bai, 2014; Zhang, 2016; Tulup, 2021).

This paper focuses on the application of wavelet decomposition and reconstruction techniques to process dynamic response signals obtained from field testing of asphalt pavements. By removing high-frequency noise, the processed signals provide a clearer and more accurate representation of the pavement's dynamic behavior. We introduce the signal-to-noise ratio (SNR) and root mean square error (RMSE) as evaluation parameters for comparing two different wavelet functions: the symlet (sym) wavelet function and Daubechies (db) wavelet function. The effectiveness of the proposed method is validated through the experimental analysis and comparison with traditional signal processing techniques. The processed data lay a valuable foundation for further analysis and decision-making in pavement engineering and maintenance.

2 Engineering background and data source

2.1 Engineering background

The original monitoring data of this study were collected from an urban road in Jinan, Shandong. Sensors were directly laid on a semi-rigid road base, and asphalt strain gauges were arranged outside of the lane. The applied sensors were coefficient-calibrated, and data acquisition was verified to be stable. The temperature and humidity sensors were, respectively, arranged between a 6-cm AC-20 asphalt mixture layer and an 8-cm AC-25 pavement layer and a 13-cm LSPM-30 base and an 18-cm cement-stabilized gravel base. A spacing of 60 cm was set between the sensors. The pavement structure and sensor layout are illustrated in Figure 1. The asphalt layer bottom sensor is grounded and shielded by the instrument, and the noise base fluctuates by only 1–3 uε to meet the acquisition conditions.
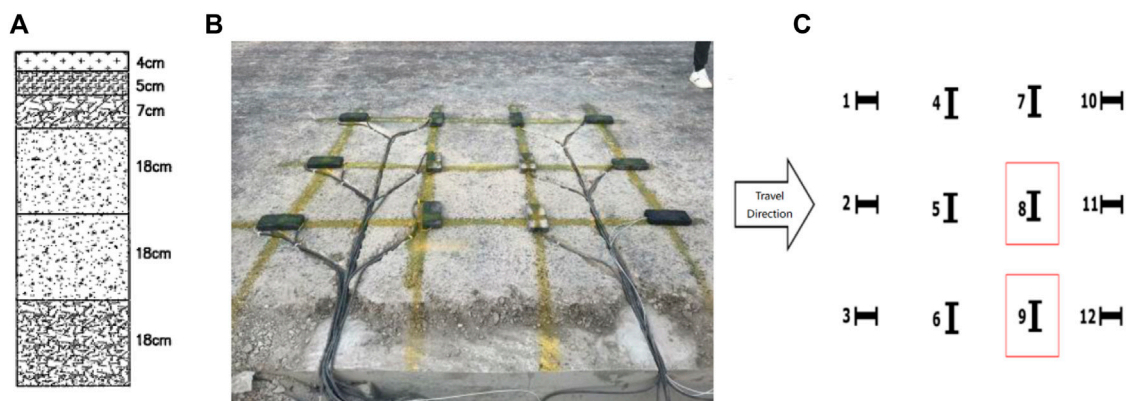
FIGURE 1
Diagram of the road surface structure and sensor placement. **(A)** Diagram of the asphalt pavement structure; **(B)** sensor location; and **(C)** diagram of sensor placement.
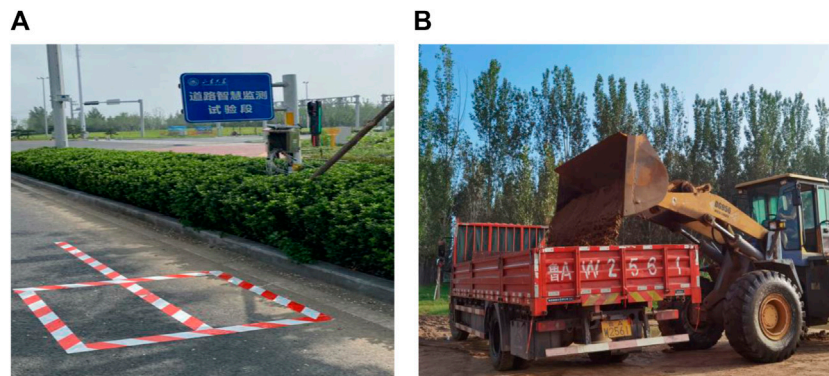
FIGURE 2
Field testing area and load-controlled vehicle. **(A)** Test section; **(B)** two-axle truck loaded with sand.

2.2 Field testing

The testing vehicle was a 6.8-m two-axle flatbed truck manufactured by Dongfeng, and the tire inflation pressure was 1.2 MPa during the test. A controlled axle weight of 10 t was set for the rear axle of the two-axle truck (single-axle twin wheelset, Figure 2B). The front-axle weight was weighed and recorded (2.8 t). The dynamic response signals of the pavement were recorded using a high-frequency data acquisition system with multiple measurement functions, solid-state relay modules, and scanning speeds of up to 800 channels/second.

2.3 Dynamic pavement response signal acquisition under loading

A dynamic load appears when the original signal of the pavement dynamic response amplitude changes with time, as shown in Figure 3. The horizontal coordinate is the time, and the vertical coordinate is the signal amplitude. The waveform graph shows that the collected pavement dynamic response signal base fluctuation is large; the data

that appeared in the three peaks are the response signals when the wheels pass through the sensor. The fluctuation region noise interference is more serious, which almost covers the characteristic peak. The noise seriously affects the subsequent pavement monitoring work, which needs to be reduced.

3 Signal processing based on wavelet decomposition and reconstruction

3.1 Wavelet decomposition and reconstruction methods

The wavelet decomposition and reconstruction processing methods have the advantages of low entropy, multi-resolution, and decorrelation (Hui et al., 2023). Wavelet decomposition requires *a priori* knowledge of the signal frequency to determine the basic functions and decomposition levels, which decomposes the signal into a set of elementary functions called wavelets; these wavelets are obtained by scaling and shifting a prototype wavelet called the mother wavelet (Hui and Yu, 2023).
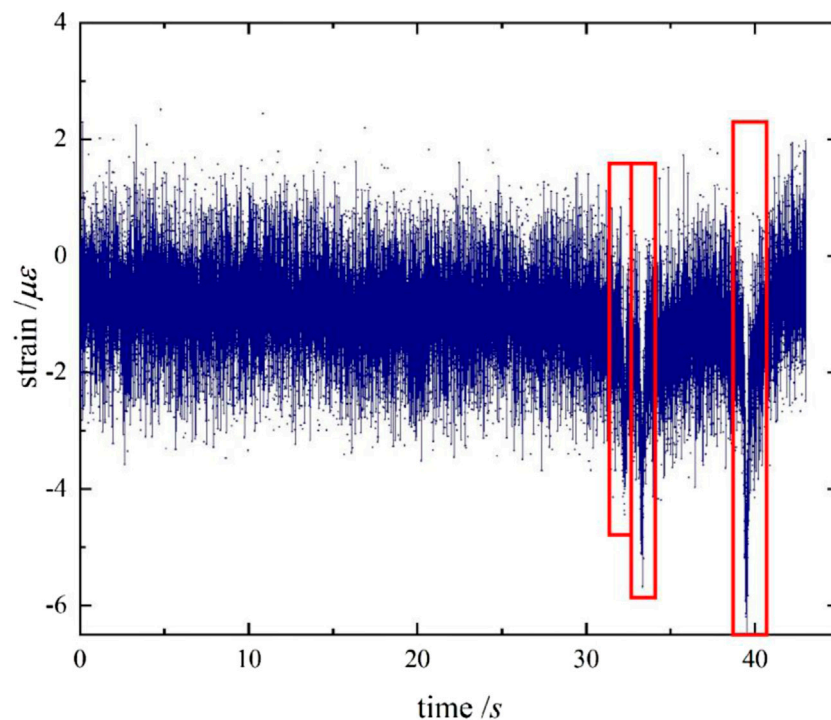
FIGURE 3
Original signal time–domain diagram.
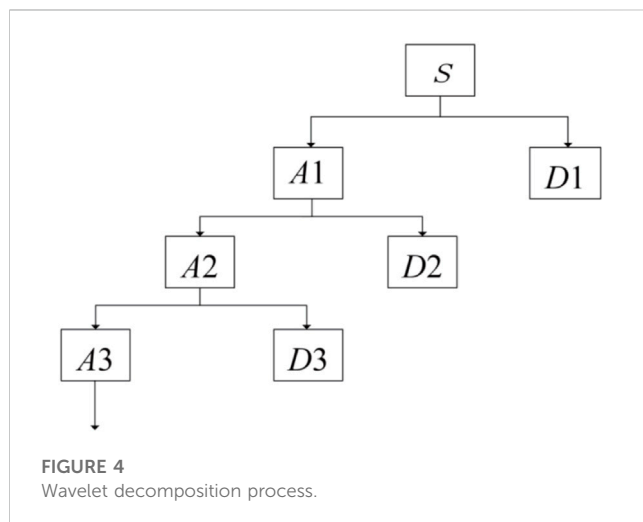
FIGURE 4
Wavelet decomposition process.

We set the mother wavelet function $\psi(t)$ with a scale factor of a and a translation factor of b; then, the wavelet analysis basis is defined as follows:

$$\varphi(t) = \frac{1}{\sqrt{|a|}} \varphi\left(\frac{t-b}{a}\right). \qquad (1)$$

(1) Discrete wavelet transformation:

Mallat proposes an efficient algorithm for decomposing signals into approximate and detailed sequences (Sun et al., 2011). The

wavelet decomposition process is shown in Figure 4, where S denotes the original signal, A denotes the approximate or low-frequency signal, and D denotes the detailed or high-frequency signal, with each level dividing the low-frequency signal into a high-frequency signal and a low-frequency signal.

$$\text{Level 1: } S = D1 + A1,$$
$$\text{Level 2: } A1 = D2 + A2,$$
$$\text{Level 3: } A2 = D3 + A3.$$

It is noteworthy that the decomposition level L and the number of samples N should satisfy the relationship $2L \leq N$. The decomposed signal consists of the approximation of level l and the details from level 1 to level l. Figure 5 shows the approximate sequence a containing the lower frequency signal and the detailed sequence $d\sim f$ containing the higher frequency signal, obtained after the four-layer wavelet decomposition of the road response monitoring signal collected in this paper. It can be seen that after four layers of wavelet decomposition, the high-frequency noise signal is decomposed layer by layer, and the low-frequency effective pavement response signal obtained retains the whole dynamic response characteristics of the pavement generated by the three-axle truck and can proceed to the next step.

The discrete wavelet transformation (DWT) discretizes the scale and translation parameters to the power of 2 and averages the time discretization usually using binary wavelet decomposition and reconstruction, with discretized scale times of 2, 4, 6, 8, and 2n (the sampling rate is required to satisfy Nyquist's sampling theorem), and is commonly used for the multi-resolution analysis
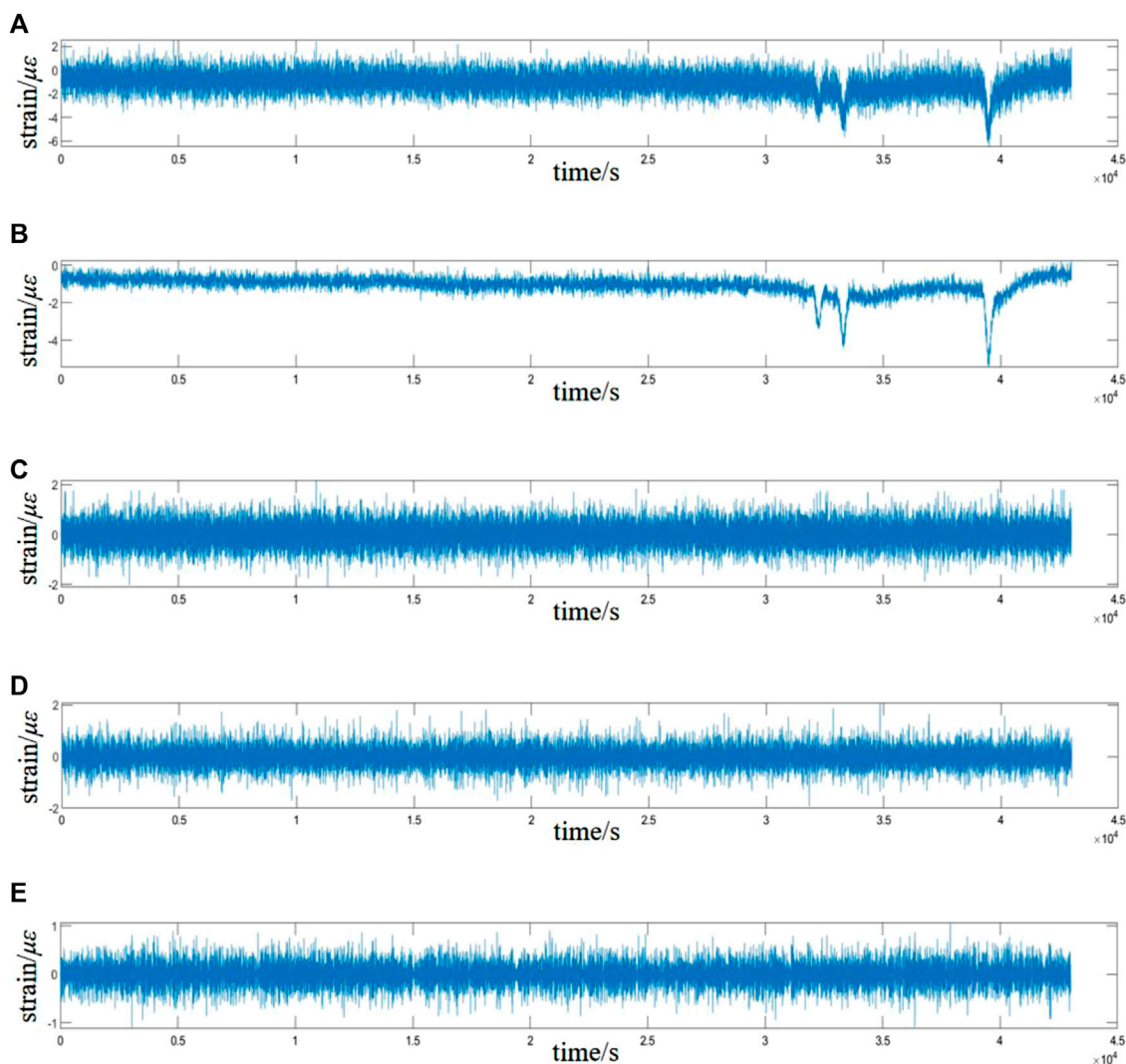
FIGURE 5
Four-layer wavelet decomposition result. **(A)** Original monitoring data; **(B)** approximate sequence a; **(C)** approximate sequence d; **(D)** approximate sequence e; **(E)** approximate sequence f.

of signals and signal decomposition and reconstruction, with the following equation:

$$DWTx(a,b) = \langle X(t), \varphi_{a,b}(t)\rangle = 2^{-\frac{a}{2}}\int_R X(t)\varphi(2^{-a}t - b)dt. \quad (2)$$

At different scales and times, the scale function vector group and the wavelet function vector group are constructed, respectively, for the scale function vector space V and the wavelet function vector space W. At a certain level, the approximate, low-frequency information of the signal is obtained by the convolution of the signal in the scale space V and the detailed, high-frequency information of the signal is obtained by the convolution of the signal in the wavelet space W.

① Scale function:

$$\phi_{jk}(t) = 2^{-\frac{j}{2}}\phi(2^{-j}t - k), j,k \in Z. \quad (3)$$

② Wavelet function:

$$\varphi_{jk}(t) = 2^{-\frac{j}{2}}\varphi(2^{-j}t - k)j,k \in Z. \quad (4)$$

③ Threshold:

Common threshold selection methods, currently available, include unbiased risk estimation thresholds (rigrsure), fixed thresholds (sqtwolog), heuristic thresholds (heursure), and very large and very small thresholds (minimaxi). There are two categories of the four methods: one of them is the conservative principle; e.g., the rigrsure criterion and the minimaxi criterion are relatively conservative (only some of the coefficients are set to zero), and therefore, the method is suitable for high-frequency information that contains noise. The second is the non-conservative principle; e.g., the sqtwolog and heursure criteria, particularly the fixed-threshold (sqtwolog) method, which removes more noise, is therefore suitable for low-frequency information (Devi et al., 2022).
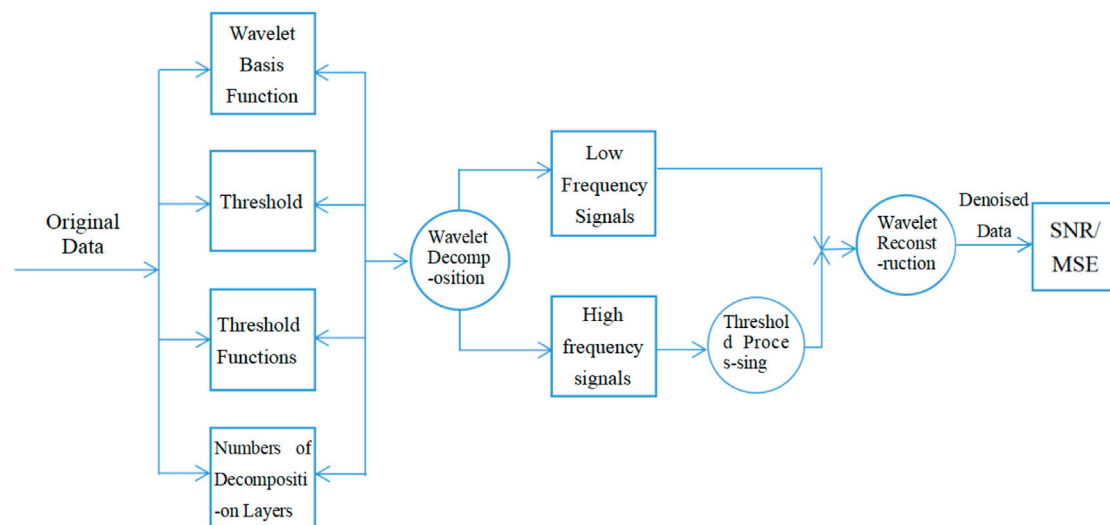
FIGURE 6
Process of discrete wavelet transformation thresholding denoising method.
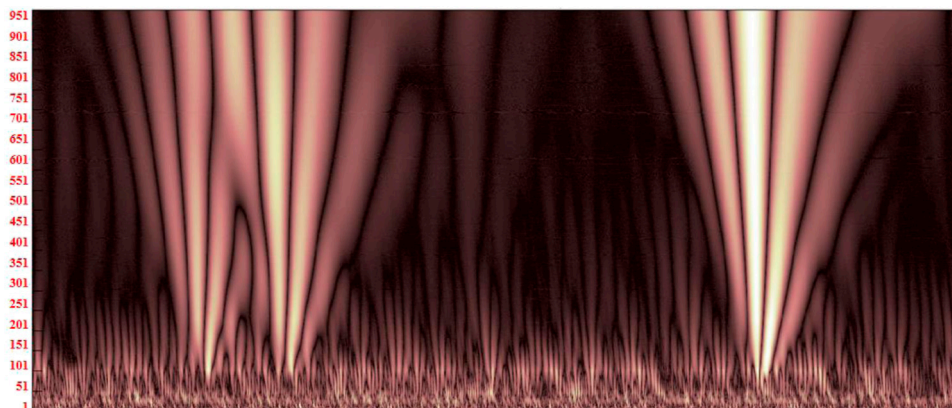
FIGURE 7
Effect of wavelet decomposition coefficients.

The mathematical formula for the generic threshold is

$$\lambda = \sigma\sqrt{2\ln(N)}, \qquad (5)$$

where λ represents the threshold of wavelet coefficients, σ represents the standard variance of the noise, N represents the length, and $\sigma = median(|w_{j,k}|)/0.6745$.

The process of discrete wavelet transformation thresholding denoising is shown in Figure 6. The wavelet basis function, threshold, queue function, and the number of decomposition layers are all key factors affecting the final denoising effect in the process of discrete wavelet transformation thresholding denoising.

The signal is processed using wavelet decomposition and reconstruction methods, and the wavelet coefficients obtained contain important information about the signal. The effect of wavelet decomposition coefficients on the dynamic response signal of the pavement is shown in Figure 7, which clearly shows the exact location of time discontinuity. The wavelet coefficient of the pavement response monitoring signal is larger after wavelet decomposition, and the wavelet coefficient of the noise is smaller than that of the effective pavement dynamic response signal. An appropriate threshold is selected, and the wavelet decomposition coefficients of each layer are quantified using the threshold function; when the wavelet coefficient is larger than the threshold, the pavement dynamic response signal is considered effective and is retained; if it is smaller than the threshold, it is considered as noise and the wavelet coefficient is set to 0, thus eliminating the noise. The essence of the wavelet decomposition and reconstruction processing method is to suppress the useless noise part of the pavement response monitoring signal and enhance the useful signal part.

FIGURE 8
Waveform results of wavelet denoising. **(A)** db4 wavelet two-layer decomposition; **(B)** db4 wavelet three-layer decomposition; **(C)** db4 wavelet four-layer decomposition; **(D)** sym6 wavelet two-layer decomposition; **(E)** sym6 wavelet three-layer decomposition; and **(F)** sym6 wavelet four-layer decomposition.
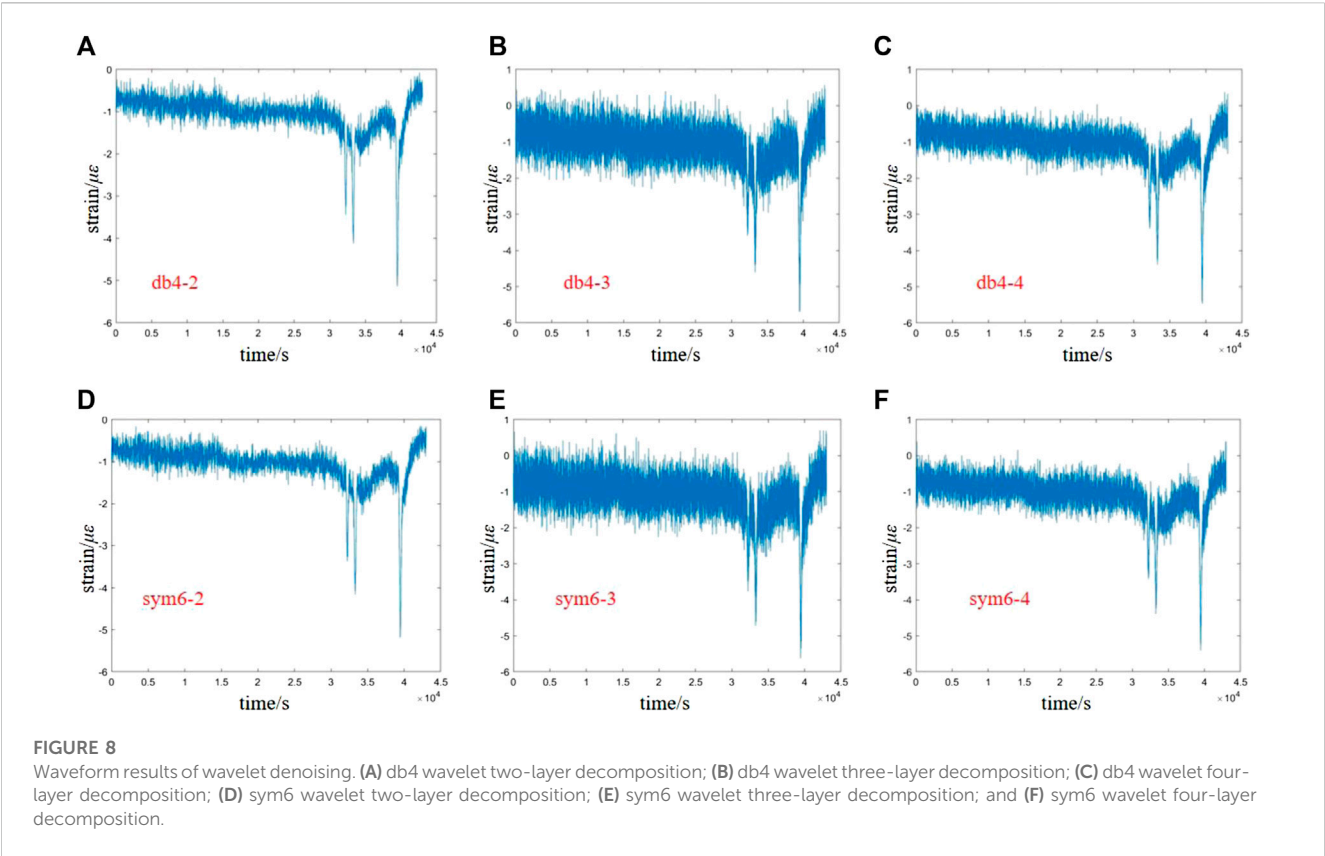
TABLE 1 SNRs and RMSEs of wavelet denoising results with different decomposition layers and wavelet functions.

Type	db4 wavelet		sym6 wavelet		Number of decomposition layers
	SNR	RMSE	SNR	RMSE	
Hard-threshold denoising	8.0819	0.52151	8.1008	0.52038	2
Soft-threshold denoising	8.0819	0.52151	8.1008	0.52038	2
Fixed-threshold denoising	8.0909	0.52097	8.1053	0.52011	2
Hard-threshold denoising	7.3455	0.56766	7.3653	0.56636	3
Soft-threshold denoising	7.3455	0.56766	7.3653	0.56636	3
Fixed-threshold denoising	7.3532	0.56715	7.3691	0.56612	3
Hard-threshold denoising	6.8295	0.6024	6.8335	0.60212	4
Soft-threshold denoising	6.8295	0.6024	6.8335	0.60212	4
Fixed-threshold denoising	6.8383	0.60179	6.8373	0.60186	4

The basic steps are as follows:

(i) Step 1: Decomposition: Select wavelets with N layers for the wavelet decomposition of the pavement response monitoring signal.
(ii) Step 2: After wavelet decomposition, select an appropriate threshold and quantify the wavelet decomposition coefficients of each layer using the threshold function.
(iii) Step 3: Reconstruction: Reconstruct the pavement dynamic response signal using the processed wavelet coefficients.

3.2 Comparative selection of wavelet basis functions and thresholds

3.2.1 Selection of wavelet basis functions

The choice of a wavelet basis function is usually based on the combination of support length, vanishing moments, symmetry, regularity, and similarity. As the support length increases, the amount of computation required is usually greater, and the resulting wavelet coefficients are larger. Long support lengths can cause boundary problems, and short support lengths have
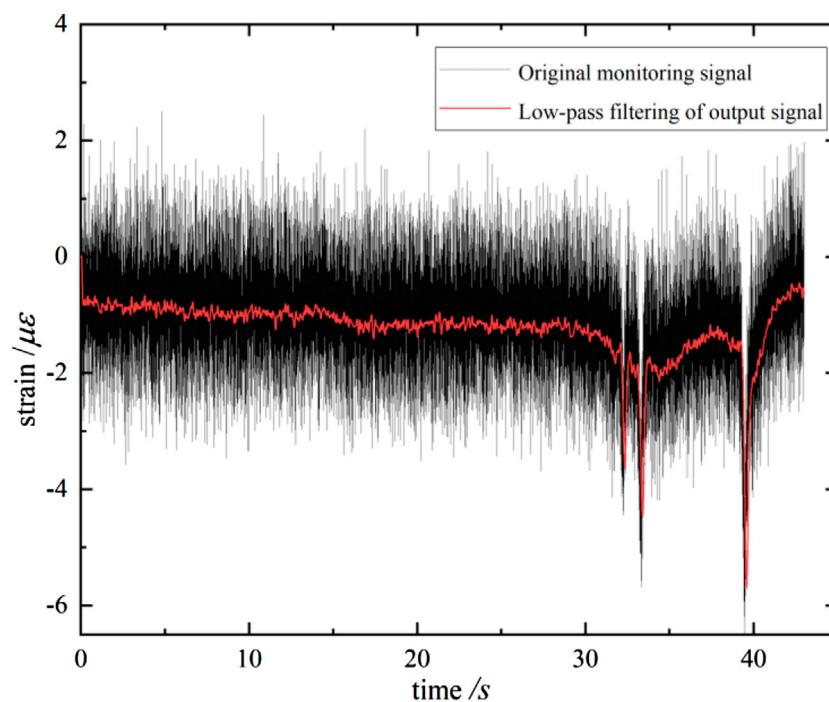
FIGURE 9
Comparison of the effect of wavelet decomposition and reconstruction on the dynamic response signal of the pavement.
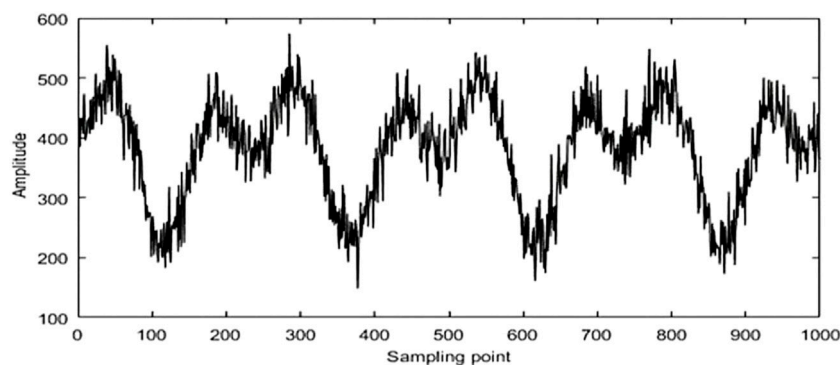
FIGURE 10
Signal characterized by noisy motor detection data in the context of a massage chair.

small vanishing moments, which are detrimental to the concentration of the signal energy. For the underlying wavelet, not only the permissible conditions must be met, but also the "vanishing moments" must be applied to it to minimize wavelet coefficients or non-zero wavelets, thus facilitating data compression and noise removal. As the vanishing moment increases, subway coefficients become smaller. However, as the vanishing moment increases, the support length increases under normal conditions. Therefore, we need to weigh the support length and vanishing moment.

Wavelet basis functions have their characteristics in signal processing, but each type of function focuses on the denoising effect of different types of information. Daubechies and symlet wavelets are the two families of wavelet bases that are better integrated and adapted to the aforementioned principles.

The Daubechies wavelet is a wavelet function proposed by the wavelet analyst Ingrid Daubechies, often abbreviated as *dbN*, where *N* represents the number of orders of the wavelet. The support region in the wavelet function $\Psi(t)$ and the scale function $\varphi(t)$ is $2N-1$, and the vanishing moment of $\Psi(t)$ is N. The *dbN* wavelet has better regularity; in other words, the smooth error introduced by this wavelet as a sparse basis is not easily detectable, making the signal reconstruction process relatively smooth. The characteristics of the dbN wavelet are as follows: as the order increases (sequence *N*), the order of the vanishing moment becomes larger, where the higher the vanishing moment, the better the smoothness, the stronger the
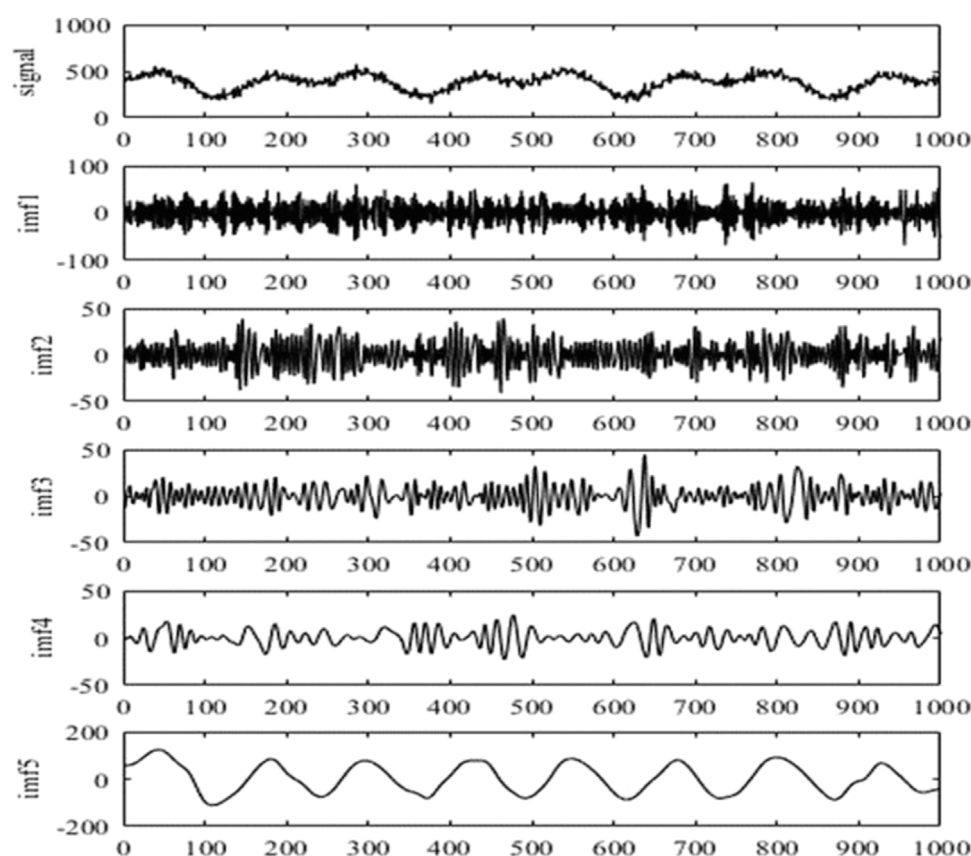
FIGURE 11
Noise reduction results of the massage chair signal.

localization ability in the frequency domain, and the better the division of the frequency band; however, it will make the compact support of the wavelet function weaker, and at the same time, the computational effort increases greatly and the real-time performance becomes worse. The sym wavelet is an improvement to the db wavelet. It has better symmetry and, to some extent, reduces phase distortion when analyzing and reconstructing the signal.

3.2.2 Selection of decomposition layers

The second key step in wavelet decomposition and reconstruction is determining the number of decomposition layers. The number of wavelet decomposition layers is essentially related to the characteristics of the signal itself and the sampling frequency. As the number of decomposition layers increases, more signals are obtained, the difference in noise characteristics and signal performance becomes greater, a more complete signal denoising is carried out, and a more beneficial separation effect is observed. However, the higher the number of decomposition layers, the bigger the distortion in the dynamic response signal of the reconstructed pavement, which may result in the loss of the effective signal, and this will affect the final noise reduction effect. Conversely, a lower number of decomposition layers may lead to incomplete denoising. Therefore, special attention should be paid to the conflict between the two functions in the process of application, and an appropriate decomposition ratio should be selected (Powers, 2022). This paper compares and analyses the decomposition effects of the db and sym functions. By comparing their intuitive graphs, detail differences, and signal-to-noise ratios, it is found that the decomposition method using the sym wavelet algorithm is more in line with the objectives.

After wavelet transformations, we adopt three methods to process the signal: hard-threshold denoising, soft-threshold denoising, and fixed-threshold denoising. By setting the appropriate wavelet bases, thresholds, threshold functions, and decomposition layers for wavelet decomposition, the approximate wavelet coefficients and detailed wavelet coefficients are obtained (Gossler et al., 2022).

To carry out the wavelet threshold denoising method, we introduce two metrics: the signal-to-noise ratio and the root mean square error for evaluation, and the pavement structure mechanical response signals are processed separately using different threshold quantization methods. Figure 8 shows the waveform effect of the fixed-threshold wavelet denoising process with a different number of decomposition layers and different wavelet functions. It can be observed from the figure that as the number of decomposition layers increases, the more obvious the waveform is, and the SNR and RMSE obtained are shown in Table 1. The results show that the difference between hard- and soft-thresholding methods is not significant since the mechanical
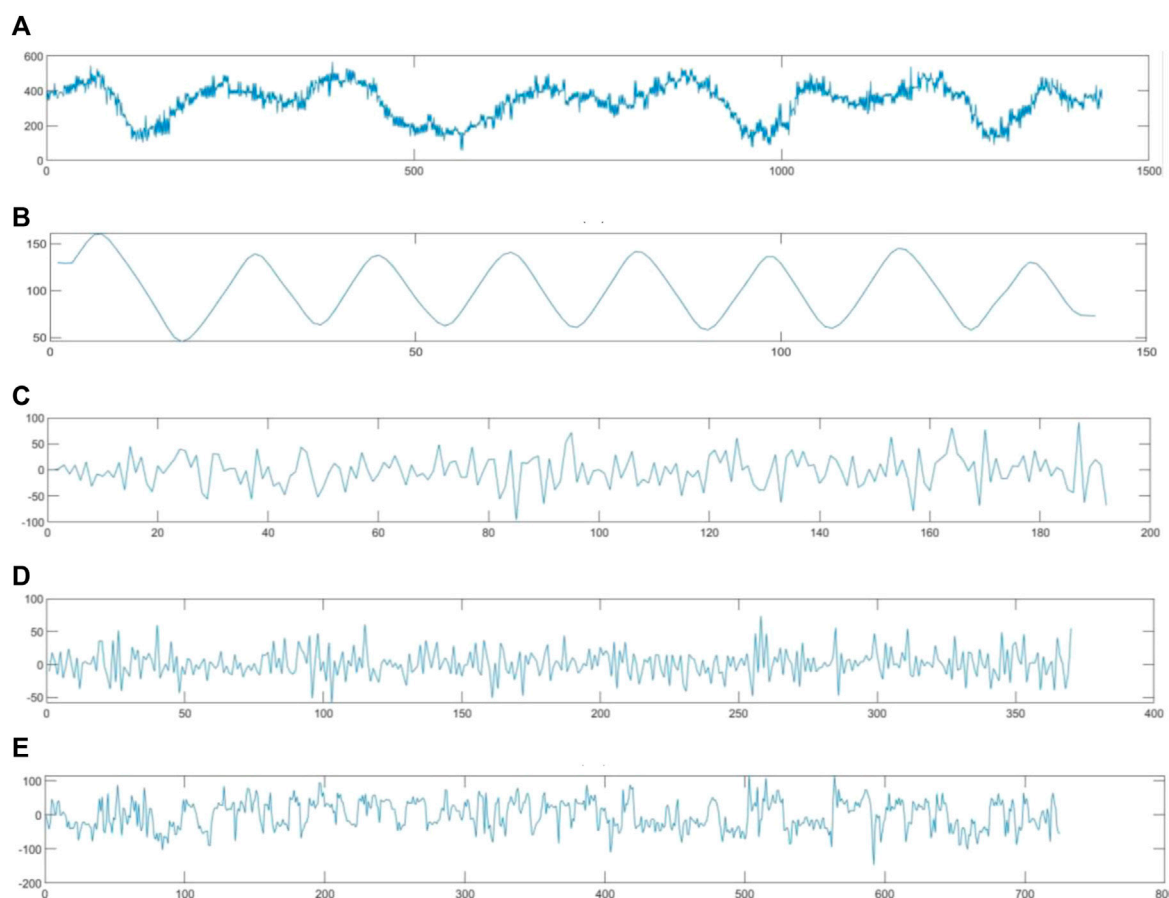
FIGURE 12
Four-layer wavelet decomposition result. **(A)** Original monitoring data; **(B)** approximate sequence a; **(C)** approximate sequence d; **(D)** approximate sequence e; and **(E)** approximate sequence f.

response of an asphalt pavement structure is a one-dimensional signal; the reconstructed signal has less loss compared to the original signal, and the decomposition and reconstruction methods both yield better results. The signal-to-noise ratio is relatively high and the root mean square error value is small after the sym wavelet fixed-threshold denoising process.

3.3 Results of wavelet decomposition and reconstruction processing

Figure 9 shows the waveform comparison between the output signal and the original pavement response monitoring signal after the selected sym6 wavelet four-layer decomposition and reconstruction. Wavelet decomposition and reconstruction retain the whole characteristics of the strain signal generated by the three-axle vehicle, where the signal first drops from the baseline to the first trough and then rises, while the second and third axle signals, in turn, pass through the sensor, generating a compression strain and a trough. In addition, the difference in signal amplitude between the wavelet decomposition reconstructed signal and the original pavement response monitoring signal is small. It can be seen that in the wavelet decomposition process, different scales have different

temporal and frequency resolutions; thus, the signal contained in different frequency intervals can be separated using wavelet decomposition, and therefore, wavelet decomposition and reconstruction have a powerful local feature portrayal capability.

3.4 Validation of applicability

In order to validate the effectiveness and applicability of the proposed wavelet decomposition and reconstruction method, a comparative analysis was conducted using a signal from the selected literature titled "Signal Detection and Noise Reduction Method of Massage Chair Based on EMD" (Lu and Yu, 2021). The chosen signal, as shown in Figure 10, is characterized by noisy motor detection data in the context of a massage chair. Figure 11 shows the result of signal denoising in the literature.

The chosen signal was processed using the sym8 wavelet with a decomposition level of 4, consistent with the methodology described in this literature. The wavelet decomposition results were obtained and compared with the denoising results presented in this paper. The obtained results demonstrated a high degree of similarity with the literature, providing evidence for the applicability of our proposed method. Figure 10 illustrates the wavelet decomposition

results, showcasing the effectiveness of the sym8 wavelet in reducing noise and preserving useful signal components. These findings validate the suitability of the proposed wavelet transformation approach for processing dynamic monitoring data in pavement applications.

Figure 12 presents the wavelet decomposition and reconstruction results for the selected signal. The comparative analysis was performed based on evaluating the signal-to-noise ratio and the preservation of useful signal characteristics.

This comparative analysis serves as compelling evidence supporting the applicability and effectiveness of the proposed wavelet decomposition and reconstruction method for noise reduction in motor detection signals of massage chairs.

The findings highlight the advantages of using the sym8 wavelet with a decomposition level of 4 for handling noisy motor detection data. This approach exhibits good localization properties in both the time and frequency domains, enabling the extraction of essential characteristics from the dynamic response signals of the motor of the massage chair. The proposed method provides a suitable approach for processing massive motor detection data, which is vital for the effective maintenance and quality control of massage chairs.

4 Conclusion

In this paper, the pavement dynamic response signal is reconstructed via wavelet decomposition, and its working principle and noise reduction process are analyzed in detail. Wavelet transformation is characterized by multiple analyses and is able to analyze local features in both time and frequency domains.

- This paper's results demonstrate the effectiveness of wavelet decomposition and reconstruction techniques in processing pavement dynamic response signals. Consequently, the signal-to-noise ratio of the signal was significantly improved. Noise reduction was successfully achieved by applying these methods, and the signal-to-noise ratio of the signal was significantly improved to obtain a clearer dynamic response signal of the pavement structure. By comparing different wavelet functions, it was found that the sym wavelet method produced good results in terms of signal-to-noise ratio and root mean square error. The wavelet decomposition and reconstruction algorithm is appropriate for the preprocessing of the dynamic response signal between different layers of the pavement.
- The selection of the wavelet basis function, decomposition layer, and threshold processing method has a great influence on the denoising results. The difference between hard and soft thresholding is not obvious for wavelet decomposition and reconstruction methods, since the mechanical response of an asphalt pavement structure is a one-dimensional signal. The sym wavelet fixed-

threshold denoising results indicated a relatively high signal-to-noise ratio and a small root mean square error.

Data availability statement

The original contributions presented in the study are included in the article/Supplementary Material; further inquiries can be directed to the corresponding author.

Author contributions

SS, project administration; ML, writing—review and editing; YJ, writing—original draft preparation; HW and CB, data curation; ZL, investigation; RZ and HL, funding acquisition; YZ, visualization; ZY and FX, formal analysis. All authors contributed to the article and approved the submitted version.

Funding

Conflict of interest

Authors SS, HW, and ZL were employed by Shandong High-Speed Infrastructure Construction Co., Ltd., and CB, RZ, HL, and YZ were employed by Shandong Hi-Speed Jiwei Expressway Co., Ltd.

The remaining authors declare that the research was conducted in the absence of any commercial or financial relationships that could be construed as a potential conflict of interest.

Publisher's note

References

Bairwa, B., and Rathod, S. (2022). "Development of fault detection method in cable using arduino UNO," in IEEE International Conference on Recent Advances and Innovations in Engineering, MANGALORE, India, 01-03 December 2022 (IEEE).

Banerjee, S., and Bhowmik, S. (2022). "Detection and location of fault in microgrid using discrete wavelet transform based technique," in IEEE International Conference on

Condition Assessment Techniques in Electrical Systems, Durgapur, India, 17-19 December 2022 (IEEE).

Cornaggia, A., Ferrari, R., Zola, M., Rizzi, E., and Gentile, C. (2022). Signal processing methodology of response data from a historical arch bridge toward reliable modal identification. *Infrastructures* 7 (5), 74. doi:10.3390/infrastructures7050074

Devi, R., Kirthika, A., Divya Priyadharshini, M., Ladha, A., Anju, A., Rajesh Kumar, T., et al. (2022). Development of symmetrical fault detection during power swing based on entropy. *J. Electr. Eng.* 17, 1533–1542. doi:10.1007/s42835-021-00994-0

Ghobber, S., and Mejjaoli, H. (2023). Deformed wavelet transform and related uncertainty principles. *Symmetry-Basel* 15, 675. doi:10.3390/sym15030675

Golestani, A., Kolbadi, S., and Heshmati, A. A. (2013). Localization and de-noising seismic signals on SASW measurement by wavelet transform. *J. Appl. Geophys.* 98, 124–133. doi:10.1016/j.jappgeo.2013.08.010

Gossler, F., Queiroz, D., and Villarreal, F. (2022). Design of nearly-orthogonal symmetric wavelet filter banks based on the wavelet orthogonalization process. *Circuits Syst. Signal Process.* 42, 234–254. doi:10.1007/s00034-022-02111-6

Guan, Z., and Zhuang, C. (2012). Accelerated loading dynamic respond of full-scale asphalt concrete pavement. *J. Traffic Transp. Eng.* 12 (2), 24–31.

Hui, W., Hu, Zh., Li, J., Zheng, J., and Ren, J. (2023). Effect of loading rate on failure characteristics of asphalt mixtures using acoustic emission technique. *Constr. Build. Mater.* 364, 129835. doi:10.1016/j.conbuildmat.2022.129835

Hui, W., and Yu, Z. (2023). Fracture characteristics of a cement concrete pavement plate considering subgrade modulus decay based on a meshless finite block metho. *Front. Mater.* 10, 1157529. doi:10.3389/fmats.2023.1157529

Janani, A., Rezaeieh, S., Darvazehban, A., Keating, S. E., and Abbosh, A. M. (2022). Portable electromagnetic device for steatotic liver detection using blind source separation and shannon wavelet entropy. *IEEE J. Electromagn. Rf Microwaves Med. Biol.* 6, 546–554. doi:10.1109/jerm.2022.3205247

Jiang, M., and Nie, M. (2015). "Signal processing of fiber optic gyro under vehicle vibration environment," in 2015 34th Chinese Control Conference (CCC), Hangzhou, China, 28-30 July 2015 (IEEE).

Ke, X., Shi, Y., Fu, X., Song, L., Jing, H., Yang, J., et al. (2023). The nth power fourier spectrum analysis for the generalized seismic wavelets. *IEEE Trans. Geoscience Remote Sens.* 61, 1–10. doi:10.1109/tgrs.2023.3243184

Li, M., and Ji, S. (2019). The pretreatment methods of pavement strain signals. *J. Shandong Univ. Sci.* 49 (03), 73–79.

Liu, F., and Li, H. (2017). Post-processing of measured straindata for asphalt pavement structure. *Highway* 5 (5), 60–63.

Liu, Z., and Qin, R. (1998). The analysis of the effect of overload truck on asphalt pavement. *J. Chang Sha Comun. Univ.* 15 (2), 59–64.

Lu, L., and Yu, H. (2021). "Signal detection and noise reduction method of massage chair based on EMD," in *Advanced manufacturing and automation X* (Spinger).

Mallat, S. (1989). A theory for multiresolution signal decomposition: the wavelet representation. *IEEE Trans. Pattern Analysis Mach. Intell.* 11 (7), 674–693. doi:10.1109/34.192463

Ministry of Transport of the People's Republic of China (2017). *Specifications for design of Highway asphalt pavement.* Beijing, China: China Communications Press.

Powers, N. P. (2022). Power factor in non-sinusoidal and non-symmetrical regimes in three-phase systems. *Energies* 15, 5130. doi:10.3390/en15145130

Qin, D. (2014). Performance analysis of FFT and DWT. *J. Guangdong Polytech. Normal Univ.* 35 (07), 12–15.

Shao, T., and Bai, Z. (2014). Decomposition and reconstruction of signal based on DWT. *Comput. Technol. Dev.* 24 (11), 159–161.

Sun, R., Shan, Y., and Wang, B. (2011). Study of pavement identification approach based on wavelet analysis. *Appl. Mech. Mater.* 44-47, 3632–3639. doi:10.4028/www.scientific.net/AMM.44-47.3632

Tan, Z., and Li, H. (2017). Study on layout of monitoring system about mechanical response of asphalt pavement. *J. Wuhan Univ. Technol.* 41 (3), 528–532.

Tulup, A. (2021). *Research on application of wavelet analysis in mutation signal processing.* Master's thesis. Urumchi: Xinjiang Normal University.

Wang, L., and Wang, H. (2019). Development and prospect of intelligent pavement. *China J. Highw. Transp.* 32 (04), 50–72.

Wei, J., and Wang, L. (2009). Asphalt pavement strain gauge data collection and signals proces. *Highw. Eng.* 34 (2), 45–47.

Yang, Y., and Wang, L. (2010). Typical pavement structure dynamic response data collection and analysis under heavy vehicle loading. *J. Highw. Transp. Res. Dev.* 27 (5), 11–16.

Zeng, S. (2007). *Wavelet denoising and applying in signal processing.* Master's thesis. Tianjin: Tianjin University.

Zhang, X. A. (2016). *Dissertation submitted to zhejiang university of technologyfor the degree of master of engineering.* Master's thesis. Hangzhou. Zhejiang University of Technology.

Investigation on permanent deformation in steel-concrete composite beam bridge deck pavement under temperature-load coupling effect

Jing Yang[1], Liming Tan[1], Xiangyu Qi[1] and Chenchen Zhang[2]*

[1]Yunnan Research Institute of Highway Science and Technology, Kunming, China, [2]Anhui Water Conservancy Technical College, Hefei, China

Rutting is one of the common distresses observed in asphalt pavement, influenced by temperature and load conditions. To clarify the permanent deformation behavior of steel-concrete composite beam (SCCB) bridge deck pavement under temperature-load coupling effect and provide references for the distress cause analysis, five typical SCCB bridge deck pavements were selected. The temperature distribution and the temperature stress of the pavement structures were analyzed by numerical simulation under periodic temperature variations. In addition, considering the daily variation in traffic volume, the permanent deformation of the five pavement structures were calculated under temperature-load coupling effect. Finally, the influence of heavy load on the development of rutting distress was also investigated. The results show that the temperature field and temperature stresses within the SCCB bridge deck pavement exhibit periodic variations under periodic temperature variations. Additionally, after 500,000 times of standard axle load application, "EA + SMA" exhibits the smallest permanent deformation and the best resistance to rutting distress under temperature-load coupling effect. Finally, heavy load conditions have a great influence on the permanent deformation of SCCB bridge deck pavement. In areas with severe rutting distresses, it is recommended to use "EA + SMA" pavement structure in SCCB bridge.

1 Introduction

Steel-concrete composite beam (SCCB) bridges, with advantages such as lightweight, large span, low cost, and rapid construction, have been widely used in China. The SCCB bridge is composed of steel box girders and reinforced concrete slabs. As an important component of the bridge traffic system, the SCCB bridge deck pavement can greatly mitigate the impact of vehicle dynamic loads on the bridge deck, protecting the bridge deck and dispersing wheel loads. It also meets the requirements of stable and comfortable driving.

With the continuous increase in traffic volume, heavy vehicles, and the impact of external natural factors such as climate, pavement distresses begin to occur. In summer, the surface temperature of the asphalt pavement layer is usually 20°C~30°C higher than the air temperature (Mallick et al., 2009), which leads to rutting distress under such high-temperature conditions.

Rutting distress is essentially the permanent deformation of the pavement layer caused by repeated vehicle loads. When the shear stress generated by the vehicle load exceeds the shear strength of the asphalt mixture, continuous flow deformation accumulates, resulting in flow rutting (Liu et al., 2021). The resistance of asphalt mixture to shear deformation is insufficient, leading to particularly pronounced rutting under high temperatures and heavy loads (Chen et al., 2021). It will not only damage the durability of the bridge deck pavement structure but also significantly affect driving safety and comfort. Therefore, it is critical to clarify the distress causes and the applicability of various pavement structures under complex environmental conditions to mitigate distresses and extend the service life of bridge deck pavement.

To control rutting distress, it is necessary to analyze the mechanical behavior of the bridge deck pavement. Unlike the design stage, the maintenance stage requires consideration of the coupling effects of multiple factors to determine the true causes of the distress. Many researchers have conducted systematic research on the temperature-load coupling effect of asphalt pavement, but they have mainly focused on ordinary asphalt pavements or steel bridge deck pavements. Huang et al. (2009) analyzed the variation of rutting under the vehicle dynamic loads based on a asphalt pavement structure model that considers temperature field changes. Swarna et al. (2018) analyzed the vertical deformation under the coupling effect of temperature and vehicle load, providing a theoretical basis for pavement design. Jiang et al. (2018) conducted repeated loading tests to simulate actual traffic loads and established the load-temperature master curve for asphalt mixture. They studied the effects of temperature and confining pressure on the permanent strain of the asphalt mixture. Zhang (2019) analyzed the mechanical response of steel bridge deck pavement under the combined effect of temperature and dynamic load under the most unfavorable load position. In addition, some scholars have analyzed the influence of the non-uniform temperature field of orthotropic steel bridge deck during the paving process on the pavement layer (Liu et al., 2016; Liu et al., 2019; Fan et al., 2021). However, there are few research on the temperature-load coupling effect in the SCCB bridge deck pavement.

Due to the influence of the supporting structure and bridge deck type, the mechanical response of the pavement layer of SCCB bridges is different from that of steel bridges, concrete bridges, and ordinary asphalt pavements. For SCCB bridges, the difference in stiffness between steel and concrete leads to a more complex stress distribution under vehicle loads. At the same time, steel and concrete belong to different thermal conductive materials, and they exhibit different deformations under the influence of solar radiation and sudden changes in external temperature. All these factors contribute to a more complex mechanical response of SCCB bridge deck pavement under the coupling effect of temperature and load. In recent years, many researchers have evaluated the mechanical response of SCCB bridge, mainly including the flexural behavior (Cheng et al., 2021; He et al., 2021), shear behavior (Kong et al., 2021), and temperature gradient effect of SCCB (Wang et al., 2021), or analyzed the properties of the concrete layer in SCCB (Zhang et al., 2021). However, existing research has relatively little consideration for the mechanical response of SCCB bridge deck pavement.

Therefore, to clarify the permanent deformation behavior of SCCB bridge deck pavement under temperature-load coupling effect and provide references for the distress cause analysis, the whole bridge analysis was firstly conducted to identify the most unfavorable beam segment based on a SCCB bridge located in Yunnan Province, China. Additionally, the most unfavorable conditions of annual temperature difference were selected, and the temperature field model for the SCCB bridge deck pavement was established. Besides, considering the influence of temperature effects, a comparative analysis was conducted on five typical pavement structures to analyze the temperature stress in the bridge deck pavement under periodic temperature variations. Finally, based on the pavement temperature field and the daily variation pattern of traffic volume, the influence of temperature-load coupling on the development of permanent deformation in SCCB bridge deck pavement was examined.

2 Mechanical analysis of whole bridge

2.1 Whole bridge model

The whole suspension bridge model was established to analyze the most unfavorable beam segment by using Midas software. The bridge is a single-span cable-stayed suspension bridge with a single tower, and the approach bridge consists of 2 m × (3 × 41.5) m of pre-stressed concrete continuous box girder bridges. The total length of the entire bridge is 1,020 m. The main bridge is a steel truss suspension bridge, and the steel truss is composed of the main truss, main cross truss, and upper and lower chord members. The main truss has a height of 6 m, a width of 27 m, and a standard segment length of 11.5 m.

In the modeling process, the stiffening girder and main tower were simulated using beam elements, while the main cables and suspenders were simulated using tension-only elements. The segment length of the main beam is 11.5 m, the segment length of approach bridge is 41.5 m, and the height of the main tower is set at 93.5 m. The whole bridge model is shown in Figure 1, and the material parameters are listed in Table 1. In the whole bridge analysis, the vehicle load was taken from the "General Specifications for Design of Highway Bridges and Culverts (JTG D60-2015)" (MOT, 2015), specifically the vehicle load for Highway Class-I. The loading method is applied as the influence line loading.

2.2 Mechanical response and analysis

The vertical bending moment envelope diagram of the whole bridge is shown in Figure 2. The maximum vertical bending moment was 5.6×10^5 kN·m, located near the mid-span of the main span, while the minimum vertical bending moment was -6.5×10^5 kN·m, located on the right side of the main girder. It can be determined that the most unfavorable beam segment was located near the mid-span of the main span and on the right side of the main girder. Therefore, the right side of the main girder was selected as the most unfavorable beam segment for the analysis of temperature stress and temperature-load coupling.

3 Temperature effect analysis

3.1 Temperature condition

A periodic temperature curve was fitted by annual temperature in a specific region in Yunnan Province in China. The average lowest temperature during the cold season was chosen as the simulated lowest temperature, and the average highest temperature during the

FIGURE 1
The whole bridge model.

TABLE 1 The component materials and their section feature value.

Component	A (m^2)	J_d (m^4)	I_y (m^4)	I_z (m^4)	E (MPa)	ρ (kg/m^3)
Main cable	0.3266	0	0	0	2.0×10^5	7,850
Hanger	0.00475	0	0	0	2.0×10^5	7,850
Main beam	1.56	8.21	192.1	3.02	2.1×10^5	7,850
Cable tower	38.172	568.448	442.210	284.638	3.45×10^4	2,600

Note: A-cross-sectional area, J_d-torsional moment inertia, I_y-moment of inertia for transverse bending, I_z-vertical bending moment of inertia, E-elastic modulus, ρ-density.
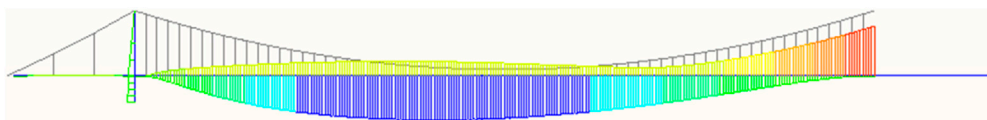
FIGURE 2
Vertical bending moment envelope of whole bridge.
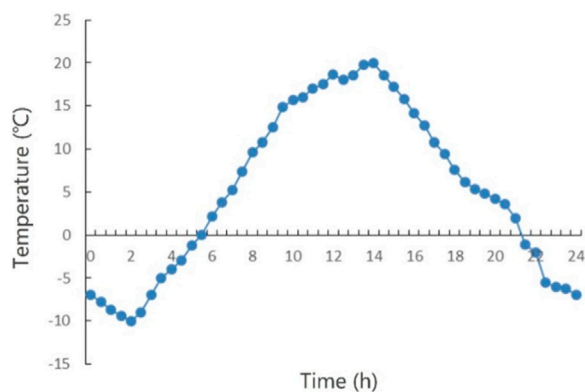
FIGURE 3
Variation curve of external temperature in 1 day.

hot season was chosen as the simulated highest temperature, which were fitted as a temperature cycle in a day, as displayed in Figure 3.

3.2 Local beam segment model

The local beam segment model was established using solid elements in ABAQUS finite element software, the pavement layer

and bridge deck were discretized using solid linear reduced integral elements C3D8R. In the meshing model, the denser mesh was partitioned for the bridge deck pavement and load position, with an element size of 5 mm, while the element size of other components was set as 10 mm. The bridge deck was made of C60 reinforced concrete with a thickness of 16 cm. Both the top and bottom layers were 4 cm thick asphalt concrete, as shown in Figure 4. Five commonly used bridge deck pavement structures were chosen to analyze the temperature distribution under periodic temperature change conditions, including "double-layer asphalt concrete (AC)," "double-layer stone mastic asphalt (SMA)," "AC + SMA," "gussasphalt concrete (GA)+SMA," and "epoxy asphalt (EA)+SMA." The thermal parameters of pavement materials are listed in Table 2, and the thermodynamic constants of temperature field analysis are shown in Table 3.

3.3 Temperature field analysis

The bridge deck pavement is fully attached to the concrete bridge deck and is subjected to both vehicle loads and the influence of external cyclic temperature variations. Due to the large temperature difference within a day in the region where the bridge is located, the bridge deck pavement exhibits complex stress characteristics. Therefore, the following basic assumptions were introduced when establishing the model:
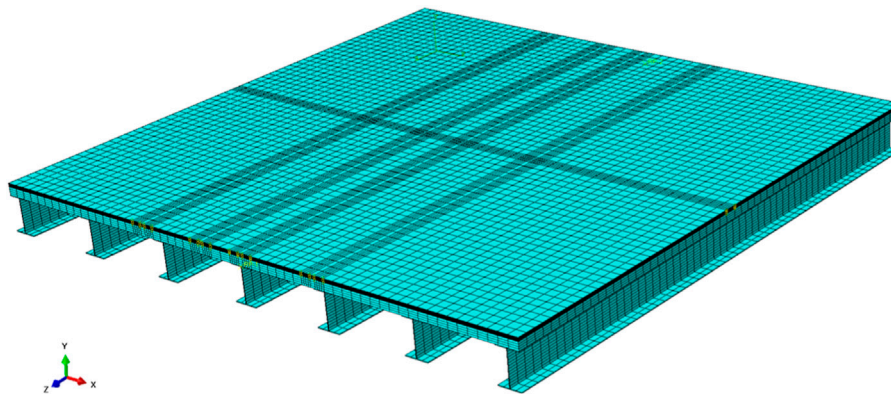
FIGURE 4
Local beam segment model.

TABLE 2 Thermal parameters of pavement materials (Jiang, 2021).

Materials	AC	SMA	EA	GA	Concrete
Thermal conductance (J/m·h·°C)	5,400	6,573	5,551	4,680	6,264
Density (kg/m³)	2,400	2,400	2,400	2,300	2,500
Thermal capacity (J/kg·°C)	920	1,168	946	942	970
Absorption factor of solar radiation			0.90		
Surface emissivity of pavement			0.81		

TABLE 3 Thermodynamic constants of temperature field analysis (Jiang, 2021).

Content	Value
Stefan-Boltzmann constant (J/h·m²·K⁴)	2.04×10^{-4}
Absolute zero (°C)	−273
Daily-mean wind speed (m/s)	3.5
Daily-mean sunshine duration (h)	8.2

(1) Each layer of the bridge deck pavement is uniform, continuous and isotropic.
(2) The interfacial contact condition between layers are completely continuous. In this case, the bonding layer was not specially treated, and its thickness was included in the asphalt concrete paving layer.

In order to facilitate calculations in temperature field analysis, the following assumptions were made in this study:

(1) The temperature and heat flow between the layers were assumed to be continuous.
(2) The heat was transferred one-dimensionally, downwards along with the traffic driving direction.
(3) Except for the given thermo-physical parameters, the other parameters were assumed to be constant.
(4) The temperature field of the bridge deck pavement structure varies cyclically on a daily basis.

(5) After several temperature cycles, the temperature field of the bridge deck pavement structure tended to change steadily and periodically.

The temperature of the bridge deck pavement structure versus time is displayed in Figure 5.

It can be observed that the temperature field variations of different pavement structures are generally consistent. Under the influence of periodic temperature variations in the external environment, the temperature of the bridge deck pavement also exhibited periodic changes, following the periodic temperature field variations in the external environment. And the temperature changed significantly, especially on the surface of the pavement. The "double-layer AC" exhibited the highest pavement surface temperature, reaching 42.16°C, while the "double-layer SMA" had a relatively lower maximum temperature of 39.40°C. The lowest pavement surface temperature followed the same pattern as the highest temperature. The "double-layer AC" had the lowest surface temperature, reaching −4.07°C, while the "double-layer SMA" had the highest minimum surface temperature, which is −3.10°C. The temperature difference on pavement surface of five pavement structures was around 45°C.

3.4 Temperature stress analysis

3.4.1 Assumptions and parameters

The thermoelastic layered system theory was adopted in this article. For the purpose of facilitating the analysis and calculations in

FIGURE 5
Temperature–time distribution of different pavement structures: **(A)** double-layer AC, **(B)** double-layer SMA, **(C)** AC + SMA, **(D)** GA + SMA, and **(E)** EA + SMA.

temperature stress, the following basic assumptions were made in this article:

(1) Each structural layer satisfies the small deformation condition, ensuring the continuity of displacements between layers. Furthermore, there is no relative displacement between the bridge deck and the steel girder.

(2) The Poisson's ratio of each structural layer remains constant, unaffected by temperature variations or load time. The shrinkage and expansion of the concrete bridge deck are not taken into account.

(3) In order to analyze the temperature stress in the bridge deck pavement under periodic temperature variations, unless otherwise specified, the analysis is conducted with reference to time $t = 0$. It is assumed that at $t = 0$, the temperature stress in the pavement is zero.

The material parameters are shown in Table 4.

3.4.2 Contact and boundary conditions

According to reference (Wang et al., 2009), it is stated that when the contact condition between pavement layers is completely smooth, the temperature stress in the pavement is minimal.

TABLE 4 Mechanical parameters and linear expansion coefficient of asphalt mixture (Ma et al., 2021).

Material	T (℃)	Elastic modulus (MPa)	Poisson's ratio	Linear expansion coefficient
AC	−10	2,800	0.35	2.5×10^{-5}
	0	2,000		
	10	900		
	20	570		
	40	250		
SMA	−10	2,600	0.35	3.0×10^{-5}
	0	1,900		
	10	1,200		
	20	870		
	40	554		
EA	−10	6,490	0.2	1.74×10^{-5}
	0	3,950		
	10	2,300		
	20	950		
	40	390		
GA	−10	2,590	0.2	2.04×10^{-5}
	15	710		
	25	320		
	40	100		

Conversely, when the contact condition between pavement layers is completely continuous, the temperature stress in the pavement is maximized. Therefore, this study defined the contact relationship between asphalt pavement layers and between asphalt pavement layer and concrete bridge deck as fully bonded.

During the temperature stress analysis, it is necessary to utilize the boundary conditions of the most unfavorable beam segment obtained from the whole bridge analysis, as discussed in Section 2.2. The vertical bending moments obtained from the most unfavorable beam segment were applied as boundary conditions in the local beam segment model. The schematic diagram of the moment loading on the local beam segment is shown in Figure 6. Simultaneously, the horizontal displacement of the bridge deck pavement was constrained. Since the bridge deck are assembled on the steel girder, it was assumed that no relative displacement occurs between them. Therefore, the bottom surface of the bridge deck was defined as fully fixed.

3.4.3 Temperature stress

When studying the daily variation pattern of temperature stress in the bridge deck pavement, the temperature fields of the pavement layer at different temporal points, obtained in the previous analysis, were imported into the finite element model as predefined fields. It was assumed that the initial temperature stress in the pavement at t = 0 was zero. The temperature stress results are presented in Figure 7.

It can be seen from the figure that for the pavement surface, the maximum tensile stress occurs at 5:30, when the pavement surface temperature is the lowest. Apart from the "double-layer AC" with a maximum tensile stress of 0.76 MPa, the maximum tensile stresses on the surfaces of the other four pavement structures are around 0.85 MPa. The "double-layer AC" exhibits the maximum compressive stress on its surface at 17:00, with a value of 0.39 MPa. On the other hand, the other four pavement structures have maximum compressive stresses around 0.87 MPa on their surface, occurring at 14:00. Based on this, it can be preliminarily inferred that the extreme values of temperature stress on the pavement surface are related to the upper layer material of the pavement. When the upper layer material is SMA, the extreme values of temperature stress on the pavement surface in the four pavement structures ("double-layer SMA," "AC + SMA," "GA + SMA," and "EA + SMA") occur at approximately the same time. This is because the upper layer of the pavement is directly influenced by solar radiation, and its temperature variation is more consistent with the external air temperature changes. Due to the fact that temperature stress is generated as a result of temperature variations within the pavement, the temperature stress variation pattern on the pavement surface is also consistent with the changes in external air temperature.

For the bottom of the upper layer, the maximum tensile stress all occurs at 6:00. The maximum tensile stress between the upper-lower layers of "double-layer AC" is 0.86 MPa, while that of the other four pavement structures are around 0.98 MPa. The maximum compressive stresses occur around 15:00. Except for "double-layer AC" which has a value of 0.35 MPa, the maximum compressive stresses of other pavement structures are around 0.77 MPa.

For the bottom of the pavement, the maximum tensile stress of all five pavement structures occurs at 6:30. Except for "GA + SMA,"
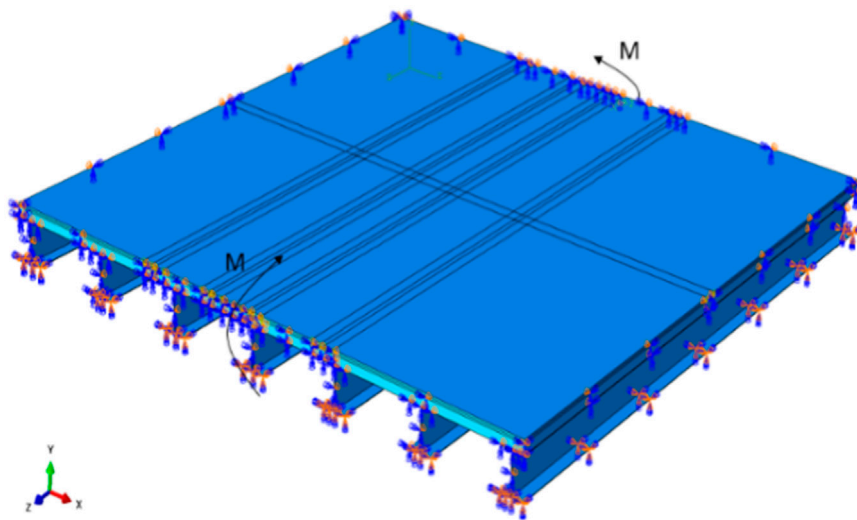
FIGURE 6
The bending moment of the most unfavorable beam segment.

which has the maximum compressive stress at 13:00, the other four pavement structures have the maximum compressive stress at 16: 00 on the bottom of the pavement. The maximum tensile stress at the bottom of the pavement in "double-layer AC," "AC + SMA," and "GA + SMA" is around 0.6 MPa, which has a big difference with that of "double-layer SMA" and "EA + SMA." This is because the elastic modulus of AC and GA is small at high temperature, and the temperature stress generated is relatively small under the condition of the same temperature. Except for "GA + SMA," where the maximum compressive stress occurs at 13:00, the maximum compressive stress at the bottom of the other four pavement structures occurs at 16:00. At the same time, "GA + SMA" has the lowest maximum compressive stress at the bottom, which is 0.12 MPa, while "double-layer SMA" has the highest maximum compressive stress at the bottom, which is 0.59 MPa.

In summary, the temperature stress in the bridge deck pavement is primarily tensile stress at night and compressive stress during the day. From 0:00 to 6:00, as the ambient temperature gradually decreases, the asphalt concrete shrinks when it gets colder, causing the tensile stress to continuously increase. From 6:00 to 14:00, especially between 6:00 and 10:30, the temperature of the bridge deck pavement rapidly increases under the influence of solar radiation. The asphalt concrete heats up and undergoes thermal expansion deformation, causing the internal temperature stress to shift from a state of tension to compression.

4 The permanent deformation of pavement under temperature-load coupling

4.1 Load condition

4.1.1 Load form

According to the "General Specifications for Design of Highway Bridges and Culverts" (JTG D60-2015), the single side of a dual-wheel rear axle with a vehicle load of 140 kN for Highway Class-I was taken, the load distribution was double-wheel rectangular uniform load. The rectangle load size was 0.25 m × 0.20 m, the distance between two vehicle tire centers was 0.30 m, and the tire contact pressure was 0.7 MPa, as shown in Figure 8.

4.1.2 Cumulative load time

The method of cumulative load time was employed in this study to transform the dynamic load into static load for the purpose of analyzing permanent deformation (Faruk et al., 2016). The load times are converted into cumulative load time according to Eq. 1.

$$t = \frac{0.36NP}{n_w pBv} \qquad (1)$$

Where, t is the action time of wheel load; N is the load application times; P is the axle load of the vehicle; n_w is the number of wheels of the shaft; p is tire grounding pressure; B is the tire grounding width; and V is the vehicle driving speed, km/h.

According to Eq. 1, it can be determined that when the vehicle speed is 80 km/h, the one action time of axle load is 0.00804 s, and the cumulative load time for 500,000 axle loads is 4,020 s.

4.1.3 Daily distribution of traffic volume

Based on the daily distribution of traffic volume and the cumulative load time mentioned above, it is possible to approximate the segmented cumulative time of load effects for each hour within a day by considering the distribution of traffic volume during different time periods, as shown in Table 5.

4.2 Material parameters

The creep parameters of asphalt mixture are presented in Table 6. Due to the excellent high-temperature performance of epoxy asphalt mixture, the rutting distress is rarely occurred.
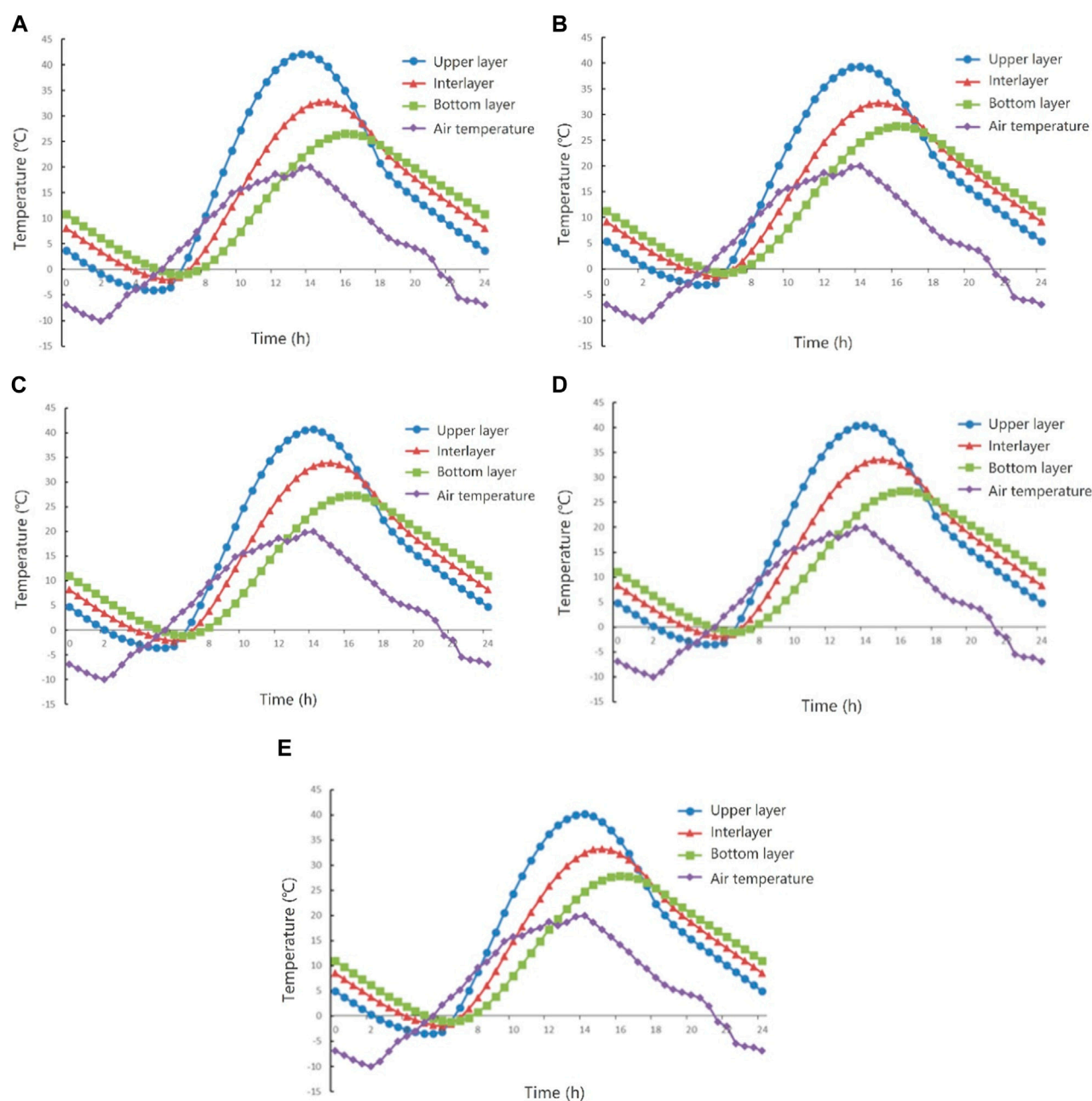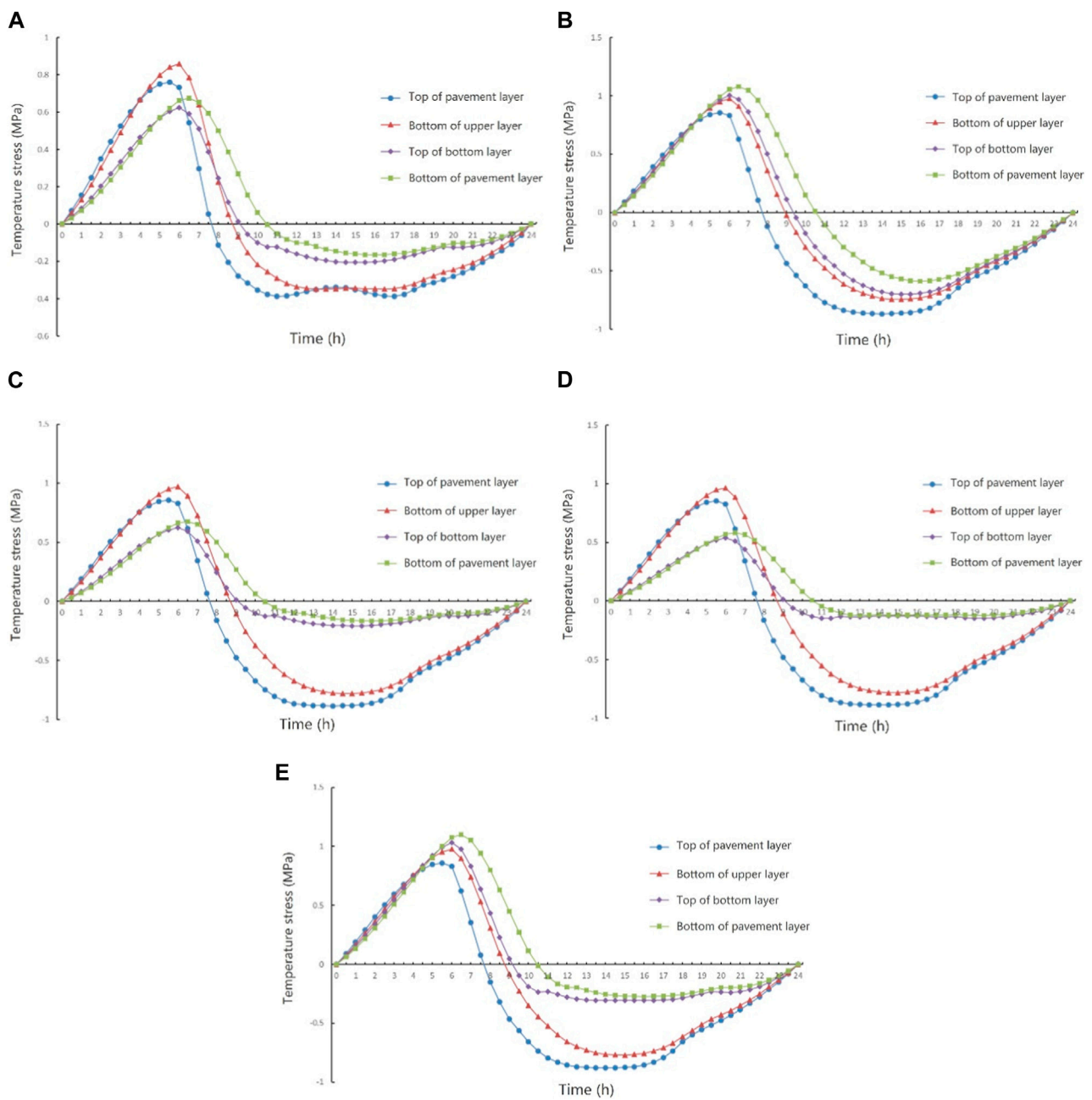
FIGURE 7
Temperature stress-time distribution of different pavement structures: **(A)** double-layer AC, **(B)** double-layer SMA, **(C)** AC + SMA, **(D)** GA + SMA, and **(E)** EA + SMA.
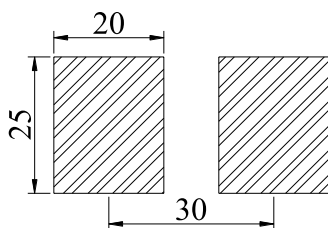
FIGURE 8
Diagram of double-wheel rectangular uniform load.

Additionally, considering the temperature conditions in this study, the internal temperature of the epoxy asphalt may not exceed 30℃. Therefore, it is assumed that the creep effect of the epoxy asphalt mixture is negligible.

4.3 Permanent deformation analysis

4.3.1 Model verification

To verify the rationality of the model, the rutting depth, which is highly sensitive to temperature and load, was chosen as the index in

TABLE 5 Cumulative load time in different periods of a day.

Time of day	Load time (s)	Time of day	Load time (s)	Time of day	Load time (s)
0:00~1:00	41.27	8:00~9:00	115.55	16:00~17:00	363.16
1:00~2:00	33.02	9:00~10:00	181.58	17:00~18:00	313.64
2:00~3:00	29.71	10:00~11:00	231.10	18:00~19:00	280.62
3:00~4:00	16.50	11:00~12:00	297.13	19:00~20:00	198.09
4:00~5:00	23.62	12:00~13:00	313.64	20:00~21:00	165.07
5:00~6:00	33.01	13:00~14:00	264.11	21:00~22:00	148.56
6:00~7:00	46.22	14:00~15:00	297.13	22:00~23:00	115.55
7:00~8:00	82.53	15:00~16:00	346.65	23:00~24:00	82.53

TABLE 6 Creep parameters of asphalt mixture (Wang, 2012; Ma et al., 2021).

Asphalt mixture	A	m	n	T (℃)
AC	4.58×10^{-11}	0.944	−0.596	20
	2.46×10^{-09}	0.796	−0.585	30
	3.67×10^{-08}	0.773	−0.570	40
SMA	6.54×10^{-11}	0.937	−0.592	20
	3.33×10^{-09}	0.862	−0.587	30
	1.45×10^{-08}	0.792	−0.577	40
GA	7.45×10^{-13}	1.352	−0.646	20
	1.88×10^{-12}	1.34	−0.629	40

Note: A, m, n are the creep parameters of the material, related to temperature and stress.

this section. A two-way four-lane SCCB suspension bridge was evaluated in this section which was comprised of 35 mm AC in the lower layer and 35 mm SMA in the upper layer. The rutting depth of two upstream lanes, Lane 1 and Lane 2, were detected after the bridge had been used for 15 months, as presented in Figure 9. The findings are displayed in Figure 10.

The rutting depth under 500,000 axle loads was calculated to be about 2.75 mm. Compared with the measured average rutting depth of Lane 1 (2.86 mm) and Lane 2 (2.80 mm), the absolute error was only 3.85% and 1.79%, respectively. Evidently, the validation of the model was verified and demonstrated by the marginal error of less than 5%.

4.3.2 Pavement structures condition

The creep strain cloud diagram and the permanent deformation at wheel track of the five bridge deck pavement structures under a ground contact pressure of 0.7 MPa are displayed in Figure 11. The horizontal axis 0 represents the position of the load center.

It can be obtained from the figure that "double-layer AC" exhibits relatively significant permanent deformation, with the deformation primarily occurring in the upper layer. Compared to "double-layer AC," "double-layer SMA" exhibits relatively smaller subsidence deformation and heave deformation, indicating better resistance to rutting distress. The deformation results obtained from "AC + SMA" and "double-layer SMA" exhibit similar variations,

which mainly occurs at upper SMA layer. The permanent deformation of "GA + SMA" is different from the above three pavement structures. The heave deformation of the upper layer primarily occurs at the center of the wheel track. Compared to "double-layer SMA," the heave deformation gradually increases from the center of the wheel track towards the sides, but the increment is relatively small, exhibiting a concave-shaped distribution. Besides, the permanent deformation of the lower layer is mainly subsidence deformation at the wheel track, with minimal occurrence of heave deformation. In addition, the deformation is reduced by approximately 30% compared to "double-layer SMA." The permanent deformation of "EA + SMA" is the smallest among the five pavement structures, which is attributed to the rutting resistance performance of epoxy asphalt concrete.

4.3.3 Periodic temperature change condition

In this section, the load time is divided into 24 analysis steps, with each step representing 1 h of a day. The objective is to analyze the variation patterns of permanent deformation in the SCCB bridge deck pavement for each hour of a day. Taking "double-layer SMA" as an example, the permanent deformation at wheel track versus time is shown in Figure 12. It can be observed that, except for the initial load stage from 0:00 to 1:00, the heave deformation between the wheel track is concentrated during the high-temperature period from 10:00 to 18:00. During this time, there is a higher frequency of vehicle load, and the effects of solar radiation are evident. Therefore, the period from 10:00 to 18:00 is the main period during which heave deformation occurs in the pavement layer, accounting for approximately 90% of the total deformation. The heave deformation in the remaining periods is relatively small, and the deformation curve exhibits a roughly inclined "S" shape distribution. The maximum value of subsidence deformation in SCCB bridge deck pavement is slightly smaller than that of heave deformation. In addition to the initial load stage from 0:00 to 1:00, the bridge deck pavement experiences a slight rebound in subsidence deformation during the time periods of 1:00 to 5:00 and 19:00 to 23:00. However, the magnitude of the rebound is relatively small. This is because these time periods correspond to the cooling phase, during which asphalt concrete exhibits shrinkage rebound due to its viscoelastic behavior. The period from 10:00 to 16:00, which corresponds to the heating phase, is the main stage for subsidence deformation in the

FIGURE 9
Rutting depth detection on the bridge deck pavement.
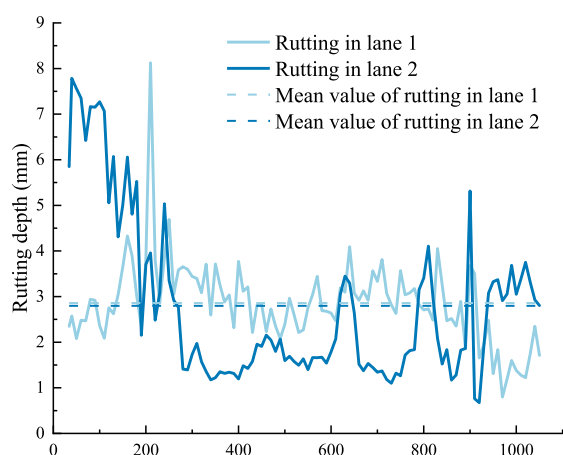
FIGURE 10
The detecting results of rutting depth on the bridge deck pavement.

pavement, accounting for approximately 70% of the total deformation. Additionally, the maximum subsidence deformation occurs during the 12:00 to 13:00 period. In conclusion, whether it is heave deformation or subsidence deformation, the maximum deformation occurs during high-temperature periods. This is because asphalt mixtures have poor stability in high-temperature conditions and are prone to shear deformation. Additionally, traffic volume is mainly distributed during high-temperature periods. Under the combined influence of these factors, significant permanent deformation occurs.

4.3.4 Heavy load condition

Due to the fact that SCCB bridges are often located in traffic throat and suffered severe heavy load condition, it is necessary to investigate the permanent deformation of bridge deck pavement under heavy load conditions in order to ensure their long-term use. Two different ground contact pressures, 0.9 and 1.1 MPa (Wang, 2014), were selected for analysis, and the results were

compared with the results of 0.7 MPa mentioned above. This section will focus only on the comparison between "double-layer SMA" and "EA + SMA." Additionally, variations in ground contact pressure due to different load levels and changes in load application shape will not be considered. The load conditions under different ground contact pressure are shown in Table 7.

The permanent deformation of SCCB bridge deck pavement after 500,000 load applications under different ground contact pressure is shown in Figure 13. The permanent deformation of the pavement increases with the increase of ground contact pressure. And the permanent deformation at wheel track follows a similar lateral distribution pattern as under non-heavy load conditions. For "double-layer SMA," when the ground contact pressure is 0.9 MPa, the heave deformation increases by 11.86% and the subsidence deformation increases by 15.12% compared to the results of 0.7 MPa. Besides, when the ground contact pressure is 1.1 MPa, the heave deformation increases by 19.62% and the subsidence deformation increases by 25.00%. For "EA + SMA," when the ground contact pressure is 0.9 MPa, the heave deformation increases by 11.56% and the subsidence deformation increases by 15.71%; when the ground contact pressure is 1.1 MPa, the heave deformation increases by 19.20% and the subsidence deformation increases by 26.00%. As the ground contact pressure increases, the increment in permanent deformation becomes relatively smaller. This is because the development of rutting distress forms a compacted and squeezed structure between the aggregates in the asphalt mixture, which hinders further rutting formation.

5 Summary and conclusion

(1) The temperature field of the SCCB bridge deck pavement exhibits significant periodic variations with the changes in external temperature, with the temperature of the pavement surface showing the largest fluctuations. Under the temperature conditions simulated in this study, the temperature range of the pavement structure is between −5°C and 45°C, and the
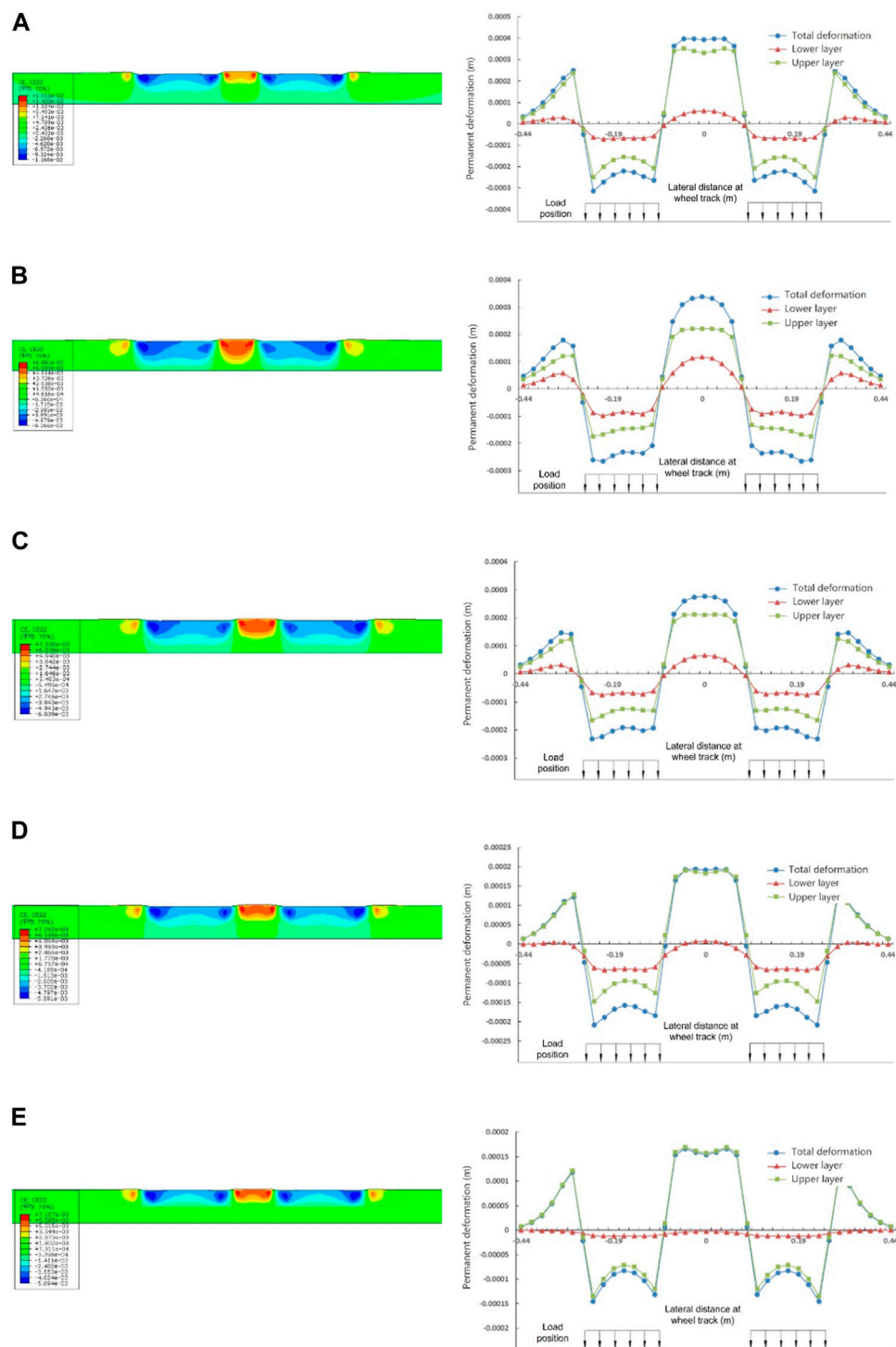
FIGURE 11
Creep strain and permanent deformation at wheel track of different pavement structures: **(A)** double-layer AC, **(B)** double-layer SMA, **(C)** AC + SMA, **(D)** GA + SMA, and **(E)** EA + SMA.

temperature field differences among the five pavement structures are relatively small.

(2) Under the periodic temperature variation conditions considered in this study, the temperature stress in SCCB bridge deck pavement exhibits periodic variations. The temperature stress is primarily tensile stress during the low-temperature periods,

while it is compressive stress during the high-temperature periods.

(3) After 500,000 times of standard axle load, the permanent deformation of "double-layer AC" and "double-layer SMA" are similar, which is around 0.30 mm, and the permanent deformation of "AC + SMA" and "GA + SMA" are around
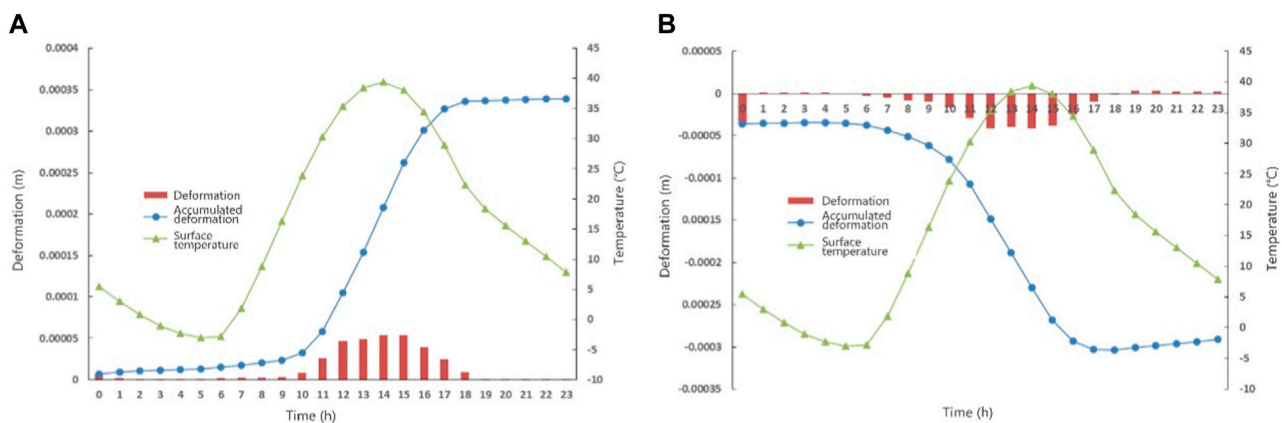
FIGURE 12
Permanent deformation at wheel track versus time of double-layer SMA: **(A)** heave deformation, and **(B)** subsidence deformation.

TABLE 7 Load conditions under different ground contact pressure.

Ground contact pressure (MPa)	Load time (s)	Cumulative load time (s)
0.7	0.00804	4,020
0.9	0.00625	3,125
1.1	0.00512	2,560
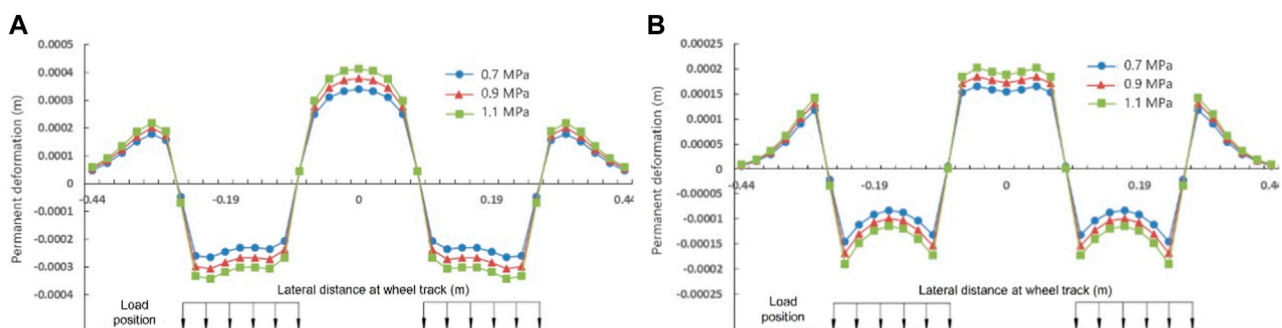
FIGURE 13
Permanent deformation under different ground contact pressure: **(A)** double-layer SMA, and **(B)** EA + SMA.

0.22 mm. The permanent deformation of "EA + SMA" is the smallest, which is 0.17 mm, indicating that "EA + SMA" has the best rutting resistance. Therefore, in areas with severe rutting distresses, it is recommended to use "EA + SMA" pavement structure in SCCB bridge.

(4) The permanent deformation of the SCCB bridge deck pavement increases rapidly during high-temperature periods, while it remains relatively small during low-temperature periods, influenced by the external temperature and traffic volume distribution. The daily deformation curve exhibits a roughly inclined "S" shape distribution.

(5) Heavy load conditions have a great influence on the permanent deformation of SCCB bridge deck pavement.

Under the same temperature conditions and cumulative load time, the permanent deformation increases with the increase of ground contact pressure. Moreover, the lateral distribution pattern of permanent deformation at the wheel track remains relatively consistent. Thus, efforts should be made to avoid overload and heavy load conditions as much as possible.

Data availability statement

The raw data supporting the conclusion of this article will be made available by the authors, without undue reservation.

Author contributions

JY: Conceptualization, Methodology, Writing–original draft. LT: Data curation, Software, Visualization, Writing–original draft. XQ: Investigation, Software, Writing–review and editing. CZ: Writing–review and editing.

Funding

Conflict of interest

The authors declare that the research was conducted in the absence of any commercial or financial relationships that could be construed as a potential conflict of interest.

Publisher's note

All claims expressed in this article are solely those of the authors and do not necessarily represent those of their affiliated organizations, or those of the publisher, the editors and the reviewers. Any product that may be evaluated in this article, or claim that may be made by its manufacturer, is not guaranteed or endorsed by the publisher.

References

Chen, L. L., Liu, G., Yao, B., and Qian, Z. D. (2021). Rutting prediction model for semirigid base asphalt pavement based on hamburg wheel tracking test. *Int. J. Geomech.* 21, 04021215. doi:10.1061/(ASCE)GM.1943-5622.0002194

Cheng, Z. Y., Zhang, Q. H., Bao, Y., Deng, P. H., Wei, C., and Li, M. Z. (2021). Flexural behavior of corrugated steel-UHPC composite bridge decks. *Eng. Struct.* 246, 113066. doi:10.1016/j.engstruct.2021.113066

Fan, L., Yang, W. P., Zhou, D., and Li, Z. Y. (2021). Temperature distribution and mechanical response of orthotropic steel bridge deck during paving of gussasphalt pavement. *Int. J. Steel Struct.* 21, 315–328. doi:10.1007/s13296-020-00440-3

Faruk, A. N. M., Liu, W., Lee, S. I., Naik, B., Chen, D. H., and Walubita, L. F. (2016). Traffic volume and load data measurement using a portable weigh in motion system: A case study. *Int. J. Pavement Res. Tech.* 9, 202–213. doi:10.1016/j.ijprt.2016.05.004

He, Z. Q., Ou, C. X., Tian, F., and Liu, Z. (2021). Experimental behavior of steel-concrete composite girders with UHPC-grout strip shear connection. *Buildings* 11, 182. doi:10.3390/buildings11050182

Huang, X. M., Yang, Y. W., Li, H., and Liu, M. (2009). Asphalt pavement short-term rutting analysis and pridiction considering temperature and traffic loading conditions. *J. Southeast Univ. En. Ed.)* 25, 385–390.

Jiang, J. W., Dong, Q., Ni, F. J., and Yu, H. f. (2018). Development of permanent deformation master curves of asphalt mixtures by load-temperature superposition. *J. Mater. Civ. Eng.* 30, 04018098. doi:10.1061/(ASCE)MT.1943-5533.0002300

Jiang, S. (2021). *Prediction of rutting of composite guss asphalt steel bridge deck pverlay* (Nanjing: Southeast Universit). [master's thesis].

Kong, F. L., Huang, P. M., Han, B., Wang, X. Z., and Liu, C. Q. (2021). Experimental study on behavior of corrugated steel-concrete composite bridge decks with MCL shape composite dowels. *Eng. Struct.* 227, 111399. doi:10.1016/j.engstruct.2020.111399

Liu, G., Chen, L. L., Qian, Z. D., Zhang, Y. H., and Ren, H. S. (2021). Rutting prediction models for asphalt pavements with different base types based on RIOHTrack full-scale track. *Constr. Build. Mater.* 305, 124793. doi:10.1016/j.conbuildmat.2021.124793

Liu, Y., Qian, Z. D., and Hu, H. Z. (2016). Thermal field characteristic analysis of steel bridge deck during high-temperature asphalt pavement paving. *KSCE J. Civ. Eng.* 20, 2811–2821. doi:10.1007/s12205-016-0027-2

Liu, Y., Qian, Z. D., and ZhengZhang, D. M. (2019). Interlaminar thermal effect analysis of steel bridge deck pavement during gussasphalt mixture paving. *Int. J. Pavement Eng.* 20, 1323–1335. doi:10.1080/10298436.2017.1413240

Ma, T., Liao, G. Y., and Huang, X. M. (2021). *Application of ABAQUS finite element software in road engineering*. Nanjing: Southeast University Press.

Mallick, R. B., Chen, B. L., and Bhowmick, S. (2009). Harvesting energy from asphalt pavements and reducing the heat island effect. *Int. J. Sustain. Eng.* 2, 214–228. doi:10.1080/19397030903121950

MOT (Ministry of Transport of P.R. China) (2015). *General specification for design of Highway bridges and Culverts, JTG D60-2015*. Beijing: China Communications Press.

Swarna, S. T., Reddy, K. S., Reddy, M. A., and Pandey, B. B. (2018). Analysis of stresses due to traffic and thermal loads in two-lift bonded concrete pavements by finite element method. *Adv. Civ. Eng. Mater.* 7, 20170028–20170222. doi:10.1520/ACEM20170028

Wang, D., Tan, B. K., Wang, X., and Zhang, Z. H. (2021). Experimental study and numerical simulation of temperature gradient effect for steel-concrete composite bridge deck. *Meas. Control-Uk* 54, 681–691. doi:10.1177/00202940211007166

Wang, H. (2012). *Analysis of steel deck pavement performance subjected to coupling of heavy load and temperature* (Nanjing: Southeast University). [master's thesis].

Wang, Q., Tong, S. J., Wang, X. C., and Zeng, W. (2009). Analysis on the temperature field and temperature stress of bridge deck pavement. *J. Xi'an Univ. Arch. Tech. Nat. Sci. Ed.)* 41, 219–224.

Wang, Y. (2014). *Study on rutting prediction of long-span steel bridge deck compound gussasphalt pavement* (Nanjing: Nanjing Forestry University). [master's thesis].

Zhang, H. T. (2019). *Asphalt concrete bridge deck analysis of mechanical response under temperature and dynamic load* (Xi'an: Chang'an University). [master's thesis].

Zhang, H., Zhang, Z. X., Gao, P. W., Cui, L., Pan, Y. Q., and Li, K. (2021). Performance of steel bridge deck pavement structure with ultra high performance concrete based on resin bonding. *Front. Struct. Civ. Eng.* 15, 895–904. doi:10.1007/s11709-021-0759-z

Comparative study of typical asphalt binders in Xinjiang region modified with warm mix additives

Bangyan Hu[1,2]*, Xianchen Ai[2,3] and Juan Feng[1]

[1]College of Civil Engineering and Architecture, Xinjiang University, Urumqi, China, [2]Xinjiang Key Laboratory of Green Construction and Smart Traffic Control of Transportation Infrastructure, Urumqi, China, [3]School of Traffic and Transportation Engineering, Xinjiang University, Urumqi, China

Xinjiang's representative asphalt binders, such as Karamay and Tahe asphalt, lack sufficient research on warm-mix additive modification effects. Given their unique microstructure and molecular composition differences, comprehensive investigations are essential for a nuanced understanding of these binders. This study added Sasobit and Evotherm warm mix additives to Karamay 90# asphalt and Tahe 90# asphalt, respectively. The evaluation of diverse warm mix additives' impact on diverse asphalt binders involved viscosity, softening point, penetration tests, Fourier transform infrared (FTIR) and analysis of saturate, aromatic, resin, and asphaltene (SARA) fractions. Additionally, molecular models of asphalt were constructed using Materials Studio software, based on the SARA test data. Molecular models of Sasobit and Evotherm were also developed, representing organic wax and a cationic quaternary ammonium surfactant, respectively. Conducting molecular dynamics simulations of warm mix additives and two asphalt molecules yielded valuable insights into solubility parameters and the radial distribution function (RDF). This approach enabled a thorough and comparative exploration of the modification mechanisms employed by various warm mix additives on different asphalt types at a molecular scale. The results indicate that, Evotherm excelled in enhancing high-temperature asphalt performance, while Sasobit surpassed it in low-temperature. The viscosity reduction by Sasobit proved more effective for K90, while for T90 asphalt, the trend was reversed with Evotherm exhibiting superior performance. The solubility parameter in MD simulations consistently correlates with asphalt viscosity results. Sasobit showed enhanced compatibility with K90 asphalt, while T90 asphalt demonstrated greater suitability for modification with Evotherm.

KEYWORDS

warm mix asphalt, Xinjiang asphalt binders, FTIR, SARA, Molecular dynamics simulation

1 Introduction

Positioned in China's northwest, Xinjiang plays a pivotal role in connecting China and Central Asia through the "Belt and Road" initiative (Transport, E. D. O. C. J. O. H. A., 2020). Its robust transportation sector amplifies infrastructure needs in the carbon-neutral era (Chen et al., 2023a; Cheng et al., 2023). Low-carbon technologies were actively pursued by industries for a green transformation, while strategies for low-carbon and decarbonization

TABLE 1 Technical indicators of the base asphalt binder.

Indicator	Unit	K90 Test data	T90 Test data	Technical requirements
Penetration (25°C,5°s,100 g)	0.1 mm	96.9	92.2	80–100
Penetration indexPI	—	−0.3692	0.5079	−1.5–1.0
Softening point (TR&B)	°C	53.6	67.5	≥45
Ductility (10°C)	cm	123.1	>150	≥20
Ductility (15°C)	cm	131.7	>150	≥100
Density	(g/cm^3)	0.981	1.024	Measurement records
After TFOT (5 h,163°C)				
Mass loss	%	−0.181	−0.359	±0.8
Residual penetration ratio	%	57.0	64.3	≥57
Residual Ductility (10°C)	cm	27.5	>150	≥8
Residual Ductility (15°C)	cm	65.9	>150	≥20

FIGURE 1
Asphalt warm mix additives.

are explored by the road building sector (Zhang L. et al., 2023; Chen et al., 2023b). Among these approaches, warm-mix asphalt (WMA) emerges as a potent method for reducing energy consumption (Rubio et al., 2012). In contrast to traditional hot-mix asphalt, WMA involved lower temperatures in mixing, paving, and compaction. This conserves fuel and reduces emissions of harmful gases and smoke (Kim et al., 2011). Furthermore, the occurrence of severe thermal aging in asphalt binders during the construction process was mitigated (Banerjee et al., 2012).

Xinjiang, endowed with abundant oil and gas resources, features Karamay asphalt (KLMY) and Tahe asphalt (TH) as its most representative petroleum products. KLMY known for its high production and convenient transportation, has been extensively utilized in road construction throughout Xinjiang (Wang et al., 2022). The chemical composition of KLMY notably differed from the commonly used road petroleum asphalt in China,

exhibiting characteristics such as minimal wax content, elevated resins content, and extremely low asphaltene content (Gao et al., 2022). Consequently, exceptional performance was exhibited in low temperatures, resistance to aging, and fatigue. Nevertheless, KLMY's unique composition, notably its limited compatibility with commonly employed modifiers, especially high-molecular-weight polymer modifiers, presents challenges in preparing modified asphalt (Yu et al., 2018; Yu et al., 2019). In contrast, TH another petroleum asphalt variety produced in Xinjiang, diverged from KLMY. With a significantly higher asphaltene content than commonly used road petroleum asphalt, TH excels in high-temperature performance but exhibited poorer low-temperature ductility, coupled with a relatively lower price (Ning et al., 2015). In practical engineering in Xinjiang, there was widespread reliance on asphalt from other provinces or imports for modification, hindering cost control and large-scale application. Consequently, a focus has been placed by researchers on investigating the mechanistic aspects of modifying Xinjiang asphalt to develop WMA tailored to the region (Jiang et al., 2021).

To address the challenge of inadequate stability between WMA and asphalt binders, the focus has been primarily placed on the structural mechanisms of asphalt, modification processes, and comprehensive performance evaluation by researchers (Oyan, 2022). In this pursuit, three main groups are identified for categorizing WMA additives: organic additives, foaming processes and additives, and chemical additives. Another approach involves the combination of two or more of the aforementioned methods to reduce binder viscosity (Jiang et al., 2021). In a study conducted by Sengoz et al., the physical and rheological properties of asphalt were examined with the inclusion of natural or synthetic zeolites. The study revealed that the asphalt stiffness and temperature susceptibility demonstrated an increase after the introduction of zeolite. However, as a hydrophilic inorganic material, zeolite demonstrated poor compatibility with asphalt, resulting in its

TABLE 2 Basic information and preparation process of WMA.

WMA additive	Content (% by weight)	Preparation process	Karamay asphalt ID	Tahe asphalt ID
Sasobit	1%, 2%, 3%, 4%, and 5%	Sheared for 20 min (160°C, 3000 rpm)	KS1, KS2, KS3, KS4, KS5	TS1, TS2, TS3, TS4, TS5
Evotherm	0.2%,0.4%, 0.6%, 0.8%, and 1%	Sheared for 10 min (160°C, 600 rpm)	KE0.2, KE0.4, KE0.6,KE0.8,KE1	TE0.2, TE0.4, TE0.6, TE0.8, TE1

FIGURE 2
Corbett separation scheme.
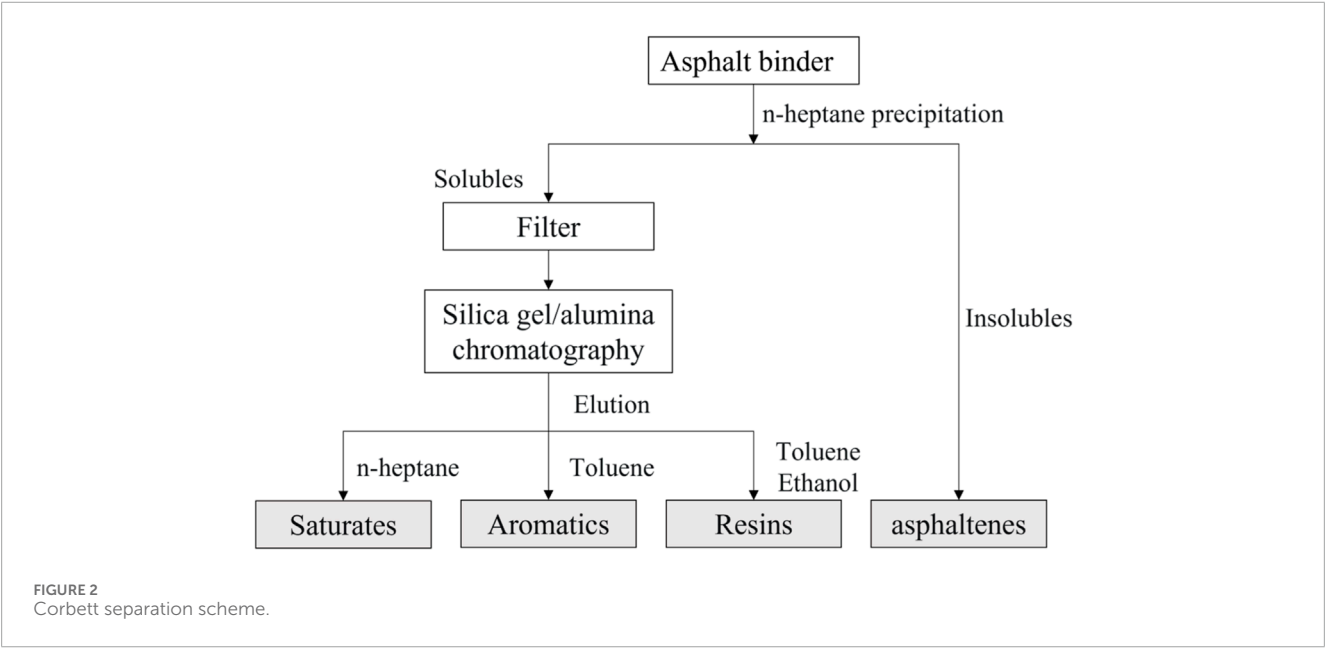
poor dispersion in asphalt (Sengoz et al., 2013; Topal et al., 2014). Hossain et al. evaluated the effects of the addition of high quantities of paraffinic waxes to a base asphalt through rheological criteria. The shear viscosity and dynamic mechanical spectra indicate that wax perturbs the overall colloidal equilibrium of the base asphalt, thereby generating highly structured asphaltic materials (Hossain et al., 2013). Yu et al. modified crumb-rubber-modified asphalt with the addition of Sasobit and Evotherm, and the two products exhibited different responses in different content and situations. It was difficult to determine which product is better or what is the optimum content. Instead, the choice of the product and content highly depended on the environment, particularly the temperature, in which they were intended to be used (Yu et al., 2013).

Overall, the main reason for the poor stability in warm-mixed modified asphalt lay in the inadequate dispersion of the modifier in the asphalt and the unsuitability of the chosen modifier for the specific asphalt and engineering requirements. Despite scholars having extensively investigated the compatibility and stability of warm-mixed modified asphalt from process parameters to additives, research on the distinctive high-gel asphalt (Karamay asphalt) and high-asphaltene asphalt (Tahe asphalt) remained relatively limited.

Therefore, this study focused on two typical types of asphalt in Xinjiang, namely KLMY and TH. Two warm mix agents, Sasobit and Evotherm, were selected for investigation. The analysis involved examining the interactions between these agents and asphalt binders. The primary emphasis was on investigating the

TABLE 3 The wavenumber of each functional groups (Wen, 2010).

Functional group	Area of peak between (cm^{-1})
Asymmetrical stretching -CH$_2$-	2936–2916
Symmetrical stretching of -CH$_2$-	2863–2843
C=C stretch in aromatics	1642–1547
C-H asymmetric deform in CH$_2$ or CH$_3$	1490–1430
C-H symmetric deform in CH$_3$	1385–1365
= C-H bending vibration of benzene ring	900-800,830-800
C-H stretching in CH$_2$ or CH$_3$	764–650

impact of varying application quantities on the fundamental properties of asphalt. Molecular dynamics (MD) simulation techniques were employed to analyze the viscosity reduction mechanisms of different warm mix agents in diverse asphalt compositions. This research aimed to offer crucial insights into the technology of WMA and base asphalt binder modification in Xinjiang.
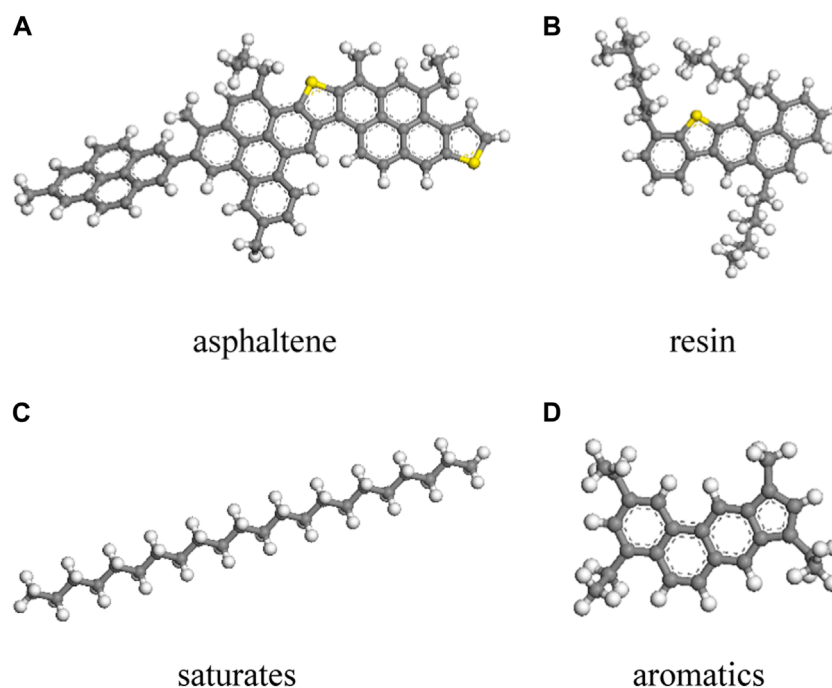
FIGURE 3
Asphalt molecules consist of these four components: **(A)** asphaltene, **(B)** resin, **(C)** saturates and **(D)** aromatics.
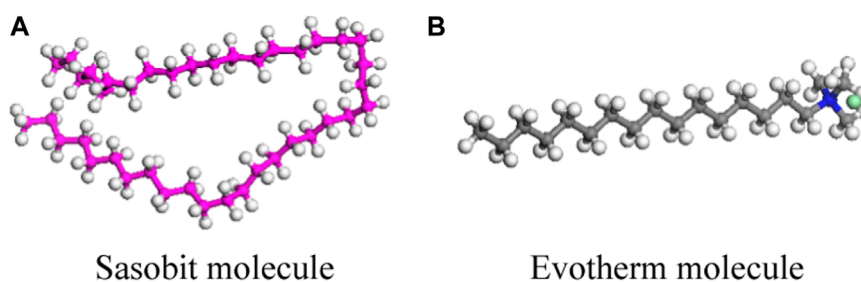
FIGURE 4
Molecular models of WMA additives: **(A)** Sasobit molecule and **(B)** Evotherm molecule.

2 Materials and methodology

2.1 Raw materials

2.1.1 Base asphalt

The base asphalt used in the research were KLMY90# asphalt (K90) and TH90# asphalt (T90), both produced by Sinopec Group. The basic properties of base asphalt were summarized in Table 1.

2.1.2 Warm-mix additives

In this study, two typical WMA additives, namely the wax-based WMA additive Sasobit and the surfactant WMA additive Evotherm, were employed. The visual representations of these additives can be observed in Figure 1. Sasobit, sourced from Sasol Chemicals in Nanjing, Jiangsu Province, China, exhibits a melting point of

approximately 100°C and effectively liquefies in asphalt above this temperature. Evotherm, a patented product of MeadWestvaco in Shanghai, China, was employed in the form of Evotherm M1 in this study.

2.1.3 Warm mix asphalt binders

Considering the disparities in physical state (solid versus liquid) and mechanisms for viscosity reduction, Sasobit and Evotherm were incorporated into the asphalt using distinct mixing procedures. In the preparation of the WMA containing Sasobit, the base asphalt was heated to 160°C in an oil bath. Once the target temperature was reached, Sasobit pellets (1%, 2%, 3%, 4%, and 5% by mass of asphalt binder) were gradually added while the binder was stirred at a relatively low speed. Subsequently, stirring was continued for an additional 20 min at a speed of 3000 rpm to ensure the formation of a homogeneous binder.
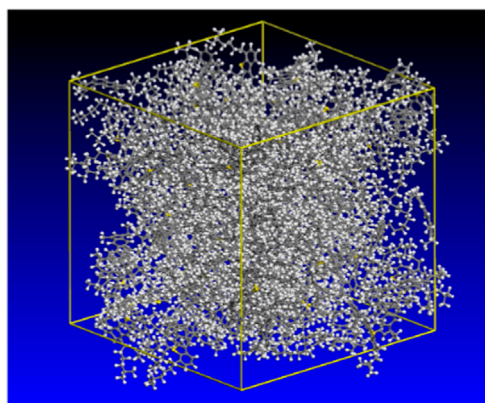
FIGURE 5
K90 asphalt molecular model.

In the formulation of the base asphalt containing Evotherm, the authors expressed concern that prolonged stirring (20 min) at 160°C could potentially compromise its functionality. Therefore, the blending time was restricted to 10 min. Table 2 outlines the key characteristics of the WMA additives and delineates the steps involved in preparing the WMA binders.

2.2 Test procedures

2.2.1 Physical indexes test

Asphalt property tests were performed on the asphalt samples, focusing primarily on penetration (at 15°C, 20°C, and 25°C), Brookfield rotational viscosity (at 90°C, 105°C, 120°C, 135°C, 150°C, and 165°C), ductility (at 10°C) and softening point assessments. The test procedures adhered to the guidelines outlined in the ASTM D5-06e1, ASTM D113-17, ASTM D4402-15, and ASTM D3461-18 standards, ensuring standardized and accurate measurements.

2.2.2 Corbett separation and colloidal index

The Corbett method has been widely employed in the fractionation of asphalt binder into saturates, aromatics, resin, and asphaltene (SARA) components (Xu et al., 2018b). This method utilizes solubility procedures and column chromatographic techniques to achieve the separation. A schematic representation of the Corbett separation process is illustrated in Figure 2.

The colloidal instability index (CII) serves as a metric to depict the intricate internal microstructure of binders (Masoumeh et al., 2016; Eltwati et al., 2022). According to the Gaestel theory, the presence of ample quantities of resins and aromatics can lead to the full peptization of asphaltenes, resulting in an effective mobility of micelles within asphalt (Siddiqui and Ali, 1999). CII is defined as the ratio of diffused components (aromatics and resins) to non-diffused compounds (saturates and asphaltenes). The following formula, Eq. 1, determines this parameter, proving to be highly useful for comparing different types of asphalt binders (Salehfard et al., 2021).

$$CII = \frac{(\text{Asphaltenes in wt\%}) + (\text{Saturates in wt\%})}{(\text{Resins in wt\%}) + (\text{Aromatics in wt\%})} \quad (1)$$

2.2.3 Fourier transform infrared (FTIR) test

The infrared spectrometer (IR), utilizing the selective absorption characteristics of the tested material for infrared radiation at different wavelengths, is an instrument employed for the analysis of molecular structures and chemical compositions. The FTIR has been recognized as a powerful tool for analyzing asphalt binders to determine functional groups, including carbonyl, hydroxyl, amine, amide, nitrile, ester, carboxylic, and aromatic groups (Brako and Wexler, 1963). The FTIR principle relies on the distinct vibration and rotation modes exhibited by various molecular bonds, which are identifiable through characteristic bands in the absorption spectrum of transmitted infrared radiation (Cheng et al., 2020). In this study, ATR-FTIR (Bruker VERTEX70) was utilized to identify the chemical functional groups of asphalt binders and their fractions. The scan ranged from 4,000 cm^{-1}–600 cm^{-1} with a 4 cm^{-1} resolution. To minimize experimental error, three replicates were tested for each specimen. Table 3 summarizes the typical peak positions of chemical functional groups.

2.3 Simulation models and methods

2.3.1 Construction of molecular model
(1) Asphalt Components

A molecular model of asphalt was constructed, providing input for Molecular Dynamic simulation. Two construction approaches were found in the literature: one involved an average model structure for the entire asphalt, and the other comprised a composition model consisting of several asphalt fractions (Chen et al., 2018). With advancements in experimental precision and an enhanced understanding of asphalt, researchers introduced asphalt models that exhibited higher levels of accuracy. In 2007, Zhang and Greenfield introduced a three-component model, utilizing two molecules to represent asphaltene, and one molecule each for resin and saturates (Zhang and Greenfield, 2007). Later, they put forth a four-component model (Zhang and Greenfield, 2008). In 2014, The 12 molecular models of SARA components proposed by Li and Greenfield, including SHRP AAA-1, AAK-1, and AAM-1, have been confirmed to be highly consistent with the real asphalt system (Li and Greenfield, 2014). In subsequent research, scholars in asphalt molecular modeling commonly adopted a twelve-molecule model (Li et al., 2022; Lu et al., 2022; Zhang J. et al., 2023). However, achieving consistency with experimental results became challenging when applying the 12 molecular models to allocate SARA, given the unique composition of Xinjiang asphalt. Hence, this paper adopted the four-molecule model proposed by Hansen in 2013 (Figures 3A–D) (Hansen et al., 2013). This relatively straightforward model has been demonstrated to predict the physical and rheological properties of asphalt binders in a general sense (Xu and Wang, 2016).

(2) Warm-Mix Additives

Sasobit® Sasol wax is a synthetic hydrocarbon hard wax obtained as by-product of the Fischer-Tropsch (FT) process, where hydrocarbons are synthesized from hydrogen and carbon monoxide. Sasobit has the molecular formula CnHn+2, and its long chain generally consists of 40–115 carbon atoms. Forty carbon atoms were selected to construct the Sasobit model (Figure 4A).

FIGURE 6
Density and energy curves of NPT equilibration process.
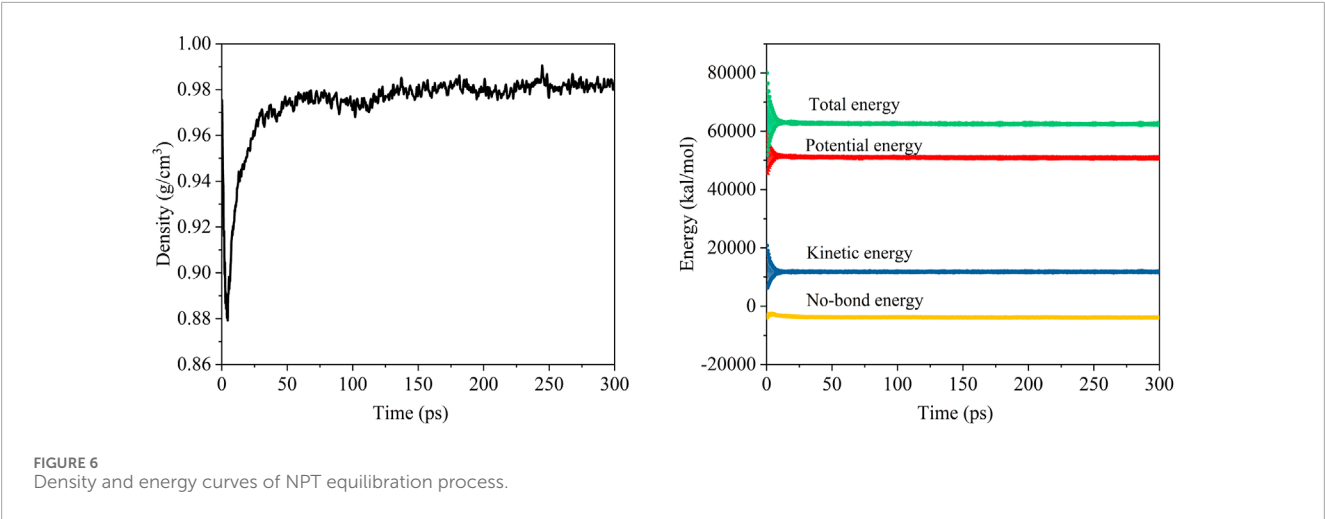
TABLE 4 Penetration correlation calculation table (Karamay asphalt).

ID	Penetration/0.1 mm			R^2	PI	T_{800}/°C	$T_{1.2}$/°C
	15°C	20°C	25°C				
K90	33.6	96.9	141.6	0.997	−0.369	47.32	−19.44
KS1	29.0	79.9	135.3	0.999	−0.699	47.38	−16.07
KS2	26.9	77.9	128.2	0.999	−0.811	47.49	−14.84
KK3	25.9	75.9	124.6	0.999	−0.867	47.53	−14.26
KS4	22.1	67.9	114.0	0.999	−1.137	47.61	−11.32
KS5	20.2	65.6	110.0	0.997	−0.345	49.27	−7.89
KE0.2	30.1	79.5	122.0	0.999	−0.131	49.81	−19.40
KE0.4	28.2	75.6	110.0	0.997	−0.016	51.13	−19.29
KE0.6	27.0	71.6	105.8	0.999	0.016	51.75	−19.02
KE0.8	26.1	69.5	101.0	0.998	0.050	52.24	−18.88
KE1	25.1	64.4	96.0	0.999	0.152	53.35	−18.87

Evotherm is a surfactant manufactured by MeadWestvaco (United States), and the surfactant is a patented product with an unknown molecular structure. However, Zhao pointed out that MeadWestvaco Company's third-generation product, Evotherm® M1, is a cationic quaternary ammonium surfactant (Zhao, 2012). Hence, in this paper, referencing literature (Wu et al., 2022), Cetyltrimethylammonium Chloride (CTAC), a cationic surfactant with the molecular formula $C_{19}H_{42}ClN$, was chosen to construct the Evotherm model, as shown in Figure 4B.

(3) Asphalt Molecular Model

The molecular model of the base asphalt was constructed according to the ratio the SARA fractions of asphalt using the Amorphous cell module in the Materials Studio; Taking the K90 as an example, as shown in the Figure 5.

2.3.2 Molecular dynamics simulation process

The Compass II force field in Materials Studio 2019 was employed in this paper. Prior to constructing the asphalt model, the component models and additive models were subjected to the Compass II force field and charges, and then underwent geometry optimization. The asphalt bulk model was created using the amorphous cell module, following 20,000 iterations of geometry optimization. A temperature range of 26.85°C–1526.85°C was established. Following geometry optimization and energy optimization, a subsequent annealing process was undertaken to refine the model, bringing it into closer approximation to the
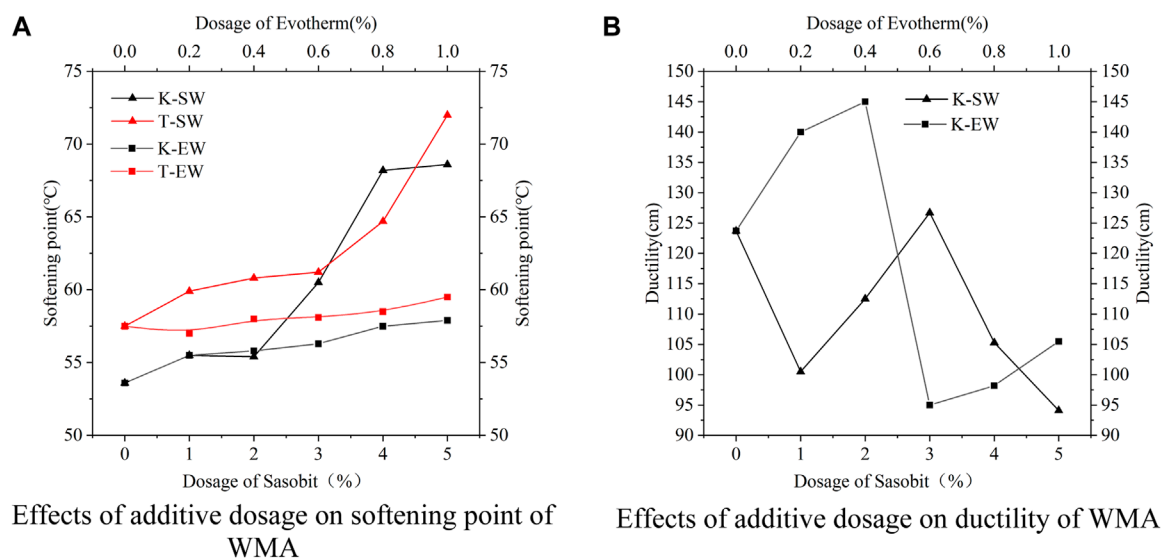
FIGURE 7
Softening point and ductility of WMA: **(A)** Softening point and **(B)** Ductility.

authentic molecular state (Yusuff et al., 2021). A 500ps dynamic equilibration simulation was conducted with the NVT ensemble (N = constant number of atoms, V = constant volume, and T = constant temperature) to transition the asphalt model from its initial state to an equilibrium state at normal temperature. Subsequently, a 500ps dynamic equilibration simulation was performed with the NPT ensemble (N = constant number of atoms, P = constant pressure, and T = constant temperature) at 1 atm to ensure that the system density matched real asphalt at 25°C. A final 500ps dynamic data collection simulation was executed to gather the required data. A Nose thermostat was employed during the dynamic equilibration process, and an Andersen thermostat was utilized in the dynamic data collection process. After the dynamic equilibration process and dynamic data collection process, all the models exhibited equilibrium density and equilibrium energy (Figure 6). To avoid data duplication, only the equilibrium curves after the NPT equilibration process of the K90 model was shown.

2.3.3 Quantitative analysis indicators
(1) Solubility Parameter

According to the derivation of Hildebrand et al.(Hildebrand and Scott, 1951), the solubility parameter enthalpy of mixing (ΔH_m) measures the compatibility of the materials and was calculated as Eqs 2–5.

$$\Delta H_m = \left[\frac{N_j V_j \cdot N_k V_k}{N_j V_j + N_k V_k} \right] \left[\delta_j - \delta_k \right] \tag{2}$$

$$\delta_j = \sqrt{\frac{\Delta E_j}{V_j}} \tag{3}$$

$$\delta_k = \sqrt{\frac{\Delta E_k}{V_k}} \tag{4}$$

$$\Delta\delta = \left| \delta_j - \delta_k \right| \tag{5}$$

The polymers j and k have relative molecular masses of N_j, N_k, their molar volumes are V_j and V_k, and their cohesive energy densities (CED) are $\frac{\Delta E_j}{V_{kj}}$ and $\frac{\Delta E_k}{V_k}$,respectively. The solubility parameters of the polymers are δ_j and δ_k, and the absolute values of the differences in solubility parameters is $\Delta\delta$.

Upon completing the processing of the Cohesive Energy Density task, the solubility parameters were obtained. A reduced difference between the solubility parameters for each molecular model indicate a higher compatibility between the two polymers.

(2) Radial distribution function

Radial distribution function (RDF) was used to quantify the cohesion between asphalt molecules in the MD. The molecular effects of warm-mix additives on cohesion can be further investigated using RDF.

The functional connection between the density and the distance from a reference point is described by the RDF, a statistical mechanics technique. The parameter g(r) Eq. 6 represents the probability of selected molecules in an asphalt molecule being at a distance from selected reference molecules and was used to define the aggregation behavior of asphalt molecules. The center of mass of the asphaltene was used as the reference point in this investigation.

$$g(r) = \frac{1}{4\rho\pi r^2 \xi r} \frac{\sum_{t=1}^{T} \sum_{j=1}^{N} \Delta N(r \to r + \xi r)}{N \times T} \tag{6}$$

where N = total number of molecules; T = total time of calculation (ps); r = distance from given reference point; ΔN = number of molecules within system interval; and ρ = system density.
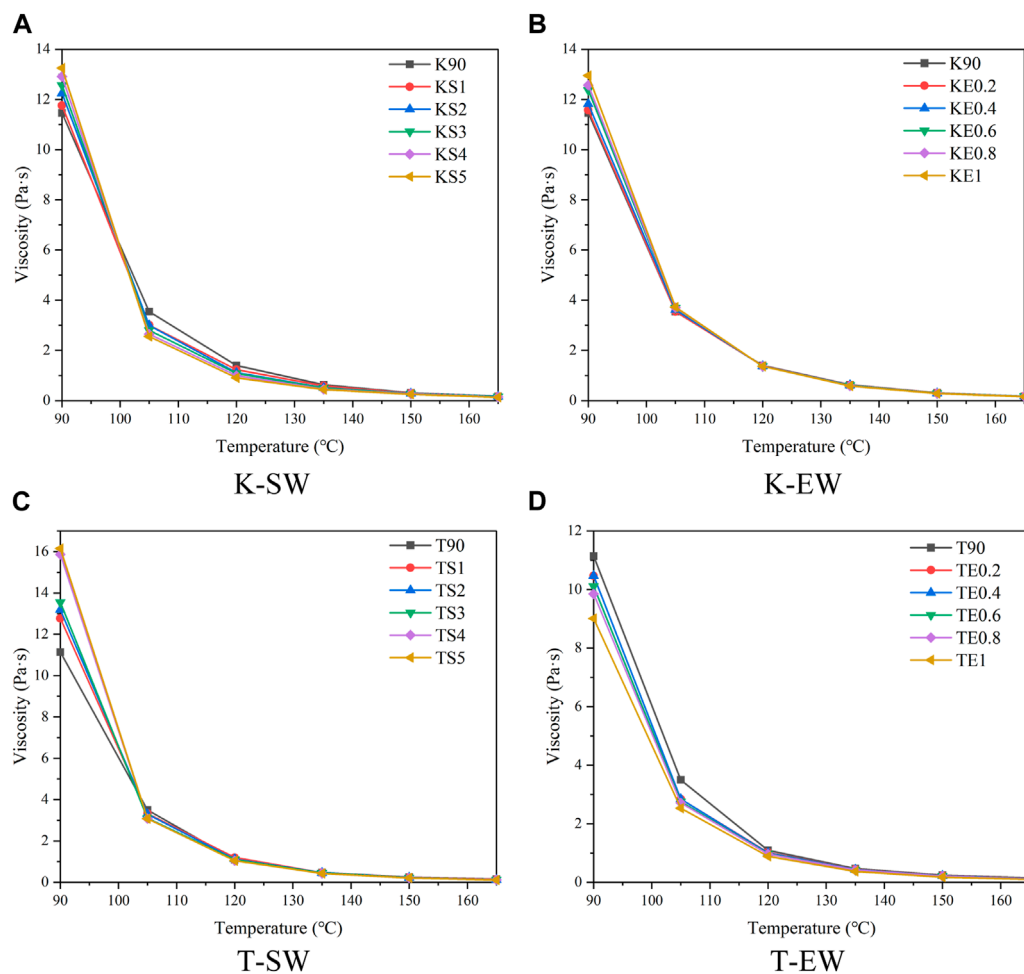
FIGURE 8
Variation curve of viscosity of base asphalt and WMA: **(A)** K-SW, **(B)** K-EW, **(C)** T-SW and **(D)** T-EW.

3 Results and discussion

3.1 Physical indexes analysis

3.1.1 Penetration analysis

According to the specifications outlined in JTG E20-2011(T0604-2011), logarithmic regression of penetration depth with temperature should be conducted as per Eq. 7. Subsequently, the penetration index (PI) was calculated using Eq. 8, the equivalent softening point (T_{800}) was determined via Eq. 9, the equivalent brittle point ($T_{1.2}$) was computed using Eq. 10, and the plastic temperature range ($\triangle T$) was evaluated following Eq. 11. Detailed results were presented in Table 4 and Table 5.

$$\lg P = K + A_{\lg Pen} \times T \tag{7}$$

$$PI = \frac{20 - 500 A_{\lg Pen}}{1 + 50 A_{\lg Pen}} \tag{8}$$

$$T_{800} = \frac{\lg 800 - K}{A_{\lg Pen}} = \frac{2.9031 - K}{A_{\lg Pen}} \tag{9}$$

$$T_{1.2} = \frac{\lg 1.2 - K}{A_{\lg Pen}} = \frac{0.0792 - K}{A_{\lg Pen}} \tag{10}$$

$$\Delta T = T_{800} - T_{1.2} = \frac{2.8239}{A_{\lg Pen}} \tag{11}$$

Note: T is the test temperature of needle penetration, °C; P is the penetration value measured at each test temperature; $A_{\lg Pen}$ is the coefficient of the regression equation. K is a constant term.

The thermal responsiveness of asphalt was illustrated by the PI, where an elevated value indicated reduced susceptibility to temperature fluctuations, while a diminished value signified heightened sensitivity. The T_{800} index reflected the asphalt's performance under high temperatures; a superior value conveyed excellent high-temperature attributes, while a lower value implied subpar performance in elevated conditions. The $T_{1.2}$ parameter was employed to evaluate the asphalt's resistance to low-temperature cracking. Additionally, the plastic temperature range ΔT was defined as the difference between T_{800} and $T_{1.2}$. This range was intricately linked to the temperature-sensitive characteristics of asphalt, serving as a direct manifestation of the material's applicable temperature spectrum.
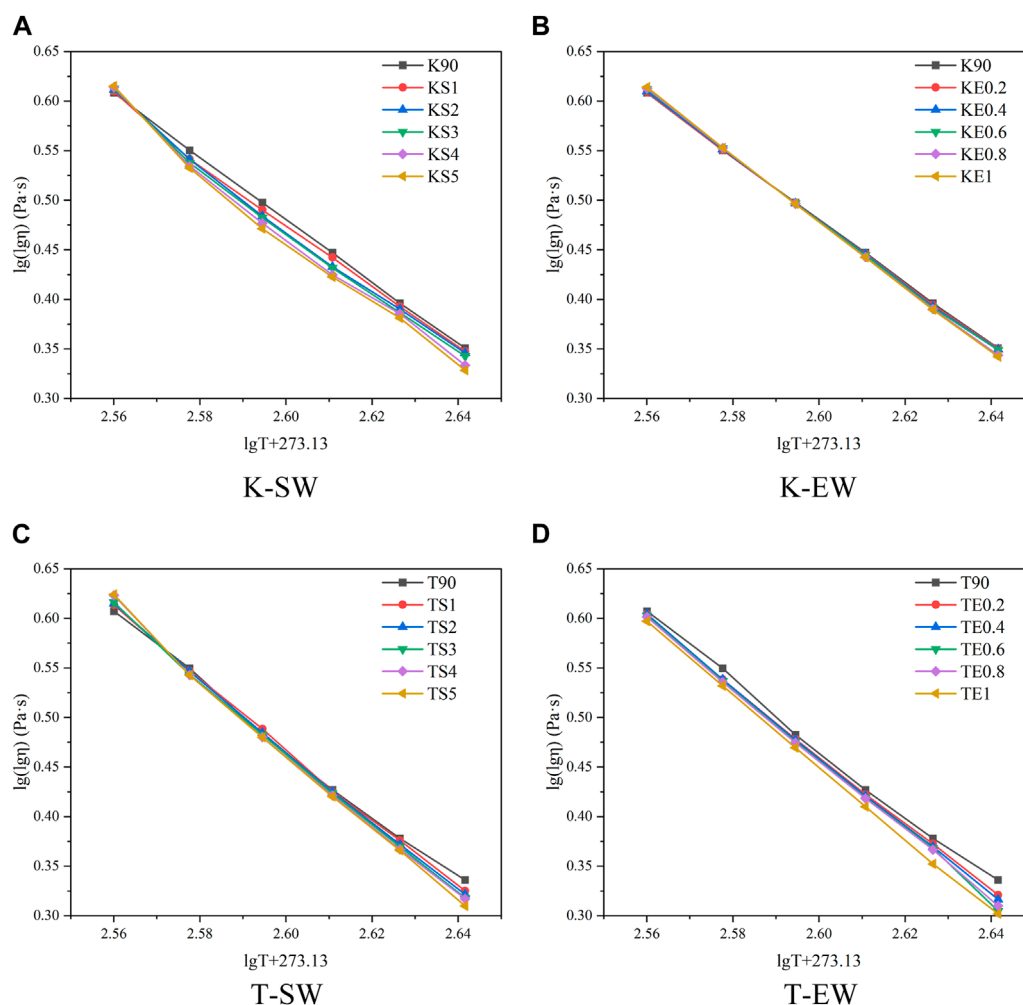
FIGURE 9
Viscosity temperature index relationship between base asphalt and WMA: **(A)** K-SW, **(B)** K-EW, **(C)** T-SW and **(D)** T-EW.

For Sasobit warm-mix modified Karamay asphalt (K-SW) and Tahe asphalt (T-SW), as well as Evotherm warm-mix modified Karamay asphalt (K-EW) and Tahe asphalt (T-EW), at temperatures of 15°C, 25°C, and 30°C, their penetration values were consistently lower than those of the base asphalt. With an increase in the dosage of warm-mix additives, the penetration values of the WMA gradually decreased. This indicated that the additives rendered the asphalt harder or increase its viscosity, thereby enhancing its resistance to deformation.

The PI values for K-SW and K-EW ranged from −1.5 to 0.5, while those for T-SW and T-EW fall within the ranged of −0.5 to 1.5. This suggests a certain relationship between the extent of temperature sensitivity improvement in WMA and the performance of the base asphalt. In the case of the two types of Xinjiang asphalt, the addition of Sasobit increased the asphalt's sensitivity to temperature, whereas Evotherm reduced its sensitivity to temperature. Additionally, an increase in the dosage of both warm-mix additives contributes to enhancing the temperature-sensitive performance of WMA.

With an increase in the dosage of both warm-mix additives, the T_{800} of WMA showed an upward trend, indicating that the

warm-mix additives enhance the high-temperature performance of the two base asphalts. Specifically, KS5 exhibited a growth rate of 4.0%, KE1 showed a growth rate of 12.7%, TS5 experienced a growth rate of 3.3%, and TE1 demonstrated a growth rate of 4.7%. It was noteworthy that the improvement in high-temperature performance by Evotherm warm-mix additive was greater than that by Sasobit, and Karamay asphalt was more sensitive to changes in the type of warm-mix additive.

As the dosage of warm-mix additives increases, the $T_{1.2}$ of WMA gradually increases. The additives enhance the low-temperature performance of asphalt, with Sasobit showing a greater improvement in Karamay asphalt compared to Evotherm, while the trend was reversed for Tahe asphalt. It can be observed that the type of asphalt influences the choice of warm-mix additive.

3.1.2 Softening point analysis

The experimental results for the softening point of WMA were depicted in Figure 7A. The addition of WMA resulted in an increasing trend in the softening point of asphalt. With the increasing dosage of the additives, the softening point of K-SW
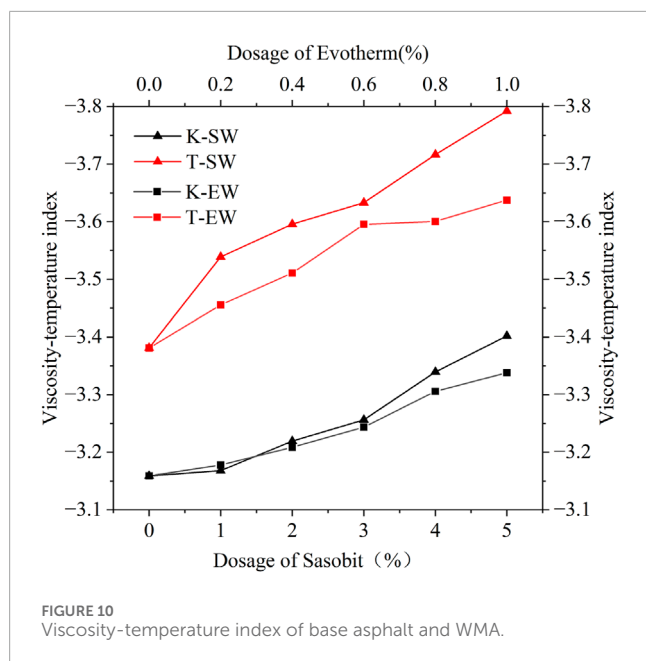
rose from 53.6 to 68.6, representing a percentage increase of 27.99%. Similarly, T-SW showed an increase from 57.5 to 72, with a percentage rise of 25.22%. This indicated that the inclusion of Sasobit improved the high-temperature performance of asphalt, enhanced its high-temperature stability. In comparison to Sasobit, Evotherm had a less pronounced effect on improving the high-temperature performance of asphalt, with softening point increases of 8.02% for K-EW and 4.39% for T-EW.

3.1.3 Ductility analysis

The experimental results for the ductility point of WMA were depicted in Figure 7B. The ductility values for T-EW and T-SW were both greater than 150 cm, therefore, they were not shown in the graph. From Figure 7B, it could be observed that the ductility of K-SW and K-EW showed no significant trend with an increase in the dosage of WMA. For T-SW and T-EW, their ductility values were both greater than 150, attributable to the better low-temperature deformation resistance of Tahe asphalt. Moreover, these values did not exhibit a clear pattern of change with an increase in the dosage of WMA. Therefore, ductility was not suitable for evaluating the low-temperature performance of WMA.

3.1.4 Viscosity temperature coefficient analysis

Figure 8 showed the viscosity curve of the base asphalt and WMA as a function of temperature.

It was observed in Figure 8 that the viscosity of WMA decreased with increasing temperature. This was because the molecular thermal motion inside asphalt accelerated with an increase in the external temperature, the intermolecular force decreased, and depolymerization occurred, which finally led to a decrease in the viscosity of asphalt.

Below 105°C, the viscosity of asphalt gradually increased with the addition of warm-mix additives at the same temperature for all four WMA types, except for T-EW. At temperatures above 105°C, at the same temperature, the viscosity of K90 was higher than that of K-SW, and the difference between their viscosities

decreased with an increase in temperature. Simultaneously, the viscosity of K-SW gradually decreased with the addition of Sasobit dosage at the same temperature. The change in viscosity for K-EW and T-SW were minimally influenced by the dosage of warm-mix additives. Above 105°C, the viscosity trend of T-EW, in relation to the variation in warm-mix additive dosage, aligns with the trend seen in K-SW. Both K-SW and T-EW, classified as warm-mix asphalt types, experienced a decrease in viscosity. Two kinds of warm mixing asphalt, K-SW and T-EW, achieved the effect of reducing viscosity.

In this study, we used viscosity–temperature index VTS to analyze the temperature sensitivity of modified asphalt. The smaller the value, the higher the temperature sensitivity of the asphalt binders. Eq. 12 shows the VTS formula.

$$VTS = \frac{\lg\left[\lg\left(\eta_{T2}\right) - \lg\left(\eta_{T1}\right)\right]}{\lg\left(T_2 + 273.13\right) - \lg\left(T_1 + 273.13\right)} \quad (12)$$

In Eq. 12, T_1 and T_2 are the test temperatures for the asphalt viscosity in °C; η_{T1} and η_{T2} are the viscosity values at temperatures T_1 and T_2, respectively, in Pa·s.

Figure 9 shows the VTS diagram of base asphalt and WMA, with the slope of the relation curve showing the VTS values of the WMA. Figure 9 summarizes the calculated results. The smaller the VTS of asphalt, the higher is the temperature sensitivity of the asphalt binder (Lu et al., 2022).

The data in Figure 10 suggest that the temperature sensitivity of Karamay asphalt was higher than that of Tahe asphalt. The temperature sensitivity of WMA modified with Evotherm is higher than that of WMA with Sasobit.

3.2 SARA analysis

According to the colloidal stability system, the lower the value of CII, the higher the asphaltene stability in asphalt binder. If CII ≥ 0.9, the asphaltene fraction was prone to instability within the crude oil. When at a level of 0.7 ≤ CII ≤ 0.9, asphaltene stability became uncertain, while if CII ≤ 0.7, the asphaltene fraction was stable (Siddiqui and Ali, 1999; Wang et al., 2019).

As shown in Figure 11, it was observed that the CII values of WMA remained within the original range, indicating that the addition of warm-mix additives had no discernible impact on the stability of the original asphaltene fraction.

Figure 11 illustrated the SARA fractions as well as the colloidal instability index for the base asphalt and WMA. The SARA fractions of K90 showed significant differences from common road asphalt, with very low Asphaltene (0.2%) and high Resins (45.46%). In comparison, binder T90 contained more Asphaltene (16.82%) and Aromatic (36.18%), but fewer Resins (19%) and Saturates (28%). This trend was attributed to the different oil source and refining process. The distinctive proportions of the SARA further highlighted the typicity of the two asphalts from Xinjiang. Furthermore, it was observed that the incorporation of the Warm mixing additive at a low dosage did not result in any significant changes in the ratio of the four asphalt components.

Figures 11A, C indicated that, as the concentration of Sasobit flux increased, the saturation hydrocarbon content gradually decreased. The wax structure of Sasobit was similar to the saturated

FIGURE 11
SARA fractions of base asphalt and WMA: **(A)** K-SW, **(B)** K-EW, **(C)** T-SW and **(D)** T-EW.
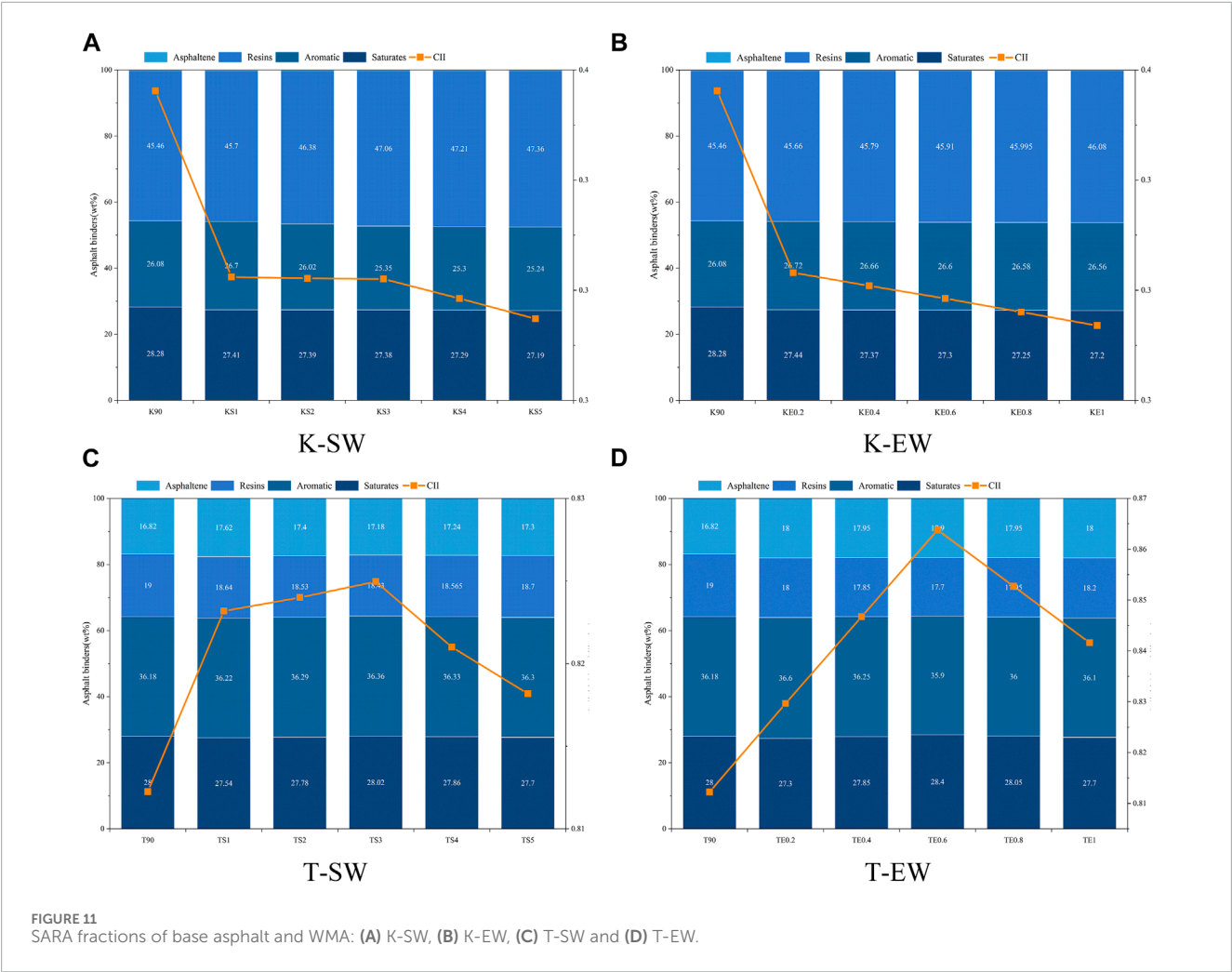
TABLE 5 Penetration correlation calculation table (Tahe asphalt).

ID	Penetration/0.1 mm			R2	PI	T_{800}/°C	$T_{1.2}$/°C
	15°C	20°C	25°C				
T90	38.3	92.2	137.1	0.999	0.507	50.50	−25.61
TS1	32.3	79.2	124.0	0.997	0.186	50.67	−21.92
TS2	29.9	74.0	116.0	0.999	0.118	51.30	−20.55
TS3	27.9	70.4	110.0	0.999	0.033	51.59	−19.36
TS4	25.5	66.0	104.0	0.999	−0.131	51.64	−17.56
TS5	24.1	60.2	100.0	0.999	−0.163	52.17	−16.70
TS0.2	38.0	91.6	136.1	0.997	0.507	50.60	−25.52
TS0.4	37.4	88.6	134.0	0.999	0.507	50.93	−25.40
TS0.6	36.3	84.1	130.1	0.999	0.526	51.42	−25.10
TS0.8	35.0	78.8	126.3	0.999	0.544	51.93	−24.59
TS 1	32.1	76.0	113.8	0.997	0.544	52.89	−23.85
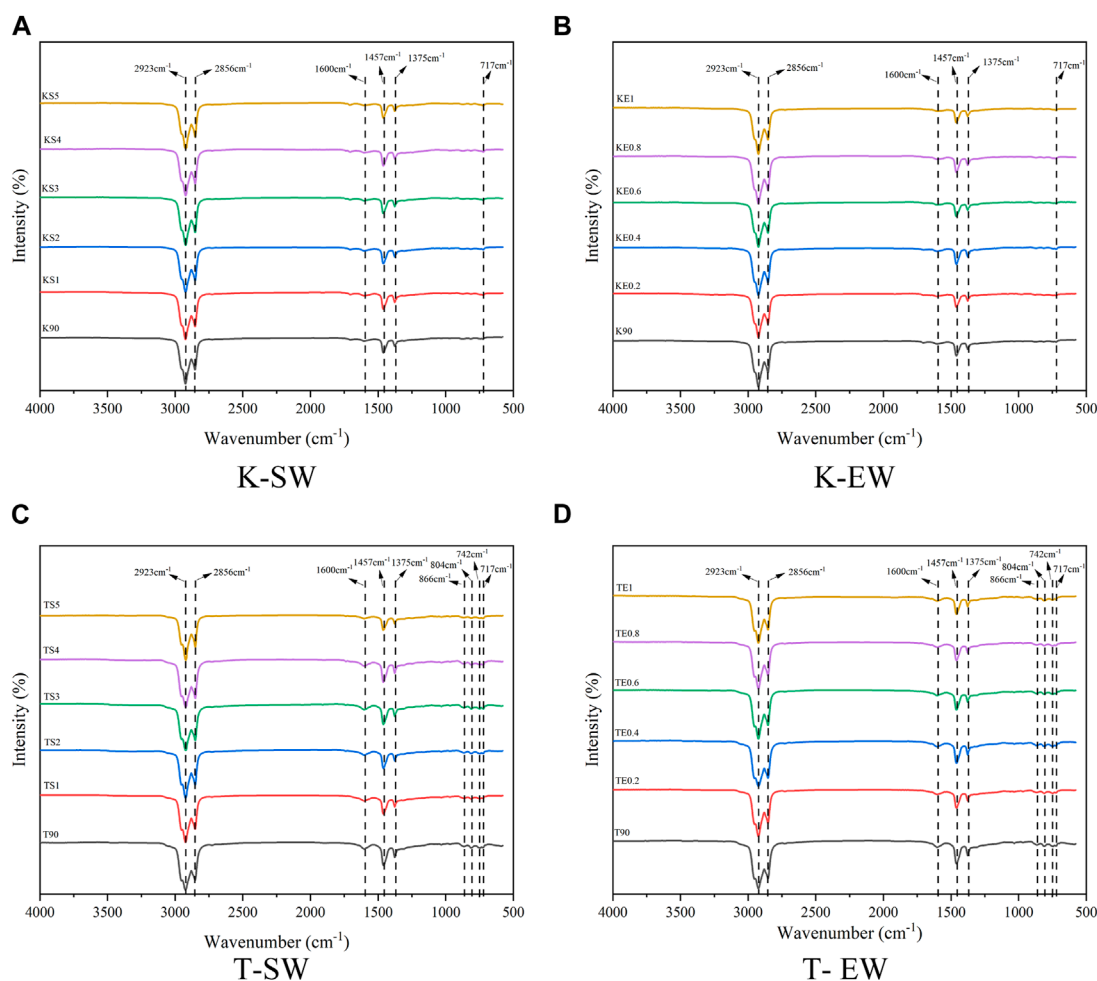
FIGURE 12
FTIR spectra of base asphalt and WMA: **(A)** K-SW, **(B)** K-EW, **(C)** T-SW and **(D)** T-EW.

TABLE 6 Solubility parameters of asphalt.

Asphalt type	K90	KS3	KE0.6	T90	TS3	TE0.6
CED(J/cm^3)	3.24	3.21	3.40	3.52	3.45	3.54
δ (J/cm^3)$^{1/2}$	18.00	17.92	18.44	18.77	18.57	18.81
$\Delta\delta$ (J/cm^3)$^{1/2}$	——	0.077	0.443	——	0.203	0.042

hydrocarbons in asphalt. When the temperature is below its melting point, Sasobit undergoes gradual crystallization and precipitation with the saturated component, effectively encapsulating saturated oil and wax components in the asphalt. This process enhances the high-temperature stability of the asphalt (Ji and Xu, 2010; Liu et al., 2019). During this process, the reagglomeration of resins or asphaltene was prevented (Butz et al., 2001; Abraham et al., 2002). Subsequently, the size of asphaltene aggregates was reduced, resulting in a decrease in the viscosity of the asphalt (Hurley and Prowell, 2005).

In K90 asphalt, where the asphaltene content is extremely low, the role of wax in binding asphaltene molecules is relatively small. Throughout the preparation of WMA, the base asphalt undergoes a certain degree of aging, leading to a decrease in the CII index of

K-SW with an increase in the warm-mix additive (Figure 11A). In T90 asphalt, where the asphaltene content is relatively high, Sasobit effectively exerts its binding effect on asphaltene, resulting in the CII status as depicted in Figure 11C.

In the asphalt colloid system, the resins component exists in two states: it is both a component of the dispersed phase and a component of the dispersed medium (Li et al., 1997). Additionally, the polar components of the resin contain surface-active agents, exhibiting good compatibility with the cationic ammonium salt in Evotherm, resulting in a synergistic enhancement effect. This leads to an increase in asphaltene component, a decrease followed by an increase in resins (Lian et al., 1994). The structures of small molecules from Evotherm can enter the
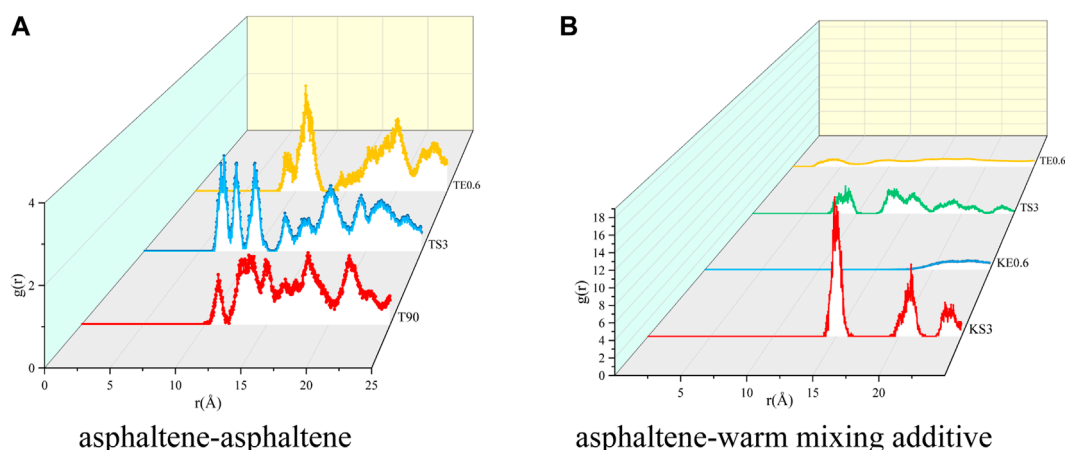
FIGURE 13
RDF of base asphalt and WMA: **(A)** asphaltene-asphaltene and **(B)** asphaltene-warm mixing additive.

aggregation gaps in asphaltene, preventing asphaltene binding and promoting the gelation of asphaltene colloids (Wang et al., 2023). In asphalts with a higher content of asphaltene and saturated fractions, the reactions with Evotherm can be fully realized. Therefore, in T-EW, the CII index exhibits a phenomenon of first increasing and then decreasing, with a turning point observed at an Evotherm content of 0.6% (Figure 11D). In K90 asphalt, due to the minimal presence of asphaltene in the asphalt, Evotherm primarily reacts with the saturated fractions. Consequently, the colloid content gradually increases in all four components, as illustrated in Figure 11B.

3.3 FTIR analysis

The FTIR spectra of base asphalt and WMA are shown in Figures 12A–D. The FTIR spectra of basic asphalt and WMA showed the same curve shape from $600 cm^{-1}$–$4,000 cm^{-1}$. The presence of saturated hydrocarbons (alkanes) is shown by the bands at $2923 cm^{-1}$ and $2856 cm^{-1}$, which are induced by asymmetrical and symmetrical stretching of $-CH_2-$, respectively. Furthermore, the bands around $1375 cm^{-1}$ show the symmetric distortion of C-H in CH_3, whereas the bands at roughly $717 cm^{-1}$ represent the stretching of C-H in CH_3 or CH_2. These bands could be seen in every FTIR spectrum, indicating that the asphalt binders and fractions had the same hydrocarbon components.

Furthermore, Aromatics, Resins, and Asphaltenes exhibited unique bands at roughly 810–$860 cm^{-1}$ and $1600 cm^{-1}$ in Tahe asphalt and its warm mixed modified asphalt. These bands correspond to the $=$ C-H and C=C stretching vibrations of benzene rings, respectively. This distinguishing trait strongly suggests that these three fractions have aromatic structures.

3.4 Molecular dynamics simulation results

In the MD simulation research process, the focus was on observing the motion and aggregation states of warm-mix additives

in asphalt. Therefore, we have chosen five types of asphalt for the study, namely K90, KS3, KE0.6, T90, KS3, KE0.6.

3.4.1 Solubility parameter analysis

Table 6 displays the solubility parameters and the differences in solubility parameters between the base asphalt and WMA. According to the data, it is evident that in both Sasobit and Evotherm warm-mix additives, K90 exhibits better compatibility with Sasobit, while T90 shows better compatibility with Evotherm. This observation is consistent with the experimental conclusions drawn from the SARA.

3.4.2 RDF analysis

MD cohesion work is thought to be primarily governed by the aggregation behavior of asphalt molecules (Xu et al., 2018a). As a result, the RDF was used to learn more about how WMA additives affect asphalt molecule aggregation. Figure 12 depicts the RDF curves.

Figure 13A shows that the asphaltene-asphaltene RDF in the T90 base asphalt had a peak between 10Å and 12 Å, and the peak value was about 1, indicating that the particles in the local structure are uniformly distributed (Samieadel et al., 2018). The value of the first peak became larger and advance after adding Sasobit, the increase in the first peak value suggests that the packing density increased and the aggregation behavior of asphaltene was enhanced. The long-chain structure of Sasobit creates a higher probability of stacking of asphaltene molecules. The increase of asphaltene in SARA test was confirmed. Similarly, the early appearance of the TE0.6 wave crest in RDF also explains the increase of asphaltene in SARA test. Because K90 contains relatively little asphaltene, the results of asphaltene-asphaltene RDF are not presented here.

Figure 13B shows that the asphaltene-warm mixing additive RDF in the WMA. In K90 asphalt, the lower content of asphaltene molecules results in the delayed appearance of the KS3 peak between 14 Å and 16 Å, with a peak value of 18 indicating strong aggregation behavior between Sasobit molecules and asphaltene. The TE0.6 peak appears between 3 Å and 5 Å, and the subsequent curve remains in this range, indicating

a uniform distribution of Evotherm within this range and its role in dispersing asphaltene.

4 Conclusion

This paper clarifies the microscopic impact mechanisms of warm-mix additives by thoroughly characterizing the performance of WMA on numerous scales. The base asphalts selected are K90 and T90. Two typical warm-mix additives were investigated: wax-based WMA additive (Sasobit) and surfactant WMA additive (Evotherm). SARA component testing, infrared spectroscopy, and basic physical investigations were carried out. Warm mix additives' molecular impacts are revealed by the construction of molecular models and the execution of MD simulations for the representative WMA additives. Several inferences are made in light of the results that have been provided:

(1) Based on the T_{800} and $T_{1.2}$ indices, it was observed that K90 exhibited excellent low-temperature performance, while T90 demonstrated superior high-temperature characteristics. The incorporation of warm mix additives was found to effectively enhance both the high-temperature and low-temperature performance of asphalt. Notably, Evotherm proved to be more effective than Sasobit in improving the high-temperature performance of asphalt, whereas Sasobit surpassed Evotherm in its impact on low-temperature performance. The conclusions drawn from the VTS and PI metrics for warm mix asphalt were contradictory, prompting the exploration of alternative methods for evaluating the sensitivity of warm mix asphalt.

(2) Regarding the reduction in asphalt viscosity, it was observed that the variations in the dosage of warm mix additives had a negligible impact on the viscosity of warm mix asphalt. The viscosity-reducing effect of the Sasobit warm mix additive was found to be superior to that of Evotherm for K90, while for T90 asphalt, the situation was reversed.

(3) The analysis of warm mix additive mechanisms from the perspective of asphalt components, through both physical index tests and MD simulations, provided mutual validation. Sasobit, functioning as a wax-type warm mix additive, crystallized with the saturated components, forming a spatial network structure while facilitating the aggregation of asphaltene components. This conclusion was evident in the SARA analysis and the RDF in MD simulations. On the other hand, Evotherm warm mix additive, while dispersing asphaltene, also synergistically interacted with the polar components of resin. The reduction of asphalt content and resin in the SARA components validated this

conclusion, with further clarification from the RDF in MD simulations.

(4) The Solubility parameter in MD simulations consistently aligns with the viscosity results of the asphalt. Concerning warm mix asphalt modification, it was observed that K90 asphalt exhibited better compatibility with Sasobit, while T90 asphalt was more suitable for modification with Evotherm.

Data availability statement

The original contributions presented in the study are included in the article/Supplementary material, further inquiries can be directed to the corresponding author.

Author contributions

BH: Writing–original draft, Methodology, Software, Investigation. XA: Conceptualization, Formal analysis, Supervision. JF: Writing–review and editing, Data curation, Formal analysis, Validation.

Funding

Conflict of interest

The authors declare that the research was conducted in the absence of any commercial or financial relationships that could be construed as a potential conflict of interest.

Publisher's note

All claims expressed in this article are solely those of the authors and do not necessarily represent those of their affiliated organizations, or those of the publisher, the editors and the reviewers. Any product that may be evaluated in this article, or claim that may be made by its manufacturer, is not guaranteed or endorsed by the publisher.

References

Abraham, J., Butz, T., Hildebrand, G., and Riebesehl, G. (2002). Asphalt flow improvers as' intelligent fillers' for hot asphalts-a new chapter in asphalt technology. *J. Appl. Asphalt Bind. Technol.* 2.

Banerjee, A., DE Fortier Smit, A., and Prozzi, J. A. (2012). The effect of long-term aging on the rheology of warm mix asphalt binders. *Fuel* 97, 603–611. doi:10.1016/j.fuel.2012.01.072

Brako, F., and Wexler, A. (1963). Determination of Functional Groups in Copolymers by Infrared Spectrometry. *Analytical Chemistry* 35, 1944–1947.

Butz, T., Rahimian, I., and Hildebrand, G. (2001). Modification of road bitumens with the Fischer-Tropsch paraffin Sasobit (R). *J. Appl. Asphalt Bind. Technol.* 1.

Cheng, L., Li, W., Chen, M., Qian, Z., Chen, X., and Zheng, Z. (2023). Bleeding mechanism and mitigation technique of basalt fiber-reinforced asphalt mixture. *Case Stud. Constr. Mater.* 19, e02442. doi:10.1016/j.cscm.2023.e02442

Cheng, L., Yu, J., Zhao, Q., Wu, J., and Zhang, L. (2020). Chemical, rheological and aging characteristic properties of Xinjiang rock asphalt-modified bitumen. *Constr. Build. Mater.* 240, 117908. doi:10.1016/j.conbuildmat.2019.117908

Chen, L., Liu, G., Pan, G., and Zhendong, Q. (2023a). Investigation on the pore water pressure in steel bridge deck pavement under the coupling effect of water and vehicle load. *Constr. Build. Mater.* 209, 134021. doi:10.1016/j.conbuildmat.2023.134021

Chen, L., Zhao, X., Qian, Z., and Li, X. (2023b). Mechanical behavior of asphalt pavement on steel-concrete composite beam bridge under temperature-load coupling. *Constr. Build. Mater.* 403, 133099. doi:10.1016/j.conbuildmat.2023.133099

Chen, Z., Pei, J., Li, R., and Xiao, F. (2018). Performance characteristics of asphalt materials based on molecular dynamics simulation – a review. *Constr. Build. Mater.* 189, 695–710. doi:10.1016/j.conbuildmat.2018.09.038

Eltwati, A., Al-Saffar, Z., Mohamed, A., Rosli Hainin, M., Elnihum, A., and Enieb, M. (2022). Synergistic effect of SBS copolymers and aromatic oil on the characteristics of asphalt binders and mixtures containing reclaimed asphalt pavement. *Constr. Build. Mater.* 327, 127026. doi:10.1016/j.conbuildmat.2022.127026

Gao, M., Chen, Y., Fan, C., and Li, M. (2022). Molecular dynamics study on the compatibility of asphalt and rubber powder with different component contents. *ACS Omega* 7, 36157–36164. doi:10.1021/acsomega.2c02813

Hansen, J. S., Lemarchand, C. A., Nielsen, E., Dyre, J. C., and SchrøDER, T. (2013). Four-component united-atom model of bitumen. *J. Chem. Phys.* 138, 094508. doi:10.1063/1.4792045

Hildebrand, J. H., and Scott, R. L. (1951). The solubility of nonelectrolytes (Hildebrand, joel H.). *J. Chem. Educ.* 29 (1), 51. doi:10.1021/ed029p51.1

Hossain, Z., Lewis, S., Zaman, M., Buddhala, A., and O'Rear, E. (2013). Evaluation for warm-mix additive-modified asphalt binders using spectroscopy techniques. *J. Mater. Civ. Eng.* 25, 149–159. doi:10.1061/(asce)mt.1943-5533.0000562

Hurley, G. C., and Prowell, B. D. (2005). Evaluation of Sasobit for use in warm mix asphalt. *NCAT Rep.* 5, 1–27.

Jiang, Q., Li, N., Yang, F., Ren, Y., Wu, S., Wang, F., et al. (2021). Rheology and volatile organic compounds characteristics of warm-mix flame retardant asphalt. *Constr. Build. Mater.* 298, 123691. doi:10.1016/j.conbuildmat.2021.123691

Ji, J., and Xu, S. 2010. Study on the impact of Sasobit on asphalt's properties and micro-structure. Pavements and Materials: Testing and Modeling in Multiple Length Scales.

Kim, H., Lee, S.-J., and Amirkhanian, S. N. (2011). Rheology of warm mix asphalt binders with aged binders. *Constr. Build. Mater.* 25, 183–189. doi:10.1016/j.conbuildmat.2010.06.040

Li, D. D., and Greenfield, M. L. (2014). Chemical compositions of improved model asphalt systems for molecular simulations. *Fuel* 115, 347–356. doi:10.1016/j.fuel.2013.07.012

Lian, H., Lin, J.-R., and Yen, T. F. (1994). Peptization studies of asphaltene and solubility parameter spectra. *Fuel* 73, 423–428. doi:10.1016/0016-2361(94)90097-3

Li, H., Liu, C., Kan, G., and Liang, W. (1997). Colloidal structure and formation of vacuum residual oil. *J. China Univ. Petroleum(Edition Nat. Sci.)* 21, 71–76.

Li, M., Min, Z., Wang, Q., Huang, W., and Shi, Z. (2022). Effect of epoxy resin content and conversion rate on the compatibility and component distribution of epoxy asphalt: a MD simulation study. *Constr. Build. Mater.* 319, 126050. doi:10.1016/j.conbuildmat.2021.126050

Liu, K., Zhu, J., Zhang, K., Wu, J., Yin, J., and Shi, X. (2019). Effects of mixing sequence on mechanical properties of graphene oxide and warm mix additive composite modified asphalt binder. *Constr. Build. Mater.* 217, 301–309. doi:10.1016/j.conbuildmat.2019.05.073

Lu, P., Ma, Y., Ye, K., and Huang, S. (2022). Analysis of high-temperature performance of polymer-modified asphalts through molecular dynamics simulations and experiments. *Constr. Build. Mater.* 350, 128903. doi:10.1016/j.conbuildmat.2022.128903

Masoumeh, M., Farideh, P., Daniel, O., Shahrzad, H., and Fini, E. H. (2016). Multiscale investigation of oxidative aging in biomodified asphalt binder. *J. Phys. Chem. C* 120 (31), 17224–17233. doi:10.1021/acs.jpcc.6b05004

Ning, A. M., Shen, B. X., Long, J., and Zhao, J. G. (2015). Comparison of the physical properties and chemical structures of the Tahe asphalt before and after oxidative aging. *Energy Sources, Part A Recovery, Util. Environ. Eff.* 37, 1495–1504. doi:10.1080/15567036.2011.621011

Oyan, M. N. S. (2022). *Feasibility assessment of warm mix asphalt in Arkansas.* Arkansas State, USA: Arkansas State University.

Rubio, M. C., MartíNEZ, G., Baena, L., and Moreno, F. (2012). Warm mix asphalt: an overview. *J. Clean. Prod.* 24, 76–84. doi:10.1016/j.jclepro.2011.11.053

Salehfard, R., Behbahani, H., Dalmazzo, D., and Santagata, E. (2021). Effect of colloidal instability on the rheological and fatigue properties of asphalt binders. *Constr. Build. Mater.* 281, 122563. doi:10.1016/j.conbuildmat.2021.122563

Samieadel, A., Oldham, D., and Fini, E. H. (2018). Investigating molecular conformation and packing of oxidized asphaltene molecules in presence of paraffin wax. *Fuel* 220, 503–512. doi:10.1016/j.fuel.2018.02.031

Sengoz, B., Topal, A., and Gorkem, C. (2013). Evaluation of natural zeolite as warm mix asphalt additive and its comparison with other warm mix additives. *Constr. Build. Mater.* 43, 242–252. doi:10.1016/j.conbuildmat.2013.02.026

Siddiqui, M. N., and Ali, M. F. (1999). Studies on the aging behavior of the Arabian asphalts. *Fuel* 78, 1005–1015. doi:10.1016/s0016-2361(99)00018-6

Topal, A., Sengoz, B., Kok, B. V., Yilmaz, M., Dokandari, P. A., Oner, J., et al. (2014). Evaluation of mixture characteristics of warm mix asphalt involving natural and synthetic zeolite additives. *Constr. Build. Mater.* 57, 38–44. doi:10.1016/j.conbuildmat.2014.01.093

Transport, E. D. O. C. J. O. H. A. (2020). Editorial department of China journal of highway and transport, 2020. Review on China's pavement engineering research-2020. *China J. Highw. Transp.* 33 (10), 1–66. (in Chinese). doi:10.19721/j.cnki.1001-7372.2020.10.001

Wang, C., Duan, K., Song, L., Ji, X., and Shu, C. (2022). Stability improvement technology of SBS/crumb rubber composite modified asphalt from Xinjiang China. *J. Clean. Prod.* 359, 132003. doi:10.1016/j.jclepro.2022.132003

Wang, J., Wang, T., Hou, X., and Xiao, F. (2019). Modelling of rheological and chemical properties of asphalt binder considering SARA fraction. *Fuel* 238, 320–330. doi:10.1016/j.fuel.2018.10.126

Wang, Y., Li, B., Li, D., Wei, D., Tu, C., Ren, X., et al. (2023). Effects of oxygen isolation and light–oxygen coupling ultraviolet aging on adhesion, micromorphology, and functional groups of warm-mix asphalt. *J. Mater. Civ. Eng.* 35, 04023309. doi:10.1061/jmcee7.mteng-15840

Wen, S. (2010). *Fourier transform infrared spectral analysis.* Peking, China: Chemical Industry Press.

Wu, M., Xu, G., Luan, Y., Zhu, Y., Ma, T., and Zhang, W. (2022). Molecular dynamics simulation on cohesion and adhesion properties of the emulsified cold recycled mixtures. *Constr. Build. Mater.* 333, 127403. doi:10.1016/j.conbuildmat.2022.127403

Xu, G., and Wang, H. (2016). Study of cohesion and adhesion properties of asphalt concrete with molecular dynamics simulation. *Comput. Mater. Sci.* 112, 161–169. doi:10.1016/j.commatsci.2015.10.024

Xu, G., Wang, H., and Sun, W. (2018a). Molecular dynamics study of rejuvenator effect on RAP binder: diffusion behavior and molecular structure. *Constr. Build. Mater.* 158, 1046–1054. doi:10.1016/j.conbuildmat.2017.09.192

Xu, T., Wang, Y., Xia, W., and Hu, Z. (2018b). Effects of flame retardants on thermal decomposition of SARA fractions separated from asphalt binder. *Constr. Build. Mater.* 173, 209–219. doi:10.1016/j.conbuildmat.2018.04.052

Yu, P., Ke-Hong, Y., XI-Xiong, L., and Xiang, L. (2018). The compatibility and stability mechanism of SBS modified Karamay asphalt. *Pet. Asph.* 32 (05), 25–32+37.

Yu, P., Liangquan, X., Wenshu, L., Nuerguli, (2019). Study of modification of Karamay asphalt by chemical method. *Petroleum Process. Petrochem.* 50 (03), 92–96.

Yusuff, A. O., Yahya, N., Zakariya, M. A., and Sikiru, S. (2021). Investigations of graphene impact on oil mobility and physicochemical interaction with sandstone surface. *J. Petroleum Sci. Eng.* 198, 108250. doi:10.1016/j.petrol.2020.108250

Yu, X., Wang, Y., and Luo, Y. (2013). Effects of types and content of warm-mix additives on CRMA. *J. Mater. Civ. Eng.* 25, 939–945. doi:10.1061/(asce)mt.1943-5533.0000765

Zhang, J., He, A., Wang, J., Zhang, Y., Yan, C., and Liu, Y. (2023). Study of bonding property of warm mix asphalt based on binder bond strength and molecular dynamics simulations. *J. Mater. Civ. Eng.* 35, 04023414. doi:10.1061/jmcee7.mteng-15678

Zhang, L., Cheng, L., Lu, Q., and Zhang, Z. (2023). Quantitative evaluation of asphalt blending characteristics in epoxy-modified hot recycled asphalt mixtures based on 3D confocal fluorescence technology. *J. Appl. Polym. Sci.*, e55073. doi:10.1002/app.55073

Zhang, L., and Greenfield, M. L. (2007). Relaxation time, diffusion, and viscosity analysis of model asphalt systems using molecular simulation. *J. Chem. Phys.* 127, 194502. doi:10.1063/1.2799189

Zhang, L., and Greenfield, M. L. (2008). Effects of polymer modification on properties and microstructure of model asphalt systems. *Energy & Fuels* 22, 3363–3375. doi:10.1021/ef700699p

Zhao, Y. (2012). Performance of warm-mix asphalt treated by quaternary ammonium salt surfactant. *J. Highw. Transp. Res. Dev.* 29 (8), 20–24.

Rheological and chemical indices to characterize long-term oxidative aging of SBS/rubber composite-modified asphalt binders

Suhua Chen[1], Shangzhi Zhuo[1], Gang Xu[1]*, Xianhua Chen[1]*, Lin Yu[2] and Qi Xu[2]

[1]School of Transportation, Southeast University, Nanjing, Jiangsu, China, [2]Jiangsu Zhonghong Environmental Protection Technology Co., Ltd., Jiangyin, Jiangsu, China

Oxidative aging of asphalt binders seriously affects the durability of asphalt pavements and causes early damage. Hence, appropriate indices that could track the extent of asphalt binder aging are of great importance to the material selection, design, and maintenance of asphalt pavement. This paper aims to select the applicable rheological and chemical indices to characterize oxidative aging degrees of polymer-modified asphalt binders. Styrene−butadiene−styrene (SBS)-modified asphalt and two kinds of SBS/crumb rubber compound-modified asphalt were subjected to a rolling thin-film oven (RTFO) test and 20 h, 40 h, and 60 h pressure aging vessel (PAV) tests. Various rheological experiments at different temperature ranges were applied to obtain rheological indices, including complex shear modulus ($|G^*|$), G−R parameter, and J' (derivative of creep compliance). A range of chemical indices were determined by Fourier transform infrared spectroscopy (FTIR). The results indicate that the carbonyl index is strongly correlated with PAV aging time. $|G^*|$ at 52°C and J' values at −18°C are the two most promising rheological indices to track the oxidative aging of asphalt binders and relate well to the chemical changes induced by PAV aging. In addition, the G−R parameter is problematic in some instances when used as the rheological index because its accuracy depends on the precise fitting of master curves.

KEYWORDS

SBS/rubber composite-modified asphalt binder, long-term oxidative aging, rheological properties, FTIR, G−R parameter

1 Introduction

Polymer modifiers are widely used in China to improve the anti-aging performance of asphalt binders and to extend the service life of asphalt pavement. Nevertheless, polymer-modified asphalt binders face an inevitable oxidative aging problem that causes asphalt materials to harden and reduce their cohesion capacity (Qin et al., 2014; Rahmani et al., 2018; Cai et al., 2024). Furthermore, due to asphalt hardening, asphalt mixtures may develop cracks and other deteriorations. The development of cracks leads to a decrease in the service performance of asphalt pavement, increasing the need for maintenance and repair (Yao et al., 2023; Yao et al., 2023). Therefore, it is of vital importance to identify appropriate

FIGURE 1
Technical flowchart.
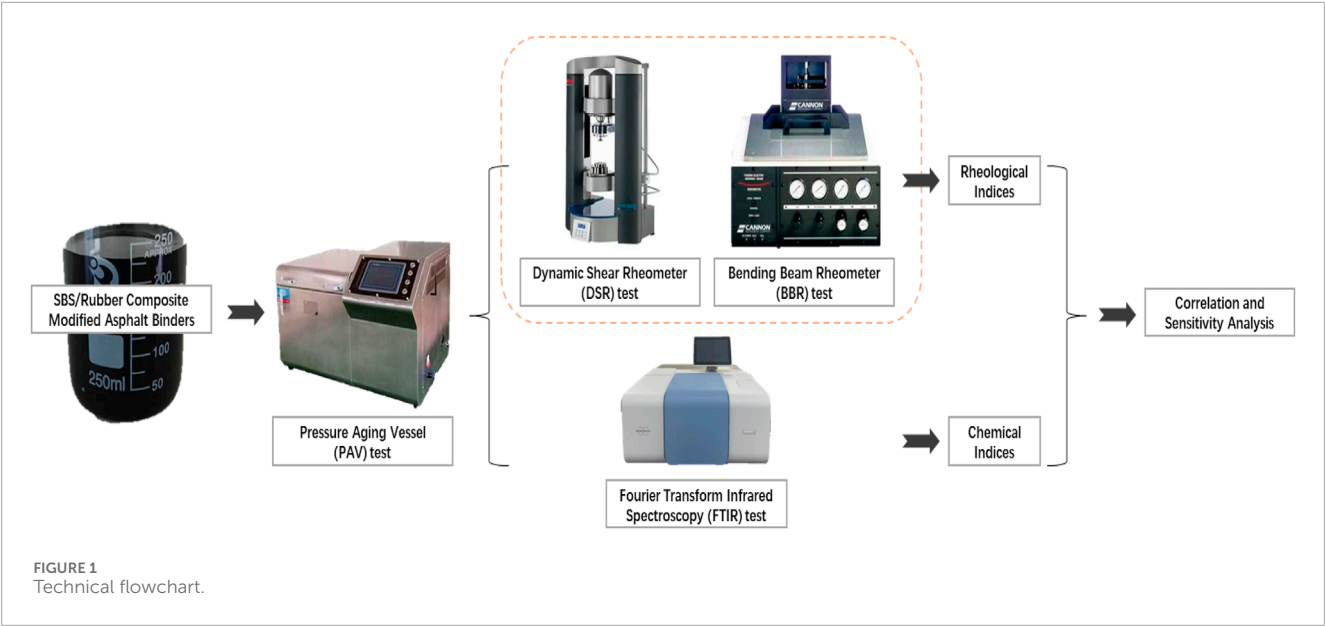
TABLE 1 Details of asphalt binders.

Asphalt type	Dosage of the modifier	Aging condition
SBS	5.5% SBS	
SR1	3% SBS+18% 40 mesh desulfurized crumb rubber	Original, RTFO, 20 h PAV, 40 h PAV, and 60 h PAV
SR2	5.5% SBS+18% 40 mesh desulfurized crumb rubber	

indices that can effectively characterize the aging degrees of polymer-modified asphalt binders and contribute to the design, construction, and maintenance of asphalt pavement.

In general, rheological parameters and chemical functional groups are the two main categories used to trace and quantify the oxidative aging of asphalt binders. Researchers have proposed many rheological indices, including rutting parameter ($|G*|/\sin\delta$), fatigue parameter ($|G*|\cdot\sin\delta$), Glover–Rowe (G–R) parameter, and so on, because they are well correlated to the physical or mechanical properties of asphalt binders and are easily obtained by a dynamic shear rheometer (DSR) test (Hao et al., 2017; Zhang et al., 2018; Zhang et al., 2023). The main drawback when these rheological indices are used to characterize the aging behavior of asphalt binders is that they only reflect the changes in the materials' physical parameters or paving performance and can hardly indicate any alteration in material components. However, the chemical indices can directly indicate the oxygen uptake during asphalt binders' oxidative aging process using a Fourier transform infrared spectroscopy (FTIR) technique. It is generally recognized that the formation and accumulation of sulfoxide and carbonyl are two major chemical reactions in the aging process of asphalt binders (Peterson, 2009). The index of the carbonyl function

group was proved to effectively determine the long-term aging behavior of asphalt binders because the formation rate of the carbonyl group remained stable throughout the aging process (Huh and Robertson, 1996). In addition, polymer degradation is a significant part of the polymer-modified asphalt binders aging process (Xu et al., 2021; Zhou et al., 2023), and thus, the relative proportion of polystyrene (PS) and polybutadiene (PB) can be reasonable indices to trace the oxidative aging of polymer-modified asphalt binders.

Although numerous indices have been proposed in the past decades, a comprehensive investigation focusing on the rheological and chemical indices and their relationships to oxidative degrees is currently missing. In addition, because most existing studies conducted the standard aging processes, including the rolling thin-film oven (RTFO) test and the pressure aging vessel (PAV) test, there is still a lack of studies on evaluation indices that consider the long-term laboratory aging effects. Hence, this paper aims to investigate various rheological and chemical indices to characterize the long-term oxidative aging of polymer-modified asphalt binders. SBS-modified asphalt and two kinds of SBS/crumb rubber (SR1 and SR2)-modified asphalt were used to extend PAV aging to simulate long-term aging. All the asphalt binders at each aging condition were subjected to a DSR test, a bending beam rheometer (BBR) test, and an FTIR test to obtain the rheological and chemical indices at different temperature ranges. Furthermore, the relationships between aging indices and PAV aging time and the interrelationship of different indices were also discussed. A technical flowchart of this paper is shown in Figure 1.

2 Materials

The details of three polymer-modified asphalt binders and the long-term aging time are shown in Table 1. All these asphalt binders were obtained from Jiangsu Baoli Asphalt Co., Ltd. All

the asphalt binders were subjected to a PAV (AASHTO R28) test to assess the rheological and chemical changes in terms of long-term oxidative aging, and the testing time was prolonged compared to standard aging time. In this procedure, 50 g of the residue from the RTFO (AASHTO T240) test was further conditioned in the PAV at 100°C and 2.1 MPa pressurized air for the corresponding testing time.

3 Measurement of aging indices

3.1 DSR procedure

The temperature sweep and frequency sweep tests were conducted using HAAKE MARS 40 model DSR. For the former test, the applied strain and frequency were 1% and 1.59 Hz, respectively. The test temperatures were 52°C, 58°C, 64°C, 70°C, and 76°C to find an appropriate index that could characterize the asphalt binders' aging degrees at a relatively higher temperature. For the frequency sweep test, a 1% strain amplitude was used to ensure the obtained rheological parameters of all asphalt binders were in their linear viscoelastic range. The test angular frequencies were set to be between 0.1 and 100 rad/s, and the same sample of each asphalt binder was tested under six temperatures (15°C, 25°C, 35°C, 45°C, 60°C, and 70°C).

3.1.1 Complex shear modulus (|G ∗ |)

The complex shear modulus ($|G*|$) can be measured directly by an oscillation test and can well track changes in a binder's physical properties induced by oxidative aging (Sun et al., 2024). Therefore, it was selected as one of the rheological indices. In addition, it is an important indicator in the Superpave performance grading specification. Figure 2A shows the variation in SBS asphalt binders $|G*|$ with the temperature increase at different aging conditions.

3.1.2 G–R parameter

The G–R parameter was also used as a rheological index in this paper. It was proposed to quantify the age-related cracking resistance of asphalt binders at the intermediate temperature range (Glover et al., 2002; Rowe, 2011) and could be obtained from the black space diagram. In addition, based on Kandhal's (1997) ductility thresholds, the G–R parameters at values 180 kPa and 600 kPa are deemed to identify the onset of cracking and significant cracking, respectively (Rowe, 2011). The following equation details the calculation formula of the G–R parameter.

$$G - R = \frac{|G*| \cdot (cos\,\delta)^2}{sin\,\delta},$$

where $|G*|$ and δ are the complex shear modulus and phase angle measured at 15°C and 0.005 rad/s, respectively.

However, testing at 0.005 rad/s is impossible, and thus, the $|G*|$ and δ values at a reduced frequency that corresponds to 15°C and 0.005 rad/s, respectively, were obtained from the master curves based on the time–temperature superposition principle. Figure 2B shows the black space diagram of the SBS-modified asphalt binder at different aging conditions.

The Christensen–Anderson–Marasteanu (CAM) model, which is widely used, was taken to construct master curves for complex shear moduli, as represented in the following equation (Yusoff et al., 2011).

$$|G*| = G_g\left[1 + \left(\frac{\omega_c}{\omega_r}\right)^v\right]^{-\frac{w}{v}},$$

where G_g, ω_c, and ω_r are glassy modulus, crossover frequency, and reduced frequency, respectively; $v = \log(2/R)$, where R is a rheological indicator defined as the ratio of G_g to the $|G*|$ at the crossover frequency; and v is one of the shape parameters of the master curve. ω addresses the issue of how fast or how slow the $|G*|$ data converge into the two asymptotes (the 45° asymptote and the G_g asymptote) as the frequency goes to zero or infinity.

Due to the addition of a relatively high content of polymer modifier, the phase angle master curves of the modified asphalt binders showed the characteristic of a plateau zone, and the CAM model could not fit very well. As a consequence, a modified double-logistic (DL) model was used to construct the phase angle master curves and was found to have a good fit with the observed data (Asgharzadeh et al., 2013). The shift factors for the construction of complex shear modulus master curves were then used to build phase angle master curves. This modified DL model is detailed in the following equation.

$$\delta = \delta_P - \delta_P \cdot H(f_{red} - f_P) \cdot \left(1 - e^{-\left(S_R \cdot log\left(\frac{f_{red}}{f_P}\right)\right)^2}\right)$$
$$+ \delta_L \cdot H(f_P - f_{red}) \cdot \left(1 - e^{-\left(S_L \cdot log\left(\frac{f_P}{f_{red}}\right)\right)^2}\right),$$

where δ_P is the plateau phase angle, f_{red} is the reduced frequency, and f_P is the frequency at which the binder attains its plateau zone. $H(f_{red} - f_P)$ and $H(f_P - f_{red})$ are two Heaviside step functions. δ_L stands for the rise or fall on the left side of the plateau zone. S_L and S_R represent the slope of the master curve to the left side and the right side of the plateau zone, respectively.

3.2 BBR test

A BBR (Cannon Instrument Company) test was conducted on these three asphalt binders after each aging condition at four different temperatures (−12°C, −18°C, −24°C, and −30°C) according to AASHTO T313 to analyze their low-temperature rheological characteristics. Two parameters, creep stiffness (S) and creep rate (m-value), could be obtained from this test. The former parameter S represented the resistance to constant loading of the binder, and the latter parameter m measured the rate change of asphalt stiffness as the loads were applied (Wang et al., 2012). The S and m values of the tested binders at any time (t) were calculated by the following equations. In addition, two replicate beams of each asphalt binder were tested, and the average values are reported.

$$S(t) = \frac{PL^3}{4bh^3\delta(t)},$$
$$m(t) = \left|\frac{d\{lg[S(t)]\}}{d[lg(t)]}\right|,$$

where $S(t)$ is the creep stiffness (Mpa) at any time t, $m(t)$ is the creep rate at any time t, P is the applied constant load (N), L is the
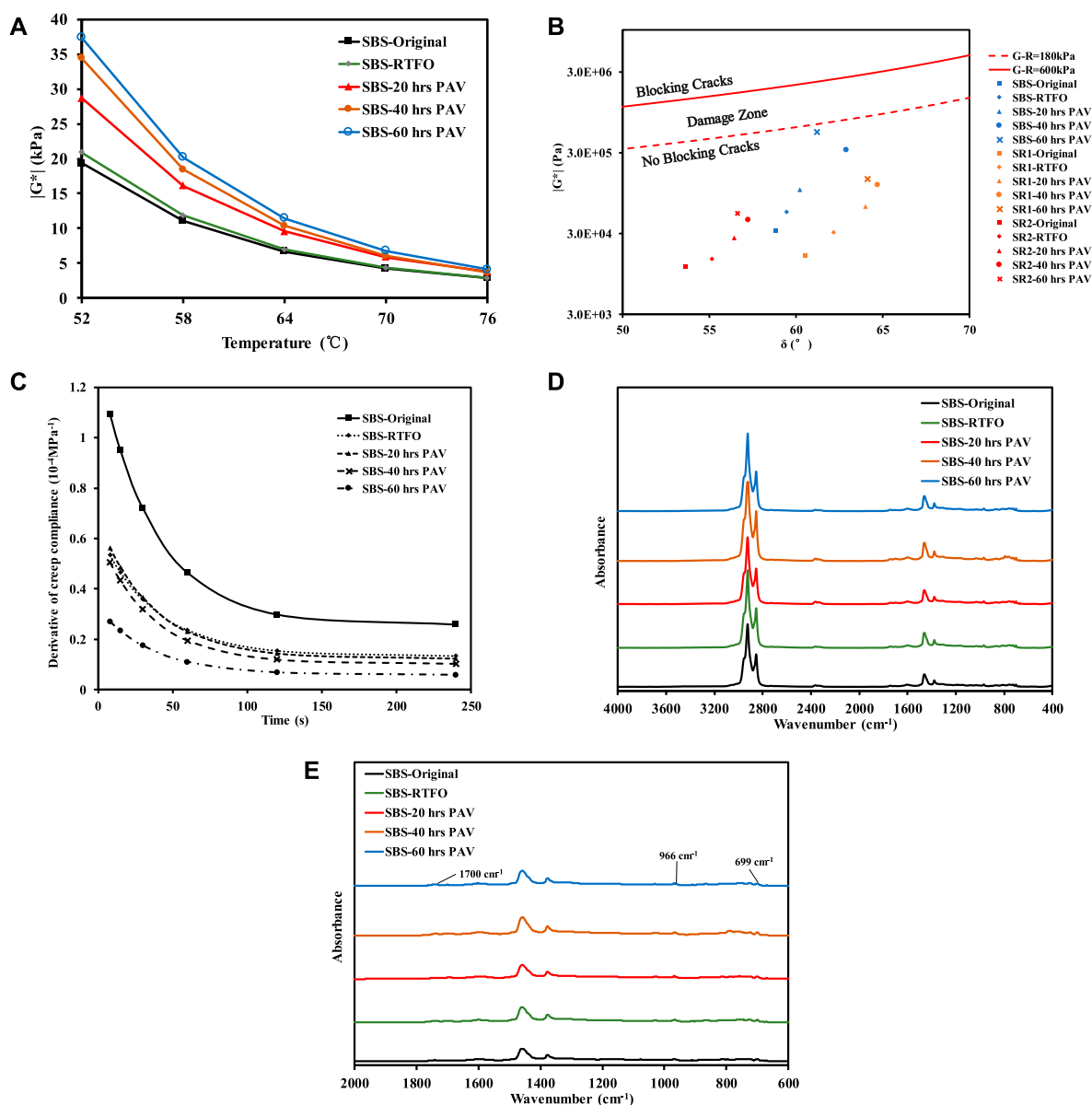
FIGURE 2
(A) $|G*|$ of the SBS-modified asphalt binder; (B) G−R parameter; (C) J' of the SBS-modified asphalt binder at −18°C; (D) FTIR spectra of the SBS-modified asphalt binder; (E) chemical indices in the fingerprint region.

distance (102 mm) between beam supports, b is the width (12.5 mm) of the asphalt beam, h is the beam thickness (6.25 mm), and $\delta(t)$ is the mid-span deflection (mm) at time t.

3.2.1 Derivative of creep compliance

Although $S(t)$ and $m(t)$ values at 60 s are widely used to describe the low-temperature performance of asphalt binders, they are used as two independent indicators for evaluation. A differential relationship exists between them in terms of mathematics. Hence, Liu et al. (2010) utilized Burgers' four-parameter model and established the physical relationship between $S(t)$ and $m(t)$ and finally proposed the derivative of creep compliance J' as a more reasonable index to characterize asphalt binders' cracking resistance at low temperatures. Therefore, J' at 60 s was also

used as a rheological index to evaluate the long-term aging effect. This relationship is shown in the following equation, and the detailed derivation process can be found in Liu et al.'s paper. Figure 2C shows the J' values of SBS-modified asphalt binders at 8 s, 15 s, 30 s, 60 s, 120 s, and 240 s, and the test temperature is −18°C.

$$J'(t) \approx \frac{m(t)}{S(t)} \times \frac{1}{t}.$$

3.3 FTIR test

In this paper, an FTIR spectrometer (Bruker, Germany) was used to quantify the functional groups of asphalt
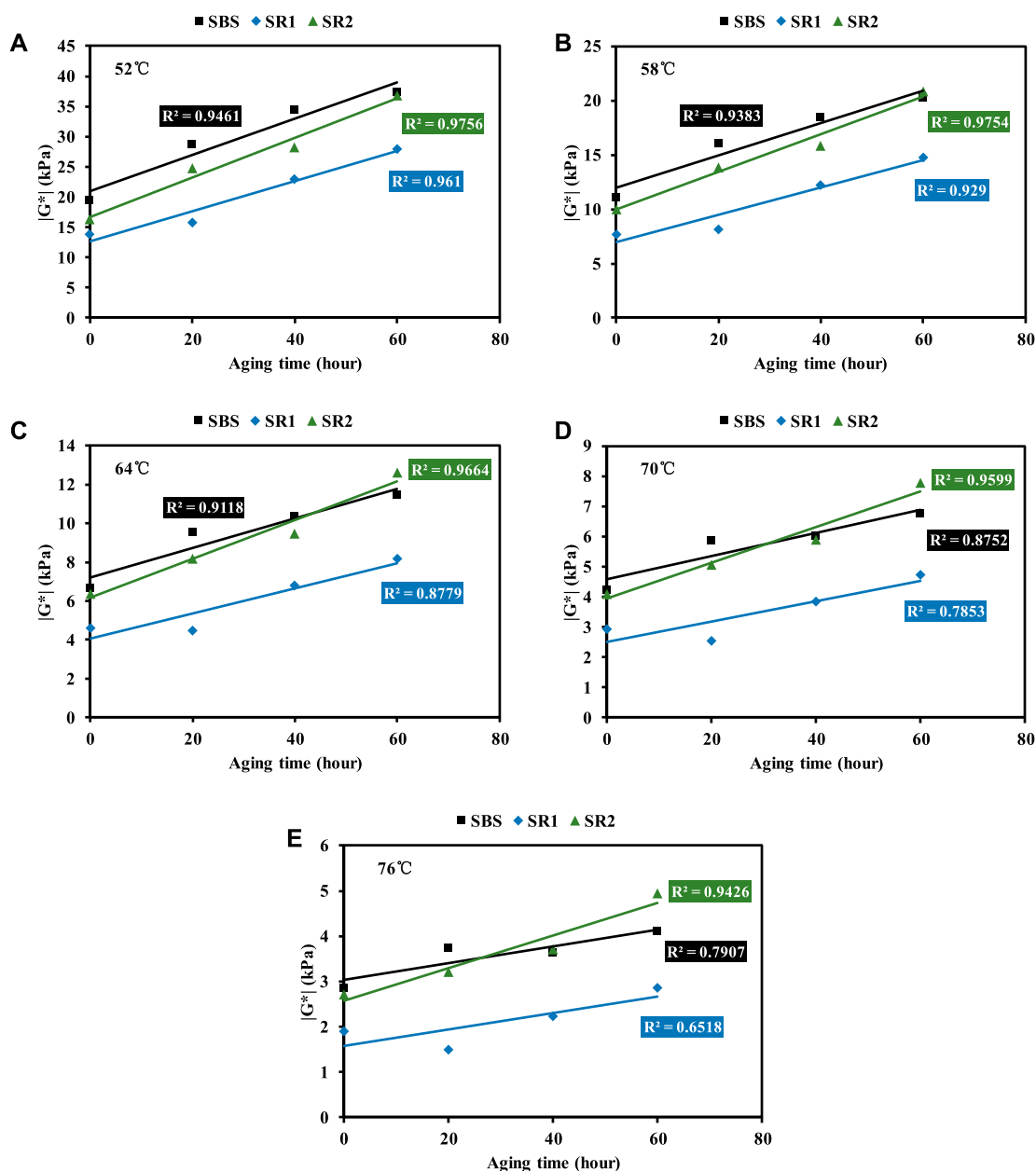
FIGURE 3
Changing curves of $|G*|$ versus aging time: **(A)** 52°C, **(B)** 58°C, **(C)** 64°C, **(D)** 70°C, and **(E)** 76°C.

binders before and after aging in the wavenumber range of 4,000–400 cm^{-1}. Spectra were recorded using 32 scans at a resolution of 4 cm^{-1}. For reliability, a minimum of six replicates were tested for each asphalt binder. Changes in carbonyl, polystyrene, and polybutadiene functions were recorded at wavenumbers 1,700 cm^{-1}, 699 cm^{-1}, and 966 cm^{-1}. An existing study (6) indicates that the number of sulfoxide functional groups determines the degree of an asphalt binder's short-term aging, while the formation rate of the carbonyl is stable throughout the aging process. Therefore, this paper did not choose sulfoxide functional groups as the chemical index. Figures 2D, E indicate examples of the FTIR spectra

and chemical indices. Chemical indices I_{CA} and I_{PB}/I_{PS} were used in this study. They are calculated as shown in the following equations:

$$Carbonyl\ Index(I_{CA}) = \frac{A_{1700}}{A},$$

$$Polystyrene\ Index(I_{PS}) = \frac{A_{699}}{A},$$

$$Polybutadiene\ Index(I_{PB}) = \frac{A_{966}}{A},$$

$$I_{\frac{PB}{PS}} = \frac{A_{966}}{A_{699}},$$

FIGURE 4
Changing curves of G−R values versus aging time.
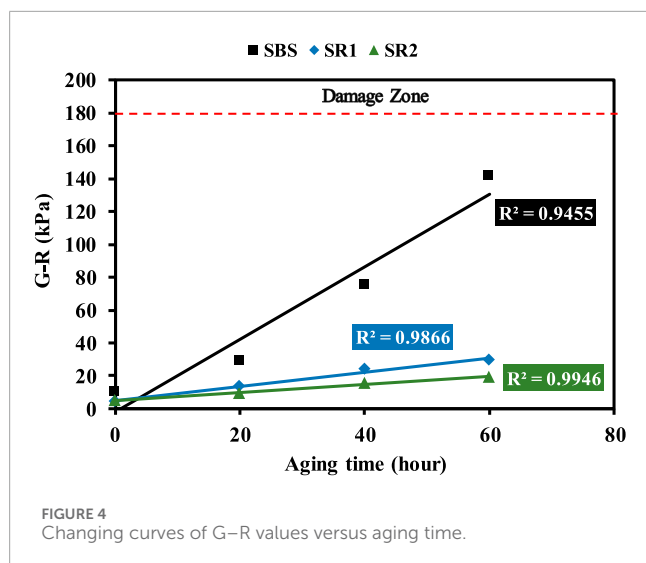
where A_{1700} is the area of the spectral bands of approximately 1,700 cm^{-1}, A_{699} is the area of the spectral bands of approximately 699 cm^{-1}, A_{966} is the area of the spectral bands of approximately 966 cm^{-1}, and A is the area of the spectral bands between 2000 and 600 cm^{-1}.

3.4 Linear regression

Linear regression is one of the most well-known modeling techniques and is a preferred technique for learning predictive models (Shen and Wang, 2024). In this technique, as the aging time is a continuous independent variable, the performance after aging (the dependent variable) can be continuous or discrete, and the property of the regression line is linear. Linear regression is very sensitive to outliers and can better identify them (Shen and Wang, 2023). Linear regression would also be convenient for practical engineering operations, predicting the performance of long-term aging asphalt.

4 Results and discussion

4.1 Evaluation of rheological indices

4.1.1 Complex shear modulus

Figure 3 shows the correlations between $|G*|$ and aging time at different temperatures. As can be seen, SBS- and SR1-modified asphalt binders' $|G*|$ show a good linear correlation with aging time; however, this relationship for the SR2-modified asphalt binder is relatively poor, especially at high temperatures. Thus, this paper chose the $|G*|$ values at 52°C for the next exploration, expecting they have a good relationship with other indices. In addition, the rate of oxidation is temperature-dependent; the slopes of regression curves decline as temperature increases. This means an appropriate rheological index that is directly related to a binder's physical property should not be tested

at a relatively high temperature because the binder's viscous characteristic will strongly affect the accuracy of experimental results. In terms of the effect of modifications, it can be seen that the $|G*|$ values of asphalt binders decrease at 52°C with the addition of crumb rubber. For SR1- and SR2-modified asphalt binders with the same crumb rubber content, the rise of the SBS modification content can significantly increase $|G*|$ values at all test temperatures.

4.1.2 G−R parameter

As can be seen from Figure 4, all asphalt binders should have no cracking-related issues. In addition, it is obvious that the SBS asphalt binder's G−R value rate of change is much larger than that of the other two asphalt binders. It indicates that adding crumb rubber effectively enhances the asphalt binder's cracking resistance and anti-aging performance at an intermediate temperature range. Generally speaking, asphalt binder modulus and phase angle values increase with the increase of aging time in shear mode tests. This is because asphalt binders become stiffer and tend to behave more elastically. According to Figure 2B, however, the phase angle values of these three asphalt binders increase at 0.005 rad/s (which corresponds to approximately −3.099 Hz reduced frequency) before the aging time reaches 40 h, while the values decline between 40 h PAV aging and 60 h PAV aging. The same result, which is triggered by a combination of factors, was found by many researchers (Isacsson and Lu, 1999; Airey, 2003; Hao et al., 2017; Subhy et al., 2018; Zhang et al., 2018). With the increase in aging time, phase angle values increase at a low-frequency range and decrease at a high-frequency range. In addition, this changing trend is more obvious when the polymer modification content is more than 3% (Isacsson and Lu, 1999). In other words, this phenomenon is highly related to the testing frequency and modification dosage. Because the calculated frequency of the G−R parameter is 0.005 rad/s, which is relatively low, it can be predicted to appear. The decrease in phase angle values when the aging time reaches 40 h may result from the fact that most polymer has been degraded, and the asphalt phase begins to play a major role (Airey, 2003).

4.1.3 Derivative of creep compliance

Figure 5 shows the correlation between J' and aging time. It can be seen that this rheological index is not well-correlated with aging duration, especially when the test temperature is −30°C. Thus, the J' values tested at −18°C were selected as the rheological index at a low-temperature range because of their relatively higher correlation. Another reason is that −18°C in the BBR test corresponds to −28°C in Superpave performance grading, which is an extreme service temperature for asphalt binders. We can see that all the J' changing rates for the three asphalt binders induced by oxidative aging are not very different, while their initial J' values are important for creep behaviors affected by oxidative aging at low-temperature conditions. Therefore, the addition of crumb rubber may not slow the asphalt binder's aging rate but could enhance cracking resistance at low temperatures, which leads to relatively better low-temperature performance when asphalt binders are subjected to long-term aging.
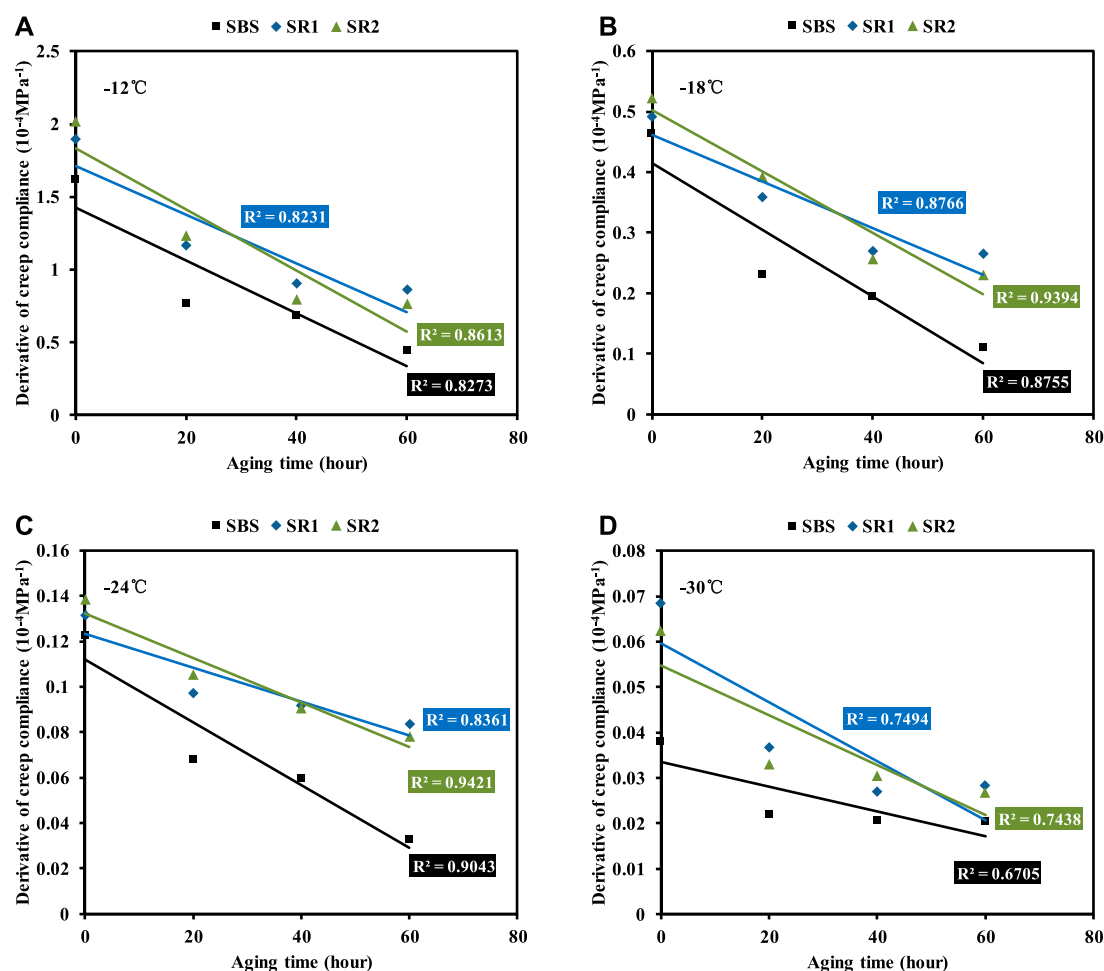
FIGURE 5
Changing curves of J' versus aging time: **(A)** −12°C, **(B)** −18°C, **(C)** −24°C, and **(D)** −30°C.

4.2 Evaluation of chemical indices

Numerous studies showed that asphalt binders exhibit an initial fast reaction period, followed by a relatively slower reaction period that has an approximately constant rate of oxidative aging (Petersen, 1998; Jin et al., 2011; Petersen and Glaser, 2011). In this paper, the chemical indices were evaluated within the constant rate period because all the asphalt binders were subjected to long-term oxidative aging.

Figure 6 compares two chemical indices with respect to aging time. The formation rate of carbonyl in the SBS-modified asphalt binder is the highest, although its initial I_{CA} is relatively low. In addition, I_{CA} and $I_{PB/PS}$ show a similar rank for base asphalt aging and polymer modifier degradation processes. It also can be seen that the $I_{PB/PS}$ values of SR1 and SR2 are higher than those of SBS, which may be because the added crumb rubber contains a certain amount of polystyrene and polybutadiene. However, the current study (Yan et al., 2018) shows that the chemical index $I_{PB/PS}$ is independent of the polymer modifier's concentration fluctuation and can effectively represent the extent of aging of the polymer-modified asphalt binder. The authors consider that all the rheological indices directly relate to asphalt binder's physical and mechanical properties, and the modifier degradation does not contribute much to oxidation products (Nivitha et al., 2016), while the volatilization of light components and the formation of macromolecules in base asphalt are the main causes of asphalt hardening. Hence, I_{CA} was selected as a promising chemical index and used in the following analysis with the rheological indices.

4.3 Correlation and sensitivity analysis

Figure 7 indicates the relationships between rheological indices, including high-, intermediate-, and low-temperature parameters, and the chemical index. As we can see, the correlation of the SBS asphalt binder's G–R parameter with the I_{CA} is not as good as the other rheological indices. This problem is related to the construction errors of $|G*|$ and phase angle master curves. The G–R parameter accuracy depends on the precise fitting of master curves. In addition, the changing rates of different indices between the latter aging condition and the former aging condition are detailed in Table 2 to evaluate the aging sensitivities of different indices.
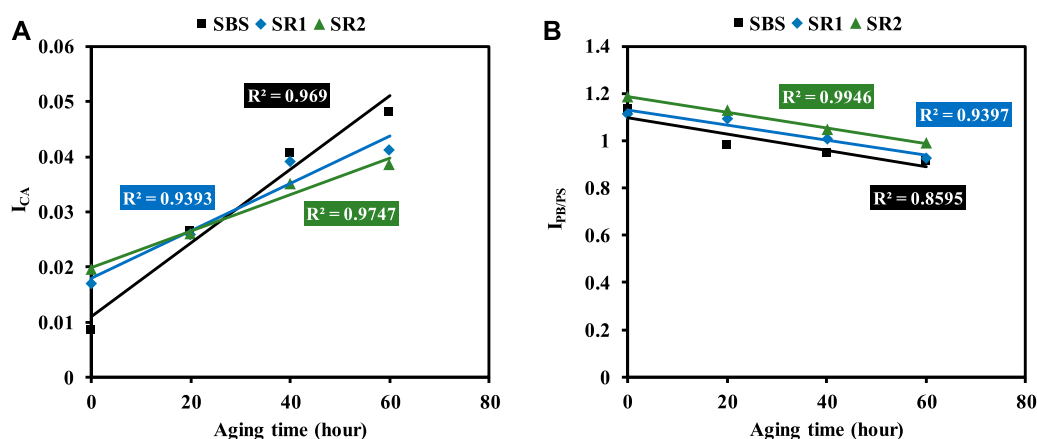
FIGURE 6
Changing curves of chemical indices versus aging time: **(A)** I_{CA} and **(B)** $I_{PB/PS}$.
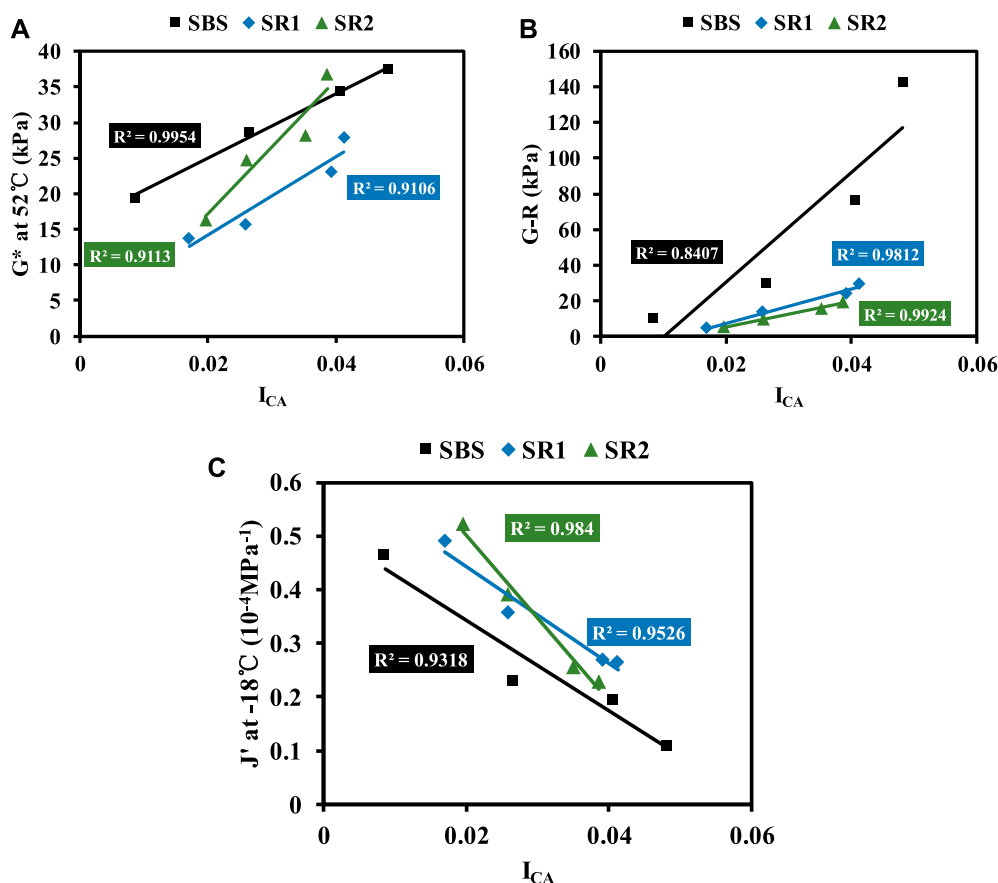
FIGURE 7
Correlations between rheological and chemical indices: **(A)** $|G*|$ versus I_{CA}; **(B)** G–R versus I_{CA}; **(C)** J' versus I_{CA}.

Based on the comprehensive analysis of all indices, the anti-aging property of SBS-modified asphalt is relatively poor, and the SR2-modified asphalt exhibits good aging resistance performance. It can be concluded that the G–R parameter is the most sensitive index to aging effects. However, it is not reliable enough because of its relatively poor correlation with the chemical index. In addition, its

calculation involves the phase angle, and the variation in the phase angle due to aging is quite complex. Therefore, based on the analysis of correlations between the different indices and their sensitivities to aging, $|G*|$ values at 52°C and J' values at −18°C are suggested as the rheological indices, and I_{CA} is an effective chemical index to characterize long-term oxidative aging.

TABLE 2 Aging indices of asphalt binders.

Asphalt type	$|G*|$/kPa	Changing rate/%	G–R parameter/kPa	Changing rate/%	J'/10^{-4}MPa^{-1}	Changing rate/%	I_{CA}	Changing rate/%
SBS-Original	19.36	-	10.26	-	0.464	-	0.0086	-
SBS-20 h PAV	28.67	48.07	29.43	186.82	0.230	50.40	0.0266	210.17
SBS-40 h PAV	34.45	20.16	75.57	156.76	0.195	15.12	0.0408	53.64
SBS-60 h PAV	37.38	8.50	142.02	87.94	0.109	44.07	0.0482	18.21
SR1-Original	13.77	-	4.47	-	0.492	-	0.0170	-
SR1-20 h PAV	15.76	14.50	13.82	208.93	0.359	27.05	0.0259	52.41
SR1-40 h PAV	23.02	46.00	24.08	74.20	0.269	24.90	0.0392	51.41
SR1-60 h PAV	27.94	21.39	29.70	23.34	0.264	1.83	0.0413	5.26
SR2-Original	16.26	-	5.09	-	0.523	-	0.0196	-
SR2-20 h PAV	24.74	52.08	9.70	90.48	0.393	24.88	0.0260	32.50
SR2-40 h PAV	28.17	13.88	15.44	59.12	0.257	34.62	0.0352	35.37
SR2-60 h PAV	36.88	30.92	19.24	24.66	0.230	10.47	0.0387	9.92

5 Conclusion

In this study, various rheological and chemical indices were evaluated to track the long-term oxidative aging of polymer-modified asphalt binders. The main conclusions that can be drawn from the experimental and analytical results of this study are as follows:

(1) $|G*|$ at 52°C and J' values at −18°C are the two most promising rheological indices to track the degree of oxidative aging. The test temperature should not exceed 52°C when using $|G*|$ as the rheological index to track the long-term oxidative aging of polymer-modified asphalt binders because the asphalt binder's viscous characteristic will strongly affect the accuracy of experimental results.

(2) The volatilization of light components and the formation of macromolecules in base asphalt are the main causes of asphalt hardening. The carbonyl index I_{CA} is suggested as an effective chemical index for characterizing long-term oxidative aging.

(3) Although the G–R parameter is the most sensitive index to aging effects, it is problematic in some instances when used as the rheological index because its reliability depends on the precise fitting of master curves.

Data availability statement

The original contributions presented in the study are included in the article/supplementary material; further inquiries can be directed to the corresponding authors.

Author contributions

SC: conceptualization, investigation, and writing–original draft. SZ: conceptualization, data curation, and writing–review and editing. GX: conceptualization, investigation, methodology, writing–original draft, and writing–review and editing. XC: funding acquisition, supervision, and writing–review and editing. LY: funding acquisition, supervision, and writing–review and editing. QX: funding acquisition, investigation, and writing–review and editing.

Conflict of interest

Authors LY and QX were employed by Jiangsu Zhonghong Environmental Protection Technology Co., Ltd.

The remaining authors declare that the research was conducted in the absence of any commercial or financial relationships that could be construed as a potential conflict of interest.

Publisher's note

All claims expressed in this article are solely those of the authors and do not necessarily represent those of their affiliated organizations or those of the publisher, the editors, and the reviewers. Any product that may be evaluated in this article, or claim that may be made by its manufacturer, is not guaranteed or endorsed by the publisher.

References

Airey, G. D. (2003). Rheological properties of styrene butadiene styrene polymer modified road bitumens. *Fuel* 82 (14), 1709–1719. doi:10.1016/S0016-2361(03)00146-7

Asgharzadeh, S. M., Tabatabaee, N., Naderi, K., and Partl, M. (2013). An empirical model for modified bituminous binder master curves. *Mater. Struct.* 46 (9), 1459–1471. doi:10.1617/s11527-012-9988-x

Cai, X., Ashish, P. K., Leng, Z., Tan, Z. F., and Wang, H. N. (2024). Effects of residual water on mechanical properties of cold mix based semi-flexible pavement composite towards a sustainable paving material. *J. Clean. Prod.* 434, 139857. doi:10.1016/j.jclepro.2023.139857

Glover, C. J., Davison, R. R., Domke, C. H., Ruan, Y., Juristyarini, P., and Knorr, D. B. (2002). *Development of a new method for assessing asphalt binder performance durability*. U.S. Department of Transportation. Washington, DC, USA,

Hao, G., Huang, W., Yuan, J., Tang, N., and Xiao, F. (2017). Effect of aging on chemical and rheological properties of SBS modified asphalt with different compositions. *Constr. Build. Mater.* 156, 902–910. doi:10.1016/j.conbuildmat.2017.06.146

Huh, J., and Robertson, R. E. (1996). Modeling of oxidative aging behavior of asphalts from short-term, high-temperature data as a step toward prediction of pavement aging. *Transp. Res. Rec. J. Transp. Res. Board* 1535 (1), 91–97. doi:10.1177/0361198196153500112

Isacsson, U., and Lu, X. (1999). Laboratory investigation of polymer modified bitumens. *J. Assoc. Asphalt Paving Technol.* 68, 35–63.

Jin, X., Han, R., Cui, Y., and Glover, C. J. (2011). Fast-rate-constant-rate oxidation kinetics model for asphalt binders. *Industrial Eng. Chem. Res.* 50, 13373–13379. doi:10.1021/ie201275q

Kandhal, P. S. (1997). Low-Temperature Ductility in Relation to Pavement Performance. Low temperature properties of bituminous materials and compacted bituminous paving mixtures. *Am. Soc. Test. Mater.* 18, 95–106. doi:10.1520/STP27096S

Liu, S., Cao, W., Shang, S., Qi, H., and Fang, J. (2010). Analysis and application of relationships between low-temperature rheological performance parameters of asphalt binders. *Constr. Build. Mater.* 24, 471–478. doi:10.1016/j.conbuildmat.2009.10.015

Nivitha, M. R., Prasad, E., and Krishnan, J. M. (2016). Ageing in modified bitumen using FTIR spectroscopy. *Int. J. Pavement Eng.* 17 (7), 565–577. doi:10.1080/10298436.2015.1007230

Petersen, J. C. (1998). A dual, sequential mechanism for the oxidation of petroleum asphalts. *Petroleum Sci. Technol.* 16, 1023–1059. doi:10.1080/10916469808949823

Petersen, J. C., and Glaser, R. (2011). Asphalt oxidation mechanisms and the role of oxidation products on age hardening revisited. *Road Mater. Pavement Des.* 12 (4), 795–819. doi:10.1080/14680629.2011.9713895

Peterson, J. C. (2009). A review of the fundamentals of asphalt oxidation: chemical, physicochemical, physical property, and durability relationships. *Transp. Res. Circular* 18. doi:10.17226/23002

Qin, Q., Schabron, J. F., Boysen, R. B., and Farrar, M. J. (2014). Field aging effect on chemistry and rheology of asphalt binders and rheological predictions for field aging. *Fuel* 121 (2), 86–94. doi:10.1016/j.fuel.2013.12.040

Rahmani, H., Shirmohammadi, H., and Hamedi, G. H. (2018). Effect of asphalt binder aging on thermodynamic parameters and its relationship with moisture sensitivity of asphalt mixes. *J. Mater. Civ. Eng.* 30 (11), 4018278. doi:10.1061/(ASCE)MT.1943-5533.0002453

Rowe, G. M. (2011). Evaluation of the relationship between asphalt binder properties and non-load related cracking (with discussion). *J. Assoc. Asphalt Paving Technol.* 80, 649–663.

Shen, K. R., and Wang, H. (2023). Impact of dynamic loading on pavement deflection measurements from traffic speed deflectometer. *Measurement* 217, 113086. doi:10.1016/j.measurement.2023.113086

Shen, K. R., and Wang, H. (2024). Prediction of critical strains of flexible pavement from traffic speed deflectometer measurements. *Constr. Build. Mater.* 411, 134770. doi:10.1016/j.conbuildmat.2023.134770

Subhy, A., Pires, G. M., Presti, D. L., and Airey, G. (2018). The effects of laboratory ageing on rheological and fracture characteristics of different rubberised bitumens. *Constr. Build. Mater.* 180, 188–198. doi:10.1016/j.conbuildmat.2018.05.273

Sun, G., Ma, T., Hu, M., Sun, X., Cao, Z., and Zhao, R. (2024). An evaluation proposal for the fatigue and healing performances of high-viscosity polymer-modified bitumen based on continuous multiple linear amplitude sweep. *Constr. Build. Mater.* 411, 134632. doi:10.1016/j.conbuildmat.2023.134632

Wang, H., Dang, Z., You, Z., Hao, P., and Huang, X. (2012). Analysis of the low-temperature rheological properties of rubberized warm mix asphalt binders. *J. Test. Eval.* 40 (7), 0147–1131. doi:10.1520/JTE20120147

Xu, G., Yu, Y. H., Yang, J. Y., Wang, T. L., Kong, P. P., and Chen, X. H. (2021). Rheological and aging properties of composite modified bitumen by styrene-butadiene-styrene and desulfurized crumb rubber. *Polymers* 13 (18), 3037. doi:10.3390/polym13183037

Yan, C., Huang, W., Xiao, F., Wang, L., and Li, Y. (2018). Proposing a new infrared index quantifying the aging extent of SBS-modified asphalt. *Road Mater. Pavement Des.* 19 (6), 1406–1421. doi:10.1080/14680629.2017.1318082

Yao, H., Liu, Y. H., Lv, H. T., Ju, H. Y., You, Z. P., and Hou, Y. (2023). Encoder–decoder with pyramid region attention for pixel-level pavement crack recognition. *Computer-Aided Civ. Infrastructure Eng.* 15. doi:10.1111/mice.13128

Yao, H., Wang, Y. R., Ma, P. R., Li, X., and You, Z. P. (2023). A literature review: asphalt pavement repair technologies and materials. *Proc. Institution Civ. Eng. -Engineering Sustain.* 0, 1–15. doi:10.1680/jensu.22.10000

Yusoff, N., Shaw, M. T., and Airey, G. D. (2011). Modelling the linear viscoelastic rheological properties of bituminous binders. *Constr. Build. Mater.* 25 (5), 2171–2189. doi:10.1016/j.conbuildmat.2010.11.086

Zhang, H., Chen, Z., Xu, G., and Shi, C. (2018). Evaluation of aging behaviors of asphalt binders through different rheological indices. *Fuel* 221, 78–88. doi:10.1016/j.fuel.2018.02.087

Zhang, T. J., Wang, D. L., and Lu, Y. (2023). RheologyNet: a physics-informed neural network solution to evaluate the thixotropic properties of cementitious materials. *Cem. Concr. Res.* 168, 107157. doi:10.1016/j.cemconres.2023.107157

Zhou, Y. X., Xu, G., Wang, H. Z., Chen, X. H., Fan, Y. L., Yang, J., et al. (2023). "Investigation of the rheological properties of devulcanized rubber-modified asphalt with different rubber devulcanization degrees and rubber contents," in *Road materials and pavement design* (Taylor & Francis). London, UK, doi:10.1080/14680629.2023.2287714

Impact of salt erosion on mechanical and drying shrinkage performance of cement stabilized macadam

Chengbin Wang[1], Yadi Chen[2]*, Baoping An[3], Qinglin Guo[4]* and Yibo Wang[4]

[1]Linxia Highway Development Center of Gansu Province, Linxia, China, [2]Kanglin Expressway Toll Station of Gansu Province, Linxia, China, [3]Gansu Province Transportation Planning Survey & Design Institute Co., Ltd., Lanzhou, China, [4]School of Civil Engineering, Hebei University of Engineering, Handan, Hebei, China

The arch expansion damage of asphalt pavement is a typical disease in desert Gobi and saline-alkali areas, and the reasons for arch expansion are very complex. Exploring the impact of salt solution on the mechanical and drying shrinkage performances of cement-stabilized macadam helps to clarify the causes of the arch expansion damage. To this purpose, this paper designed a salt solution infiltration experiment, using salt solution infiltration to simulate the transmission and accumulation of salts in cement-stabilized macadam, and carried out the compressive and flexural tests of cement-stabilized mortar and cement-stabilized macadam, and measured the drying shrinkage performance of cement-stabilized mortar and macadam. The results show that the type of salt solution has a significant influence on the weight of the cement-stabilized mortar samples, sulfates will cause the samples to lose weight, while chlorides and mixed solutions cause the increase in weight. Chlorides and sulfates lead to the decrease in the strengths of cement-stabilized mortar and macadam. The salt crystallization will lead to the decline of the drying shrinkage strains of cement-stabilized mortar and macadam, which has a positive action for reducing the drying shrinkage deformation. However, under the combined action of chlorides and sulfates, cement-stabilized macadam expands with the moisture loss. This may be one of the important causes of the arch expansion of asphalt pavement in the Gobi area and saline-alkali area.

KEYWORDS

cement-stabilized macadam, arch expansion, salt erosion, mechanical property, drying shrinkage

1 Introduction

The subbase layer is an important structure of asphalt pavement, which directly affects the stability, service life, and operational efficiency of the asphalt pavement. The subbase using cement-stabilized macadam has the advantages of high strength, large rigidity, strong integrity, and good stability and durability, therefore, it is a commonly used subbase form for asphalt pavement in many countries. However, salt erosion inside of cement or lime-modified materials can lead to the formation of expansive crystals, resulting in the arching up phenomenon of the road surface. After a period of construction, roads such as the

U.S. Route 82, US 67, I-635 (Chen et al., 2005), the main road in Las Vegas (Mitchell, 1986), and the Bush Road in Georgia (Rollings et al., 1999) have all experienced arching up phenomenon, mainly due to the formation of ettringite crystals by sulfate erosion of cement-stabilized materials. Similarly, many roads in Inner Mongolia and Xinjiang, China (Song et al., 2019; Wang et al., 2020) have also exhibited similar diseases about arching up phenomenon. Arching up of the road surface gradually appears 1–2 years after construction, with the highest arching height reaching up to 10 cm. The most severe arching occurred in summer, the spacing of the most severe section is less than 50 m. The arching up phenomenon of the asphalt pavement is generally characterized by the overall uplift of the subbase or the appearance of bumps, which in turn causes the road surface to arch up. The severe bumps on the road surface greatly restricts the road travelling capacity and poses a threat to driving safety (Tang et al., 2020; Tang, 2022). Therefore, it is necessary to carry out research on the damage mechanism of arching up of cement-stabilized macadam.

In order to reveal the mechanism of arching up of asphalt pavement, many scholars have conducted many meaningful works. Huang et al. (2017) found that the pavement surface of the Lina section of the Beijing-Xinjiang Expressway in China appeared to arch up, and the arching up phenomenon occurred in the third year after the construction of the subbase. The longer the continuous construction length of the cement-stabilized subbase, the more the arching ups. Zhang et al. (Zhang, 2018) conducted a disease investigation on the roads in Inner Mongolia, China and found that the degree of pavement surface uplift varied, with a spacing of 10–30 m, and the direction of the uplift was mainly transverse. Wang et al. (Hong, 2019) and Xie et al. (2019) investigated the road sections of the Beijing-Xinjiang Expressway and S312, found that the arching up phenomenon mostly happens in summer. The maximum height of arching part on the Beijing-Xinjiang Expressway was about 20cm, and the maximum height of the arching section in S312 was about 10 cm. The higher the cement content, the more severe the subbase arching up, and the degree of salinization in the subbase at the arching site was high. Yao et al. (2021) pointed out that the arching up of asphalt pavement with cement-stabilized subbase in the desert and Gobi areas of Inner Mongolia were mainly caused by high-temperature expansion and uplift deformation. Temperature has a significant impact on the uplift and cracking of asphalt pavement with cement-stabilized macadam. Under the same thermal condition, the subbase is more prone to expansive than the surface layer. Yao et al. (2020) also designed a test to determine the coefficient of expansion of the cement-stabilized macadam, pointing out that the gradation, cement dosage and curing age have significant impacts on the coefficient of expansion, while the sulfate content has almost no effect on the expansion of cement-stabilized macadam. When the temperature rises from 10°C to 50°C, the coefficient of expansion reaches its maximum. Dai et al. (2021) pointed out that the arching disease of asphalt pavement has spatial regional attributes and is periodic in occurrence. The unconfined compressive strength of the subbase of the section without arching is greater than that of the arching section, and the content of sulfate in the arching section is higher than that of the non-arching section. The crystallization of sulfates has caused damage to the microstructure of the subbase at the arching up site. The combined action of heat and salt is the main cause of the arching up of the

asphalt pavement with cement-stabilized subbase in the Gobi areas, and the pavement surface arching is caused by the combined action of temperature and salt expansion caused by sulfate.

Based on the above analysis, it can be seen that the arching of asphalt pavement mostly occurs in desert and Gobi areas, and the probability of arching in saline land areas is greater. The arching of the pavement layer mainly occurs in summer, and gradually stops after entering autumn. Besides, the material strength at the arching site of the road surface will be damaged. Teng et al. (Jidong et al., 2016) pointed out that in areas with very little rainfall and large evaporation, due to the large temperature difference between day and night, the migration of water vapor leads to a significant 'lid effect' at the bottom of the surface layer, that is, moisture will accumulate under the asphalt surface layer, which will lead to the continuous accumulation of salts in the subbase and ultimately cause the arching and destruction of the asphalt pavement. The crystallization and precipitation of salts directly related to the evaporation of water. Herein, exploring the impact of salts on the strength and shrinkage performance of cement-stabilized macadam can clarify the cause of the arching up.

In summary, this work determined the optimal moisture content of cement-stabilized mortar and macadam mixture through compaction tests, designed indoor salt erosion orthogonal experiments, measured the mechanical strength of cement-stabilized mortar and macadam mixture after salt erosion, and conducted drying shrinkage experiments, analyzed the drying shrinkage state of cement-stabilized macadam under different salt erosion conditions. The work in this paper confirms the adverse effect of salt erosion on the drying shrinkage performance of cement-stabilized macadam and has good reference significance for improving the design of cement-stabilized macadam in the Gobi area.

2 Materials and experimental

2.1 Raw materials

This work conducts the tests using P•O42.5 Portland cement. The properties of the cement are shown in Table 1. The aggregate used in this paper is limestone, and the performances of the macadam are listed in Table 2. The gradations of cement-stabilized mortar and cement-stabilized macadam mixture are shown in Figure 1.

This experiment uses analytically reagent produced by Tianjin Zhiyuan Chemical Reagent Co., Ltd. to simulate the salt environment in saline soil. The properties of sodium sulfate and sodium chloride are shown in Table 3.

2.2 Experimental

2.2.1 Salt erosion scheme

Under the influence of salt erosion, the crystallization not only alters the internal pore structure of the cement-stabilized macadam but also causes local expansion damage, thereby inducing changes in the strength of the cement-stabilized macadam. To clarify the changes in mechanical properties and volume stability of cement-stabilized macadam under the influence of salt, a salt solution migration and infiltration method is used to simulate the

TABLE 1 Properties of cement.

Indicators		Test value
Fineness (%)		2.51
Initial Setting Time(min)		155
Final Setting Time(min)		223
Flexural strength of mortar (MPa)	3d	4.5
	28d	9.0
Compressive strength of mortar (MPa)	3d	26.1
	28d	51.8

erosion effect. Since the migration process of salts in saline soil is complex and the salt solution immersion cannot simulate the salt migration phenomenon at road sites, this work uses the infiltration method to simulate the migration effect of salts with water, using a sponge containing salt solution to simulate the underlying road subgrade. The same wet sponge is placed above the specimen to cover it, and the infiltration treatment process of the specimen is shown in Figure 2. Each infiltration lasts for 12 h, followed by the drying at room temperature about 23°C for 12 h, completing one cycle every 24 h. After the infiltration treatment, mechanical property and volume stability tests are conducted.

This paper uses the orthogonal test to explore the effects of salt type, solution concentration, and erosion cycles on the mechanical properties and drying shrinkage of cement-stabilized macadam. According to existing results (Wang, 2023), the concentration of salt solution is generally between 3% and 10%, and this work adopts salt solution concentrations of 3wt%, 5wt%, and 10wt%. The types of salt solutions include sulfates, chlorides, and the mixed solution of sulfates and chlorides. The upper limit of erosion cycles is set to 5. Based on the design principle of L9(3³), the orthogonal groups can be determined, as shown in Table 4.

Based on the condition of the lowest mechanical strength of cement-stabilized mortar in the orthogonal experiment as the most unfavorable condition, in addition, most areas of saline-alkali land contain sulfates and chlorides, it is also necessary to investigate the impact of mixed salts on the stability of cement-stabilized macadam. Therefore, this work carries out salt erosion treatment for cement-stabilized macadam under the following conditions, as shown in Table 5.

2.2.2 Ion titration method

To evaluate the distribution of salts in the specimen after the migration of the salt solution, the silver nitrate titration method is used to determine the content of NaCl, and the ethylene diamine tetraacetic acid (EDTA) complexometric titration method is used to determine the concentration of Na_2SO_4, in accordance with the Chinese specification JTG 3430-2020 (Ministry of Transport's Research Institute of Highway RIH, 2021). Samples are taken from different parts of the specimen, as shown in Figure 3. The preparing process of test solution is shown in Figure 4.

The silver nitrate titration method is used to determine the chloride ion content of the test solution. Methyl orange is used as an indicator, and 0.02 mol/L $NaHCO_3$ is added until the solution turns pure yellow, ensuring a pH value of 7. Six drops of K_2CrO_4 with the 5% molar concentration are added as chemical indicator, and the silver nitrate standard solution is titrated until brick-red precipitate forms. The consumed volume of $AgNO_3$ solution is recorded. The entire titration process is shown in Figure 5. The chloride ion content is calculated using the Equations 1, 2.

$$Cl^-(mmol/kg) = \frac{v \times c}{m} \times 1000 \tag{1}$$

$$Cl^-(\%) = Cl^-(mmol/kg) \times 0.0355 \times 10^{-1} \tag{2}$$

Where, c represents the concentration of the silver nitrate solution, mol/L; v represents the volume of the titrated solution, mL; m is the dry weight of the mixture taken from the volume of the leachate, g.

The EDTA indirect complexometric titration method is used to determine the sulfate ion content of the test solution. The specific procedure can refer to the standard JTG 3430-2020. After the titration, the content of sulfate ions is calculated according to Equations 3, 4.

$$SO_4^{2-}\left(mmol\frac{1}{2}SO_4^{2-}/kg\right) = \frac{2c(V_2 + V_3 - V_1)}{m} \times 1000 \tag{3}$$

$$SO_4^{2-}(\%) = SO_4^{2-}\left(mmol\frac{1}{2}SO_4^{2-}/kg\right) \times 0.0480 \times 10^{-1} \tag{4}$$

Where, c is the concentration of the EDTA standard solution, mol/L; m represents the weight of dry mixture corresponding to the sodium sulfate content in the leachate, g. V_1 represents the volume of EDTA solution consumed when the standard solution changes from a wine-red to a pure blue color during titration, ml; V_2 represents the volume of EDTA solution consumed when the blank control group solution changes from a wine-red to a pure blue color during titration, ml; V_3 represents the volume of EDTA solution consumed during titration of the test solution, ml.

2.2.3 Mechanical performances test

To evaluate the effect of salt erosion on the strength of cement-stabilized mortar and cement-stabilized macadam mixture, compressive and flexural tests were conducted. According to the Chinese standard GB/T 17,671-2021 (Standardization Administration of ChinaSAC, 2021), cement-stabilized mortar specimens with a dimension 40 mm × 40 mm × 160 mm are molded using a static compression method and cured in an environment of 20°C and 95% relative humidity. Tests are performed at the age days. The loading rate for the flexural test of cement-stabilized mortar is 50N/s, and each group of experiments is conducted with three replicates. Compressive tests are performed using the failure samples from the flexural test, with a loading rate of 2.4 kN/s for the compressive test. It should be noted that for the 7-day test, the specimens should be soaked in water on the last day of curing. The flexural and compressive strengths are determined using Equation 5.

$$R_f = \frac{1.5F_f \cdot L}{b^3} \tag{5}$$

TABLE 2 Properties of coarse aggregate.

Properties	Apparent specific gravity	Moisture absorption(%)	Crushing value (%)	Los Angeles Abrasion value (%)	Flake and elongated particle content (%)
Value	2.711	0.53	19.6	17.2	13.5
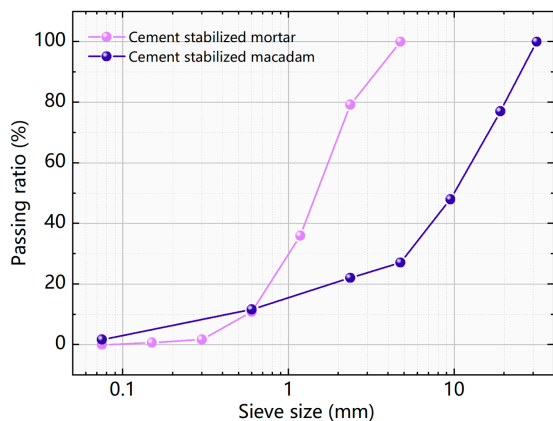
FIGURE 1
Gradations of cement stabilized mortar and macadam.

Where, R_f is the flexural strength, MPa; F_f represents the failure load. N; L represents the support span of the beam specimen, mm; b represents the width of the specimen's cross section, mm.

$$R_c = \frac{F_c}{A} \qquad (6)$$

Where, R_c is the compressive strength, MPa; F_c represents the failure load, N; A is the area bearing the compressive load, mm^2.

In addition, to evaluate the impact of salt erosion on the strength of cement-stabilized macadam, cylindrical specimens with dimensions of $\Phi150$ mm $\times$ 150 mm were prepared using the compaction method according to JTG 3430-2020. After curing, the specimens were subjected to salt erosion treatment and their compressive strength was tested. The loading rate was 1 mm/min, and the compressive strength was calculated according to Equation 6.

2.2.4 Drying shrinkage test

The migrating of salt solution into cement-stabilized macadam not only affects its strength, but also, after the evaporation of water, salt crystallization occurs, generating crystallization pressure that causes volume expansion of the cement-stabilized macadam. In contrast, cement-stabilized macadam without salt will undergo drying shrinkage as water evaporating. For the mixture containing salt solution, the expansion effect caused by salt crystallization and the drying shrinkage are coupled. Therefore, this paper carries out drying shrinkage test on cement-stabilized mortar and cement-stabilized macadam to clarify the expansion of cement-stabilized macadam mixtures affected by salt erosion.

The specimens of cement-stabilized mortar with dimension of 40 mm $\times$ 40 mm $\times$ 160 mm were prepared in lab, and the specimens of cement-stabilized macadam with dimension of 100 mm $\times$ 100 mm $\times$ 400 mm also were prepared. After the compaction, they are cured in an environment with a temperature of 20°C $\pm$ 1°C and a relative humidity above 95% for 7 days, and then placed in an environment with a temperature of 20°C $\pm$ 2°C and a relative humidity of 50% $\pm$ 5% for shrinkage tests. Due to the rough surface of the beam specimen, if the dial indicator is directly in contact with the specimen surface, the dial indicator is very susceptible to disturbance. Therefore, organic glass plates are glued to both ends of the specimens to ensure good contact between the dial indicator and the glass plates.

The moisture loss and drying shrinkage coefficient can be determined using Equations 7–10.

$$\omega_i = (m_i - m_{i+1})/m_p \qquad (7)$$

$$\delta_i = \sum_{j=1}^{2} X_{i,j} - \sum_{j=1}^{2} X_{i+1,j} \qquad (8)$$

$$\varepsilon_i = \delta_i/l \qquad (9)$$

$$\alpha_{di} = \varepsilon_i/\omega_i \qquad (10)$$

Where, m_i, m_{i+1} represent the specimen weight at the ith and ($i+1$)th weighing, respectively. m_p refers to the weight of the specimen after drying. δ_i is the drying shrinkage deformation at the ith measurement, mm. $X_{i,j}$ and $X_{i+1,j}$ represent the dial reading value of the jth dial indicator at the ith and ($i+1$)th measurement, respectively, mm. ε_i is the shrinkage strain at the ith measurement. l represents the length of the specimen, mm; α_{di} represents the shrinkage coefficient of the ith test; %; ω_i represents the moisture loss of the specimen at the ith measurement, %.

3 Result and discussions

3.1 Determination of the optimal moisture content

According to the specifications (Ministry of Transport's Research Institute of Highway RIH, 2021) and experience, the amount of cement used in this paper is 5%. Due to the abundance of fine aggregates in the cement-stabilized mortar, the moisture content of 6%–10% is selected for the compaction test; whereas the coarse aggregates in cement-stabilized macadam have a low specific surface area, hence the moisture content of 3%–7% is chosen for the

TABLE 3 Properties of Na_2SO_4 and NaCl.

Chemical formula	Molar Mass (g/mol)	Density(g/cm³)	Melting point (°C)	Boiling point (°C)	Solubility (g/100 mL, 25 °C)
Na_2SO_4	142.04	2.664	884	1429	28.1
NaCl	58.44	2.17	802.018	1465	36.0

FIGURE 2
Salt erosion infiltration process.
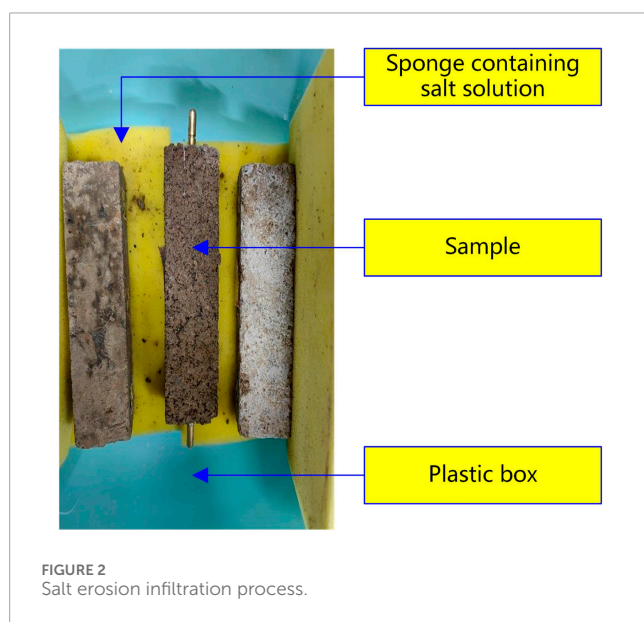
compaction test. The diameter of the sample is 152 mm, and each layer of the mixture is compacted 98 times. The dry densities of the cement-stabilized mortar and the cement-stabilized macadam were measured, as shown in Figure 6.

From Figure 7, it can be seen that the dry density first increases and then decreases with the increase of moisture content. Based on the principle that the higher the dry density, the greater the load-bearing capacity of the mixture, the moisture content and density corresponding to the peak point are the optimal content and maximum dry density. Therefore, it can be determined that the optimal moisture content for cement-stabilized mortar is 7%, and the maximum dry density is 1.95 g/m³. The optimal moisture content for cement-stabilized macadam is 5%, and the maximum dry density is 2.504 g/cm³. Cement-stabilized mortar and cement-stabilized macadam mixtures are prepared according to the optimal moisture content. Flexural and compressive strengths are tested to determine whether they meet the strength requirements for the use in road engineering. The results are listed in Table 6. The data in the table show that the unconfined compressive strength of cement-stabilized macadam prepared with 5% cement after 7 days exceeds 5 MPa, meeting the strength requirements of the Chinese specification JTG D50-2017 (Ministry of Transport's Research Institute of Highway RIH, 2017), meaning that the amount of cement selected in this paper is feasible.

3.2 Weight changing and strength of cement-stabilized mortar

During the salt solution infiltration process, due to the capillary action, cement-stabilized mortar and cement-stabilized macadam will absorb the salt solution as the time extends, thereby causing changes in the weight of the mixture. The results of the weight changing after salt solution treatment are listed in Table 7.

As shown in Table 7, the weight changing of cement-stabilized mortar to different solutions is not consistent. It should be noted that specimens containing sulfate solution experience a reduction in weight, while those infiltrated in chloride and mixed solutions both result in an increase in weight. The decrease of the specimen weight primarily due to the erosion of the specimen surface by the sulfate solution, which leads to the detachment of some materials. The detachment does not occur in the case of chloride and mixed solutions. Comparing the six groups where the weight changing is greater than zero, the highest moisture absorption is for the group #3, reaching 2.71%, while the lowest is for group #8, at only 0.68%, the maximum absorption is approximately four times that of the minimum. Thus, the concentration of the solution, the solution type, and the infiltration cycles can lead to significant differences in the weight changing. This further leads to variations of salt concentration inside the mixture, which in turn affects the mechanical properties of the cement-stabilized mixture.

Salt solutions can cause physico-chemical erosion effects on cement-stabilized mixture, leading to a reduction in strength. Therefore, this paper measured the compressive and flexural strengths of cement-stabilized mortar, the results is listed in Table 8. It should be clarified that after curing the specimens for 7 days, they are subjected to infiltration, and their strength is measured after the soaking treatment.

As listed in Table 8, it can be seen that salt solution erosion has a significant impact on the strength of cement-stabilized mortar, with compressive strength ranging from 2.29 to 9.0 MPa, and flexural strength ranges from 1.03 to 4.57 MPa. The maximum compressive strength is 3.9 times the minimum, while the difference in flexural strength is more pronounced, with the maximum flexural strength being 4.4 times the minimum. This indicates that the impact of salt solution erosion on flexural strength is significant, suggesting that after salt solution migration into cement-stabilized macadam, the flexural strength decays more rapidly, leading to premature cracking in the cement-stabilized subbase layer. Compared with the untreated cement-stabilized mortar, for groups #1 and #6, the compressive strength has already exceeded the 28-day compressive strength of the control group, indicating that the salt erosion has a positive role in the compressive strength of cement-stabilized mortar. Both groups of mixtures also have higher flexural strength than the 28-day

TABLE 4 Orthogonal test groups.

No.	A Solution concentration (%)	B Solution type	C Erosion cycles	Level combination (C)
1	3	Sodium sulfate solution	1	A_1B_{11}
2	3	Sodium chloride solution	3	A_1B_{22}
3	3	Mixed solution	5	A_1B_{33}
4	5	Sodium sulfate solution	3	A_2B_{12}
5	5	Sodium chloride solution	5	A_2B_{23}
6	5	Mixed solution	1	A_2B_{31}
7	10	Sodium sulfate solution	5	A_3B_{13}
8	10	Sodium chloride solution	1	A_3B_{21}
9	10	Mixed solution	3	A_3B_{32}

TABLE 5 Experimental conditions for cement-stabilized macadam.

No.	A Solution concentration (%)	B Solution type	C Erosion cycles
1	0	No salt	0
2	10	Sodium chloride solution	5
3	10	Mixed solution	5

FIGURE 3
Schematic diagram of sampling positions.

flexural strength of the control group. It is found that all these groups contain sodium sulfate solution, and the solution concentration does not exceed 5%. Therefore, it is inferred that when the concentration of sulfate is low, it has a certain strengthening effect on cement-stabilized mortar, which can increase the compressive strength by up to 1.16 times. Zhang et al. (Zhang et al., 2022) indicated that the porosity of cement-stabilized macadam declined with the

extension of drying period. It means that the few crystal particles just fill the micro-pores inside the mortar, making the mixture more compact, which is manifested as an increase in compressive strength. For groups #2-#5 and #7-#9, the compressive strengths all decrease after salt erosion. On the one hand, the corrosive effect of chloride salts affects the cement hydration reaction, leading to reduced hydration. On the other hand, the higher concentration of salt solution results in more salt crystal particles precipitating, and the massive crystal precipitation generates expansion and pressure, causing micro-cracks and damage inside the mortar, ultimately leading to a decrease in the compressive strength. The specific mechanism of strength decay is shown in Figure 7.

It can be found that the weight changes in the infiltration process, the compressive and flexural strengths also influenced by salt solution. But the significance what affects these properties is unknown. For this purpose, statistical analysis methods were used to evaluate the significance of solution concentration, solution type and infiltration cycles. The significance level (α) employed in this investigation was 0.05. The F-test, Levene's test and Welch's test were performed according to a confidence level of 95%. It should be noted that before conducting variance analysis, Levene's test is first used to determine whether there is a significant difference in variance between the test data. If the p-value of Levene's Test is less than 0.05, the variances among different data groups are significantly different, and in this case, Welch's test should be conducted. Conversely, when the p-value of Levene's Test is greater than 0.05, it is believed that there is no significant difference in variance, and an F-test can be performed. If the p-value of the F-test is less than 0.05, it is considered that the source of variance has a significant impact on the test indicator. The analysis results were listed in Table 9.

The statistical results from Table 9 indicate that the effect of salt solution concentration on the weight of the samples follows the

FIGURE 4
Preparation of test solution.
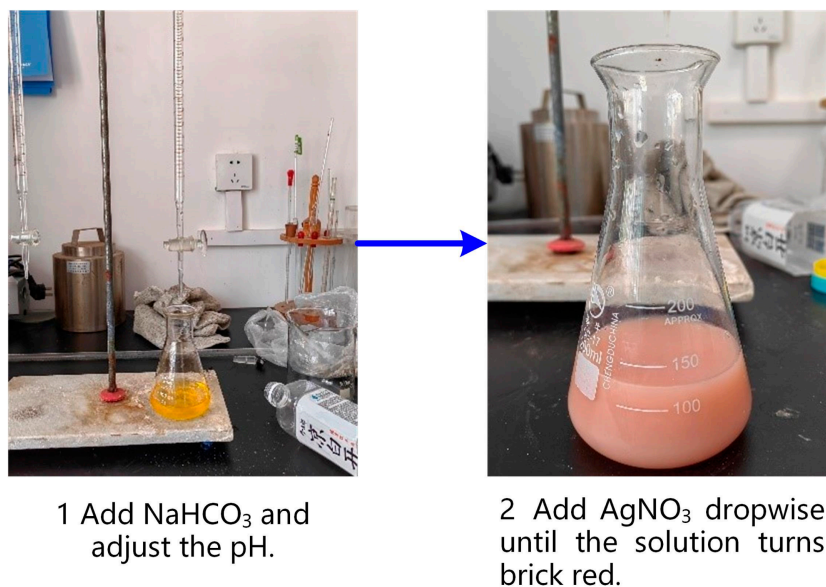
FIGURE 5
Chloride ion titration test procedure.

F-test, while the effects of solution type and infiltration cycles on flexural strength also conform to the F-test. The influence of solution concentration, solution type, and infiltration cycles on compressive strength all follow the Welch test. Based on the *p-value* of the hypothesis test, the solution type has a significant impact on the change in the weight of the samples, and the solution concentration, solution type, and infiltration cycles all have significant impacts on the compressive and flexural strengths of cement-stabilized mortar.

3.3 Weight changing and strength of cement-stabilized macadam

The weight changing of the cement-stabilized macadam is shown in Figure 8.

As described in Figure 8, the weight changing of the cement-stabilized macadam mixture varies with the type of salt solution. Since the weight change is greater than zero, it indicates that the cement-stabilized macadam has absorbed moisture during the infiltration treatment process. In conjunction with the groups in Table 5, it can be seen that the mixture absorbs the most water when subjected to infiltration in a mixed solution. The moisture absorption of specimens infiltrated with a sodium chloride solution is higher than that of pure water. Since the internal pore structure of the cement-stabilized macadam mixture is essentially consistent under the standard compaction, the volume of water absorbed by the mixture also is consistent; the higher the concentration of the solution, the greater the specific gravity of the solution, thus leading to an apparent increase in the moisture absorption. Comparing the weight changing of cement-stabilized macadam and mortar reveals

FIGURE 6
Dry density of compaction test.
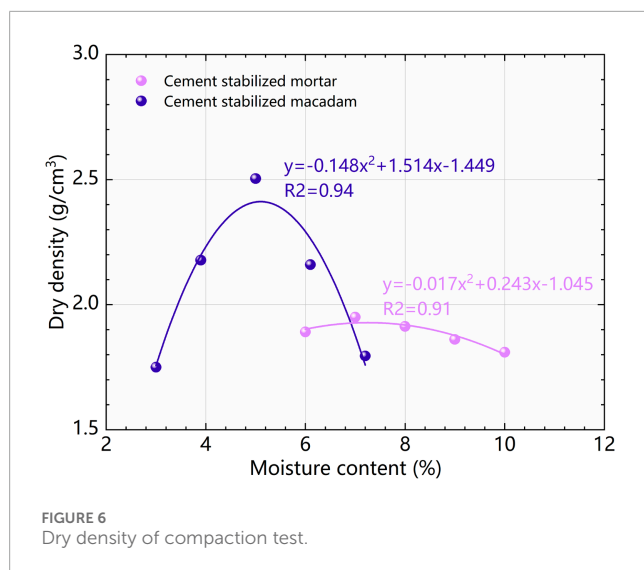
that the moisture absorption of the cement-stabilized macadam is lower than that of the cement-stabilized mortar. This is because the cement-stabilized mortar is composed of fine particles with a larger specific surface area and stronger capillary absorption within, resulting in a higher moisture absorption. This also indirectly proves that using a coarse gradation can reduce the moisture absorption of the cement-stabilized macadam, thereby decreasing the probability of drying shrinkage and cracking caused by moisture fluctuation in the subbase layer. The compressive strength of cement-stabilized macadam mixture after solution treatment is listed in Figure 9.

From Figure 9, it can be observed that the compressive strength of group #1(control) is the highest, reaching 5.1MPa, followed by group #2, with group #3 being the lowest. Compared with the samples that have not undergone salt solution treatment, the sodium chloride solution treatment (#2) resulted in a 19.6% reduction in the compressive strength, while the mixed solution caused a 29.4% decrease in the strength of the cement-stabilized macadam. So, the mixed solution has the most significant impact on the compressive strength of the cement-stabilized macadam. The reduction in compressive strength is mainly due to the dissolution of some calcium aluminate hydrates in the cement by the chloride salts, and the crystallization pressure induced by the crystallization of salts leading to the formation of micro-cracks. The salt crystallization phenomenon is evident on the surface of the samples.

3.4 Effect of salt erosion on drying shrinkage performance

From the analysis in Section 3.2, 3.3, it can be seen that the salt solutions will produce a corrosive effect, and the crystallization of salts will generate expansive pressure, both of which lead to a decrease in the strength of cement-stabilized mortar and cement-stabilized macadam. For cement-stabilized materials, shrinkage occurs with the moisture loss, and salt-containing cement-stabilized macadam will simultaneously undergo shrinkage and crystallization expansion. To clarify the impact of salt erosion on the drying shrinkage performance of cement-stabilized mortar and

cement-stabilized macadam, the shrinkage performance of cement-stabilized mortar and cement-stabilized macadam was measured, and the test results are shown in Figure 10.

As described in Figure 10, it can be observed that compared to the control group, the shrinkage strains at 168 h of groups #1 to #9 have all decreased, indicating that the salt solution treatment reduced the degree of drying shrinkage of the cement-stabilized mortar. During the dehydration and shrinkage process, the crystallization of salts generated expansive pressure, causing the cement-stabilized mortar to expand. However, the expansion effect did not change the fundamental characteristic of the mortar undergoing shrinkage. By comparing the shrinkage strain of groups #1 to #9, it can be seen that the shrinkage strain of groups #7 to #9 is significantly smaller than that of the control group, about one-third of the strain of the control group. These three groups had a salt solution concentration of 10%, thus it can be seen that the higher the concentration of the salt solution, the stronger the crystallization expansion, leading to a significant reduction in drying shrinkage strain. If the minimum shrinkage strain is taken as the criterion, then salt erosion has a positive effect on reducing the shrinkage degree.

Considering the actual service state of subbase layer, salts gradually migrate day by day, and multiple salt erosions lead to a decline in the performance of cement-stabilized mortar, which involves complex physical and chemical processes. During the erosion processes, phenomena such as salt accumulation, crystal formation, dissolution of cement-based materials, and internal structure damage occur, which are the main reason for strength degradation. In this paper, when evaluating the shrinkage performance of cement-stabilized macadam, Infiltration cycles were set to 5. The drying shrinkage strain and moisture loss of cement-stabilized macadam are shown in Figure 11.

As shown in Figure 11, the drying shrinkage strain of the control group (#1) gradually increases with the extension of the drying time and approaches stable after reaching 60 days, with no further increase in shrinkage strain. This is consistent with the test results of Tran et al. (2021). Throughout the whole test process, the cement-stabilized macadam of the control group (#1) continues to shrinkage. The mixture treated by the solution of sodium chloride undergo shrinkage deformation in the early stage (not exceeding 20 days), and as the drying time extends, the shrinkage strain begins to gradually decrease, indicating that the mixture has generate expansion deformation, which is caused by the crystallization of salts due to the moisture loss. After the macadam was treated by the mixed salt solution (#3), the cement-stabilized macadam undergoes expansion strain, and this expansion strain gradually increases with the extension of the drying time. The expansion strain gradually stabilizes, reaching 147×10^{-6} after 60 days. Comparing the three groups, it can be determined that the effect of chloride components on the shrinkage of cement-stabilized macadam has a lag, and although expansion strain has occurred, the mixture still shows a general shrinkage characteristic. The coupled action of sulfates and chlorides will lead to a large expansion strain in the cement-stabilized macadam mixture, which is not conducive to maintaining the stability of the cement-stabilized subbase layer. When the cumulative expansion strain exceeds the limit of material, the subbase layer will arch up. Therefore, it is reasonable to infer that in saline areas, the arching up and bulging damage of asphalt

FIGURE 7
Strength decay mechanism of cement stabilized mortar.
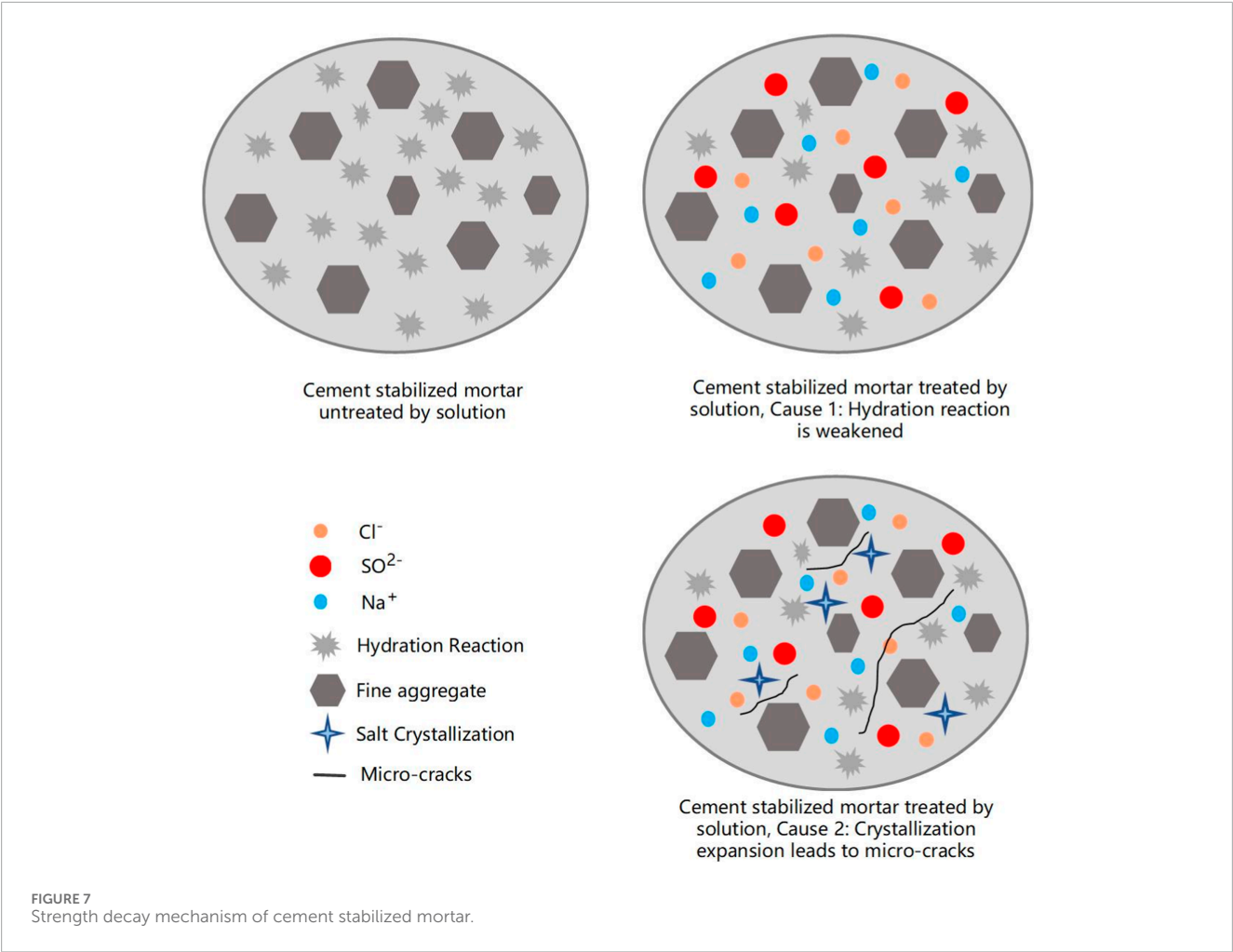
TABLE 6 Strength of cement-stabilized mortar and macadam.

Type	Value	7d		28d	
		Flexural strength (MPa)	Compressive Strength (MPa)	Flexural strength (MPa)	Compressive Strength (MPa)
Cement-stabilized mortar	Mean	1.81	7.26	2.25	7.76
	SD	0.048	0.346	0.042	0.182
	CV (%)	2.67	4.77	1.87	2.34
Cement-stabilized macadam	Mean	—	5.45	—	—
	SD	—	0.23	—	—
	CV (%)	—	4.15	—	—

pavement is closely related to the combined action of sulfates and chlorides.

From Figure 11, it can also be seen that the moisture losses of the specimens for three groups follow the same trend, with the maximum moisture loss at 90 days being about 3.6%. Thus, the moisture loss of the cement-stabilized macadam will not undergo significant changes under the same environmental condition. However, the salts that entering the mixture will gradually crystallize and precipitate as the increase of moisture loss, and different types of salts have significant impact on the drying shrinkage of the cement-stabilized macadam. To determine the shrinkage coefficient of the cement-stabilized macadam, a linear fitting was performed on the

TABLE 7 Weight changing of cement-stabilized mortar.

No.	Solution concentration (%)	Solution type	Infiltration cycles	Weight changing (%)
#1	3	Sodium sulfate solution	1	−1.52
#2	3	Sodium chloride solution	3	1.61
#3	3	Mixed solution	5	2.71
#4	5	Sodium sulfate solution	3	−1.79
#5	5	Sodium chloride solution	5	2.24
#6	5	Mixed solution	1	0.81
#7	10	Sodium sulfate solution	5	−1.34
#8	10	Sodium chloride solution	1	0.68
#9	10	Mixed solution	3	1.86

TABLE 8 Strengths of cement-stabilized mortar.

No		#1	#2	#3	#4	#5	#6	#7	#8	#9
Compressive strength (MPa)	Mean	8.86	3.60	7.16	7.62	2.29	9.00	5.13	5.56	4.97
	SD	0.15	0.03	0.03	0.09	0.12	0.09	0.06	0.08	0.03
Flexural strength (MPa)	Mean	3.12	1.22	2.51	2.53	1.03	4.57	1.55	1.49	1.50
	SD	0.12	0.03	0.04	0.08	0.04	0.04	0.04	0.06	0.03

TABLE 9 Statistical analysis on the properties of cement-stabilized mortar ($\alpha = 0.05$).

Item	Source of variance	P-value of Levene's Test	P-value of F-test	P-value of Welch's test	Significance
Weight Changing	Solution concentration	0.418	0.755	—	No
	Solution type	0.009	—	5.84×10^{-9}	Yes
	Infiltration cycles	0.041	—	0.291	No
Compressive strength	Solution concentration	9.6×10^{-13}	—	0.000001	Yes
	Solution type	4.3×10^{-13}	—	6.4×10^{-12}	Yes
	Infiltration cycles	0.000025	—	0.000029	Yes
Flexural strength	Solution concentration	7.3×10^{-16}	—	0.005	Yes
	Solution type	0.496	6.4×10^{-13}	—	Yes
	Infiltration cycles	0.512	6.73×10^{-8}	—	Yes

shrinkage strain, and the process is shown in Figure 12. Results are listed in Table 10.

From Figure 12, it can be observed that for the control group (#1), the shrinkage strain gradually increases with the increase of moisture loss, and it continues to show a trend of shrinkage throughout the test period. However, for group #2 treated by sodium chloride solution, an obvious shrinkage pattern is exhibited in the initial stage of moisture loss. When the moisture loss exceeds 2.5%, the shrinkage strain begins to decrease, indicating that the sample has transitioned from a shrinkage mode to an expansive mode.

FIGURE 8
Weight changing of cement-stabilized macadam.

FIGURE 9
Compressive strength of cement-stabilized macadam.

FIGURE 10
Shrinkage strain of cement-stabilized mortar.

FIGURE 11
Shrinkage strain and moisture loss of cement-stabilized macadam.

FIGURE 12
Shrinkage strain vs. moisture loss.
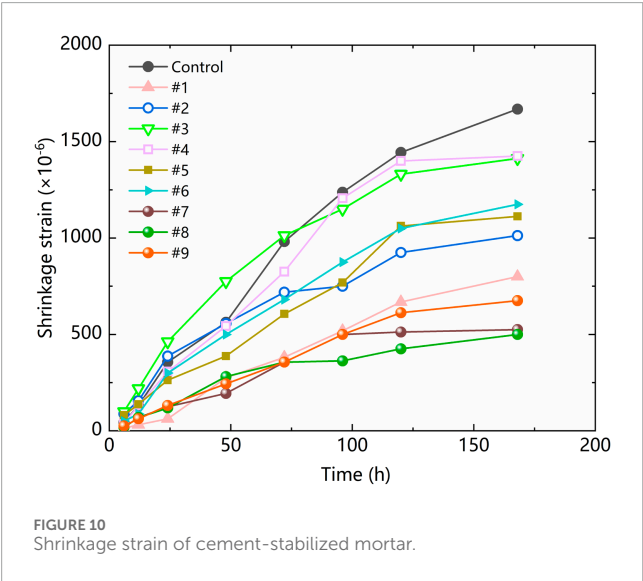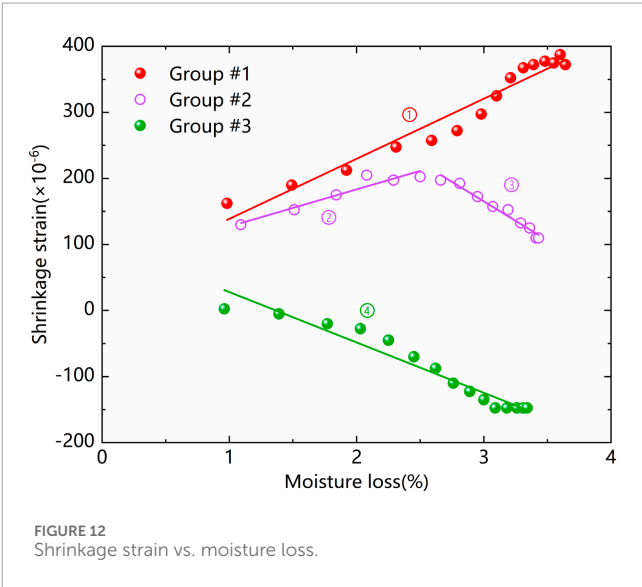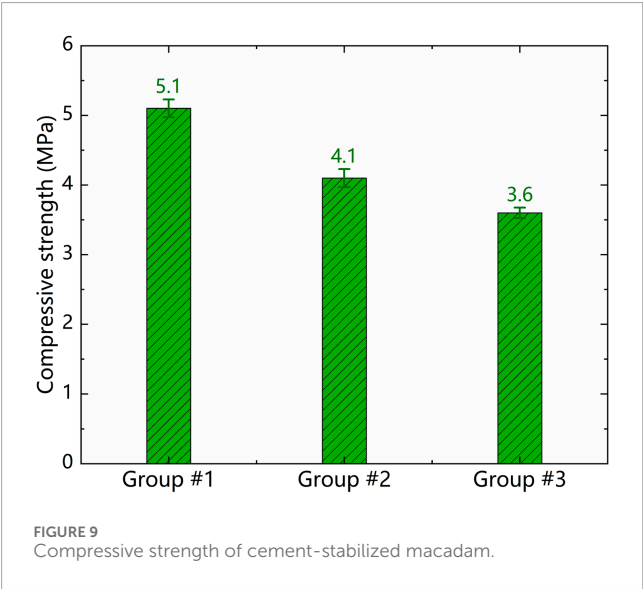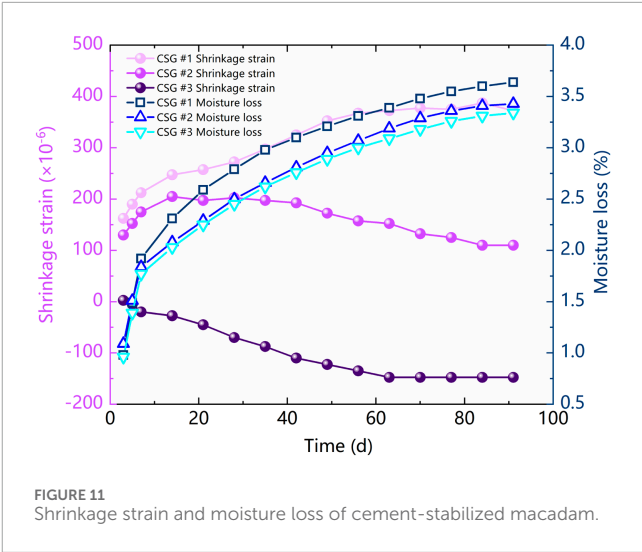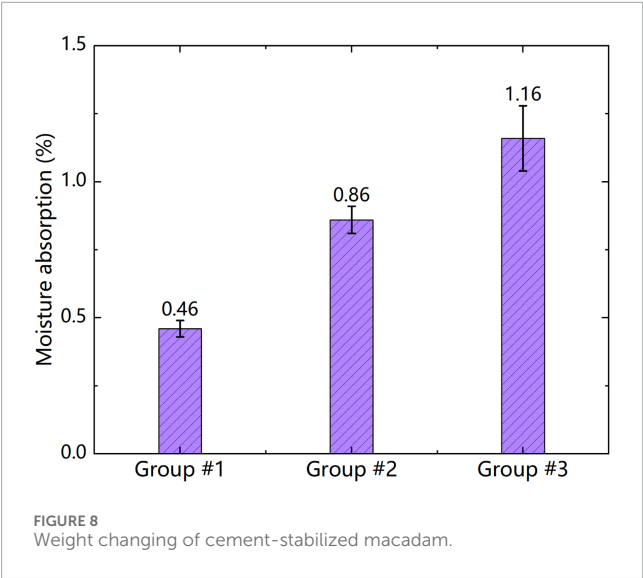
TABLE 10 Drying shrinkage coefficient.

No.	Fitting no.	Drying shrinkage coefficient($\times 10^{-6}$)	R^2
#1	①	91	0.946
#2	②	56	0.915
	③	−118	0.971
#3	④	−76	0.938

At this point, due to the significant moisture loss, the proportion of salt crystallization increases, leading to expansion strain, which offsets part of the shrinkage strain. For group #3, the expansion is evident from the initial stage of moisture loss. The results in Table 10 show that the R^2 for the linear fitting is greater than 0.9, indicating that the expansion caused by salt crystallization

TABLE 11 Content of SO_4^{2-} and Cl^- in cement-stabilized mortar.

No.	Content of SO_4^{2-} (%)			Content of Cl^- (%)			Mean (%)		SD (%)	
	Area #1	Area #2	Area #3	Area #1	Area #2	Area #3	SO_4^{2-}	Cl^-	SO_4^{2-}	Cl^-
#1	0.188	0.135	0.197	—	—	—	0.173	—	0.034	—
#2	—	—	—	0.179	0.129	0.187	—	0.165	—	0.031
#3	0.341	0.24	0.345	0.325	0.229	0.328	0.309	0.294	—	0.056
#4	0.573	0.411	0.598	—	—	—	0.527	—	0.102	—
#5	—	—	—	0.509	0.365	0.532	—	0.468	—	0.091
#6	0.222	0.159	0.232	0.174	0.126	0.182	0.204	0.16	—	0.030
#7	1.086	0.764	1.096	—	—	—	0.982	—	0.189	—
#8	—	—	—	0.237	0.17	0.247	—	0.218	—	0.042
#9	0.922	0.661	0.963	0.571	0.391	0.569	0.849	0.51	—	0.103

FIGURE 13
Correlation between the strength and ion content. **(A)** strength VS SO_4^{2-}; **(B)** strength VS Cl^-.
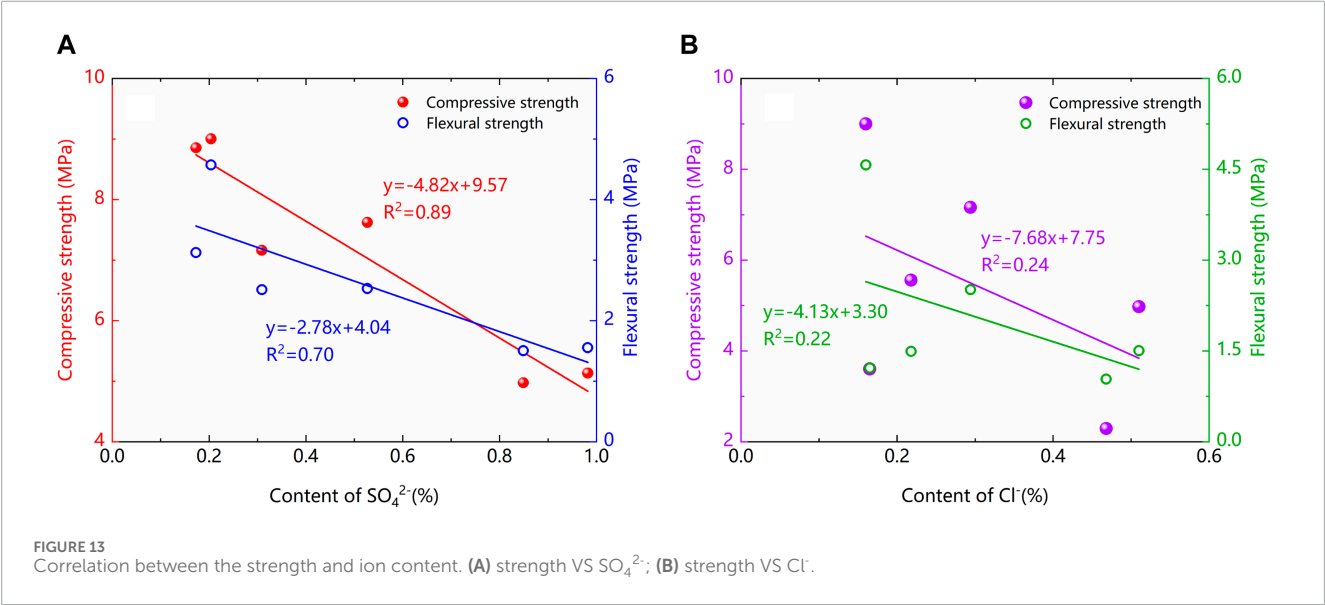
and shrinkage present a linear relationship with the moisture loss, consistent with the shrinkage pattern of commonly cement-stabilized macadam (Tran et al., 2021). Comparing the shrinkage coefficients of fitting ① and ②, it can be seen that sodium chloride helps to reduce the shrinkage coefficient of cement-stabilized macadam, and chloride salts may have a positive effect in reducing the shrinkage cracks of the cement-stabilized macadam mixture. However, when the moisture loss reaches 2.5%, the amount of sodium chloride crystallization continuously increases, leading to a significant expansion in the cement-stabilized macadam (fitting ③). The expansion effect is greater than the shrinkage according to the absolute value of the shrinkage coefficient. The samples infiltrated with a mixed solution exhibit an expansion from the initial stage of moisture loss, once again proving that the coupling of

sodium chloride and sodium sulfate will have an adverse influence on the volume stability of cement-stabilized macadam. Comparing the shrinkage coefficients in Table 10, the chloride salts will lead to a reduction in shrinkage, while the coupling action of sodium chloride and sodium sulfate will lead to expansion of cement-stabilized macadam. In saline areas, if the content of chloride and sulfate in the subbase layer continuously increases, it inevitably causes expansion due to salt crystallization and precipitation. When the expansion strain exceeds the limit of the subbase layer, the pavement will bulge, resulting in road arching up. Therefore, it can be inferred that the arching up of the asphalt pavement in saline areas is closely related to the salt type and concentration. The combined action of chloride and sulfate salts is the main reason of road arching up.

3.5 Ions concentration in cement-stabilized mortar

The content of SO_4^{2-} and Cl^- in the cement-stabilized mortar was determined by titration, as listed in Table 11.

From Table 11, it can be determined that both the sulfate ion content and the chloride ion content exhibit a characteristic of higher concentrations at the ends and lower concentrations in the middle of the specimen, which may be caused by the microstructure of the cement-stabilized mortar. During the sample molding process, due to the boundary effect of the mold, the compaction degree at both ends of the sample is lower than that of the central area, leading to an increase in micro-pores and a stronger capillary action, which is conducive to the rapid migration of the salt solution, manifesting as a higher ion content at the ends. Comparing the conditions of groups #1 to #9, the ion concentration increases with the increase of solution concentration and also gradually increases with the infiltration cycles. The relationship between ion content and the strength of cement-stabilized mortar is shown in Figure 13.

From Figure 13A, it can be seen that there is a good linear correlation between the compressive and flexural strengths of cement-stabilized mortar and the content of SO_4^{2-}. The slope of linear fitting indicates that the decay rate of compressive strength is greater than that of flexural strength, suggesting that compressive strength is more sensitive to changes in SO_4^{2-}. Figure 13B shows that chloride salts also lead to a decline in the strengths, but there is a general correlation between chloride ion content and strength, which may be due to the coupling effect caused by coexisting sulfates. Comparing Figures 13A, B, the variation in chloride ion content has significant impact on the compressive and flexural strengths of cement-stabilized mortar, as the decay rate of both strengths with the chloride ion is greater than that of sulfate ions.

4 Conclusion

This paper investigates the impact of salt erosion on the mechanical properties and shrinkage performance of cement-stabilized macadam, and determines the internal chloride and sulfate ion concentrations of cement-stabilized mortar through ion titration experiments, analyzing the salt erosion damage mechanism. The following conclusions can be drawn from this study.

- During the infiltration process, the type of salt solution has different effects on the weight change of cement-stabilized mortar, sulfate solution causes a reduction in sample weight, while chloride solution and mixed solutions lead to an increase in sample weight.
- Salt solution will lead to a decrease in the strength of cement-stabilized mortar and cement-stabilized macadam, with the strength of cement-stabilized mortar potentially dropping to 22.7% of the control group, and the strength of cement-stabilized macadam potentially dropping to 71% of the control group. In saline areas, the transport and accumulation

of chloride and sulfate salts will have adverse effects on the strength of cement-stabilized subbase layer, leading to a significant decrease in strength.

- The migration of salt solution into the cement-stabilized macadam mixture changes the drying shrinkage properties, causing it to expand during the drying process. When the moisture loss is sufficiently high (exceeding 2.5%) or the salt solution concentration is high, the cement-stabilized macadam transitions from shrinkage to expansion. This can lead to the arching disease of the cement-stabilized subbase layer.

Data availability statement

The original contributions presented in the study are included in the article/supplementary material, further inquiries can be directed to the corresponding authors.

Author contributions

CW: Data curation, Investigation, Validation, Writing–original draft. YC: Data curation, Writing–review and editing. BA: Conceptualization, Methodology, Writing–review and editing. QG: Conceptualization, Formal Analysis, Funding acquisition, Writing–review and editing. YW: Data curation, Software, Visualization, Writing–review and editing.

Funding

Conflict of interest

Author BA was employed by Gansu Province Transportation Planning Survey & Design Institute Co., Ltd.

The remaining authors declare that the research was conducted in the absence of any commercial or financial relationships that could be construed as a potential conflict of interest.

Publisher's note

All claims expressed in this article are solely those of the authors and do not necessarily represent those of their affiliated organizations, or those of the publisher, the editors and the reviewers. Any product that may be evaluated in this article, or claim that may be made by its manufacturer, is not guaranteed or endorsed by the publisher.

References

Chen, D., Harris, P., Scullio, T., and Bilyeu, J. (2005). Forensic investigation of a sulfate-heaved project in Texas. *J. Perform. Constr. Facil.* 19 (4), 324–330. doi:10.1061/(asce)0887-3828(2005)19:4(324)

Dai, Z., Mao, X., Xu, W., Tang, K., Wu, Q., and Tang, W. (2021). Investigation and analysis of the causes of arch expansion of cement stabilized macadam base asphalt pavement in Gobi saline soil area. *China Sci. Pap.* 16 (4), 444–449.

Hong, W. (2019). Investigation of asphalt pavement blow-up on cement stabilized macadam base and preventive measures in Gobi desert. *Highway* 64 (03), 266–274.

Huang, X. (2017). Research on the bulging phenomenon of semi-rigid base course in road surfaces and strategies for elimination. *Highway* 62 (12), 59–61.

Irakoze, W., Prodjinoto, H., Nijimbere, S., Bizimana, J. B., Bigirimana, J., Rufyikiri, G., et al. (2021). NaCl- and Na$_2$SO$_4$-induced salinity differentially affect clay soil chemical properties and yield components of two rice cultivars (*Oryza sativa* L.) in Burundi. *Agronomy* 11, 571. doi:10.3390/agronomy11030571

Jidong, T., He, Z., Sheng, Z., and Daichao, S. (2016). Moisture transfer and phase change in unsaturated soils: physical mechanism and numerical model for two types of "canopy effect". *Chin. J. Geotechnical Eng.* 38 (10), 1813–1821. doi:10.11779/CJGE201610010

Ministry of Transport's Research Institute of Highway (RIH) (2017). Specifications for design of highway asphalt pavement. *JTG D50-2017*, 9.

Ministry of Transport's Research Institute of Highway (RIH) (2021). *Test methods of soils for Highway engineering*, 1. JTG 3430-2020.

Mitchell, J. K. (1986). The twentieth terzaghi lecture. *J. Geotechnical Engineering-Asce* 112 (3), 255–289. doi:10.1061/(asce)0733-9410(1986)112:3(255)

Rollings, R. S., Burkes, J. P., and Rollings, M. P. (1999). Sulfate attack on cement-stabilized sand. *J. Geotechnical Geo-environmental Eng.* 125 (5), 364–372. doi:10.1061/(asce)1090-0241(1999)125:5(364)

Song, L., Song, Z., Wang, C., Wang, X., and Yu, G. (2019). Arch expansion characteristics of highway cement-stabilized macadam base in Xinjiang, China. *Constr. Build. Mater.* 215, 264–274. doi:10.1016/j.conbuildmat.2019.04.193

Standardization Administration of China(SAC) (2021) *Test method of cement mortar strength*. ISO method.GB/T 17671-2021.

Tang, Ke (2022). *Study on arch expansion and damage mechanism of cement stabilized macadam base under the action of temperature and salt*. Xi'an, China: Chang'an University. PhD dissertation.

Tang, Ke, Mao, X. S., Wu, Q., Zhang, J. X., and Huang, W. J. (2020). Influence of temperature and sodium sulfate content on the compaction characteristics of cement-stabilized macadam base materials. *Materials* 13 (16), 3610. doi:10.3390/ma13163610

Tran, N. P., Gunasekara, C., Law, D. W., Houshyar, S., Setunge, S., and Cwirzen, A. (2021). A critical review on drying shrinkage mitigation strategies in cement-based materials. *J. Build. Eng.* 38, 102210. doi:10.1016/j.jobe.2021.102210

Wang, P., Ye, Y., Zhang, Q., Liu, J., and Yao, J. (2020). Investigation on the sulfate attack-induced heave of a ballast less track railway subgrade. *Transp. Geotech.* 23 (C), 100316–100318. doi:10.1016/j.trgeo.2020.100316

Wang, Y. (2023). *Effect of salt erosion on pavement performance of cement stabilized macadam and interaction mechanism*. Master Disseration. Handan, China: Hebei University of Engineering.

Xie, H. (2019). Mechanism analysis and preventive measures of arch expansion of asphalt pavement on cement stabilized macadam base in Gobi desert. *Highw. Eng.* 44 (05), 180–187.

Yao, A., Han, F., Xu, M., Wang, J., and Yu, S. (2020). Swelling analysis of cement stabilized macadam mixture. *Sci. Technol. Eng.* 2020 (12), 4902–4908.

Yao, A., Wang, J., Xu, M., Yang, M., and Yang, T. (2021). Numerical analysis of the uplift of cement stabilized macadam base asphalt pavement. *J. Chongqing Jiaot. Univ. Nat. Sci.* 40 (6), 105–111.

Zhang, H. (2018). *The cause and mechanical analysis on the transverse uplift of asphalt concrete pavement in desert are*. Huhehot, China: Inner Mongolia University. Master Thesis.

Zhang, M., Zhang, J., Ding, L., Wang, X., and Wang, Z. (2022). Sulfate-induced expansion of cement treated road base: deterioration law of performance and air-void structure change under water-heat-salt coupling effect. *Constr. Build. Mater.* 359, 129475. doi:10.1016/j.conbuildmat.2022.129475

Strength characteristics of cement stabilized construction waste slurry modified by polyacrylamide with different moisture contents

Feng Guo[1]* and Jiabin Hu[2]

[1]Luoyang Institute of Science and Technology, Luoyang, China, [2]School of Civil Engineering, Shaoxing University, Shaoxing, China

Waste slurry is a major component of construction waste, and its resource utilization can effectively reduce its environmental impact. The effect of polyacrylamide (PAM) content and moisture content on the strength characteristics of PAM modified cement stabilized construction waste slurry (PCMS) was studied using unconfined compressive strength (UCS) and triaxial tests. It can be concluded that, 1) The UCS of PCMS increases with the increase of curing age and significantly decreases with the increase of moisture content. As the content of PAM increases, it first increases and then decreases, with UCS reaching its maximum at a PAM content of 0.5%. 2) When the moisture content is 50%, PAM can increase the elastic modulus of PCMS. When the content of PAM is 0.5%, the elastic modulus reaches its maximum value. When the moisture content is 80% and 100%, the effect of PAM on the elastic modulus of PCMS is not significant. 3) The addition of PAM can improve the shear strength of PCMS. Under the same confining pressure, the shear strength of PCMS increases first and then decreases with the increase of PAM content, and the optimal content is 0.5%. 4) The variation pattern of PCMS cohesion is basically consistent with the shear strength. PAM improves the shear strength of PCMS by enhancing its cohesion. The addition of PAM has a relatively small impact on the internal friction angle of PCMS. These findings provide valuable insights for research into modification technology and the resource utilization of construction waste slurry.

KEYWORDS

construction waste slurry, polyacrylamide, moisture content, unconfined compressive strength, shear strength

1 Introduction

In recent years, with the advancement of urbanization, numerous construction projects have begun. However, the amount of engineering waste generated has also increased significantly. These engineering wastes not only cause serious waste of resources, but also pollute the environment, which is a difficult problem to be solved in future urban construction. Construction waste slurry is a serious engineering waste in construction, which is a suspended system composed

of water, bentonite particles, cohesive soil particles, and additives (Sun et al., 2023; Sun et al., 2024). Slurry as an auxiliary material in engineering, plays an indispensable role in the construction process of foundation engineering. However, after multiple cycles of use, a large amount of waste slurry will inevitably be generated. Waste slurry on construction sites often occupies construction land, affecting the environment and progress of the construction site. Unreasonable discharge treatment can also lead to serious environmental pollution (Chen et al., 2022; Wang D. et al., 2023).

Although slurry plays a significant role in engineering construction, the disposal of excess mud and waste slurry has always been a major challenge for people. At present, the methods for treating waste slurry include direct discharge method, incineration method, chemical solidification method, mechanical treatment method, and chemical flocculation precipitation method (Ye et al., 2023; Jiang et al., 2021a; Jiang et al., 2021b; Jiang et al., 2019; Jiang et al., 2022). The direct discharge method and incineration method cannot recycle and reuse slurry and cause pollution to the environment. The mechanical processing method has limited processing scope and can only handle the separated soil. The chemical flocculation precipitation method has poor treatment effect on high-density slurry, and the solid phase of the slurry is not easy to coagulate and precipitate. The chemical solidification treatment method directly adds a solidification agent to the slurry, improving its properties and facilitating the resource utilization of waste slurry (Grohs, 2002; Li et al., 2019; He et al., 2020). In the initial research on curing agents, only ordinary Portland cement was generally added as the curing agent. However, adding cement alone as a curing agent poses issues such as carbon dioxide emissions and adverse effects on the strength and durability of the solidified material (Ma et al., 2019; Craeye et al., 2011; Lin and Zhang, 2016).

At present, there has been a continuous emergence of research on the modification of slurry by adding curing agents, and many research results have been achieved. Wang et al. (Wang Q. et al., 2023) used water glass solution and carbide slag as activators to study the solidification effect of fly ash on waste slurry. The research results indicate that when the ratio of carbide slag to water glass is 6:4, the strength of the cured product after 28 days can reach 2.2 MPa. Wang et al. (Wang et al., 2024) used kaolin, slag, and carbide slag to solidify waste slurry in engineering projects. This composite curing agent can achieve a 7-day strength of 3 MPa for cured specimens. Katsioti et al. (Katsioti et al., 2008) found that when cement: bentonite = 0.6:0.4, the best solidification effect of waste slurry was achieved, with a compressive strength of 350 kPa at 28 days. Xu H. et al., 2023) mixed slag and carbide slag to solidify the slurry soil and found that the compressive strength of the modified slurry soil after 7 days could reach 3.73 MPa when the mixed amount of binder was as high as 25%. However, they found that as the wet dry cycle progressed, the strength loss of modified slurry soil with a longer curing period was actually faster. Cao et al. (Cao et al., 2006) conducted indoor experiments by adding different proportions of lime, soil, and fly ash to slurry, and studied the engineering properties of solidified slurry under different mix ratios. The study found that under appropriate mix ratios, the strength of solidified slurry met the requirements of landfill, and the permeability was also greatly improved. Yang et al. (Yang et al., 2017) used lime as the main agent and cement and gypsum as auxiliary agents to improve Tianjin coastal soft soil. The experimental results showed that using

unconfined compressive strength as the standard for determining the solidification effect, the optimal cement content only changed with different lime content. For example, in 12% lime solidified soil, a cement content of no more than 3% can best improve the strength of lime solidified soil. Gypsum cannot improve the strength of soil and can lead to poor water stability and cracking when exposed to water. Although inorganic curing agents have been effective in solidifying waste slurry, due to the high moisture content of waste slurry, direct addition of inorganic curing agents not only increases the proportion of cured materials, but also the strength of cured products is usually not high (Shao et al., 2018; Zhang et al., 2022).

Flocculation and dehydration of waste slurry is usually an economically reasonable approach. It is crucial to choose efficient flocculants in order to reduce the moisture content of waste slurry. Therefore, many researchers have made tremendous efforts to find suitable flocculants. Xiao et al. (Xiao et al., 2021) prepared three flocculants with different functional groups to coagulate wastewater containing heavy metal ions. The research results indicate that the magnetic carboxymethyl chitosan flocculant (MCAA) grafted with 2-acrylamide-2-methylpropane sulfonic acid copolymer has a good flocculation effect. Patra et al. (Patra et al., 2020) used branched starch as a flocculant to treat coal suspension and found that this flocculant has a good effect and helps with rapid settling. Flocculants can not only promote the settling of suspended particles and achieve solid-liquid separation, but also have the effect of solidification enhancement. Tong et al. (Tong et al., 2021) added ion curing agents to iron tailings and natural soil, and found that the compressive strength of the mixed material first increased and then stabilized with the increase of ion curing agent dosage.

Polyacrylamide (PAM) is a water-soluble polymer, white powder, insoluble in most organic solvents, and is a relatively new type of curing agent. It is often used in combination with other traditional inorganic curing agents in soft soil solidification technology or soft soil foundation treatment methods. At present, there are also studies on its incorporation into cement. PAM is mainly used as an additive to play a flocculation role and also has a good reinforcement effect. Qin et al. (Qin et al., 2023) utilized industrial solid waste such as construction waste powder and slag powder, and introduced PAM as a flocculant to solidify waste slurry with different moisture contents. The superiority of this curing agent combination in solidifying waste slurry was verified through a combination of macroscopic and microscopic experiments. Zhang et al. (Fengjun et al., 2020) prepared a new type of flocculant by combining three flocculants to solidify waste slurry. The results showed that the best flocculation effect was achieved when the ratio of polyacrylamide, joint branch powder, and flocculation settling promoter was 1:0.75:0.5. Xu et al. (Xu S. et al., 2023) studied the flocculation and dehydration of kaolin slurry treated with single and double polymer flocculants. The research results indicate that non-ionic PAM has the best flocculation effect. This is attributed to the strongest adsorption and bridging ability of PAM. Deng et al. (Deng et al., 2022) found through a series of indoor experiments that adding PAM to cement soil can improve the plastic deformation ability of solidified soil. An appropriate content of PAM can significantly increase the ultimate strain of solidified soil at shear failure. The permeability of cement soil decreases with the increase of cement content and curing age, but adding a certain amount of PAM to cement soil can effectively improve its permeability.

Chang et al. (Chang and Chang, 2010) pointed out that adding a certain amount of cement to hydraulic fill sand can significantly improve its liquefaction resistance, but the cement hydraulic fill sand is easily dispersed when soaked in water. Adding PAM can enhance the aggregation force between cement hydraulic fill sand particles. Under the condition of constant cement addition, the unconfined compressive strength of solidified soil initially increases with the increase of PAM content. After reaching its peak, the unconfined compressive strength gradually decreases with the increase of PAM content, and PAM has the most optimal addition amount. Kim et al. (Kim, 2016) jointly used aluminum chloride and PAM to treat wastewater. Research has shown that this composite flocculant has better performance and faster settling speed. According to these researches, the use of polyacrylamide can improve the mechanical properties of high water content (≥50%) slurry, and the appropriate dosage of polyacrylamide is less than 1%.

In summary, PAM can improve the deformation ability of cementitious soil, enhance the polymerization force between cement and slurry, and thus enhance the strength of cementitious soil. Therefore, PAM was added to improve the strength of cement modified slurry. But the strength characteristics of polyacrylamide modified waste slurry (PCMS) under axial and triaxial loads under different moisture contents and curing ages need further investigation. So the strength characteristics of PAM modified cement stabilized construction waste slurry (PCMS) were studied through unconfined compressive strength (UCS) tests and triaxial tests, providing reference for the resource utilization of slurry.

2 Materials and methods

2.1 Materials

2.1.1 Slurry

The slurry used in the experiment comes from a construction site in Shaoxing City, China, and the slurry is dark brown in color, as shown in Figure 1. After drying, as shown in Figure 2, it appears light brown. The main physical and mechanical indicators include specific gravity, liquid plastic limit, plasticity index, water moisture, and organic matter content, as shown in Table 1. The drying temperature is 105°C and the drying time is 24 h. After drying, the slurry was subjected to XRF testing, and the compound composition was obtained as shown in Table 1.

It can be seen that the mud is mainly composed of sheet-like particles, with the main elemental components being Si, Al, Ca, and O. The main compounds are SiO_2, Al_2O_3, CaO, Fe_2O_3, and K_2O.

2.1.2 Cement

The cement used in the experiment is M32.5, sourced from Shaoxing Zhaoshan Building Materials Co., Ltd. China, as shown in Figure 3. M32.5 cement has the characteristics of high later strength, moderate setting time, low hydration, good workability, low water bleeding, and high water retention rate.

2.1.3 Polyacrylamide

Polyacrylamide (PAM) is a water-soluble polymer material with the chemical formula $(C_3H_5NO)_n$. The PAM used in this study is produced by Xinlida Water Treatment Company

FIGURE 1
Slurry.

FIGURE 2
Dehydrated slurry.

in Zhengzhou City, China, and appears as white particles, as shown in Figure 4. Molecular weight of PAM is 1800×10^4, pH value is five to eight, solid content is 8.5% and insoluble substances is 26.5%.

2.2 Sample production and curing

According to Chinese code GBT 50123–2019 (GB/T 50123, 2019), both the unconfined compression strength (UCS) and triaxial samples in this test are cylindrical, with a diameter of D = 39.1 mm and a height of H = 80 mm. The specific steps for sample production are as follows:

(1) Prepare the raw materials for the sample. Before the experiment, put the air dried slurry into an oven for

TABLE 1 Basic index of mechanical properties and XRF test results of slurry.

Specific gravity		Liquid limit/%	Plastic limit/%		Plasticity index/%	Water solubility content/%		Organic matter content/%
2.65		46.4	25.4		21.0	0.23		1.03
Type of compound	SiO2	Al2O3	CaO	Fe2O3	K2O	MgO	Na2O	Other
Content/%	61	16.5	7.7	5.9	3.2	2.4	1.1	2.2

FIGURE 3
Cement.

FIGURE 4
PAM.

further drying, and sieve the impurities in the slurry soil through a 2 mm aperture standard sieve to obtain fine powder soil.

(2) Assemble the test mold. First, tighten the clamp sleeve of the mold with a screwdriver, then evenly apply Vaseline inside the mold barrel, seal one end of the mold with a plastic film and tighten it with a rubber band. Finally, use the rubber band to fix the two end bearing plates with the mold and assemble it into a vibrator. The assembled mold is shown in Figure 5A.

(3) Prepare the mixture. According to the predetermined experimental plan, weigh the corresponding masses of slurry soil, water, cement, PAM, and put each material into a mixing pot. First, manually mix until it is initially uniform, and then place it on a mixer for secondary mixing. The mechanical mixing time is about 5 min. As shown in Figure 5B, obtain the experimental mixture.

(4) Injecting and compacting. Pour the mixed material evenly into the compactor in three parts, and vibrate for about 40 s each time to make it compact. After the compaction is completed, let it stand for about 4–6 h.

(5) Sample trimming and curing. After the sample is left to stand, remove the two end bearing samples, scrape the two ends flat, as shown in Figure 5C, and fix the filter paper with rubber rings at both ends of the mold cylinder, as shown in Figure 5D. Then immerse the sample in water for curing to simulate an environment of air isolation and saturated curing, as shown in Figure 5E. Finally, place it in a standard curing room with a temperature of 20°C ± 2°C and a humidity of 95%.

(6) Sample demolding. After curing the sample to the testing age, remove the mold cylinder and shape the sample, as shown in Figure 5F.

2.3 Test plan

Compressive strength and shear strength are the two most basic strength indicators of geotechnical materials, so this study adopts unconfined compressive strength test and triaxial test to study the strength performance of PCMS. The influence of different PAM content and moisture content on the strength characteristics of modified mud was studied using unconfined compressive strength tests and triaxial tests. The specific test plan is shown in Table 2. Moisture content refers to the ratio of the mass of water to the mass of dry slurry.

To ensure the authenticity and reliability of the measured test data, the UCS test is repeated in groups of five specimens.
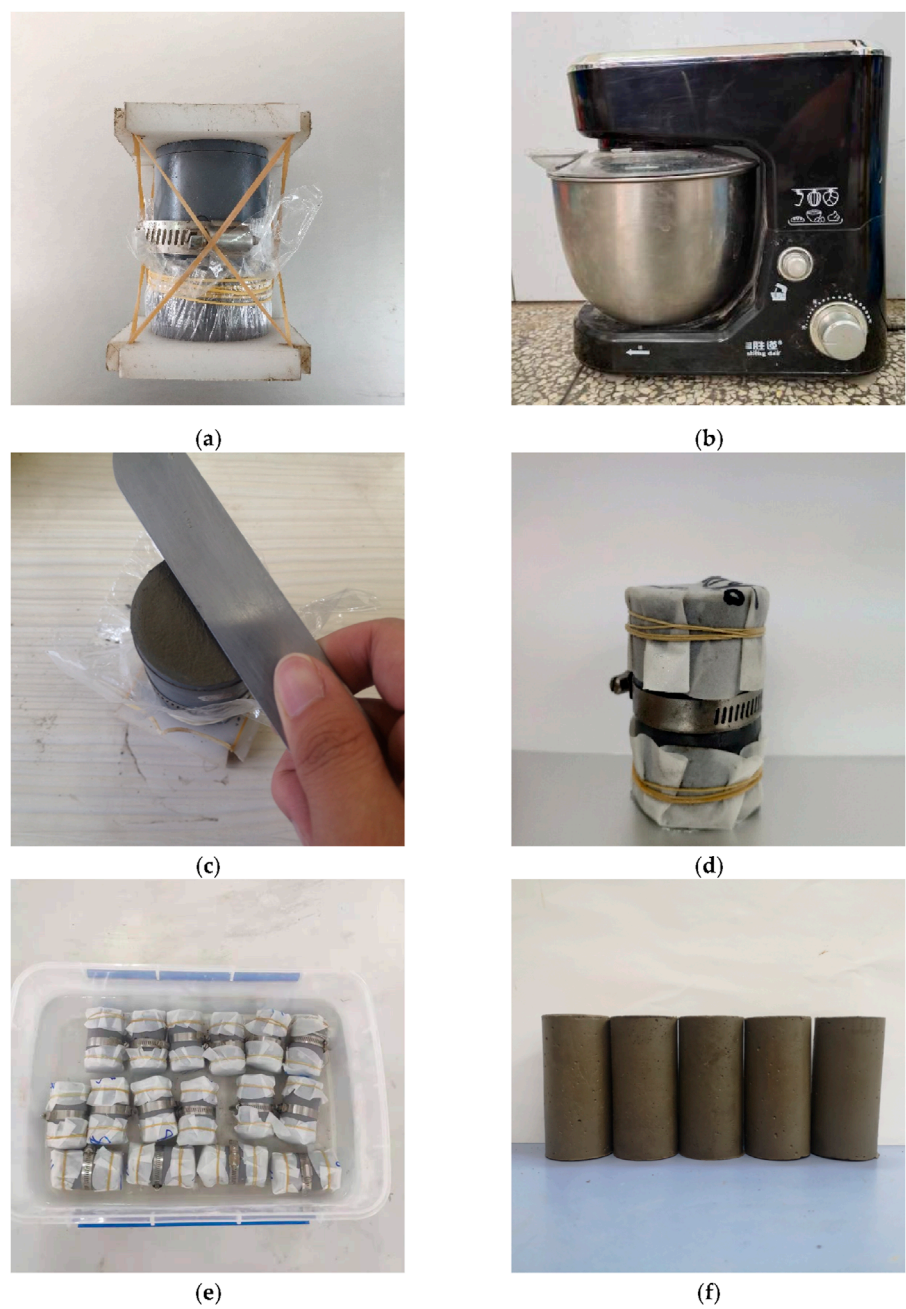
FIGURE 5
Sample preparation procedures: **(A)** Assembled mold; **(B)** Mixer; **(C)** Sample trimming; **(D)** Sample binding; **(E)** Sample curing; **(F)** Samples.

TABLE 2 Test plan.

PAM/%	Cement content/%	Moisture content/%	Curing age/d	Test method
0, 0.2, 0.5, 0.8	20	50, 80, 100	7, 28	UCS test, triaxial test

Using triaxial tests to obtain the mechanical properties of PCMS under different stress conditions. The study primarily considers the influence of confining pressures of 50 kPa, 100 kPa, 150 kPa, and 200 kPa. In both the UCS and triaxial tests, the shear rate of the sample is set to 1 mm/min, and the test is halted when the axial strain reaches 15%.

3 Results and analysis

3.1 Unconfined compressive performance

3.1.1 Unconfined compressive stress-strain curve

Conduct UCS tests on PCMS and obtain 24 sets of unconfined stress-strain curves. As shown in Figure 6.

From Figure 6, it can be seen that: The stress-strain curves of PCMS all have similar curve patterns and are all softening type curves. With the increase of PAM content, the peak stress of PCMS first increases and then decreases, and the peak strain continues to increase. When the moisture content is 50% and 80%, regardless of whether it is at the curing age of 7 days or 28 days, the slope of the stress-strain curve in the elastic stage is the highest when the content of PAM is 0.5%, which means that the rate of stress increasing with strain is the highest. When PAM content is 0.5%, the stress growth rate of PCMS is the fastest. When the moisture content is 100%, at the curing age of 7 days, the slope of the stress-strain curve in the elastic stage is the highest when the content of PAM is 0.5%. At the curing age of 28 days, the slope of the stress-strain curve in the elastic stage is the highest when the content of PAM is 0.2%. This indicates that as curing age increases and PAM content rises, the effect on the stress growth rate becomes less significant. This is because, with longer curing, the hydration products in the PCMS continue to increase, making PAM's modifying effect on PCMS less pronounced.

3.1.2 Unconfined compressive strength analysis

In order to facilitate the analysis of the modification effect of PAM on the compressive performance of PCMS, the UCS of each proportion of PCMS varies with the content of PAM, as shown in Figure 7.

From Figure 7, it can be seen that: (1) When the moisture content is 50%, whether at the curing age of 7 days or 28 days, only when the content of PAM is 0.5%, the UCS of PCMS can be improved. The remaining PAM content has a negative effect on the UCS of PCMS. When the moisture content is 80%, the UCS of PCMS at 7d and 28d curing ages increases first and then decreases with the increase of PAM content. When the content is 0.5%, the optimal values are 531 kPa and 1,036 kPa, respectively, with an increase of 31% and 53%. The moisture content is 100%, and its variation pattern is consistent with that at 80% moisture content. When the PAM content is 0.5%, the optimal strength values are reached at 7 days and 28 days curing age, which are 349 kPa and 495 kPa, respectively, with an increase of 35% and 28%. When the moisture content is 50%, the moisture content is low, the PAM introduces closed bubbles into PCMS, thereby reducing the strength of PCMS. When the moisture content is greater than 50%, PAM makes the hydration products of the cement matrix more dense, thereby increasing the strength of PCMS. Therefore, when the moisture content of PCMS is high, the strengthening effect of PAM on PCMS is greater than the weakening effect. (2) When the moisture content and PAM content of PCMS are constant, the UCS of PCMS increases with curing age. When the moisture content is 50%, the UCS of PCMS with a curing age of 28 days increased by 81%, 85%, 96%, and 119% at PAM's content of 0%–0.8% compared to the UCS at 7 days curing age, respectively. When the moisture content is 80%, the UCS of PCMS with a curing age of 28 days increased by 66%, 87%, 95%, and 107% at PAM's content of 0%–0.8%

compared to the UCS at 7 days curing age, respectively. When the moisture content is 100%, the UCS of PCMS with a curing age of 28 days increased by 51%, 48%, 42%, and 46% at PAM's content of 0%–0.8% compared to the UCS at 7 days curing age, respectively. From this, it can be seen that when the moisture content is 50%, PCMS is most affected by the curing age, and the effect of curing age is most significant when the content of PAM is 0.8%. (3) When the curing age of PCMS and the content of PAM are constant, the UCS of PCMS decreases significantly with the increase of moisture content.

3.1.3 Elastic modulus

Select the linear elastic stage on the stress-strain curve of UCS test, and fit the data of the linear elastic stage with a straight line. The slope of the straight line is the elastic modulus. The elastic modulus of each mix proportion of PCMS is shown in Figure 8.

From Figure 8, it can be seen that: (1)When the moisture content is 50%, PAM cannot increase the elastic modulus of PCMS at the curing age of 7 days. At 28 days curing age, the elastic modulus of PCMS increases with the increase of PAM content, reaching the optimal value of 304 MPa at a content of 0.5%, with an increase of 18.2%. When the moisture content is 50%, PAM can effectively improve the elastic modulus of PCMS at 28 days of curing age. (2)When the moisture content is 80%, at the curing age of 7 days, only when the content of PAM is 0.2%, the elastic modulus of PCMS can be improved, but the increase is not significant. At 28 days curing age, the addition of 0.5% PAM can significantly improve the elastic modulus of PCMS. When the moisture content is 80%, PAM can still improve the elastic modulus of PCMS. (3) At a moisture content of 100% and a 7-day curing age, PAM cannot increase the elastic modulus of PCMS. At 28 days of curing age, the addition of 0.2% PAM can increase the elastic modulus of PCMS.

When the moisture content is 50% and 100%, at the curing age of 7 days, PAM cannot increase the elastic modulus of CMS. This is because PAM introduces closed bubbles into PCMS, thereby reducing the elastic modulus of PCMS. At the age of 28 days, when the PAM content is 0.2%, the elastic modulus of CMS can be increased because the particles in the PCMS also have a strong adsorption effect on PAM molecules. When these PAM molecules adsorb on the surface of the particles, they will greatly improve the surface characteristics of these microparticles. Forming a water film on the surface of the cement particles ensures sufficient hydration of the cement. This allows for more complete contact between water and cement, leading to a more compact structure. Consequently, this increases the stiffness and improves the elastic modulus of the cement.

3.2 Triaxial shear performance

3.2.1 Triaxial shear stress-strain curve

Part of the triaxial test stress-strain curves of the PCMS sample are shown in Figure 9. They are first classified into three categories based on different moisture contents, and then classified according to different PAM content.

From Figure 9, it can be seen that: (1)When the confining pressure is between 50 kPa and 200 kPa, the shear strength and peak strain of PCMS increase with the increase of confining pressure under different moisture content conditions. The stress-strain curves
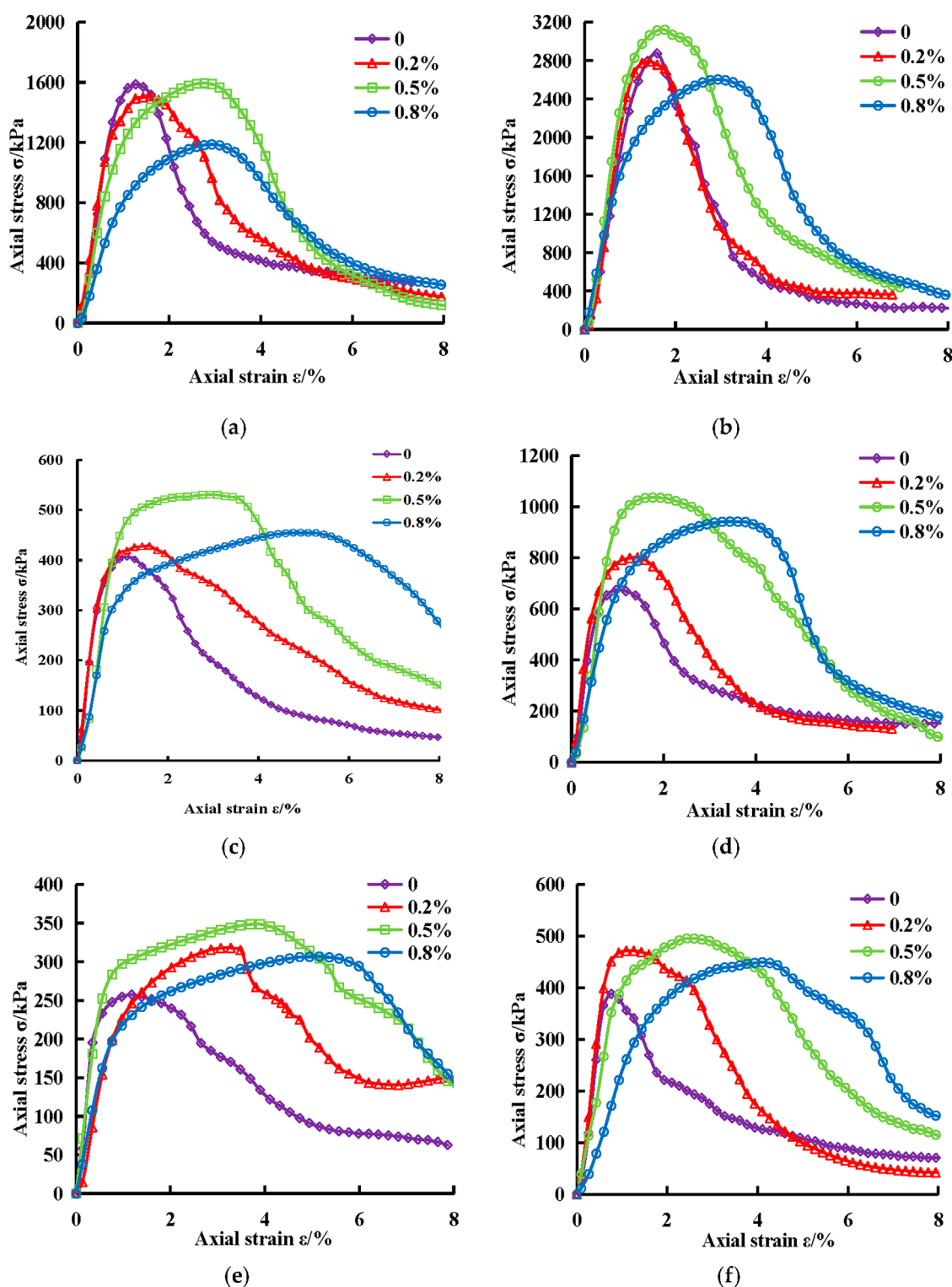
FIGURE 6
Unconfined compressive stress–strain curves of PCMS: **(A)** 50% moisture content and 7d curing age; **(B)** 50% moisture content and 28d curing age. **(C)** 80% moisture content and 7d curing age; **(D)** 80% moisture content and 28d curing age. **(E)** 100% moisture content and 7d curing age; **(F)** 100% moisture content and 28d curing age.

of PCMS are all softening type, and the smaller the confining pressure, the more obvious the softening trend of PCMS. (2)Under high moisture content (80% and 100%) and high confining pressure

(200 kPa), the stress-strain curve of PCMS exhibits a weak softening curve. With the addition of PAM, the softening trend of the stress-strain curve of PCMS first increases and then decreases. (3)With
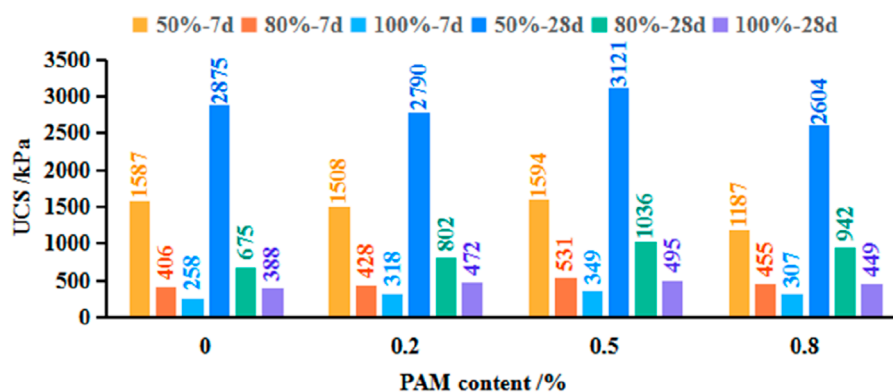
FIGURE 7
UCS of PCMS at 7d and 28d curing age.
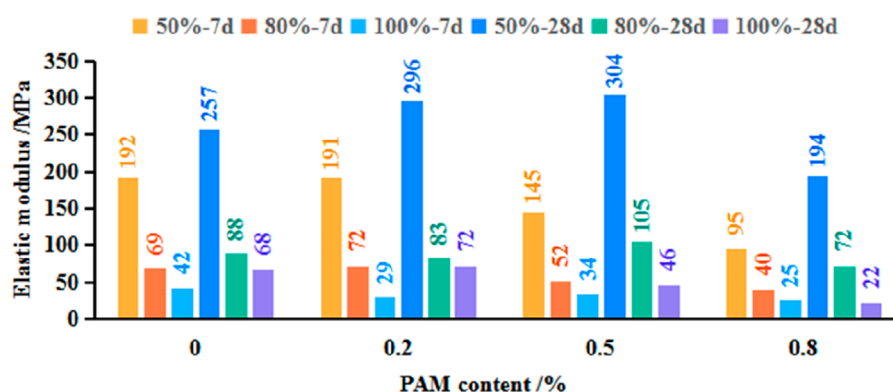
FIGURE 8
Elastic modulus of PCMS at 7d and 28d curing age.

the increase of curing age, the softening trend of the stress-strain curve of PCMS at 50% moisture content increases, all of which become strong softening curves. When the moisture content is high, the form of the stress-strain curve of PCMS does not change significantly, and it still remains a weak softening curve under high confining pressure.

3.2.2 Triaxial shear strength analysis

The shear strength of the PCMS corresponds to the maximum deviatoric stress in the deviatoric stress-strain curve. The relationship curve between the content of PAM and the shear strength of PCMS is shown in Figure 10.

According to Figure 10, the addition of PAM can improve the shear strength of PCMS. Under the same confining pressure, the shear strength of PCMS increases first and then decreases with the increase of PAM content.

When the moisture content is 50% and the curing age is 7 days, the effect of PAM on the shear strength of PCMS is relatively small. Under confining pressures of 50 kPa, 100 kPa, 150 kPa, and 200 kPa, the corresponding shear strength of PCMS is 606 kPa, 657 kPa, 711 kPa, and 758 kPa, respectively. The shear strength of PCMS with 0.2% and 0.5% PAM content increased by 4%–8% and

5%–9% compared with PCMS without PAM (CMS), respectively. When the confining pressure is between 50 kPa and 200 kPa, with a negative increase at 0.8% content of PAM. When the curing age is 28 days, the modification effect of PAM on shear strength increases, and the best modification effect is achieved at a 0.2% content. Under confining pressures of 50 kPa, 100 kPa, 150 kPa, and 200 kPa, the corresponding shear strength of PCMS is 950 kPa, 1,063 kPa, 1,158 kPa, and 1,234 kPa, respectively. The shear strength of PCMS with 0.2%, 0.5%, and 0.8% PAM content increased by 38%–61%, 38%–49%, and 23%–37% compared with CMS, respectively.

When the moisture content is 80% and the curing age is 7 days, the corresponding shear strength of PCMS under confining pressures of 50 kPa, 100 kPa, 150 kPa, and 200 kPa is 184 kPa, 209 kPa, 242 kPa and 268 kPa, respectively. The shear strength of PCMS with 0.2%, 0.5%, and 0.8% PAM content increased by 16%–22%, 35%–42%, and 24%–33% compared with CMS, respectively. The maximum increase was observed at 0.5% content of PAM. When the curing age is 28 days, the corresponding shear strength of PCMS under confining pressures of 50 kPa, 100 kPa, 150 kPa and 200 kPa is 251 kPa, 290 kPa, 365 kPa, and 403 kPa, respectively. The shear strength of PCMS with 0.2%, 0.5%, and 0.8% PAM content increased by 55%–70%, 60%–98%, and 55%–92%
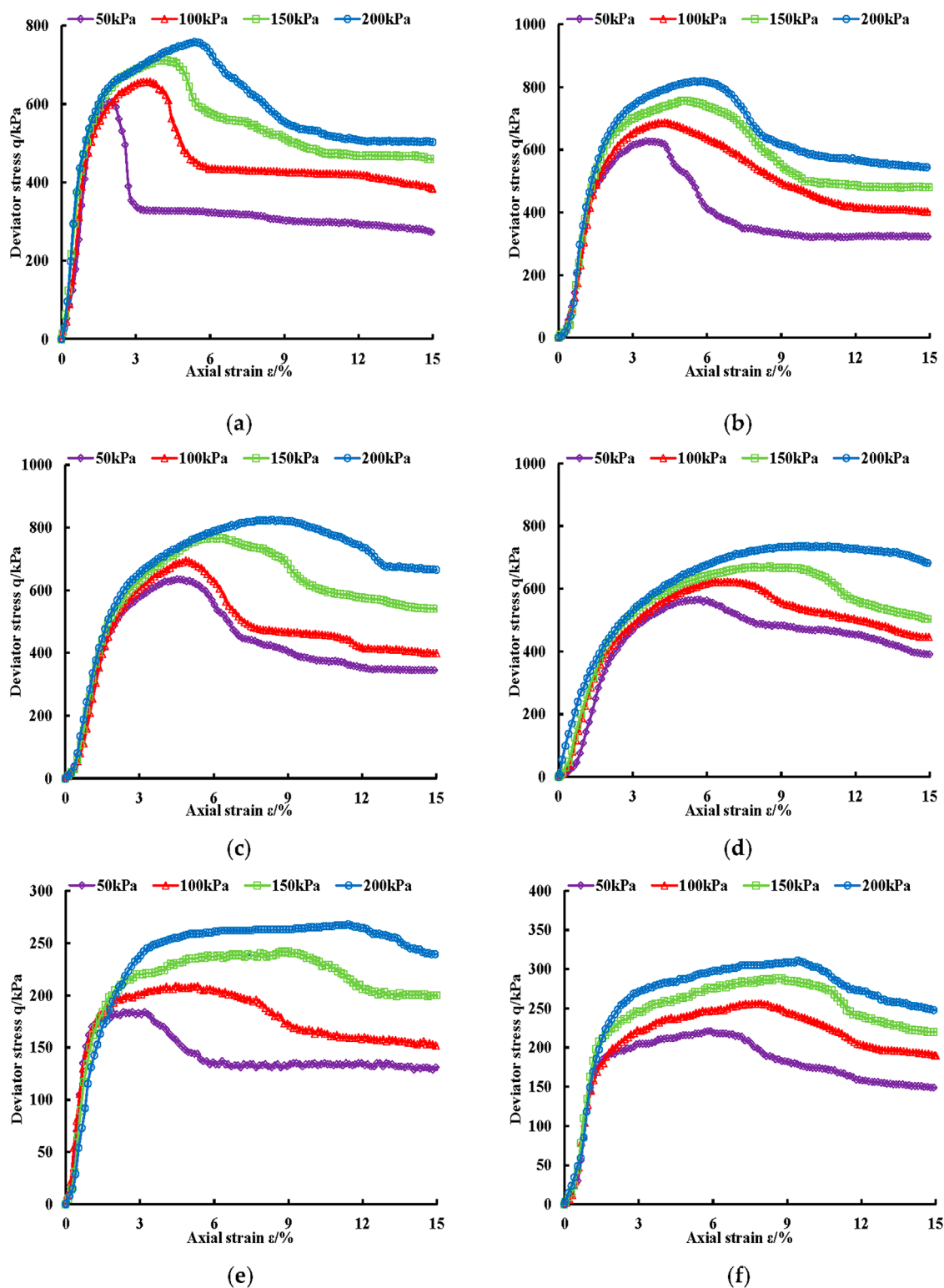
FIGURE 9
Deviatoric stress-strain curve of PCMS: **(A)** 50% moisture content and 7d curing age with 0% PAM content; **(B)** 50% moisture content and 7d curing age with 0.2% PAM content. **(C)** 50% moisture content and 7d curing age with 0.5% PAM content. **(D)** 50% moisture content and 7d curing age with 0.8% PAM content. **(E)** 80% moisture content and 7d curing age with 0% PAM content; **(F)** 80% moisture content and 7d curing age with 0.2% PAM content.
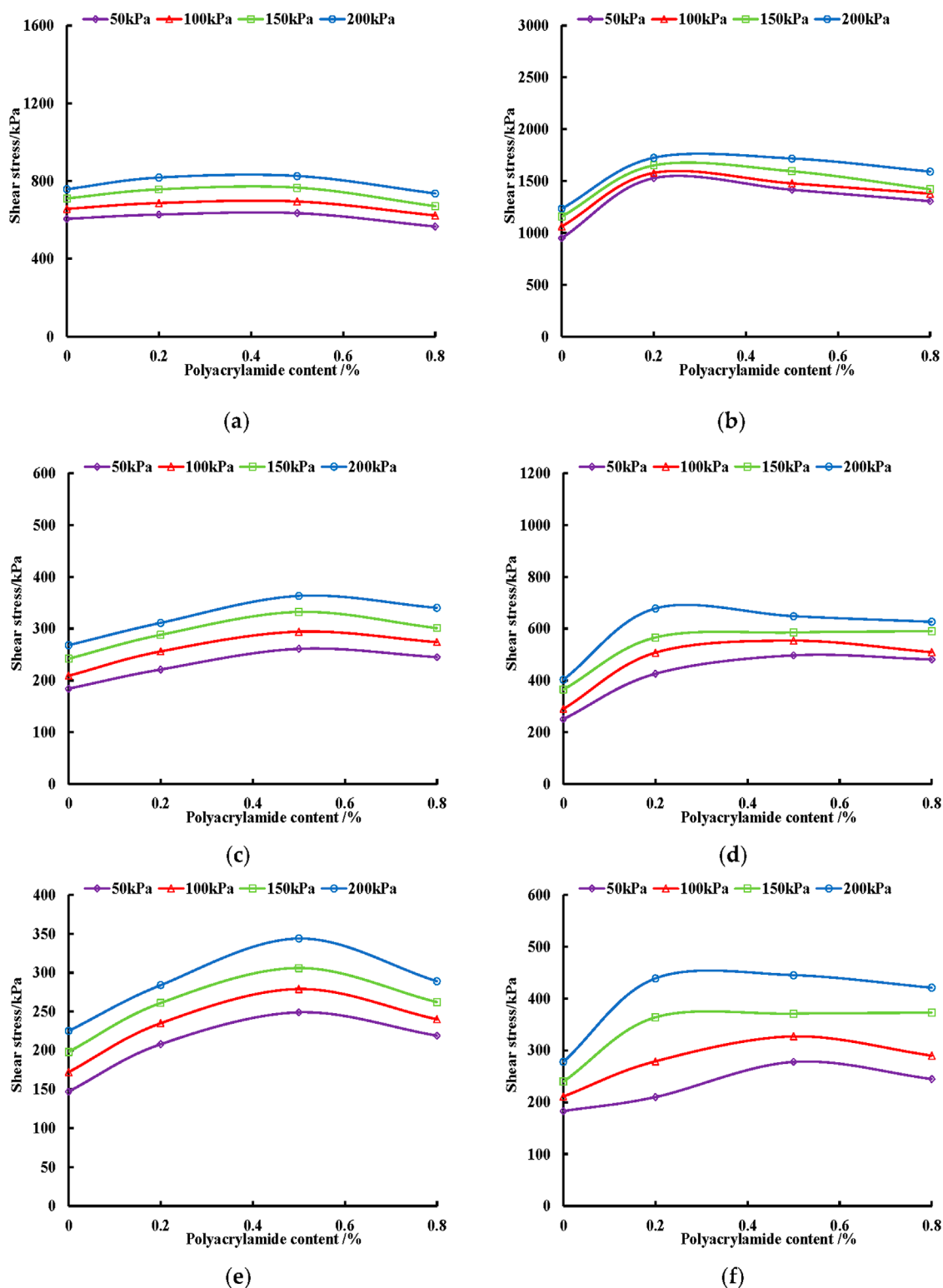
FIGURE 10
Relationship between the content of PAM and PCMS Shear strength: **(A)** 50% moisture content and 7d curing age; **(B)** 50% moisture content and 28d curing age. **(C)** 80% moisture content and 7d curing age; **(D)** 80% moisture content and 28d curing age. **(E)** 100% moisture content and 7d curing age; **(F)** 100% moisture content and 28d curing age.
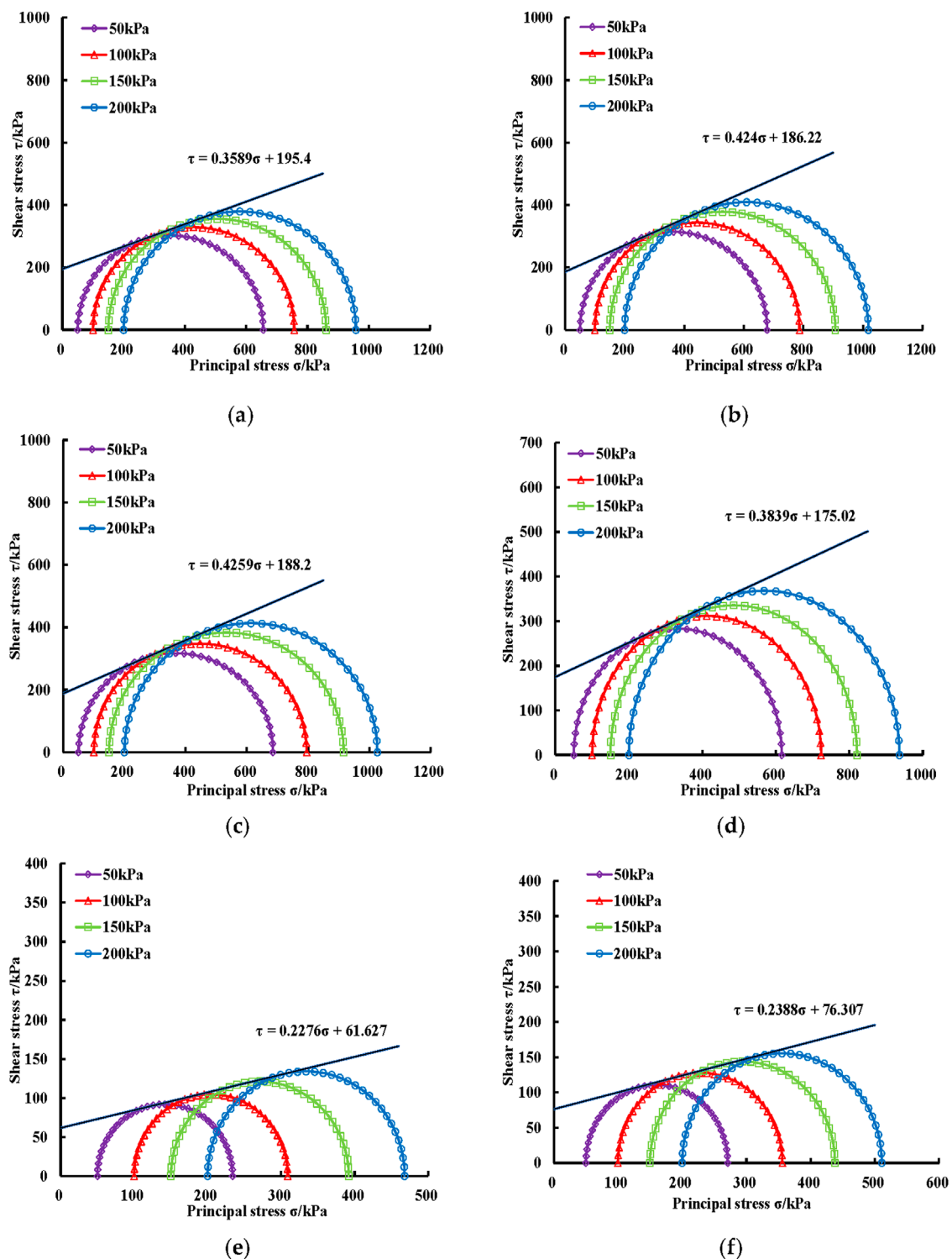
FIGURE 11
Shear strength envelope of PCMS: **(A)** 50% moisture content and 7d curing age with 0% PAM content; **(B)** 50% moisture content and 7d curing age with 0.2% PAM content. **(C)** 50% moisture content and 7d curing age with 0.5% PAM content. **(D)** 50% moisture content and 7d curing age with 0.8% PAM content. **(E)** 80% moisture content and 7d curing age with 0% PAM content; **(F)** 80% moisture content and 7d curing age with 0.2% PAM content.

compared with CMS, respectively. The best improvement effect was achieved with 0.5% PAM content.

When the moisture content is 100% and the curing age is 7 days, the corresponding shear strength of PCMS under confining

pressures of 50 kPa, 100 kPa, 150 kPa, and 200 kPa is 147 kPa, 172 kPa, 198 kPa, and 225 kPa, respectively. The shear strength of PCMS with 0.2%, 0.5%, and 0.8% PAM content increased by 26%–41%, 53%–69% and 28%–49% compared with CMS,
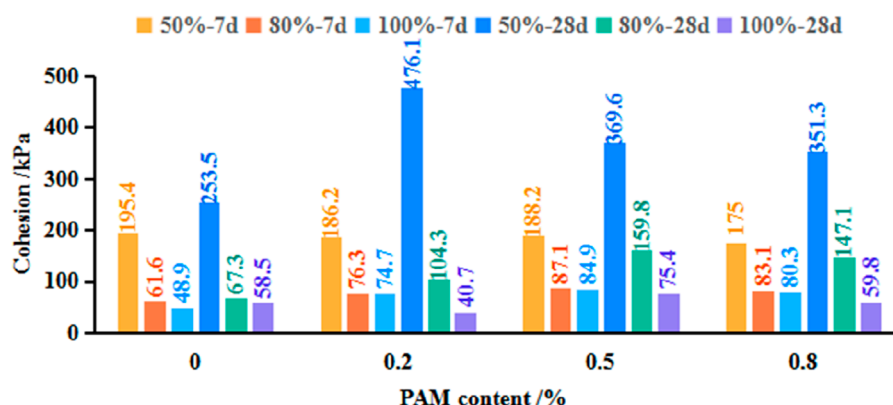
FIGURE 12
Cohesion of PCMS.
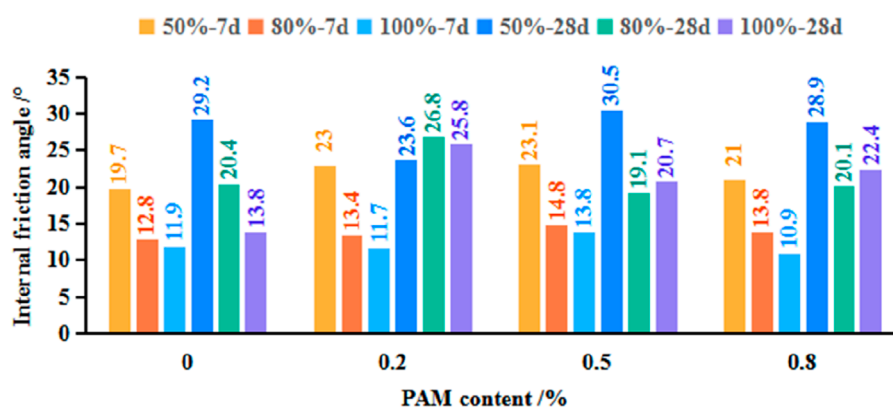
FIGURE 13
Internal friction angle of PCMS.

respectively. The maximum increase was observed at 0.5% content. When the curing age is 28 days, the corresponding shear strength of PCMS under confining pressures of 50 kPa, 100 kPa, 150 kPa, and 200 kPa is 183 kPa, 211 kPa, 240 kPa, and 278 kPa, respectively. The shear strength of PCMS with 0.2%, 0.5%, and 0.8% PAM content increased by 15%–58%, 52%–60% and 34%–55% compared with CMS, respectively. The best improvement effect was achieved with 0.5% PAM content.

The porosity of PCMS increase with the increase of moisture content. According to references [(He and Lu, 2023; He et al., 2023; Chen et al., 2021a; Chen et al., 2021b)], the strength change of PCMS is mainly due to the increase of its porosity.

In summary, the addition of PAM can improve the shear performance of PCMS, and the improvement rate of PAM on the shear strength of PCMS increases with the increase of curing age. The optimal PAM content of PCMS for shear strength at 50% moisture content is 0.2%, and the optimal PAM content of PCMS for shear strength at 80% and 100% is 0.5%. It can be seen that moisture content has a certain influence on the optimal content of PAM.

3.2.3 Analysis of shear strength indicators

In order to further investigate the modification effect of PAM on the shear strength of CMS, the strength envelope diagram of PCMS was drawn based on the Mohr Coulomb theory. According to Figure 9, the peak value of deviatoric stress is taken as the failure point. When there is no peak value, the difference in principal stress at 15% axial strain is taken as the failure point. Using normal stress σ as the x-axis and shear stress τ as the y-axis, draw a failure stress diagram on the τ - σ stress plane with $(\sigma_1+\sigma_2)/2$ as the center and $(\sigma_1-\sigma_2)/2$ as the radius, and plot the envelope of the Mohr stress circle under different confining pressures. Some strength envelope diagrams were as shown in Figure 11.

Based on the above shear strength envelope diagram, the shear strength indicators of PCMS with different moisture content and PAM content, such as cohesion c and internal friction angle φ, are obtained. The variation of the shear strength index of PCMS with the content of PAM was obtained under different moisture contents and different curing age, as shown in Figures 12, 13, respectively.

From Figures 12, 13, it can be seen that: When the moisture content is 50%, the addition of PAM cannot increase the c of PCMS at 7 days of curing age, but it has a certain improvement in the φ

of PCMS. The maximum improvement is achieved at a 0.5% PAM content, which is 17% higher than CMS. At 28 days of curing age, the c of PCMS increases first and then decreases with the increase of PAM content. The optimal content is 0.2%, which is 88% higher than CMS. This is consistent with the shear strength of PCMS at a 50% moisture content. But the φ only increased by 4% when the PAM content was 0.5%.

When the moisture content is 80%, PAM can improve the c of CMS at both 7d and 28d curing ages, and it first increases and then decreases with the increase of PAM content. The maximum value is reached at 0.5% PAM content, which is 41% and 137% higher than the c of CMS at 7d and 28d curing age, respectively. It can be seen that the improvement of c at 28d curing age is significant and still consistent with the change law of PCMS shear strength. At the curing age of 7 days, the variation pattern of φ and c is consistent, reaching its maximum at 0.5% PAM content and increasing by 16%. At 28 days of curing age, the φ only increased by 31% with a 0.2% PAM content.

When the moisture content is 100%, at the 7d curing age, the c of PCMS increases first and then decreases with the increase of PAM content, reaching its maximum value at 0.5% PAM content, which is 74% higher than CMS. At this point, the φ is also at its maximum, increasing by 16%, while the φ decreases under other doping levels. At 28d curing age, the c of PCMS was improved at a PAM content of 0.5% and 0.8%, with the maximum increase at a 0.5% content, which was 29%. The φ was improved with the addition of PAM, and the maximum increase was observed at a 0.2% PAM content, with an increase of 87%.

4 Conclusion

By conducting unconfined compressive strength tests and triaxial shear tests on PCMS, the effects of factors such as moisture content, curing age, and PAM content on the unconfined compressive and shear properties of PCMS were studied. The following conclusions can be drawn:

(1) Under axial stress, the stress-strain curves of PCMS are all softening curves. The UCS of PCMS increases with the increase of curing age and significantly decreases with the increase of moisture content. As the content of PAM increases, it first increases and then decreases, with UCS reaching its maximum at a PAM content of 0.5%.

(2) When the moisture content is 50%, PAM can increase the elastic modulus of PCMS. When the content of PAM is 0.5%, the maximum elastic modulus is achieved at 304 MPa. When the moisture content is 80% and 100%, the effect of PAM on the elastic modulus of PCMS is not significant, and the range of elastic modulus variation is 22–105 MPa.

(3) The stress-strain curves of PCMS under triaxial stress are all softening type curves. The addition of PAM can improve the shear strength of PCMS. Under the same confining pressure, the shear strength of PCMS increases first and then decreases with the increase of PAM content.

(4) The variation pattern of PCMS cohesion is basically consistent with the shear strength. The maximum cohesion is achieved at 50% moisture content and 0.5% PAM content, with a maximum cohesion of 476.1 kPa. The variation range of internal friction angle with moisture content and PAM content is 10.9°–30.5°. The improvement of shear performance of PCMS by PAM is mainly achieved by enhancing the cohesion of PCMS, and the addition of PAM has a relatively small impact on the friction between particles inside PCMS.

Data availability statement

The raw data supporting the conclusions of this article will be made available by the authors, without undue reservation.

Author contributions

FG: Writing–original draft, Writing–review and editing, Conceptualization. JH: Investigation, Writing–review and editing.

Funding

Conflict of interest

The authors declare that the research was conducted in the absence of any commercial or financial relationships that could be construed as a potential conflict of interest.

Publisher's note

All claims expressed in this article are solely those of the authors and do not necessarily represent those of their affiliated organizations, or those of the publisher, the editors and the reviewers. Any product that may be evaluated in this article, or claim that may be made by its manufacturer, is not guaranteed or endorsed by the publisher.

References

Cao, Y., Yan, S., and Zhao, L. (2006). Engineering properties and microstructure feature of solidified sludge. *Roc. Soil Mech.* 27 (5), 740–744. doi:10.16285/j.rsm.2006.05.011

Chang, T.-H., and Chang, H.-W. (2010). Improvement of liquefaction resistance of reclaimed sand in water-an experimental study. *J. Geoengin.* 5 (2), 39–49.

Chen, H., Huang, X., He, R., Zhou, Z., Fu, C., and Wang, J. (2021b). Mechanical properties of polypropylene fiber cement mortar under different loading speeds. *Sustainability* 13, 3697. doi:10.3390/su13073697

Chen, H., Zhou, X., Li, Q., He, R., and Huang, X. (2021a). Dynamic compressive strength tests of corroded SFRC exposed to drying–wetting cycles with a 37 mm diameter SHPB. *Materials* 14, 2267. doi:10.3390/ma14092267

Chen, X., Wu, J., Ning, Y., and Zhang, W. (2022). Experimental study on the effect of wastewater and waste slurry of mixing plant on mechanical properties and microstructure of concrete. *J. Build. Eng.* 52, 104307. doi:10.1016/j.jobe.2022.104307

Craeye, B., Geirnaert, M., and De Schutter, G. (2011). Super absorbing polymers as an internal curing agent for mitigation of early-age cracking of high-performance concrete bridge decks. *Constr. Build. Mater.* 25 (1), 1–13. doi:10.1016/j.conbuildmat.2010.06.063

Deng, Y., Jiang, Y., Wu, J., Sun, H., and Geng, X. (2022). Desert silty sand modified by anionic PAM and ordinary portland cement: microfabric reinforcement and durability. *Transp. Geotech.* 37, 100846. doi:10.1016/j.trgeo.2022.100846

Fengjun, Z., Cui, K., Xianyang, S., Xuan, L., Jin, L., and Qianbao, C. (2020). Study on preparation and properties of novel ternary flocculant for rapid separation of underground continuous wall waste mud. *Pigm. Resin Technol.* 49 (6), 421–429. doi:10.1108/prt-08-2019-0073

GB/T 50123-2019; Chinese code. Standard for Geotechnical Testing Method National Standards of the People's Republic of China: Beijing, China, 2019.

Grohs, H. (2002). Cost-efficient regeneration of bore slurry for driving of the weser tunnel. *Aufbereitungstechnik* 43 (11), 30–37.

He, R., and Lu, N. (2023). Unveiling the dielectric property change of concrete during hardening process by ground penetrating radar with the antenna frequency of 1.6 GHz and 2.6 GHz. *Cem. Concr. Comp.* 144, 105279. doi:10.1016/j.cemconcomp.2023.105279

He, R., Nantung, T., Olek, J., and Lu, N. (2023). Field study of the dielectric constant of concrete: a parameter less sensitive to environmental variations than electrical resistivity. *J. Build. Eng.* 74, 106938. doi:10.1016/j.jobe.2023.106938

He, X., Zheng, Z., Ma, M., Su, Y., Yang, J., Tan, H., et al. (2020). New treatment technology: the use of wet-milling concrete slurry waste to substitute cement. *J. Clean. Prod.* 242, 118347. doi:10.1016/j.jclepro.2019.118347

Jiang, P., Chen, Y., Zhou, L., Mao, T., Wang, W., Yuan, J., et al. (2021b). The time effect and micromechanism of the unconfined compressive strength of cement modified slurries. *Adv. Mater. Sci. Eng.* 2021, 5597275. doi:10.1155/2021/5597275

Jiang, P., Mao, T., Li, N., Jia, L., Zhang, F., and Wang, W. (2019). Characterization of short-term strength properties of fiber/cement-modified slurry. *Adv. Civ. Eng.* 2019, 3789403. doi:10.1155/2019/3789403

Jiang, P., Zhou, L., Mao, T., Yuan, J., Wang, W., and Li, N. (2022). Damage model and time effect of cement-modified waste slurry. *J. Jilin Uni. Eng. Tech. Edi* 52 (12), 2874–2881. doi:10.13229/j.cnki.jdxbgxb20210430

Jiang, P., Zhou, L., Wang, Y., Qian, B., Wang, W., Li, N., et al. (2021a). Freeze–thaw damage model of polypropylene fiber reinforced cement stabilized waste construction slurry under uniaxial action. *Minerals* 11, 743. doi:10.3390/min11070743

Katsioti, M., Katsiotis, N., Rouni, G., Bakirtzis, D., and Loizidou, M. (2008). The effect of bentonite/cement mortar for the stabilization/solidification of sewage sludge containing heavy metals. *Cem. Concr. Compos.* 30 (10), 1013–1019. doi:10.1016/j.cemconcomp.2008.03.001

Kim, S.-C. (2016). Application of response surface method as an experimental design to optimize coagulation–flocculation process for pre-treating paper wastewater. *J. Ind. Eng. Chem.* 38, 93–102. doi:10.1016/j.jiec.2016.04.010

Li, N., Zhu, Q., Wang, W., Song, F., An, D., and Yan, H. (2019). Compression characteristics and microscopic mechanism of coastal soil modified with cement and fly ash. *Materials.* 12, 3182. doi:10.3390/ma12193182

Lin, B., and Zhang, Z. (2016). Carbon emissions in China´s cement industry: a sector and policy analysis. *Ren. Sust.e Ener. Rev.* 58, 1387–1394. doi:10.1016/j.rser.2015.12.348

Ma, X., Liu, J., and Shi, C. (2019). A review on the use of LWA as an internal curing agent of high performance cement-based materials. *Constr. Build. Mater.* 218, 385–393. doi:10.1016/j.conbuildmat.2019.05.126

Patra, A. S., Patra, P., Chowdhury, S., Mukherjee, A., and Pal, S. (2020). Cationically functionalized amylopectin as an efficient flocculant for treatment of coal suspension. *Colloids Surf. A* 586, 124229. doi:10.1016/j.colsurfa.2019.124229

Qin, X., Zhou, Z., He, B., Xu, B., Yu, S., Qin, G., et al. (2023). Characteristics of waste mud treated by construction waste-slag based flocculation-solidification combined method. *Constr. Build. Mater.* 370, 130699. doi:10.1016/j.conbuildmat.2023.130699

Shao, Z.-B., Zhang, M.-X., Li, Y., Han, Y., Ren, L., and Deng, C. (2018). A novel multi-functional polymeric curing agent: synthesis, characterization, and its epoxy resin with simultaneous excellent flame retardance and transparency. *Chem. Eng. J.* 345, 471–482. doi:10.1016/j.cej.2018.03.142

Sun, X., Chen, Z., Sun, Z., Wu, S., Guo, K., Dong, Z., et al. (2023). High-efficiency utilization of waste shield slurry: a geopolymeric flocculation-filtration-solidification method. *Constr. Build. Mater.* 387, 131569. doi:10.1016/j.conbuildmat.2023.131569

Sun, X., Zhang, H., Han, Z., Huang, S., Wu, S., Tian, Z., et al. (2024). Mechanism of geopolymeric solidification in shield-tunnelling slurry from diverse sources: the role of bentonite adsorption in influencing the reaction process. *Constr. Build. Mater.* 431, 136627. doi:10.1016/j.conbuildmat.2024.136627

Tong, J., Niu, X., Wang, Y., and Lu, Y. (2021). Strength characteristics of iron tailings blended soil as a road base material. *Appl. Sci.* 11 (16), 7587. doi:10.3390/app11167587

Wang, D., Min, F., Lyu, H., Chen, J., Wang, B., and Zhang, J. (2023a). Recycling waste sand from slurry shield tunneling: a sustainable filter aid for waste slurry dehydration. *J. Clean. Prod.* 383, 135387. doi:10.1016/j.jclepro.2022.135387

Wang, Q., Zhang, R., Guo, J., Cai, G., and Li, Y. (2024). Study on mechanical properties and microstructure of metakaolin-slag-calcium carbide residue synergistic solidifying waste engineering mud. *Constr. Build. Mater.* 438, 137135. doi:10.1016/j.conbuildmat.2024.137135

Wang, Q., Zhang, R., Xu, H., Li, M., and Fang, Z. (2023b). Study on mechanical properties and microstructure of fly-ash-based geopolymer for solidifying waste mud. *Constr. Build. Mater.* 409, 134176. doi:10.1016/j.conbuildmat.2023.134176

Xiao, X., Yu, Y., Sun, Y., Zheng, X., and Chen, A. (2021). Heavy metal removal from aqueous solutions by chitosan-based magnetic composite flocculants. *J. Environ. Sci.* 108, 22–32. doi:10.1016/j.jes.2021.02.014

Xu, H., Wang, Q., Zhou, W., Li, M., and Cai, G. (2023a). Study on compressive strength and microstructure of slag–calcium carbide residue solidified mud under wetting–drying cycles. *Arab. J. Sci. Eng.* 48 (4), 5087–5096. doi:10.1007/s13369-022-07302-6

Xu, S., Shi, J., Deng, J., Sun, H., Wu, J., and Ye, Z. (2023b). Flocculation and dewatering of the kaolin slurry treated by single-and dual-polymer flocculants. *Chemosphere* 328, 138445. doi:10.1016/j.chemosphere.2023.138445

Yang, A., Zhong, X., Liang, C., and Li, Y. (2017). Experiment study of solidification performance and long-term mechanical properties of dredger filled mud. *Roc. Soil Mech.* 38 (9), 2589–2596. doi:10.16285/j.rsm.2017.09.016

Ye, J., Jiang, P., Chen, L., Zhou, X., Rao, F., and Tang, X. (2023). Strength and deformation characteristics of fiber and cement-modified waste slurry. *Polymers* 15, 3435. doi:10.3390/polym15163435

Zhang, B., Jiang, W., Xu, Q., Yuan, D., Shan, J., and Lu, R. (2022). Experimental feasibility study of ethylene-vinyl acetate copolymer (EVA) as cement stabilized soil curing agent. *Road. Mater. Pave.* 23 (3), 617–638. doi:10.1080/14680629.2020.1834442

Frontiers | Frontiers in Materials

Gradation optimization of AC-20 asphalt mixture based on the fuzzy analytic hierarchy process and comprehensive evaluation method

Fu Zhu, Shengyu Zhang, Wenyi Chen and Hua Rong*

School of Transportation Science and Engineering, Jilin Jianzhu University, Changchun, China

The aggregate gradation of asphalt mixture is one of the most important factors affecting the service life of asphalt pavement. In order to study the gradation of asphalt mixture with the best comprehensive performance, this study puts forward a new method of mineral aggregate gradation optimization based on the fuzzy analytic hierarchy process and comprehensive evaluation method, aiming at the multi-level and multi-index evaluation of the road performance of asphalt mixture. First, the orthogonal test design method is applied to design nine target gradations with coarse aggregate (>4.75 mm) and fine aggregate (<4.75 mm) of AC-20 (asphalt concrete) mixture serving as two factors and the upper, middle, and lower positions of the gradation curve as three levels, and then the road performance test research is carried out. Second, a comprehensive model for evaluation of road performance of mineral aggregate gradation is established. A fuzzy complementary judgment matrix is constructed, and the index weights of each level and the hierarchical total ranking weight are calculated. Then, the membership function is introduced into the comprehensive evaluation model for the road performance of mineral aggregate gradation, and the membership values of each index of asphalt mixture road performance are obtained. Finally, the fuzzy comprehensive evaluation method is used to find out the comprehensive evaluation value of the road performance of the nine graded asphalt mixtures, and the mineral aggregate gradation is optimized. The research results show that the 1# gradation of the asphalt mixture has the highest comprehensive road performance evaluation value, and the combination of the fuzzy hierarchical analysis process and comprehensive evaluation method can more objectively and comprehensively evaluate the comprehensive road performance of the asphalt mixture and provide a useful reference for the optimal selection of asphalt mixture mineral gradation.

1 Introduction

The performance of asphalt pavements will inevitably degrade gradually due to all the year round exposure to traffic loads and environmental factors (Chen et al., 2020). In

addition, mineral aggregate gradation has an important influence on the tensile strength, fatigue resistance, deformation resistance at high temperature, crack resistance at low temperature, and water damage resistance of the asphalt mixture (Tayfur et al., 2007; Moghaddam et al., 2011; Li et al., 2020; Zhai, et al., 2019). Due to the wide gradation range of the specifications and the differences in climatic conditions and materials in each region, it is often impossible to completely apply the specification in gradation design. The orthogonal test design method deals with multi-factor tests, which can infer better test conditions through fewer test times and provide more comprehensive test results (Lu and Zhang, 2018). For the multi-index orthogonal test of asphalt mixture, the comprehensive scoring method and comprehensive balance method are often used to transform it into a single-index test problem for comprehensive optimization, and the results often lose comprehensiveness because of the differences in each index (Hu et al., 2021; Cheng et al., 2019).

In recent years, scholars around the world have used mathematics and machine algorithms to optimize mineral aggregate gradation. Pan et al. (2020) developed a gradation segregation model based on the fractal dimension to evaluate the variability of reclaimed asphalt pavement (RAP) gradation and then proposed an optimized gradation design method based on Mohr–Coulomb theory to reduce the variability of RAP gradation. Xue and Jiang (2022) used the discrete element method to obtain the interlock-coarse gradation of the AC-20 asphalt mixture and determined the interlock-dense gradation, and compared with the specific gradation, the Marshall stability, dynamic stability, shear strength, and splitting strength of the AC-20 asphalt mixture with interlocking dense gradation are all improved. Sivilevičius et al. (2011) constructed the models of constrained and unconstrained non-linear optimization to choose the best HMA mixture gradation. Sebaaly et al. (2018) developed simple multilayer perceptron structure artificial neural network (ANN) models and used a non-linear constrained genetic algorithm to call the ANN model to optimize the aggregate gradation of the asphalt mixture. Wang et al. (2021) proposed a gradation optimization method based on the fractal theory method and trial calculation method, and the gradation obtained by the two methods was simulated based on particle flow code in two dimension (PFC2D); the results showed that the asphalt mixture with optimized gradation based on the fractal theory method had higher strength and better stability. Most of these gradation optimization methods are based on the performance of the asphalt mixture, but the results obtained are different. In order to solve the problems encountered when using the conventional methods mentioned above, this article takes the AC-20 asphalt mixture as an example, uses the fuzzy analytic hierarchy process and fuzzy comprehensive evaluation method to fully characterize multiple factors and indicators of asphalt mixture road performance, conducts fuzzy comprehensive evaluation on the experimental results of asphalt mixture road performance of nine mineral aggregate gradations, and selects the mineral aggregate gradation with the best comprehensive performance.

Fuzzy analytic hierarchy process and fuzzy comprehensive evaluation, as fundamental fuzzy mathematical methods, have certain universality and scalability, and are widely used in various fields (Xu et al., 2023; Li et al., 2023; Arman, 2023). However, few studies have comprehensively applied the two methods to the

optimization of asphalt mixture gradation. This paper proposes a mineral aggregate gradation optimization method that is suitable for the results of multi-index orthogonal experiments of asphalt mixtures by combining the fuzzy analytic hierarchy process and fuzzy comprehensive evaluation method. The application of fuzzy mathematical methods has established a theoretical foundation for the analysis of multi-index orthogonal test results of asphalt mixtures, enriching the multi-index evaluation system of asphalt mixtures. First, on the basis of completion of the road performance tests of asphalt mixture with nine mineral aggregate gradations designed by the orthogonal test, the road performance evaluation model of the asphalt mixture with mineral aggregate gradation is constructed. Second, by constructing the fuzzy complementary judgment matrix, consistency test, and calculating the index weights, the total ranking weight of the comprehensive evaluation index of aggregate gradation road performance is calculated. Finally, on the basis of completion of the evaluation object, evaluation index, membership function, and fuzzy comprehensive evaluation matrix, the fuzzy comprehensive evaluation values of nine mineral aggregate graded asphalt mixtures are calculated, the comprehensive road performance ranking is determined, and the best mineral aggregate gradation is presented.

2 Methodology

The method flow of this study is shown in Figure 1.

2.1 Fuzzy analytic hierarchy process

In the 1970s, Saaty T. L., an American expert in operational research, put forward a systematic decision analysis method combining qualitative and quantitative analyses, namely, the analytic hierarchy process (Saaty, 1990). However, the traditional analytic hierarchy process has some problems, such as difficulty in testing the consistency of the judgment matrix, the complexity of adjustment, and the lack of scientificity. Meanwhile, due to the uncertainty of human thinking, ignoring the fuzziness of human behavior may lead to mistakes in decision (Ahmed and Kilic, 2019; Jaganathan et al., 2007; Zhang et al., 2021). Therefore, in view of the fuzziness of the target to be evaluated, this paper introduces the fuzzy mathematical analysis method into the analytic hierarchy process and establishes a multi-level comprehensive evaluation model.

2.1.1 Establish hierarchical analytic structure model

The fuzzy analytic hierarchy process can be used to construct a multi-level hierarchical analytic structure model according to the different attributes of the problem to be evaluated. The basic principle is to decompose first and then synthesize, select some factors and indexes related to the target to be evaluated, and then construct a hierarchical analytic structure model according to the relative importance and affiliation between the factors and indexes (Han et al., 2020).

FIGURE 1
Flowchart of the fuzzy analytic hierarchy process and comprehensive evaluation method.
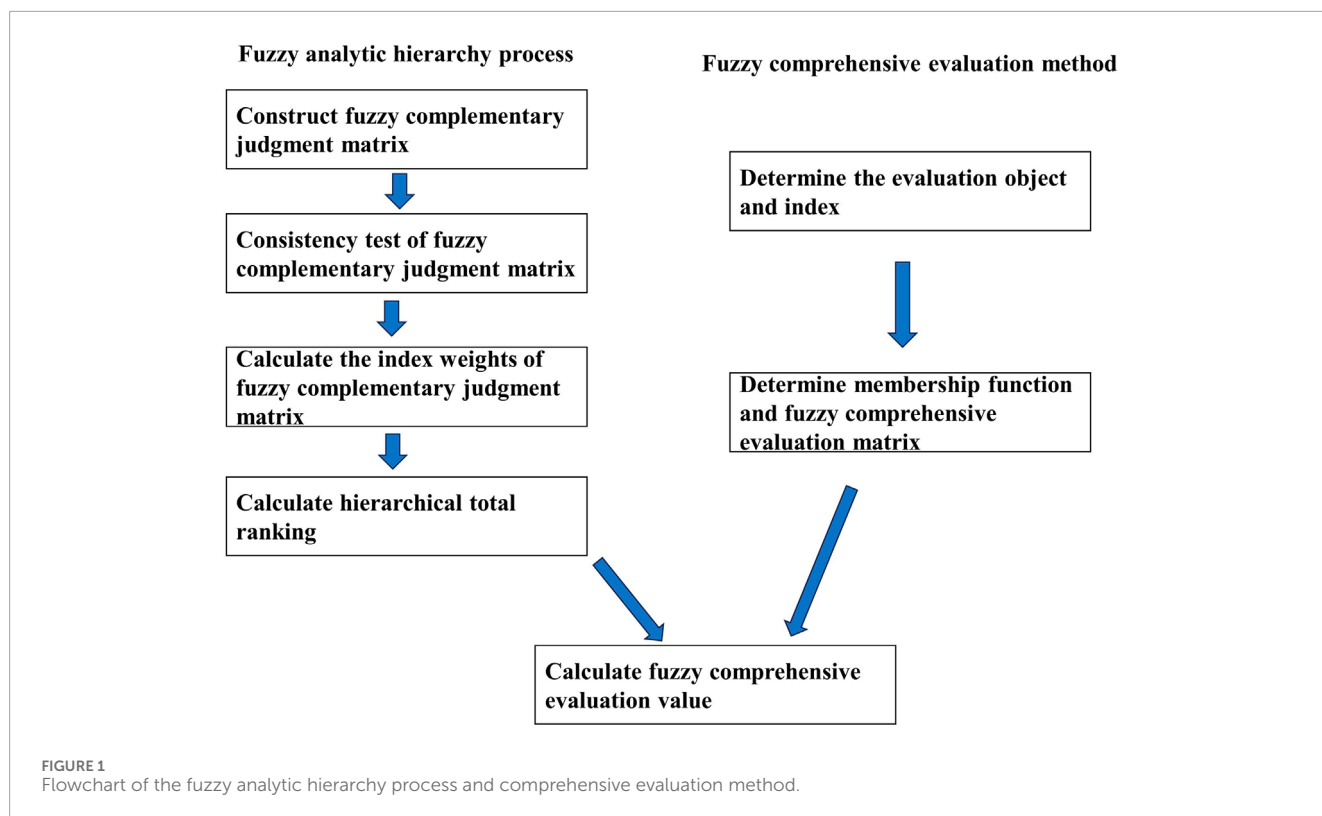
2.1.2 Construct fuzzy complementary judgment matrix

When the multi-level analytic structure model is established, for the factors or indexes of the same level, the target or factors of the previous level need to be used as a criterion for two comparisons, and the importance of the indexes can be assigned by the "0.1–0.9" comparison scale. A comparison scale a_{ij} can be used to express the relative importance of two factors in the next level, and the rules for the value of a_{ij} are shown in Table 1.

2.1.3 Consistency test of the fuzzy complementary judgment matrix

After constructing the fuzzy complementary judgment matrix, it is necessary to check its consistency, and if Equation 1 is not satisfied, the non-consistency matrix needs to be transformed into a new fuzzy consistency judgment matrix by Equation 2 (Xu, 2001).

$$r_{ij} = r_{ik} - r_{jk} + 0.5, \tag{1}$$

$$r_{ij} = \frac{r_i - r_j}{2(n-1)} + 0.5, \tag{2}$$

where $i = 1, 2, \ldots, n$; $j = 1, 2, \ldots, n$; $k = 1, 2, \ldots, n$.

2.1.4 Calculate the index weights of the fuzzy complementary judgment matrix

By comparing the relative importance between two elements, the fuzzy complementary judgment matrix

TABLE 1 Scale value and definition (Xie and Liu, 2006).

Scale value	Definition
0.1	In comparing two elements, the latter is extremely more important than the former
0.3	In comparing two elements, the latter is significantly more important than the former
0.5	In comparing two elements, the latter is as important as the former
0.7	In comparing two elements, the former is significantly more important than the latter
0.9	In comparing two elements, the former is extremely more important than the latter
0.2, 0.4, 0.6, 0.8	The middle value of the two adjacent scales above

The matrix $A = \left(a_{ij}\right)_{n \times n}$ based on the scale value a_{ij} is called the fuzzy complementary judgment matrix.

$A = \left(a_{ij}\right)_{n \times n}$ is obtained, and the weight vector of matrix A is $W = [w_1, w_2, \ldots, w_n]^T$, and the weight calculation equation is as follows (Xu, 2001).

$$w_i = \frac{\sum\limits_{j=1}^{n} a_{ij} + \frac{n}{2} - 1}{n(n-1)}, \tag{3}$$

where $i = 1, 2, \ldots, n$; $j = 1, 2, \ldots, n$.

TABLE 2 Main technical indexes test results of modified asphalt.

Technical index	Unit	Standard value	Test value
Penetration degree (25°C)	0.1 mm	60~80	66.3
Penetration index	—	≥−0.4	−0.25
Ductility (5°C)	cm	≥30	75
Softening point	°C	≥55	58
Density (15°C)	g/cm^3	Measured value	1.0091
Mass loss after aging	%	−0.1~0.1	0.035
Penetration ratio after aging	0.1 mm	≥60	63
Residual ductility (5°C)	cm	≥20	37

TABLE 3 Main technical indexes test results of aggregate.

Technical index	Unit	Standard value	Test value
Crushing value of the coarse aggregate	%	≤28	10.69
LA abrasion value of the coarse aggregate	%	≤30	14.94
Relative density of 19–26.5 mm andesite	—	—	2.686
Relative density of 9.5–19 mm andesite	—	—	2.659
Relative density of 2.36–4.75 mm andesite	—	—	2.626
Relative density of 0–2.36 mm andesite	—	—	2.739
Adhesion between asphalt and aggregate	Level	—	3

2.1.5 Calculate hierarchical total ranking

Assume that there are K layers in an evaluation index system and in order to determine the ranking weight of each element in the Kth layer corresponding to the relative importance of the target layer, it is necessary to multiply the weight of each element layer by layer, as shown in Equation 4.

$$W^K = \left[w_1^K, w_2^K, \cdots, w_{n_K}^K \right]^T = \left[W_1^K, W_2^K, \ldots, W_{K-1}^K \right] W^{K-1}. \quad (4)$$

2.2 Fuzzy comprehensive evaluation method

2.2.1 Determine the evaluation object and index

In order to evaluate the comprehensive road performance of the AC-20 asphalt mixture, it is necessary to determine the evaluation object and evaluation index of the evaluation model first. The road performance test results of nine mineral aggregate gradations are taken as the evaluation object, and the evaluation index set is composed of six indexes, namely, dynamic stability, Marshall stability, voids filled with asphalt, void ratio, immersion Marshall stability, and freeze–thaw splitting tensile strength ratio.

2.2.2 Determine membership function and fuzzy comprehensive evaluation matrix

Since different evaluation indexes have different representational meanings and dimensions, if the indexes are to be comparable with each other, the indexes can be standardized. According to the Technical Specification for Construction of Highway Asphalt Pavements (JTG F40-2004, 2004) of China, the evaluation index properties can be divided into maximal, intermediate, and minimal indexes. The Marshall stability is not less than 8 kN, the dynamic stability is not less than 2,400 times/mm, the immersion Marshall stability is not less than 85%, and the freeze–thaw splitting tensile strength ratio must be at least 80%: these four indexes can be regarded as maximum indexes. The recommended range of void ratio is 3%–6%, and that of effective asphalt saturation is 55%–70%, which can be regarded as intermediate indexes.

Dynamic stability, Marshall stability, immersion Marshall stability, and freeze–thaw splitting tensile strength ratio are all maximum indexes, and the membership function is shown in Equation 5.

$$r_{ij} = \frac{a_{ij}}{\max\limits_{j} \left\{ a_{ij} \right\}}. \quad (5)$$

Void ratio and voids filled with asphalt are intermediate indexes, and their membership function is shown in Equation 6.

$$r_{ij} = 1 - \frac{\left| a_{ij} - k \right|}{\max \left\{ \left| a_j - k \right| \right\}}, \quad (6)$$

where i = 1, 2, … , 9; j = 1, 2, … , 6; k is the middle value of the recommended range in the specification (JTG F40-2004, 2004).

Through the above membership function equation to obtain the membership value of each evaluation index for the road performance, the fuzzy comprehensive evaluation matrix R can be established.

2.2.3 Calculate fuzzy comprehensive evaluation value

According to the fuzzy comprehensive evaluation matrix and the hierarchical total ranking weight, the fuzzy comprehensive evaluation value F can be determined, as shown in the following equation.

$$F = R \times W^K. \quad (7)$$

3 Engineering example

3.1 Raw material test

The Jicao Expressway is located in the transitional zone from the hinterland of Changbai Mountain in central and southern Jilin Province to the Songnen Plain. It belongs to a seasonal frozen soil area, and the road surface damage caused by repeated

TABLE 4 Orthogonal design factor and level table of AC-20.

Level	Percentage passing of each sieve (%)											
	Coarse aggregate						Fine aggregate					
	26.5	19	16	13.2	9.5	4.75	2.36	1.18	0.6	0.3	0.15	0.075
1	100	95	85	71	61	41	30	22.5	16	11	8.5	5
2	100	97.5	88.5	75.5	66.5	41	37	27.75	20	14	10.75	6
3	100	92.5	81.5	66.5	55.5	41	23	17.25	12	8	6.25	4

TABLE 5 Synthetic aggregate gradation of AC-20.

Gradation	Percentage passing of each sieve (%)											
	26.5	19	16	13.2	9.5	4.75	2.36	1.18	0.6	0.3	0.15	0.075
1#	100.0	92.6	85.4	74.4	58.7	41.1	28.8	22.6	17.5	12.3	8.2	4.6
2#	100.0	92.6	85.0	73.3	56.6	41.3	31.9	27.3	21.9	15.1	9.7	5.1
3#	100.0	92.5	85.4	74.4	58.8	40.6	24.8	16.4	11.7	8.6	6.2	3.8
4#	100.0	94.8	88.3	78.2	63.8	41.3	28.1	22.0	17.0	12.0	8.1	4.5
5#	100.0	95.3	88.6	78.1	63.1	41.6	31.7	27.6	22.3	15.4	9.9	5.3
6#	100.0	95.2	89.9	79.0	64.9	40.7	24.4	16.4	11.8	8.6	6.2	3.7
7#	100.0	89.9	82.0	70.0	53.0	41.3	29.0	21.9	16.7	11.9	8.1	4.6
8#	100.0	89.9	81.6	69.1	51.3	41.4	32.1	26.8	21.4	15.0	9.9	5.4
9#	100.0	89.9	82.2	70.7	54.4	41.0	25.4	16.4	11.5	8.5	6.2	3.8

TABLE 6 Road performance test results of AC-20 (Zhu, 2010).

Gradation	Coarse aggregate level	Fine aggregate level	Oil–stone ratio (%)	Dynamic stability (times/ mm)	Marshall stability (kN)	Voids filled with asphalt (%)	Void ratio (%)	Immersion residual stability (%)	Freeze–thaw splitting tensile strength ratio (%)
1#	P_1	Q_1	5.3	7,875	11.9	67.8	4.6	124.2	102.98
2#	P_1	Q_2	5.3	3,500	12.0	71.1	4.1	112.8	92.06
3#	P_1	Q_3	5.3	3,938	8.5	47.6	10.3	97.1	73.16
4#	P_2	Q_1	5.3	7,000	8.4	63.5	5.1	97.4	90.17
5#	P_2	Q_2	5.3	6,300	12.9	68.1	4.7	97.2	104.36
6#	P_2	Q_3	5.3	3,000	8.1	55.0	7.8	101.9	98.59
7#	P_3	Q_1	5.3	7,000	11.5	74.7	3.5	109.3	103.98
8#	P_3	Q_2	5.3	2,625	14.4	77.6	3.0	87.3	96.96
9#	P_3	Q_3	5.3	7,875	8.5	56.1	7.6	101.7	100.4

FIGURE 2
Comprehensive evaluation model of aggregate gradation road performance.
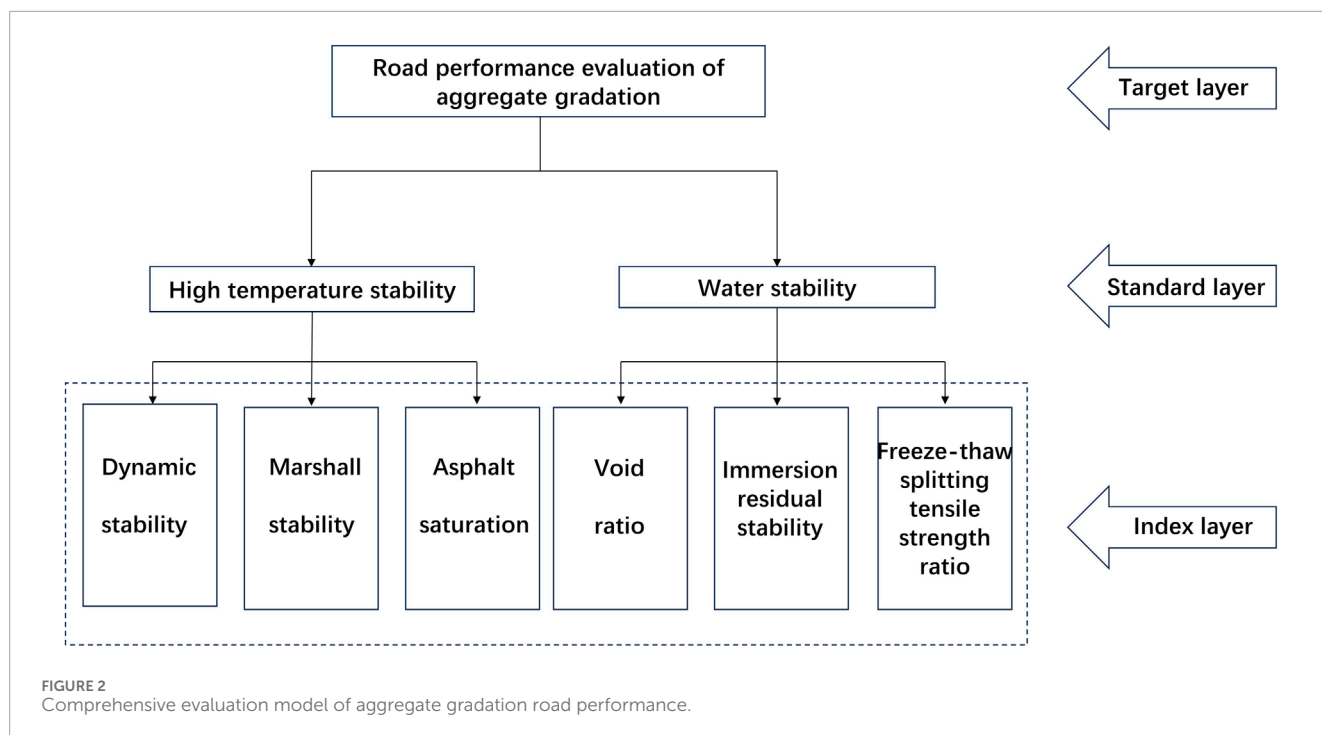
TABLE 7 Evaluation index weights.

Target layer	Standard layer	Weight	Index layer	Weight	Hierarchical total ranking weight
L	M_1	0.450	N_1	0.383	0.172
			N_2	0.321	0.145
			N_3	0.296	0.133
	M_2	0.550	N_4	0.383	0.211
			N_5	0.308	0.169
			N_6	0.308	0.169

freeze–thaw cycles is severe, requiring high road performance. The Jicao Expressway used the modified AC-20 asphalt mixture as the middle layer material of asphalt pavement, coarse aggregate and fine aggregate were used as andesite, and the filler was andesite mineral powder. The technical performance test results of raw materials are shown in Tables 2, 3.

3.2 Design and synthesis of mineral aggregate gradation

In this paper, within the range of gradation given in the specification (JTG F40-2004, 2004), the 4.75-mm sieve is used as the dividing sieve, and coarse aggregate (>4.75 mm) and fine aggregate (<4.75 mm) are two factors affecting the road performance of asphalt mixture, and each factor selects three levels, namely, middle, upper, and lower positions of the gradation curve, with the middle position being the middle

value of the gradation range, the upper position being the bisector of the upper limit and middle of the gradation range, and the lower position being the bisector of the middle and the lower limit of the gradation range, as shown in Table 4. For two factors and three levels, nine initial design gradations were obtained by using the L_9 (3^4) orthogonal table (Zhu, 2010), and then the synthetic gradations were calculated according to the design gradations and aggregate sieving results, as shown in Table 5.

According to the Standard Test Methods of Bitumen and Bituminous Mixtures for Highway Engineering (JTG, E20-2011, 2011) of China, the density test (T 0706-2011) and Marshall stability test (T 0709-2011) of the asphalt mixture composed of nine synthetic gradations were carried out. The test results showed that the best oil–stone ratio of asphalt mixture specimens of nine gradations was close to 5.3%. Therefore, in order to avoid the influence of oil–stone ratio factor on the road performance of the asphalt mixture, the oil–stone ratio of nine gradations was taken as 5.3%.

TABLE 8 Membership value of evaluation indexes.

Gradation	Dynamic stability (times/mm)	Marshall stability (kN)	Voids filled with asphalt (%)	Void ratio (%)	Immersion Marshall stability (%)	Freeze−thaw splitting tensile strength ratio (%)
1#	1	0.826	0.649	0.983	1	0.987
2#	0.444	0.833	0.430	0.931	0.908	0.882
3#	0.500	0.590	0.013	0	0.782	0.701
4#	0.889	0.583	0.934	0.897	0.784	0.864
5#	0.800	0.896	0.629	0.966	0.783	1
6#	0.381	0.563	0.503	0.431	0.820	0.945
7#	0.889	0.799	0.192	0.828	0.880	0.996
8#	0.333	1.000	0	0.741	0.703	0.929
9#	1	0.590	0.576	0.466	0.819	0.962

Under the optimal oil–stone ratio conditions, Marshall stability and immersion Marshall test (T 0709-2011), rutting test (T 0719-2011), and freeze–thaw splitting test (T 0729-2011) were carried out according to specification (JTG, E20-2011, 2011), and the test results of asphalt mixture road performance indexes were obtained as shown in Table 6.

3.3 Establish the comprehensive evaluation model for road performance

The AC-20 asphalt mixture as the pavement middle layer material, its high-temperature stability, and water stability should be the primary considerations. Therefore, this paper uses the principle of the analytic hierarchy process, takes the road performance of mineral aggregate gradation as the target layer (L), takes the high-temperature stability and water stability of the asphalt mixture as the two major factors in the standard layer (M), and the dynamic stability, Marshall stability, voids filled with asphalt, void ratio, immersion Marshall stability, and freeze–thaw splitting strength ratio of six indexes included in the index layer (N) so as to construct a comprehensive evaluation model of mineral aggregate gradation road performance, as shown in Figure 2.

3.4 Determine the fuzzy complementary judgment matrix and the evaluation index weight

According to the comprehensive evaluation model of mineral aggregate gradation road performance established in Figure 1, consulting with road industry experts and using the 0.1–0.9 scale method in Table 1, a fuzzy judgment matrix for the target layer based on two factors in the criterion layer is constructed as shown in

A1. The fuzzy judgment matrix for high-temperature stability based on three indicators, namely, dynamic stability, Marshall stability, and effective asphalt saturation, is constructed as shown in A2. The fuzzy judgment matrix for water stability based on three indicators, namely, porosity, immersion Marshall stability, and freeze–thaw splitting tensile strength ratio, is constructed as shown in A3.

$$A_1 = \begin{bmatrix} 0.5 & 0.4 \\ 0.6 & 0.5 \end{bmatrix}.$$

$$A_2 = \begin{bmatrix} 0.5 & 0.7 & 0.7 \\ 0.3 & 0.5 & 0.6 \\ 0.3 & 0.4 & 0.5 \end{bmatrix}.$$

$$A_3 = \begin{bmatrix} 0.5 & 0.7 & 0.7 \\ 0.3 & 0.5 & 0.5 \\ 0.3 & 0.5 & 0.5 \end{bmatrix}.$$

3.5 Consistency test of the judgment matrix

Because the second-order matrix itself has consistency, it is not necessary to check the consistency of A_1, but only to check the consistency of A_2 and A_3. The transformed consistent complementary judgment matrices are as follows.

$$A_2 = \begin{bmatrix} 0.500 & 0.625 & 0.675 \\ 0.375 & 0.500 & 0.550 \\ 0.325 & 0.450 & 0.500 \end{bmatrix}.$$

FIGURE 3
Influence of gradation curve position on high-temperature stability.
(A) Dynamic stability. **(B)** Marshall stability. **(C)** Voids filled with asphalt.

FIGURE 4
Influence of gradation curve position on water stability. **(A)** Void ratio.
(B) Immersion Marshall stability. **(C)** Freeze−thaw splitting tensile
strength ratio.

FIGURE 5
Fuzzy comprehensive evaluation value.
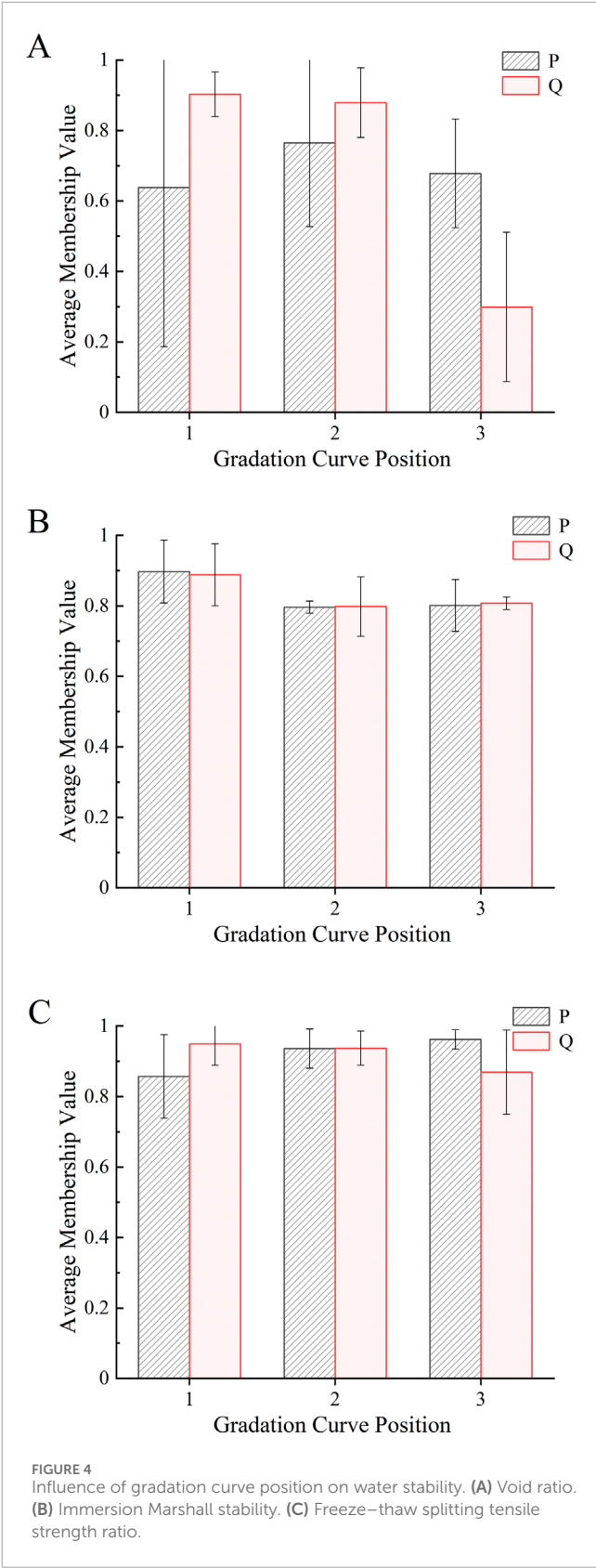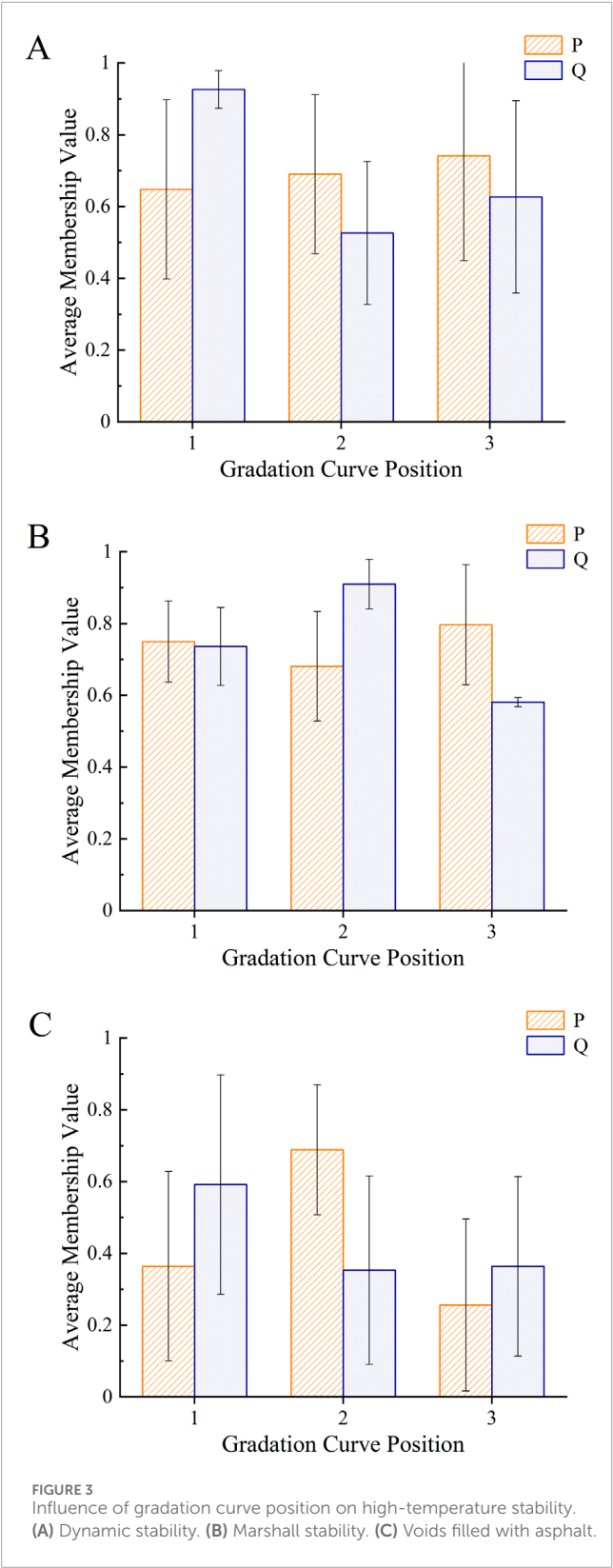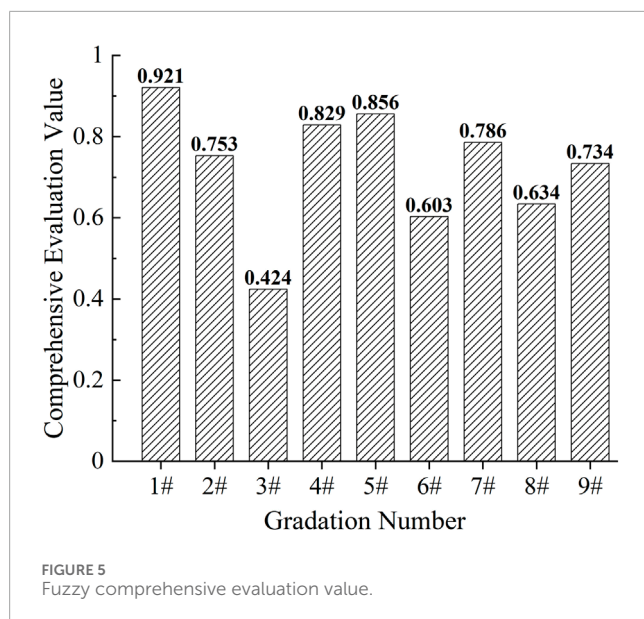
$$A_3 = \begin{bmatrix} 0.500 & 0.650 & 0.650 \\ 0.350 & 0.500 & 0.500 \\ 0.350 & 0.500 & 0.500 \end{bmatrix}.$$

By substituting A1, as well as the transformed A2 and A3 consistent complementary judgment matrices, into Formula 3, the weights of each evaluation factor can be obtained. Then, according to Formula 4, the ranking weight vector of the evaluation indicators relative to the overall goal can be obtained. The specific data are shown in Table 7.

3.6 Fuzzy comprehensive evaluation

After determining the hierarchical total ranking weight of the index layer, the aggregate gradation is optimized by combining fuzzy comprehensive evaluation, and the membership values of each index in nine gradations are calculated according to Equations 5, 6, as shown in Table 8. Calculate the average membership value of six indexes under different factors and levels, and obtain the change relationship diagram between each index and factor and level, as shown in Figures 3A–C, 4A–C.

As can be seen from Figure 3A, the dynamic stability of mineral aggregate gradation obtained by combining the lower position of the coarse aggregate gradation curve with the middle position of the fine aggregate gradation curve (P_3Q_1) is better, and the asphalt mixture composed of it has higher rutting resistance under high temperature. A large amount of coarse aggregates bear the main load, while the fine aggregates in the middle fill the pores. These two types of aggregates are mutually embedded and squeezed, forming a good skeleton structure with high resistance to shear slip and compression deformation. Therefore, it has high dynamic stability, fewer ruts, and good high-temperature stability. As can be seen from Figure 3B, the combination of the lower position of the coarse aggregate gradation curve and the upper

position of the fine aggregate gradation curve (P_3Q_2) gives the best Marshall stability of the mineral aggregate gradation, so the strength of the asphalt mixture is higher. Because the structural changes of fine aggregates can better affect the Marshall stability of asphalt mixtures, Q2 has more fine aggregates and bears stronger extrusion pressure during the experimental process, resulting in higher stability (Xu et al., 2008). As can be seen from Figure 3C, the voids filled with asphalt of mineral aggregate gradation formed by the upper position of the coarse aggregate gradation curve and the middle position of the fine aggregate gradation curve (P_2Q_1) is the closest to the median, and the asphalt mixture is more durable.

It can be seen from Figure 4A that the combination of the void ratio closest to the median is the upper position of the coarse aggregate gradation curve and the middle position of the fine aggregate gradation curve (P_2Q_1), and the asphalt mixture formed by its mineral aggregate gradation has better water resistance and plastic deformation resistance. Figures 4B, C show that the mineral aggregate gradation formed by the combination of middle position of coarse aggregate gradation curve and middle position of fine aggregate gradation curve (P_1Q_1) and middle position of coarse aggregate gradation curve and lower position of fine aggregate gradation curve (P_1Q_3) has the best immersion Marshall stability and freeze–thaw splitting tensile strength ratio, and asphalt mixture has the best water stability. An appropriate proportion of coarse and fine aggregates can improve the water resistance of asphalt mixtures, reduce the likelihood of water loss and damage, and avoid cracking and damage.

According to Equation 7, the fuzzy comprehensive evaluation value F of nine gradations can be obtained as shown in Figure 5.

From Figures 3, 4, it can be seen that the evaluation of high-temperature stability and water stability of asphalt mixture needs single-index analysis, and the optimal combination scheme determined by different indexes is different. However, the fuzzy comprehensive evaluation method can be used to obtain the membership value of each index of each gradation, and finally the gradation with the best comprehensive performance of asphalt mixture can be determined by the fuzzy comprehensive evaluation value. According to the maximum membership principle of fuzzy theory, it can be seen from Figure 5 that the comprehensive road performance of nine gradations is ranked as 1# > 5#>4# > 7#>2# > 9#>8# > 6#>3#, so the best aggregate gradation is the 1# gradation.

The use of the fuzzy analytic hierarchy process and comprehensive evaluation method can enable us to have better grading selection. By selecting a better grading, we can improve the material performance, save costs and resources, improve construction quality, and extend project life, thereby promoting the development and progress of engineering and materials fields. Therefore, precise selection and optimization of gradation have important practical significance and value.

4 Conclusion

This article is based on the Jicao Expressway project to conduct research on the optimal gradation of intermediate layer

asphalt mixtures and proposes a theoretical system suitable for gradation optimization analysis. First, the Marshall stability test, immersion Marshall test, rutting test, and freeze–thaw splitting test were conducted on nine experimental groups to obtain the road performance indicators of asphalt mixture. Then, the fuzzy analytic hierarchy process and fuzzy comprehensive evaluation method were used to evaluate the road performance of nine graded asphalt mixtures and select the gradation ratio. The main conclusions are as follows.

(1) This study established a multi-level evaluation model for the performance of AC-20 asphalt mixture pavement using the analytic hierarchy process (AHP). Six indicators affecting the two factors were determined with the high temperature stability and water stability of the intermediate layer as the primary consideration factors. The relative importance and membership relationship between each factor and indicator were fully considered, improving the objectivity and accuracy of the comprehensive evaluation of asphalt mixture pavement performance.

(2) Using fuzzy mathematics theory and analytic hierarchy process to calculate the evaluation index weight of asphalt mixture road performance and determining the index weight vector through the fuzzy consistent judgment matrix can reduce the subjective one-sidedness of the traditional expert scoring method. The membership function is introduced, and the membership value is calculated, which solves the incomparability between indexes. The proposed evaluation system and weight determination method provide a theoretical basis for subsequent research on the road performance of asphalt mixtures.

(3) This study solves the problem of only obtaining the optimal combination scheme for a single indicator and is unable to obtain the optimal gradation for comprehensive road performance. Based on the fuzzy analytic hierarchy process and comprehensive evaluation method, the optimal gradation for the AC-20 asphalt mixture mineral aggregate is proposed as the 1 # gradation, providing a reference for the selection of asphalt mixture gradation in research.

Data availability statement

The original contributions presented in the study are included in the article/Supplementary Material; further inquiries can be directed to the corresponding author.

Author contributions

FZ: conceptualization, methodology, and writing–review and editing. SZ: data curation, formal analysis, investigation, methodology, and writing–original draft. WC: resources, validation, writing–original draft, and writing–review and editing. HR: resources, validation, and writing–review and editing.

Funding

Conflict of interest

The authors declare that the research was conducted in the absence of any commercial or financial relationships that could be construed as a potential conflict of interest.

Publisher's note

All claims expressed in this article are solely those of the authors and do not necessarily represent those of their affiliated organizations, or those of the publisher, the editors, and the reviewers. Any product that may be evaluated in this article, or claim that may be made by its manufacturer, is not guaranteed or endorsed by the publisher.

References

Ahmed, F., and Kilic, K. (2019). Fuzzy Analytic Hierarchy Process: a performance analysis of various algorithms. *Fuzzy Sets Syst.* 362, 110–128. doi:10.1016/j.fss.2018.08.009

Arman, H. (2023). Fuzzy analytic hierarchy process for pentagonal fuzzy numbers and its application in sustainable supplier selection. *J. Clean. Prod.* 409, 137190. doi:10.1016/j.jclepro.2023.137190

Chen, A., Zhao, Y., Li, P., Li, Y., Mohammed, M., and Guo, P. (2020). Crack propagation prediction of asphalt pavement after maintenance as a function of initial cracks distribution. *Constr. Build. Mater.* 231, 117157. doi:10.1016/j.conbuildmat.2019.117157

Cheng, Y., Li, L., Zhou, P., Zhang, Y., and Liu, H. (2019). Multi-objective optimization design and test of compound diatomite and basalt fiber asphalt mixture. *Materials* 12 (9), 1461. doi:10.3390/ma12091461

Han, Y., Zhou, R., Geng, Z., Bai, J., Ma, B., and Fan, J. (2020). A novel data envelopment analysis cross-model integrating interpretative structural model and analytic hierarchy process for energy efficiency evaluation and optimization modeling: application to ethylene industries. *J. Clean. Prod.* 246, 118965. doi:10.1016/j.jclepro.2019.118965

Hu, J., Ma, T., Zhu, Y., Huang, X., Xu, J., and Chen, L. (2021). High-viscosity modified asphalt mixtures for double-layer porous asphalt pavement: design optimization and evaluation metrics. *Constr. Build. Mater.* 271, 121893. doi:10.1016/j.conbuildmat.2020.121893

Jaganathan, S., Erinjeri, J. J., and Ker, J.-i. (2007). Fuzzy analytic hierarchy process based group decision support system to select and evaluate new manufacturing technologies. *Int. J. Adv. Manuf. Technol.* 32, 1253–1262. doi:10.1007/s00170-006-0446-1

JTG E20-2011 (2011). *Standard test methods of bitumen and bituminous mixtures for Highway engineering*. Beijing, China: China Ministry of Communications.

JTG F40-2004 (2004). *Technical specification for construction of Highway asphalt pavements*. Beijing, China: China Ministry of Communications.

Li, P., Su, J., Ma, S., and Dong, H. (2020). Effect of aggregate contact condition on skeleton stability in asphalt mixture. *Int. J. Pavement Eng.* 21 (2), 196–202. doi:10.1080/10298436.2018.1450503

Li, X., Chen, D., Fu, J., Liu, S., and Geng, X. (2023). Construction and application of fuzzy comprehensive evaluation model for rockburst based on microseismic monitoring. *Appl. Sci.* 13 (21), 12013. doi:10.3390/app132112013

Lu, X., and Zhang, S. (2018). Study on influencing factors of performance indexes of AC-20 modified asphalt mixture based on orthogonal experimental design. *Highway* 11, 177–181.

Moghaddam, T. B., Karim, M. R., and Abdelaziz, M. (2011). A review on fatigue and rutting performance of asphalt mixes. *Sci. Res. Essays* 6 (4), 670–682.

Pan, Y., Li, J., Yang, T., Liu, G., Zhou, J., Guo, P., et al. (2020). Optimization of gradation design of recycled asphalt mixtures based on fractal and Mohr-Coulomb theories. *Constr. Build. Mater.* 248, 118649. doi:10.1016/j.conbuildmat.2020.118649

Saaty, T. L. (1990). How to make a decision: the analytic hierarchy process. *Eur. J. operational Res.* 48 (1), 9–26. doi:10.1016/0377-2217(90)90057-I

Sebaaly, H., Varma, S., and Maina, J. W. (2018). Optimizing asphalt mix design process using artificial neural network and genetic algorithm. *Constr. Build. Mater.* 168, 660–670. doi:10.1016/j.conbuildmat.2018.02.118

Sivilevičius, H., Podvezko, V., and Vakrinienė, S. (2011). The use of constrained and unconstrained optimization models in gradation design of hot mix asphalt mixture. *Constr. Build. Mater.* 25 (1), 115–122. doi:10.1016/j.conbuildmat.2010.06.050

Tayfur, S., Ozen, H., and Aksoy, A. (2007). Investigation of rutting performance of asphalt mixtures containing polymer modifiers. *Constr. Build. Mater.* 21 (2), 328–337. doi:10.1016/j.conbuildmat.2005.08.014

Wang, Z., Liang, Q., Yan, F., and Bian, G. (2021). Strength improvement of cement emulsified asphalt mixture through aggregate gradation design. *Constr. Build. Mater.* 299, 124018. doi:10.1016/j.conbuildmat.2021.124018

Xie, J., and Liu, C. (2006). *Fuzzy mathematical method and its application*. Wu Han: Huazhong University of Science and Technology Press.

Xu, H., Tan, Y., Li, X., and Tian, Y. (2008). Research on the relationship between Marshall stability and grading curve characteristics of asphalt mixtures. *Highway*, 213–217.

Xu, S. l., Yeyao, T., and Shabaz, M. (2023). Multi-criteria decision making for determining best teaching method using fuzzy analytical hierarchy process. *Soft Comput.* 27 (6), 2795–2807. doi:10.1007/s00500-022-07554-2

Xue, J., and Jiang, Y. (2022). Gradation optimization and evaluation of AC-20 mixtures. *Constr. Build. Mater.* 350, 128893. doi:10.1016/j.conbuildmat.2022.128893

Xu, Z. (2001). An algorithm for fuzzy complementarity judgment matrix sorting. *J. Syst. Eng.* 16 (4), 311–314. doi:10.3969/j.issn.1000-5781.2001.04.012

Zhai, Y., Zhang, B., Wang, F., Zhong, Y., and Li, X. (2019). Composite dielectric model of asphalt mixtures considering mineral aggregate gradation. *J. Mater. Civ. Eng.* 31 (6), 04019091. doi:10.1061/(asce)mt.1943-5533.0002642

Zhang, Z., Liu, P., Rochlani, M., Falla, G. C., Leischner, S., and Oeser, M. (2021). A fuzzy comprehensive evaluation method to select the optimal mineral filler for optimization of the performance of asphalt mastics. *Constr. Build. Mater.* 298, 123847. doi:10.1016/j.conbuildmat.2021.123847

Zhu, Fu. (2010). *Research on the optimization of asphalt pavement mix proportion of ji-cao Expressway*. Changchun: Jilin Institute of Civil Engineering and Architecture.

frontiers | Frontiers in Materials

Rheological properties and 3D printability of SBS/CR-modified asphalt binder with C9 petroleum resin for crack filling

Yanhui Niu[1]*, Xinyu Wang[1], Igor Burmistrov[2] and Dongyu Niu[1]

[1]School of Materials Science and Engineering, Chang'an University, Xi'an, Shaanxi, China, [2]Engineering Center, Plekhanov Russian University of Economics, Moscow, Russia

Introduction: This study investigates rheological behavior and 3D printability of SBS-, CR-, SBS/CR-modified asphalt binder with C9 petroleum resin (C9PR) for crack filling.

Methods: Thirteen types of modified asphalt binders with respective C9PR of 0 wt%, 1 wt%, 2 wt%, 3 wt% were prepared and evaluated for their microstructure, physical properties, compatibility, rheological properties, and 3D printability.

Results: The results show that SBS, CR, and C9PR influenced significantly on rheological properties and 3D printability of modified asphalt binders. Physical blending and improved storage stability of modified asphalt binders were observed with the addition of C9PR. In addition, the combination of SBS and CR showed enhanced viscoelastic behavior and temperature sensitivity compared to the base asphalt binder due to the increased swelling behavior of SBS and CR in asphalt binders by C9PR.

Discussion: Asphalt binder with 3 wt% SBS, 15 wt% CR, and 1 wt% C9PR showed improved viscosity, elasticity, compatibility, high-temperature rutting resistance, and fatigue resistance. Additionally, C9PR expanded 3D printable temperature range of modified asphalt binder, leading to its potential use as an additive in 3D printed asphalt binders.

KEYWORDS

styrene−butadiene−styrene, crumb rubber, C9 petroleum resin, rheological properties, compatibility, 3D printability, 3D-printed asphalt binder

1 Introduction

Pavement cracks easily cause surface water or other harmful substances to enter the surface layer and road base, resulting in the structural damage of the road and driving hazards (Zhang et al., 2023). In China, cracks are often treated by measures such as crack filling and crack banding (Cao et al., 2022; Li et al., 2017). However, these traditional maintenance methods have problems, such as low construction efficiency, difficulty in ensuring the safety of construction workers, and maintenance effects affected by environmental factors. In recent years, 3D printing technology has been gradually applied in the field of road engineering, especially in the crack repair project of asphalt pavements, due to its advantages of

automation, precision, and rapidity. It can effectively improve the level of engineering automation, ensure the quality of crack repair, and reduce safety risks faced by staff (Jackson et al., 2018; Ma et al., 2017).

As a new type of pavement crack-repair material, 3D-printed asphalt binder needs to have good high-temperature rheological properties and printability, and it is difficult to satisfy these requirements using base asphalt binder (Aamer et al., 2022; Gong et al., 2023). High-quality modified asphalt binders commonly used in engineering include styrene–butadiene–styrene (SBS)-modified asphalt binder and crumb rubber (CR)-modified asphalt binder. SBS is commonly used to modify asphalt binder for improving both high- and low-temperature performance, and CR is commonly used to improve viscoelastic properties. However, it is still difficult to satisfy the requirements of 3D printing technology to repair cracks using single-modifier-modified asphalt binders. The lower workability and higher production cost of SBS-modified asphalt binder limit its application. CR-modified asphalt binder is also difficult to handle due to its poor processability, and it cannot be stored for a long time due to its phase separation problems. At the same time, the swelling process of CR usually requires continuous stirring of the mixture at high temperatures, which imposes higher requirements on the preparation process (Mturi et al., 2014; Presti, 2013; Shatnawi and President, 2010). SBS/CR composite-modified asphalt binder makes up for the insufficient performance of the single-modifier-modified asphalt binder, but there is still a problem of insufficient compatibility, which makes it difficult to satisfy the printability requirements of 3D-printed asphalt binder.

In face of the limitations of traditional CR-modified asphalt binder, an alternative material called wet-process terminal blend has attracted more and more attention. This alternative material overcomes the problem of segregation by using less and finer CR and introducing high-temperature shear (Cai et al., 2014; Presti, 2013; Presti et al., 2012). Unlike the swelling mechanism of general CR, terminal blend technology primarily relies on the desulfurization or depolymerization of rubber in hot asphalt binder and the full dispersion of rubber in the blend to obtain a homogeneous and stable modified binder (Presti, 2013; Presti et al., 2012; Zhang J. et al., 2021). Researchers have found that terminal blend binder has many advantages, such as good workability, especially suitable for dense graded mixtures, and is suitable for almost all fields where traditional CR asphalt binder can be used (Cai et al., 2014; Presti, 2013; Presti et al., 2012; Shatnawi and President, 2010). However, terminal blend binder still needs to solve many problems before it is widely used in engineering. For example, the deformation and fatigue resistance of the terminal blend binder may be reduced due to reduced viscosity and elasticity loss caused by the desulfurization effect (Glover et al., 2000; Presti, 2013; Presti et al., 2012). In response to the above, SBS is often used to modify terminal blend binder to compensate for the loss of viscosity and elasticity (Presti, 2013; Shatnawi and President, 2010; Zhang W. et al., 2021). However, SBS- and terminal blend–CR composite-modified asphalt binder still has the problem of insufficient compatibility. Based on this, C9 petroleum resin (C9PR) was considered a compatibilizer (Wu et al., 2022; Zhang J. et al., 2021; Zhao and Dong, 2021).

C9PR, also known as aromatic petroleum resin, is a functional resin polymerized from an unsaturated C9 fraction, a by-product of the petrochemical industry, containing unsaturated bonds and

a benzene ring structure. It is easily soluble in organic solvents and characterized by good compatibility with thermoplastic rubber, a high softening point, good aging resistance, and low price. Zhang W. et al. (2021) and Wu et al. (2022) found that petroleum resin can promote the swelling behavior of polymer in asphalt binder by reducing the particle size of the polymer modifier and finally improve the high- temperature performance of the modified asphalt binder. Cong et al., (2016) found that the high-temperature performance of SBS-modified asphalt binder with C9PR was better than that of the SBS-modified asphalt binder. Li Z. et al. (2019), Nie et al. (2019a), and Nie et al. (2019b) found that adding C9PR to the SBS/asphalt binder/oil mixture can further improve the compatibility of SBS and asphalt binder without increasing the oil content and effectively reduce the negative reaction caused by the addition of aromatic oil while increasing viscosity. However, Kim et al. (2020) found that the viscosity of composite-modified asphalt binder with C9PR was reduced. Cong et al. (2016) and Gong et al. (2022) found that when the C9PR level exceeded a certain amount, the viscosity of polymer-modified asphalt binder decreased. Most scholars have added C9PR to modified asphalt binders with a high SBS content (such as 6% and 8%) and concluded that the improvement in the performance of asphalt binder is proportional to the content of C9PR. However, according to a few researchers, C9PR has a peak effect on the performance improvement of modified asphalt binder when using SBS-modified asphalt binder purchased directly from certain companies. This means that the effect of C9PR on the performance of SBS-modified asphalt binder is not only closely related to the content of C9PR but also closely related to the content of SBS. In most studies on SBS-modified asphalt binders, researchers replaced part of SBS by adding a certain amount of CR with the aim of increasing economy and sustainability while maintaining performance. Therefore, it is necessary to study the effect of C9PR on the performance of the lower-content modifier-modified asphalt binder in the context of sustainable development.

Based on the above discussion, this study selected SBS and CR (treated by terminal blend) as the main modifiers and selected C9PR as an additive and compatibilizer to prepare modified asphalt binders. The road performance of modified asphalt binders was evaluated using microscopic tests, physical property tests, and rheological tests. The effect of C9PR on the performance of binders was investigated. After the performance tests, suitably modified asphalt binders were selected for 3D printing tests to verify whether the prepared modified asphalt binders show potential to be used as crack-filling material for 3D printing. The purpose of this study was to prepare a modified asphalt binder suitable for 3D printing to fill and repair cracks. A technical flowchart of this paper is shown in Figure 1.

2 Materials

The base asphalt binder used in this study was SK-70 road petroleum asphalt binder. SBS used in this study was T161B linear SBS produced by Xinjiang Dushanzi Petrochemical Company, and its block ratio was 30:70. In this study, 80 mesh CR was used, and C9PR used in this study was produced by Shandong Yousuo Chemical Technology Co., Ltd. Modified asphalt binders

FIGURE 1
Experimental flow diagram.
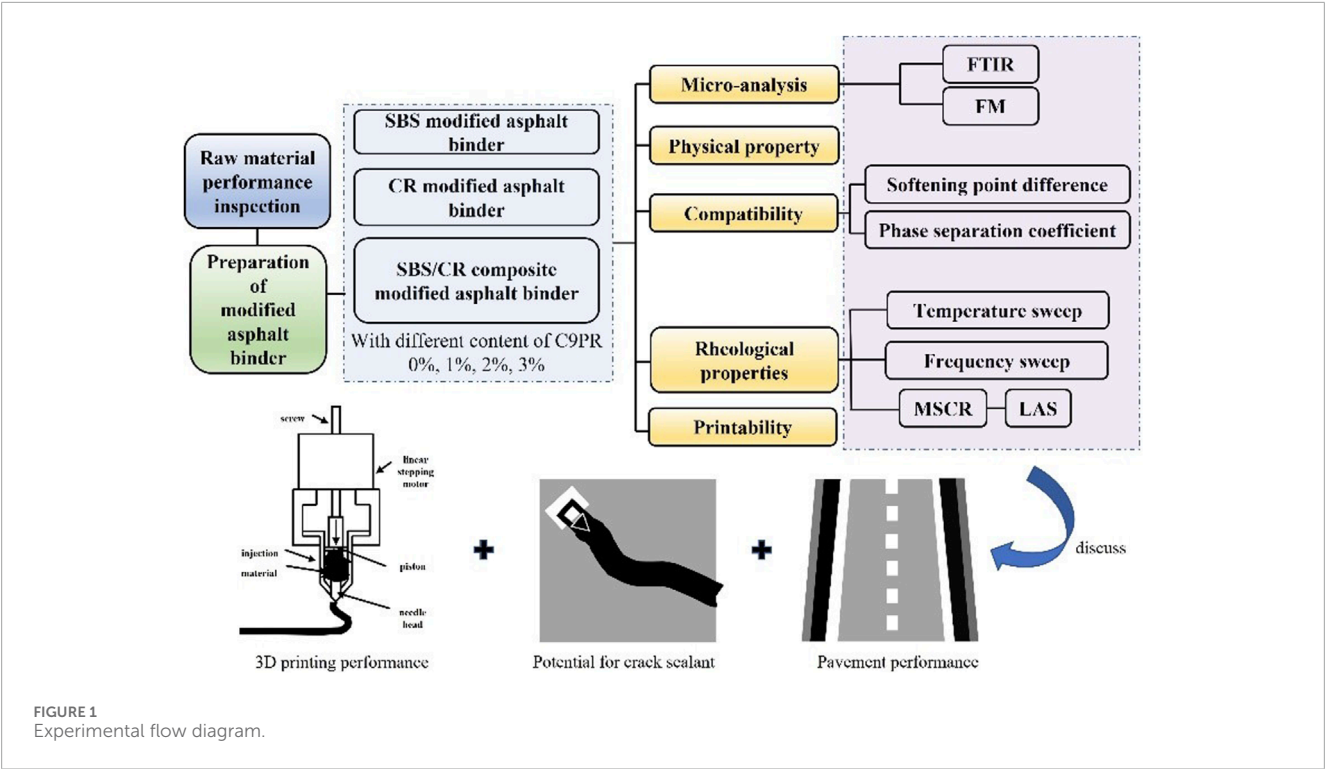
were prepared with C9PR of 0 wt%, 1 wt%, 2 wt%, and 3 wt%, respectively.

(1) The base asphalt binder was heated to approximately 200°C. After adding 15 wt% CR, it was quickly heated to 220°C and sheared at a high speed of 5,000 r/min for 1 h. This step needs to be omitted for modified asphalt binders with SBS alone (Cai et al., 2014; Presti, 2013; Presti et al., 2012).

(2) The base (or modified) asphalt binder was cooled (or heated) to approximately 175°C; 3 wt% SBS and C9PR with different contents were added; and after keeping temperature dissolved for 30 min, the asphalt binder was sheared at a high speed of 5,000 r/min for 1 h.

(3) Then, a 0.15-wt% sulfur stabilizer was added to the modified asphalt binder, and the binder was sheared at a high speed of 5,000 r/min for 20 min.

(4) Finally, the asphalt binder sample was heated in an oven at 165 C for 30 min.

The abbreviated name of each modified asphalt binder sample is shown in Table 1.

3 Measurement

3.1 Fourier-transform infrared spectroscopy

In this study, Fourier-transform infrared (FTIR) spectroscopy was conducted using a Bruker TENSOR II FTIR spectrometer equipped with a reflection diamond ATR accessory. Scans within wavenumbers ranging from 400 cm^{-1} to 4,000 cm^{-1} were obtained

TABLE 1 Detailed information about asphalt binders.

Designation	Asphalt binder
BA	Base asphalt binder
S_3	3 wt% SBS
S_3C_1	3 wt% SBS + 1 wt% C9PR
S_3C_2	3 wt% SBS + 2 wt% C9PR
S_3C_3	3 wt% SBS + 3 wt% C9PR
R_{15}	15 wt% CR
$R_{15}C_1$	15 wt% CR + 1 wt% C9PR
$R_{15}C_2$	15 wt% CR + 2 wt% C9PR
$R_{15}C_3$	15 wt% CR + 3 wt% C9PR
S_3R_{15}	3 wt% SBS + 15 wt% CR
$S_3R_{15}C_1$	3 wt% SBS + 15 wt% CR + 1 wt% C9PR
$S_3R_{15}C_2$	3 wt% SBS + 15 wt% CR + 2 wt% C9PR
$S_3R_{15}C_3$	3 wt% SBS + 15 wt% CR + 3 wt% C9PR

and averaged for each sample. The intensity of the FTIR spectrum can be plotted as the percentage of light transmittance or absorbance at each wavenumber. The spectrum baseline correction was performed using OMNIC software.

3.2 Fluorescence microscopy

In this study, the Imager.Z2 electric fluorescence microscope (FM) of Carl Zeiss Optics Co., Ltd., Germany, was used to excite the asphalt binder samples by using an ultraviolet light source with a short wavelength and high frequency filtered by a point-light source of high-efficiency light emittance, and the micro-morphological characteristics of each modified asphalt binder sample were observed. The dispersion effect of the modifier and its compatibility with the asphalt binder were analyzed and evaluated. The samples were observed at an ambient temperature and 200× magnification.

3.3 Physical properties

In this study, the 25-C penetration, softening point, 15-C ductility, and rotational viscosity of modified asphalt binders were tested according to the Standard Test Methods of Bitumen and Bituminous Mixture for Highway Engineering (JTG E20-2011). The elastic recovery rate and cone penetration of the modified asphalt binders were tested according to the Standard Test Method of Hot-poured Sealants for Pavement (JT/T 740-2015).

3.4 Compatibility

The phase separation of polymer-modified asphalt binders is a serious issue in the asphalt binder industry. Therefore, a hot storage test is necessary to characterize the high-temperature storage stability of modified binders during transportation and storage periods. Experimental methods and analytical approaches were combined with Chinese Standard JTG E20-2011 and European Standard EN 13399 methods. Approximately 35 g modified binder was poured into an aluminum cigar tube (32-mm diameter and 160-mm height), and then, the tube was sealed carefully using pliers. The tube was moved to an oven and kept vertically at 163°C ± 5°C for 48 h. Then, the cigar tube was taken out of the oven and cooled in a refrigerator at 5°C for 4 h. Subsequently, the frozen cigar tubes were cut into three equal sections. The samples from the top and bottom sections were utilized and evaluated for storage stability using the softening point test (experimental methods and equipment follow JTG E20-2011) (Galooyak et al., 2010; Hallmark-Haack et al., 2019; Leng et al., 2018; Qian et al., 2018; Qian et al., 2019) and segregation index (SI) [obtained from the dynamic shear rheometer (DSR) test results]. SI was defined as the following equation (Hallmark-Haack et al., 2019; Hosseinnezhad et al., 2019; Kabir et al., 2020; Li Z. et al., 2019; Xu et al., 2017; Yu et al., 2018):

$$SI = \frac{\left(\frac{G^*}{\sin \delta}\right)_{max} - \left(\frac{G^*}{\sin \delta}\right)_{avg}}{\left(\frac{G^*}{\sin \delta}\right)_{avg}},$$

where $(G^*/\sin\delta)_{max}$ is the higher value of either the top or bottom section of the cigar tube and $(G^*/\sin\delta)_{avg}$ is the average value of both sections. G^* and δ were measured using the Superpave 102 DSR. The test temperature was set to 60°C, the shear strain was set to 0.1%, and the loading frequency was 10 rad/s. The smaller the SI value, the better the compatibility between the modifiers and asphalt binders.

3.5 Temperature sweep

The temperature scanning program in the DSR was used to test the high-temperature deformation resistance of modified asphalt binders. In this test, a flat rotor with a diameter of 25 mm was selected. The flat gap was 1 mm; the test temperature was set at 30°C, 40°C, 50°C, 60°C, 70°C, and 80°C; the strain level was 0.1%; and load frequency was fixed at 10 rad/s. The phase angle and rutting factor were used to evaluate the shear deformation resistance and high-temperature performance of the modified asphalt binders.

3.6 Frequency sweep

The frequency scanning test program in the DSR was used to test the modified asphalt binder samples to obtain the rheological parameters of asphalt binder samples at different loading frequencies, loading temperatures, and shear stress levels. In the frequency scanning test program, a 25-mm parallel plate was selected for the test rotor, and the plate gap was 1 mm. The load frequency range was 0.1 Hz ~ 100 Hz; the temperature range was 30°C, 40°C, 50°C, 60°C, 70°C, and 80°C; and the shear strain value was controlled to be 0.1%. According to test results, the Williams–Landel–Ferry (WLF) function was used to fit displacement factors of all samples with 35°C as a reference temperature, and the generalized logistic sigmoidal model was used to fit the complex shear modulus and phase angle based on the time–temperature superposition principle (Rowe and Sharrock, 2009; Yusoff et al., 2011).

3.7 Multiple stress creep–recovery

The multiple stress creep–recovery (MSCR) test is used to characterize modified asphalt binders and has good correlations with asphalt mixture rutting. The MSCR test was performed on a DSR to test elastic recovery behavior and stress-dependent behavior at 64°C under a creep stress of 0.1 kPa and 3.2 kPa, following AASHTO MP 19. Before the test, all asphalt binders were subjected to the short-term aging treatment (Rolling Thin-Film Oven Test, RTFOT). Two stress levels of 0.1 kPa and 3.2 kPa were used, of which 20 creep (1 s)–recovery (9 s) cycles were performed at the stress level of 0.1 kPa, and 10 cycles were performed at the stress level of 3.2 kPa for a total of 300 s. The stress-dependent behavior and unrecoverable behavior of binders were characterized by the creep characteristics of samples during the 100 s–300-s loading cycle.

3.8 Linear amplitude sweep

According to AASHTO TP101, the fatigue performance of the modified asphalt binders was studied by the linear amplitude scanning (LAS) test. LAS test samples were all asphalt binder samples after 20 h of pressure aging vessel (PAV). DSR equipment was used in this test, and the temperature was set to 25°C. The LAS test program mainly includes two stages. In the first stage,
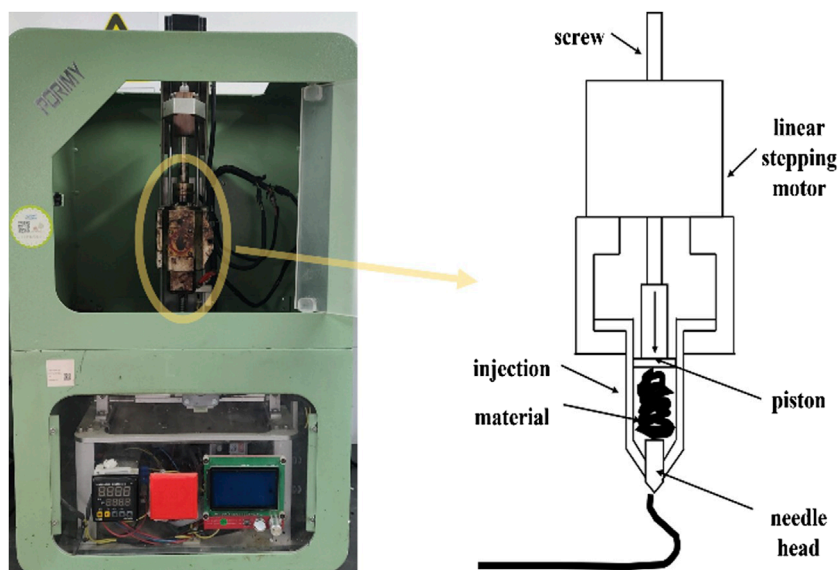
FIGURE 2
3D printer: internal structure and key equipment.

a frequency scan with a constant shear strain amplitude of 0.1% was applied to the samples, and the loading frequency range was 0.2 Hz~30 Hz to obtain the undamaged rheological properties of asphalt binder samples in the LVE range. In the second stage, amplitude scanning was performed on the samples to obtain the damage characteristics of asphalt binder samples, in which the oscillatory shear strain increased linearly from 0% to 30% within 5 min at a loading frequency of 10 Hz. After the test, the predicted fatigue life of each modified asphalt binder was calculated by VECD theory (Park et al., 1996).

3.9 3D printing

The 3D printer used in this study is a plunger extruder and is shown in Figure 2. The printer is designed as a three-axis system, in which the needle head is moved by a single-stepper motor to print to a flat plate. The printer is composed of an extrusion plunger, a stepper motor driving the screw, a heating barrel, and a printing needle head. The maximum print size is 100 mm × 100 mm × 50 mm.

4 Results and discussion

4.1 FTIR analysis

The FTIR spectroscopy results and functional groups corresponding to the characteristic absorption peaks of C9PR, BA, and each modified asphalt binder are shown in Figure 3 and Table 2, respectively. Figure 3A shows that the absorption peak of C9PR at 3,445 cm^{-1} is the stretching vibration absorption peak of -OH. The absorption peak at 3,000~3,100 cm^{-1} is the stretching vibration absorption peak of olefin C-H and aromatic compound C-H. The absorption peak at 2,900~3,000 cm^{-1} is the antisymmetric stretching vibration absorption peak of -CH2-. The absorption peak at 1,500~1,700 cm^{-1} is the vibration absorption peak of the olefin double bond and benzene ring skeleton. The absorption peak at 1,479 cm^{-1} is generated by the vibration of the C-S bond, indicating that C9PR contains other impurity atoms in addition to C and H. The absorption peak at 1,032 cm^{-1} is the sulfoxide absorption peak. The absorption peak at 748 cm^{-1} is the absorption peak of the substituent on the benzene ring. The absorption peak at 699 cm^{-1} is the C-H vibration absorption peak on the benzene ring of the polystyrene segment.

Figures 3B–D show that the infrared spectrum of the SBS-modified asphalt binder has obvious absorption peaks at 966 cm^{-1} and 699 cm^{-1}, which is the result of C-H vibration on the carbon–carbon double bond of the polybutadiene segment and benzene ring of the polystyrene segment in the SBS component, respectively. Compared with the single-modifier-modified asphalt binder, the SBS/CR composite-modified asphalt binder has no new characteristic peak, but the absorption peak intensity at 1,600, 1,455, 1,375, 966, and 699 cm^{-1} is weakened, which indicates that in the process of SBS and CR composite modification, chemical reactions mainly occur on the conjugated double bond on the benzene ring, i.e., -CH$_3$, -CH$_2$-, -C=C-, and C-H on the benzene ring, among which the absorption peak intensity at 966 cm^{-1} (-C=C-) changes most obviously. This is because -C=C- is unstable, easily opens during heating and shearing, and has strong activity after opening, thus undergoing a branching reaction with CR.

With the increase in the C9PR content, no new characteristic peaks appeared in each modified asphalt binder, indicating that the modification effect of C9PR on each modified asphalt binder was physical and no chemical change occurred. With the increase in

FIGURE 3
FTIR spectra of C9PR, BA, and modified asphalt binders. **(A)** C9PR and BA. **(B)** SBS-modified asphalt binder. **(C)** CR-modified asphalt binder. **(D)** SBS/CR composite-modified asphalt binder.
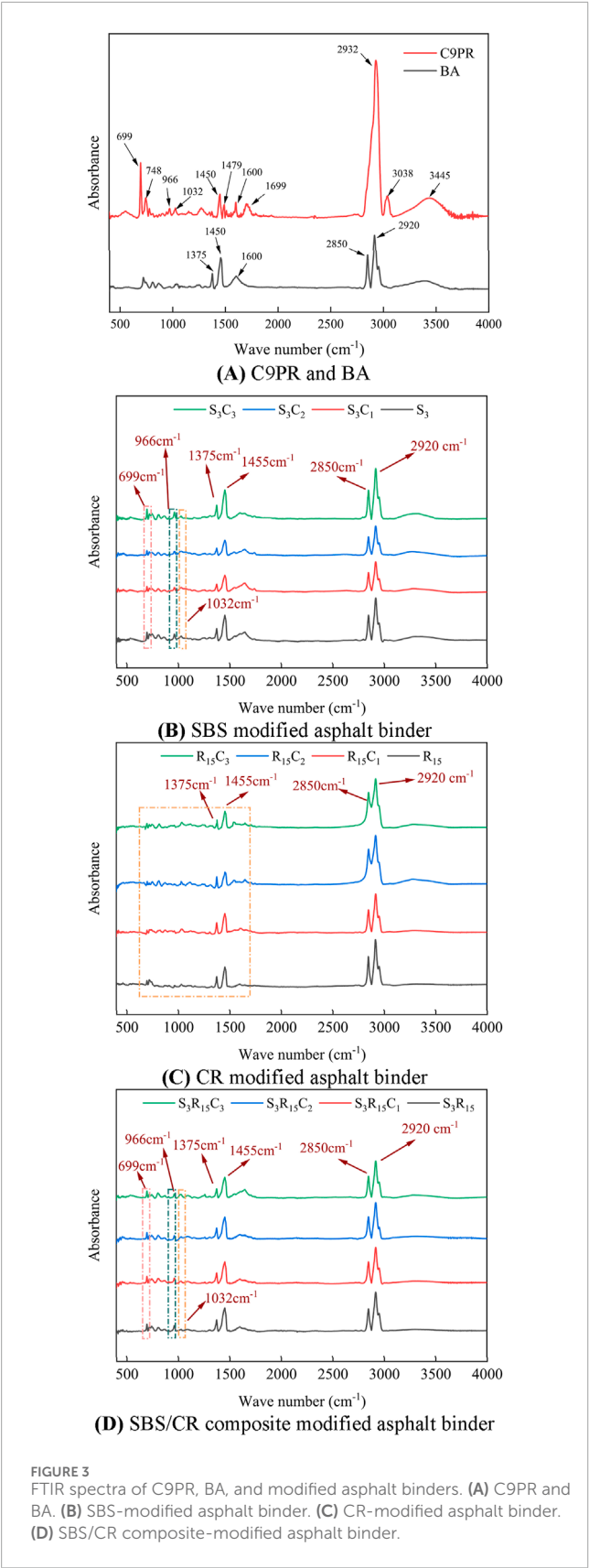
the C9PR content, the peak area at 900~650 cm^{-1} of each modified asphalt binder increased slightly, indicating that C9PR introduced aromatics into the modified asphalt binder system.

TABLE 2 Location of absorption peaks and corresponding functional groups in the infrared spectra of modified bituminous binders (Hou et al., 2018).

Peak position/cm^{-1}	Functional groups and vibrational types
3,400	Stretching vibration of -OH
2,920	Antisymmetric stretching vibration of -CH$_2$-
2,850	Symmetric stretching vibration of -CH$_2$-
1,600	Conjugated double bond (benzene ring backbone vibration)
1,455	-C-H stretching vibration in CH$_3$ (variable angle vibration)
1,375	C-H surface stretching vibration (bending vibration) in -CH$_2$-
1,032	Sulfinyl group -S=O
966	Polybutadiene segment -C=C-
813	C-H out-of-plane bending vibration on the benzene ring
699	C-H vibration on the benzene ring of the polystyrene segment

4.2 FM analysis

FM images of each modified asphalt binder magnified 200 times are shown in Figure 4. Comparing images of each sample showed that the different fluorescence characteristics of BA and polymer modifiers lead to obvious color differences between two phases in a miscible system. The brighter fluorescence points are various modifier particles, while C9PR and BA are similar in color under the fluorescence microscope. Figures 4A–D show that SBS modifier particles are large, and the dispersion in the asphalt binder is not uniform. However, with the increase in C9PR incorporation, the size of SBS particles gradually decreases, and the distribution gradually becomes uniform.

From Figures 4E–L, it can be found that CR-modified asphalt binder and SBS/CR composite-modified asphalt binder showed similar rules. This may be because C9PR, which is rich in aromatics, can promote the swelling of SBS and CR in the asphalt binder, thus promoting the swelling of modifier particles in the preparation process of modified asphalt binders. Particles are sheared into smaller particles at high speed, which ultimately increases the dispersion and compatibility of each modifier in the asphalt binder. Therefore, C9PR shows potential to be an additive used to increase the 3D printing performance of modified asphalt binders.

4.3 Physical property analysis

Table 3 shows that with the increase in C9PR content, the penetration and cone penetration of each modified asphalt binder decrease. The softening point of each modified asphalt binder
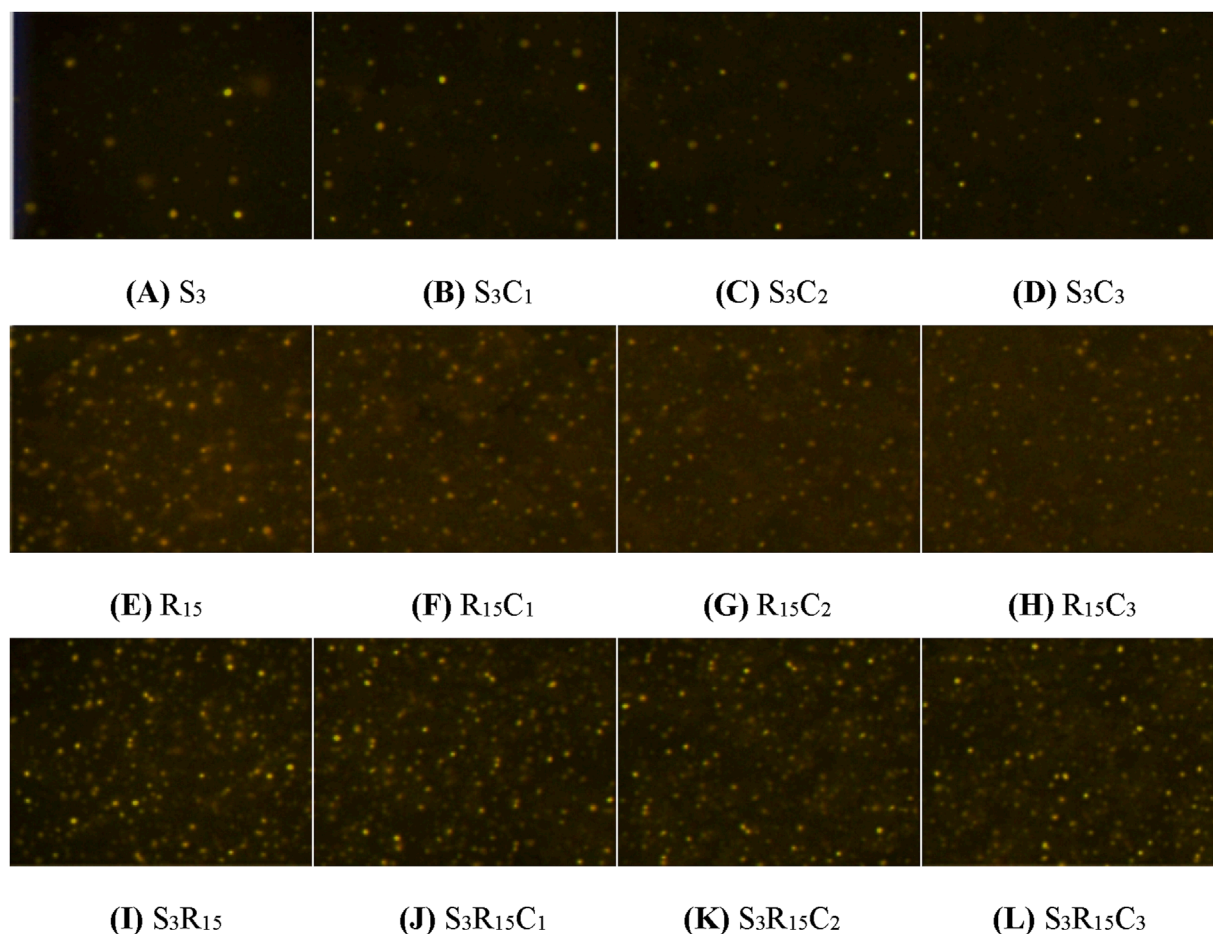
FIGURE 4
FM images of each modified asphalt binder. **(A)** S_3. **(B)** S_3C_1. **(C)** S_3C_2. **(D)** S_3C_3. **(E)** R_{15}. **(F)** $R_{15}C_1$. **(G)** $R_{15}C_2$. **(H)** $R_{15}C_3$. **(I)** S_3R_{15}. **(J)** $S_3R_{15}C_1$. **(K)** $S_3R_{15}C_2$. **(L)** $S_3R_{15}C_3$.

increases with the increase in C9PR content, but the increasing trend gradually weakens. This may be because C9PR is rich in aromatic components, and the addition of a small amount can improve the dispersion of polymer copolymers and the uniform dispersion of modifiers. However, when the C9PR content exceeds a certain level, the enhancement effect of the polymer copolymer on modified asphalt binders is less than the compatibility effect of the aromatic component. In this case, the improvement of C9PR on the high-temperature stability of the modified asphalt binder is limited.

Rotational viscosity at 135°C of the single SBS or CR-modified asphalt binder is much smaller than that of the SBS/CR composite-modified asphalt binder, indicating that the performance of the composite-modified asphalt binder is better. The increase in the rotational viscosity of asphalt binders caused by the addition of 1 wt% C9PR may be due to the compatibilization effect of C9PR on SBS- and CR-modified asphalt binders, which promotes the performance of the modified asphalt binder. Viscosity reduction caused by C9PR with more than 1% content may be due to the excessive compatibilization of aromatics, which weakens the crosslinking effect between macromolecules, resulting in a decrease in viscosity.

With the increase in C9PR content, the ductility and elastic recovery rate of modified asphalt binders decreased slightly, and the decrease rate increased. This may be because C9PR has a rigid side-chain benzene ring. With the increase in C9PR content, modified asphalt binders show greater brittleness at low temperature, and elastic properties and low-temperature ductility are also affected.

According to JT/T 740–2015, the requirements of a high-temperature sealant are as follows: softening point ≥90°C, cone penetration ≤70 (0.1 mm), and elastic recovery 30%~70%. Combined with specification, it can be found that single-modifier-modified asphalt binders do not meet the technical requirements of various sealants in the specification, while composite-modified asphalt binders with any content of C9PR can meet the specification requirements of a high-temperature sealant.

4.4 Compatibility analysis

SBS and CR are incompatible with asphalt binder thermodynamics, and segregation will occur during storage, which will affect the road performance of the modified asphalt binder and printability as a 3D-printed asphalt binder. Therefore, based on the

TABLE 3 Physical properties of modified asphalt binders.

Asphalt binder sample	Softening point, °C	Penetration at 25°C, 0.1 mm	Ductility at 15°C, cm	Rotational viscosity at 135°C, Pa·s	Elastic recovery rate, %	Cone penetration, 0.1 mm
S_3	76.0	68.0	51.0	0.99	48.4	69.7
S_3C_1	78.0	67.0	50.0	1.36	48.0	68.1
S_3C_2	79.3	66.1	48.0	1.18	47.0	67.6
S_3C_3	79.2	65.4	45.0	0.86	45.5	67.0
R_{15}	71.0	69.0	57.0	0.91	43.6	70.1
$R_{15}C_1$	74.0	68.0	56.0	1.21	43.3	69.0
$R_{15}C_2$	76.7	66.8	53.0	1.01	42.9	68.3
$R_{15}C_3$	76.8	66.2	47.0	0.78	41.7	67.7
S_3R_{15}	88.0	46.0	34.2	3.51	47.4	50.4
$S_3R_{15}C_1$	90.1	43.0	33.2	4.09	47.0	49.0
$S_3R_{15}C_2$	90.6	42.0	31.0	3.81	46.2	48.3
$S_3R_{15}C_3$	90.6	41.0	27.1	3.08	45.3	47.2

segment test, the effect of C9PR on the compatibility of SBS-, CR-, and composite-modified asphalt binders was evaluated by the softening point difference method and phase separation coefficient method, respectively.

The softening point difference of each modified asphalt binder is shown in Figure 5A. The results show that the softening point difference of the single SBS-modified asphalt binder and SBS/CR composite-modified asphalt binder does not satisfy the requirements of segregation softening point difference less than 2.5°C in the specification without adding C9PR. With the increase in C9PR content, the softening point difference of each asphalt binder sample showed a decreasing trend, indicating that C9PR played a positive role in the compatibility of modified asphalt binders. The compatibility effect of C9PR on the modifier and asphalt binders decreases with increasing content, which may indicate that for 3 wt% SBS and 15 wt% CR, the compatibility effect of 2 wt% C9PR is not much different from that of 3 wt% C9PR, and the compatibility effect of C9PR gradually approaches saturation.

However, some scholars believe that the softening point difference test is simple to operate and has poor detection sensitivity (Yu et al., 2018). When evaluating the compatibility of the polymer modifier and petroleum asphalt binders, the phase change in the heat storage process of the two-phase system cannot be detected. Polymer-modified asphalt binder is a viscoelastic material. The dynamic mechanical method based on rheology is very suitable to detect differences between the petroleum asphalt binder and polymer modifier. Therefore, some researchers have proposed a phase separation coefficient based on rheological test methods to evaluate the compatibility of the polymer modifier and petroleum asphalt binder (Hallmark-Haack et al., 2019; Hosseinnezhad et al.,

2019; Kabir et al., 2020; Li J. et al., 2019; Xu et al., 2017; Yu et al., 2018). The degree of phase separation of the polymer modified asphalt binder calculated quantitatively by the phase separation coefficient (Equation 1) is shown in Figure 5B. With the addition of C9PR, the SI of each modified asphalt binder sample showed a decreasing trend, which indicated that the addition of C9PR was favorable to the compatibility of SBS and CR in the asphalt binder, thus improving the high-temperature storage stability of modified asphalt binders. It is worth noting that when the C9PR content increased from 0% to 3%, the SI value of S_3C_1 decreased by 7.95% compared with S_3, the SI value of S_3C_2 decreased by 5.61% compared with S_3C_1, and the SI value of S_3C_3 decreased by 2.73% compared with S_3C_2, and the CR-modified asphalt binders and SBS/CR composite-modified asphalt binders also showed a similar pattern. The trend of the SI graph is similar to that of the softening point difference graph. This proves the conclusion of the softening point difference test, i.e., C9PR promotes the compatibility of SBS, CR, and BA, and the compatibilization effect is closely related to the content of the modifier and its own content.

4.5 Temperature sweep analysis

4.5.1 Phase angle analysis

In Superpave specification, the phase angle is defined as the time lag between strain and stress under traffic loads, which is highly dependent on temperature and loading frequency. It can be used as an indicator of the viscosity and elasticity of binders. When the phase angle is close to 90°, the asphalt binder tends to exhibit the behavior of a viscous liquid, and there is no obvious elastic effect.

FIGURE 5
Compatibility analysis of each modified asphalt binder sample. **(A)** Softening point difference **(B)** Separation.
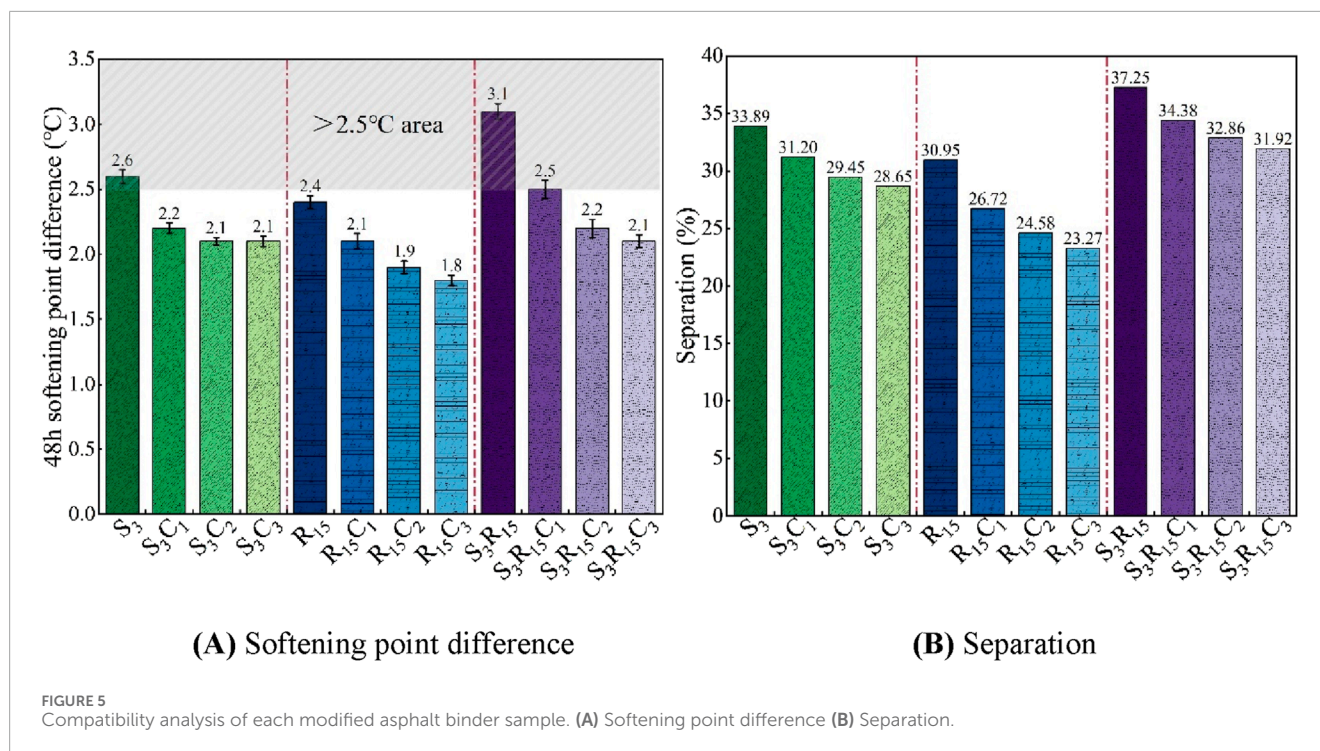
The relationship curve of the phase angle of each asphalt binder sample with temperature change is shown in Figure 6A. It can be seen that the trend of the phase angle of SBS-modified asphalt binders and CR-modified asphalt binders with temperature change is similar to that of BA, and both show a gradual upward trend with the increase in temperature. However, when the temperature reaches 60°C, the phase angles of S_3R_{15}, $S_3R_{15}C_1$, $S_3R_{15}C_2$, and $S_3R_{15}C_3$ peaks show an abnormal downward trend. This may be because under high-temperature conditions, the network-reinforced structure formed by the polymer dominates the rheological response of the binder and increases the friction between asphalt binder molecules. This resists the viscous flow of asphalt binders. In addition, when the content of C9PR is 1%, modified asphalt binders show a lower phase angle at different temperatures, but when the content of C9PR exceeds 1%, the phase angle increases slowly, indicating that the addition of excessive C9PR reduces the viscosity and elastic properties of modified asphalt binders.
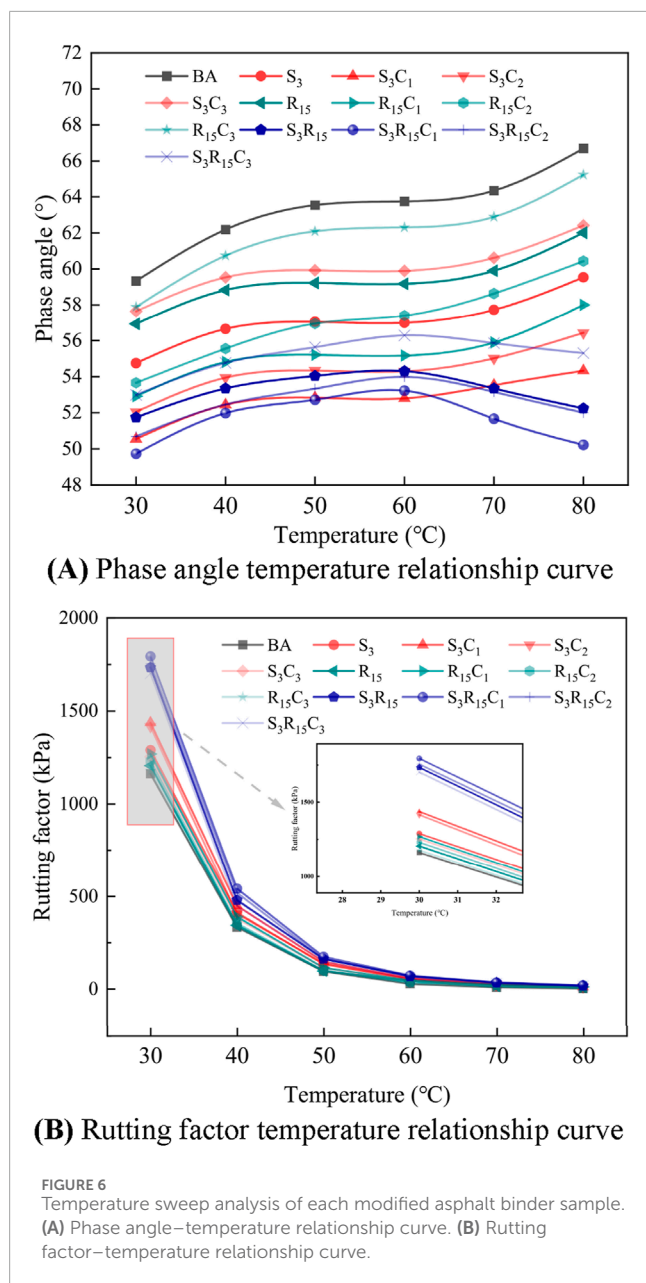
4.5.2 Rutting factor analysis

To characterize the anti-rutting performance of the prepared asphalt binder samples, the trend curve of each asphalt binder rutting factor ($G^*/\sin\delta$) with temperature was plotted, as shown in Figure 6B. Figure 6B shows that the rutting factor decreases with the increase in temperature. In the case of high temperature, asphalt binders exhibit almost pure viscous liquid behavior, poor deformation resistance, and inability to better resist external pressure, thus becoming more prone to deformation. Under the condition of the same temperature, the type and content of the modifier have an obvious influence on the rutting factor. The experimental results showed that the order of high-temperature rutting resistance of each modified asphalt binder sample is as follows: $S_3R_{15}C_1 > S_3R_{15}C_2 > S_3R_{15} > S_3R_{15}C_3 > S_3C_1 > S_3C_2 >$

$S_3 > R_{15}C_1 > S_3C_3 > R_{15}C_2 > R_{15} > R_{15}C_3 > BA$. This shows that for 3 wt% SBS and 15 wt% CR, C9PR has a critical blending value between 0% and 2%. When the content of C9PR reaches this critical value, the high-temperature anti-rutting performance of the composite-modified asphalt binder can be maximum. Once the content of C9PR exceeds this critical value, the high-temperature anti-rutting performance of the composite-modified asphalt binder will be weakened. This is consistent with the results of previous high-temperature PG classification.

4.6 Frequency sweep analysis

A temperature of 35°C was selected as the reference for drawing the master curve. Master curves of the complex shear modulus and phase angle corresponding to each modified asphalt binder sample are shown in Figure 7. Figure 7A shows that the increase in reduction frequency leads to the increase in complex shear modulus. In a low-frequency domain, the difference in the complex shear modulus of each sample is obvious. It can be found that BA has the smallest shear resistance in the same temperature and frequency range. The addition of SBS and CR will cause the master curve of the complex modulus to move up, which means that the addition of SBS or CR can improve the shear resistance of the modified asphalt binder. When the content of C9PR in each modified asphalt binder gradually increases from 0% to 3%, the master curve shows a trend of moving up first and then decreasing, which indicates that the excessive addition of C9PR has a negative impact on the deformation resistance of composite asphalt binders.

Figure 7B shows that the phase angle of each modified asphalt binder sample shows an approximately linear downward trend with the increase in the reduction frequency. In all samples, the phase

(A) Phase angle temperature relationship curve

(B) Rutting factor temperature relationship curve

FIGURE 6
Temperature sweep analysis of each modified asphalt binder sample.
(A) Phase angle−temperature relationship curve. **(B)** Rutting
factor−temperature relationship curve.

(A) Complex modulus master curve

(B) Phase angle master curve

FIGURE 7
Frequency sweep analysis of each modified asphalt binder sample at
35°C. **(A)** Complex modulus master curve. **(B)** Phase angle
master curve.

angle of BA is the largest, and the phase angle of $S_3R_{15}C_1$ is the smallest. The addition of SBS and CR will lead to a downward shift in the phase angle curve, indicating that both polymers can improve the shear resistance and elastic properties of the modified asphalt binder, and it is difficult to show the shear lag effect. When the content of C9PR exceeds 1%, the curve will move up again, which is consistent with the change rule of the abovementioned complex modulus master curve.

4.7 MSCR analysis

At stress levels of 0.1 kPa and 3.2 kPa, the average recovery rate and unrecoverable creep compliance of asphalt binders for 10 creep recovery cycles are expressed as R (0.1), R (3.2), J_{nr} (0.1), and
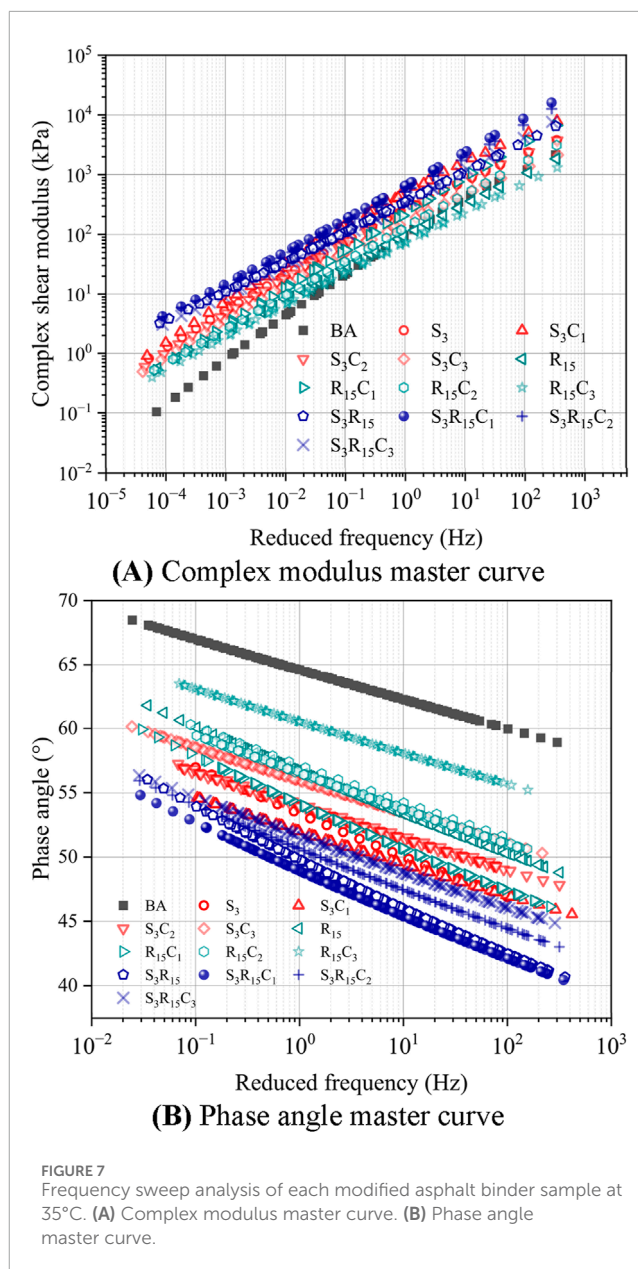
J_{nr} (3.2), respectively. R represents the percentage of recoverable strain to total strain, and J_{nr} indicates the unrecoverable residual deformation. The rutting resistance of an asphalt binder with a larger R and smaller J_{nr} is stronger.

At a temperature of 64°C, R and J_{nr} of each modified asphalt binder are shown in Figure 8. Figure 8A shows that BA has the smallest R value, while the R value of the SBS/CR composite-modified asphalt binder is higher, which indicates that the SBS and CR composite can effectively improve the creep recovery ability of the asphalt binder. The test result of non-recoverable creep compliance of each sample is opposite to that of the creep recovery rate, as shown in Figure 8B. The experimental results show that the SBS/CR composite-modified asphalt binder has a smaller J_{nr} value as a whole, while BA shows a higher J_{nr} value. This shows that the presence of the SBS/CR composite modifier can inhibit the generation of irreversible deformation of the asphalt binder.

(A) Average creep recovery rate and stress sensitivity **(B)** Non-recoverable creep compliance and stress sensitivity

FIGURE 8
MSCR test results. **(A)** Average creep recovery rate and stress sensitivity. **(B)** Non-recoverable creep compliance and stress sensitivity.
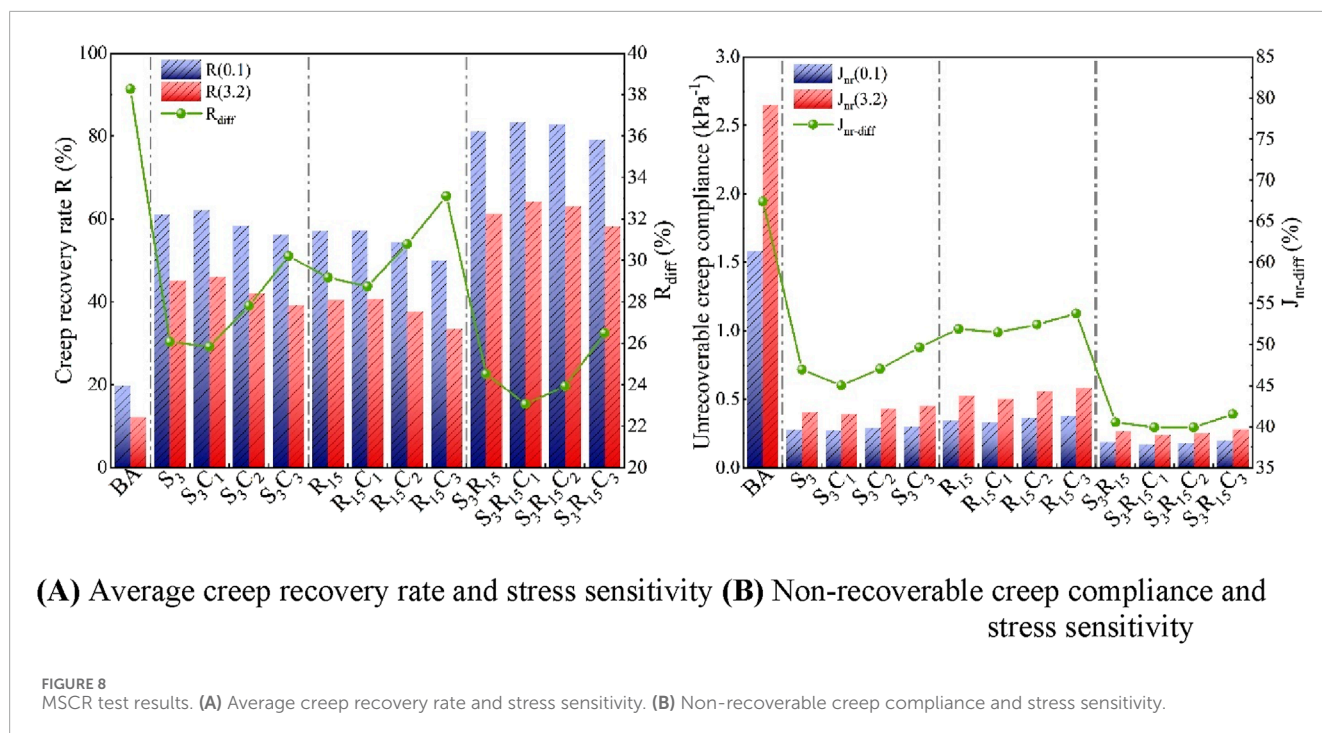
Compared with SBS, CR single modifier, and even BA, composite modifier-modified asphalt binders show more excellent anti-rutting performance.

The effect of C9PR on the high-temperature viscoelastic properties of the modified asphalt binder obtained by the MSCR test is consistent with the high-temperature rheological test results of the unaged asphalt binder. The test results show that the increase in the C9PR content at each stress level first increases and then decreases R of each modified asphalt binder sample and first decreases and then increases J_{nr}. This shows that based on the modified asphalt binder with 3 wt% SBS and 15 wt% CR, C9PR has an optimal content in the range of 0%~2%. When the content of C9PR is optimal, C9PR plays a dominant role in compatibilization between the modifier and asphalt binder. At this time, the role of C9PR in the modified asphalt binder system is equivalent to enhancing the high-temperature elasticity of the modified asphalt binder, which is reflected in the increase in the R value and the decrease in the J_{nr} value. When C9PR exceeds its optimum content, the material properties of C9PR itself lead to a brittleness enhancement effect of the modified asphalt binder higher than the elasticity enhancement effect, which eventually leads to the decrease in the creep recovery ability and the increase in non-recoverable complex creep compliance.

To further characterize the sensitivity of each asphalt binder sample to load size, the stress sensitivity (R_{diff} and $J_{nr\text{-}diff}$) of non-recoverable creep compliance and the creep recovery rate of different binders were calculated, and the calculation results are shown in Figure 8. It can be found that $S_3R_{15}C_1$ presents the smallest R_{diff} and $J_{nr\text{-}diff}$ values, while BA has the largest R_{diff} and $J_{nr\text{-}diff}$ values, which indicates that the contents of SBS, CR, and C9PR can make the nonlinear viscoelasticity of the asphalt binder more significant. $S_3R_{15}C_1$ has a more prominent low stress sensitivity, indicating that the addition of an appropriate amount of C9PR

content can make the polymer-modified asphalt binder have a more stable structure under the action of shear load.

4.8 LAS analysis

The predicted fatigue life of each asphalt binder sample calculated at two strain levels is shown in Figure 9. Under the condition of 2.5% strain, the predicted fatigue life of the single SBS-modified asphalt binder is higher than that of the single CR-modified asphalt binder, which indicates that the effect of a low content of CR on the fatigue resistance of asphalt binder is weaker than that of SBS. The fatigue life of S_3R_{15} is 5.22 times and 6.21 times higher than that of S_3 and R_{15}, respectively, which indicates that the compound content of the modifier has a great effect on the fatigue resistance of the asphalt binder. Under the condition of 5% strain, the fatigue life of each binder sample is greatly reduced, and the relationship between the fatigue lives of each asphalt binder is highly consistent with the 2.5% strain level. In general, the addition of the SBS/CR composite modifier is beneficial to improve the fatigue resistance of the asphalt binder, and this improvement effect is also prominent at a low strain level and high strain level.

The LAS test showed that the effect of C9PR on the predicted fatigue life of each modified asphalt binder was related to the dosage. Under the condition of 2.5% strain, N_f of SBS-modified asphalt binders, CR-modified asphalt binders, and SBS/CR composite-modified asphalt binders with 1 wt% C9PR increased by 3.45%, 2.10%, and 6.53%, respectively, compared with those without C9PR. When the content of C9PR is 3%, S_3C_3, $R_{15}C_3$, and $S_3R_{15}C_3$ are 5.90%, 10.01%, and 3.10% lower than S_3, R_{15}, and S_3R_{15}, respectively. The fatigue life of each modified asphalt binder increases first and then decreases with the increase in C9PR content, which is
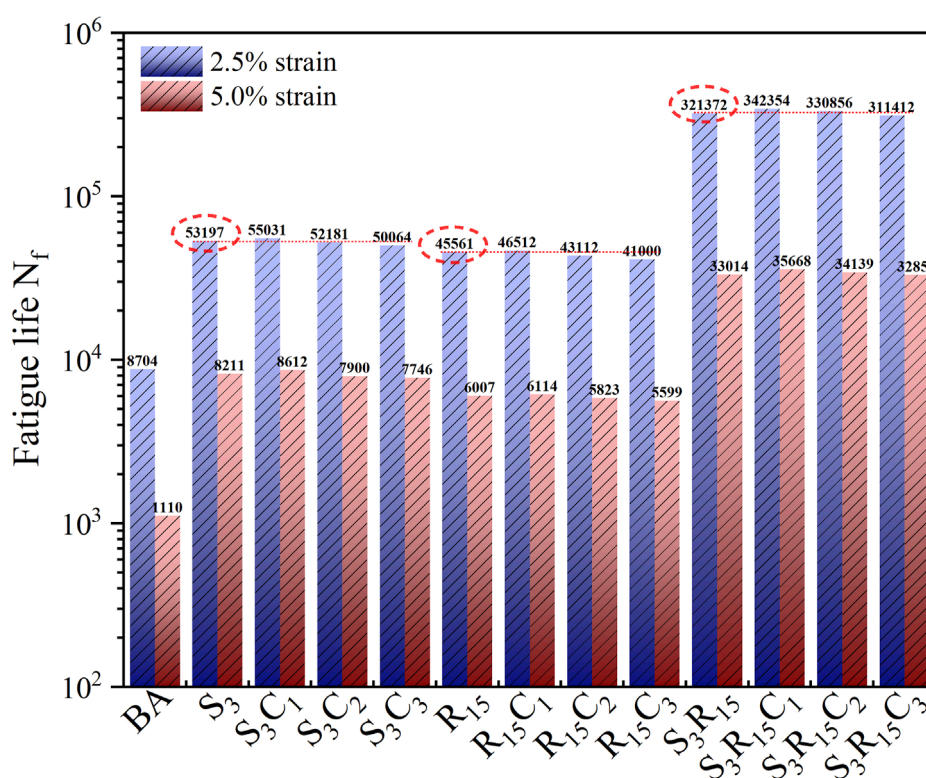
FIGURE 9
LAS test results.

consistent with the influence of C9PR on the high-temperature performance of the modified asphalt binder.

It is worth noting that when the strain condition is 2.5% and the content of C9PR is 2%, N_f of S_3C_2 and $R_{15}C_2$ is 1.91% and 5.38% lower than that of S_3 and R_{15}, respectively, indicating that the effect of 2 wt% C9PR on the fatigue life of asphalt binder exceeded the effect of 3 wt% SBS or 15 wt% single-modifier CR on the performance of the asphalt binder. N_f of $S_3R_{15}C_2$ increased by 2.95% compared with S_3R_{15} and still maintained a slight enhancement effect, which indicated that the improvement effect of C9PR on the modified asphalt binder was related to the content and type of other modifiers.

Under the condition of 5% strain, the fatigue life of each binder sample is greatly reduced, and the relationship between the fatigue lives of each modified asphalt binder is highly consistent with the 2.5% strain level. In general, the addition of SBS, CR, and an appropriate amount of C9PR content is beneficial to improve the fatigue resistance of the asphalt binder, and this improvement effect is also prominent at a low strain level and high strain level.

## 4.9 Analysis of the 3D printing performance of composite-modified asphalt binders

The plunger extruder used in this study softens asphalt binders by simultaneously heating the plunger sleeve and nozzle, and the softened asphalt binders are extruded through the nozzle by the motor-driven plunger. Before formal printing, the plunger is set

to push slowly until the filament is extruded at the nozzle. After removing the excess material wire at the nozzle, the relevant model parameters are entered in Simplify3D slicing software (Wu, 2023; Xue, 2023; Yang, 2023).

Previous laboratory research found that when the printing temperature suitable for a certain asphalt binder was not explored, the asphalt binder could not be successfully extruded no matter how the extrusion rate of the plunger and printing speed of the equipment were changed. Once the appropriate printing temperature was obtained through the test, changing the extrusion rate of the plunger and printing speed of equipment had little effect on asphalt binder formation. This shows that the influence of temperature on the 3D-printed asphalt binder is higher than the extrusion rate and printing speed. Therefore, in this study, a 0.8-mm diameter printhead was used to adjust the printing temperature and printing speed to conduct a trial printing study of the 3D printing of composite-modified bitumen with different C9PR doping levels to explore the appropriate printing temperature, as well as to evaluate the 3D printing moldability of composite-modified bitumen. Because only the composite-modified bitumen binder meets the requirements of the sealant specification, this vignette only 3D prints the composite-modified asphalt binder for the test.

4.9.1 Printing temperature

A relatively simple line segment model printing test was carried out on the composite-modified asphalt binder with different C9PR contents. The segment model and printed results are shown in
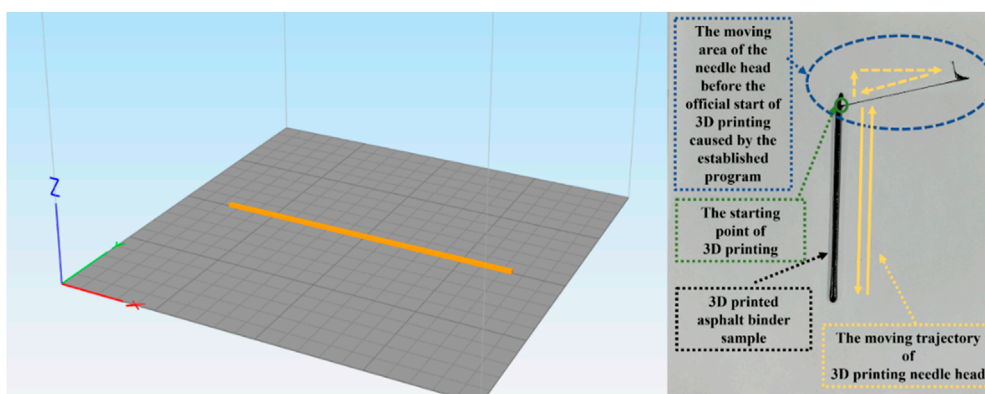
(A) Segment model for 3D printing
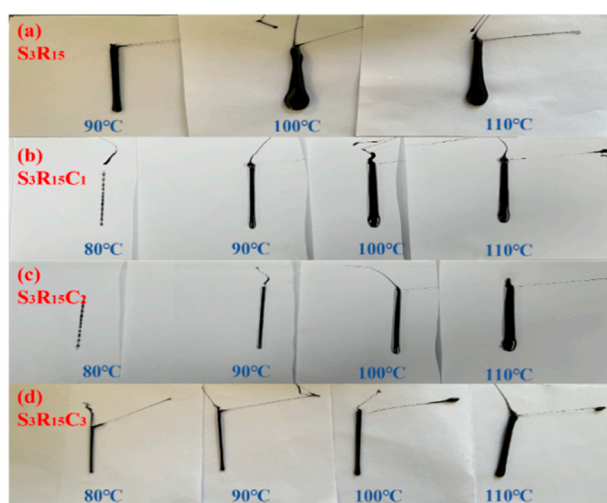
(B) Segment model printing results

FIGURE 10
Segment model and printing results of each modified asphalt binder under different temperature conditions. **(A)** Segment model for 3D printing. **(B)** Segment model printing results.

Figures 10A, B. Figure 10B shows that S_3R_{15} without C9PR failed to be successfully extruded at 80°C. At the same time, $S_3R_{15}C_1$ and $S_3R_{15}C_2$ were printed out of incoherent line segments at 80°C, which was because the asphalt binder was difficult to be extruded from the nozzle at this temperature. $S_3R_{15}C_3$ can be printed most smoothly at 80°C, which may indicate that C9PR can broaden the lower limit of temperature for the 3D-printed modified asphalt binder.

Furthermore, when the temperature increased to 90°C, segments printed by each modified asphalt binder are roughly in line with the designed model, and the thickness of line segments is relatively uniform. When temperature increases to 100°C and above, the S_3R_{15} sample segment produces obvious thickening and unevenness, while the modified asphalt binder mixed with C9PR is less affected by temperature, which indicates that C9PR has a favorable effect on the printability of the 3D-printed asphalt binder.

4.9.2 Printing speed

Print speed and the 3D printing process are a matching process; if too fast or too slow, the model cannot be printed successfully. For asphalt binder material, under a constant extrusion rate, if the nozzle moves too fast, asphalt binder material near the nozzle that has not finished adhering to the bottom will be pulled by the nozzle movement, which will affect the degree of precision of the printed object size; if the nozzle moves too slowly, it may produce a material accumulation phenomenon, which easily builds up and blocks the nozzle. According to the experimental results in the previous subsection, we consider the shape stability of the asphalt binder material extrusion; fix the printing temperature at 90°C; and select printing speeds of 2 mm/s, 4 mm/s, and 6 mm/s, respectively, to study the influence of the printing speed, i.e., the nozzle movement speed, on the 3D printability of the composite-modified asphalt binders. At the same time, we consider the existence of a certain depth and shape of the cracks in the actual application process and
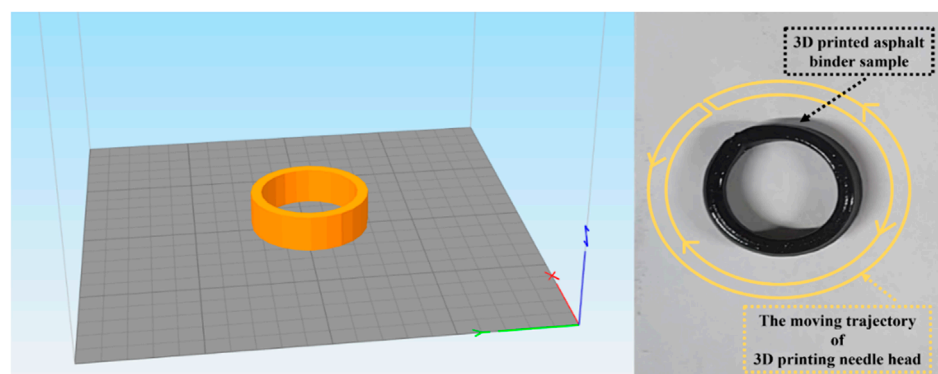
(A) Ring model for 3D printing
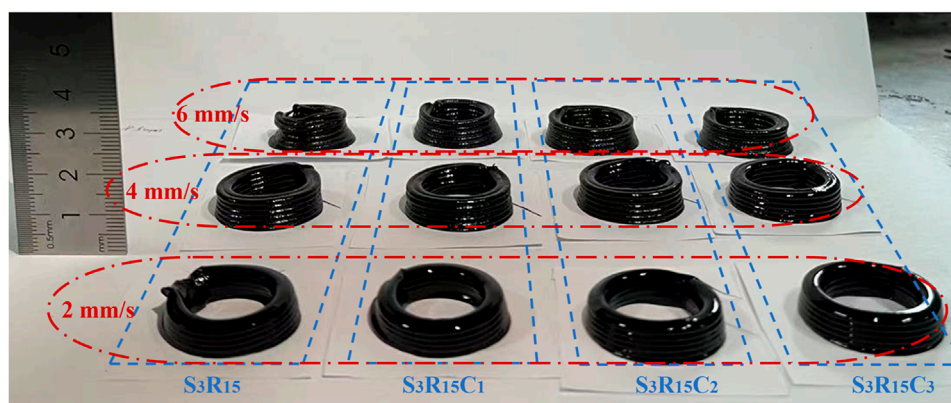
(B) Ring model printing results

FIGURE 11
Ring model and printing results of each modified asphalt binder under different temperatures. **(A)** Ring model for 3D printing. **(B)** Ring model printing results.

use circular modeling to explore the impact of printing speed on the shape of the composite-modified asphalt binder printability.

The bottom diameter of the simple circle model constructed using Simplify3D software is set to 2 cm, and the height is set to 1 cm. The model and the printing results are shown in Figures 11A, B. Figure 11B shows that the asphalt binder ring printed at a printing speed of 6 mm/s has a middle and high level of the outer wall concaved inward. To summarize the phenomenon of printing, there is, in the middle and high level of the outer wall of the asphalt binder ring, an inward depression, which is precisely because the printing speed is too fast, resulting in the new printing of asphalt binder material that has not been completely docked and adhered to the bottom of the layer. The asphalt binder material is removed from the nozzle, pulling the asphalt filament to the center of the circle to the inner movement of the outer wall of the situation caused by the invagination. When the printing speed was 4 mm/s, the shape of the printed asphalt binder circle was consistent with the model setup. When the printing speed was 2 mm/s, the asphalt binder ring tended to couch, the height became less than 1 cm, and the lines become rounded. A slight fusion of the upper and lower layers of the situation occurs, which is because the nozzle moves too slowly. However, at high temperature, the nozzle slightly softened the bottom of the asphalt binder, resulting in the slight collapse of the bottom, so that the printed asphalt binder specimens failed to reach the established height.

5 Conclusion

In this study, the impact of C9PR of 0 wt%, 1 wt%, 2 wt%, and 3 wt% on the rheological properties and 3D printability of modified asphalt binders was investigated. The key findings are as follows:

(1) FTIR and FM test results indicated that the reaction between C9PR, SBS, CR, and BA is mainly a physical reaction. C9PR can promote the swelling of SBS and CR particles in the asphalt binder, promoting compatibility by dispersing the modifier into smaller particles through high-speed shearing.

(2) $S_3R_{15}C_1$ exhibited the best high-temperature rutting resistance, elastic performance, and low-temperature ductility, but an excessive amount of C9PR weakened the performance of the modified asphalt binder.

(3) MSCR and LAS test results showed that $S_3R_{15}C_1$ maintained excellent high-temperature rutting resistance and fatigue

resistance after short-term and long-term aging. An appropriate amount of C9PR content promoted a more stable structure and improved the durability of the polymer-modified asphalt binder.

(4) The addition of C9PR facilitates smoother extrusion and molding of the SBS/CR composite-modified asphalt binder, reduces the lower limit of 3D-printable temperature, and enhances the construction and ease of use. For composite-modified asphalt binders prepared in this paper, the recommended printing temperature is 90°C, and the recommended printing speed is 4 mm/s.

In conclusion, this study investigated the effects of different contents of C9PR on the properties of the modified asphalt binder and revealed the potential application of C9PR as an additive for the 3D-printed asphalt binder. However, the optimal content of each polymer modifier and C9PR still needs to be explored. The use of modified asphalt binders for crack filling by 3D printing still needs to be practiced in engineering.

Data availability statement

The original contributions presented in the study are included in the article/Supplementary Material; further inquiries can be directed to the corresponding author.

Author contributions

YN: Methodology, Supervision, Writing–original draft, Writing–review and editing. XW: Data curation, Methodology, Writing–original draft. IB: Investigation, Writing–review and editing. DN: Methodology, Supervision, Writing–review and editing.

Funding

Conflict of interest

The authors declare that the research was conducted in the absence of any commercial or financial relationships that could be construed as a potential conflict of interest.

Publisher's note

All claims expressed in this article are solely those of the authors and do not necessarily represent those of their affiliated organizations, or those of the publisher, the editors, and the reviewers. Any product that may be evaluated in this article, or claim that may be made by its manufacturer, is not guaranteed or endorsed by the publisher.

Supplementary material

The Supplementary Material for this article can be found online at: https://www.frontiersin.org/articles/10.3389/fmats.2024.1416246/full#supplementary-material

References

Aamer, N., Minchih, L., Yangwei, Z., and Nazir, U. (2022). Design and evaluation of asphalt concrete incorporating plastic aggregates fabricated using 3D printing technology. *3D Print. Addit. Manuf.* 9 (3), 212–222. doi:10.1089/3dp.2020.0347

Cai, C., Huang, W., and Lv, Q. (2014). Properties and application of terminal blending rubber asphalt. *J. Chongqing Jiaot. Univ. Sci.* 33 (4), 51–55. doi:10.3969/j.issn.1674-0696.2014.04.11

Cao, L., Yang, C., Dong, Z., Wang, W., and Yin, H. (2022). Aging mechanism of hot-poured sealants for asphalt pavement under natural environmental exposure. *Int. J. Pavement Eng.* 23 (2), 197–206. doi:10.1080/10298436.2020.1736296

Cong, Y., Xu, J., Huang, W., Zhang, C., and Liu, J. (2016). Study on modification of asphalt by SBS-C9 petroleum resin. *J. Build. Mater.* 19 (03), 602–605. doi:10.3969/j.issn.1007-9629.2016.03.032

Galooyak, S. S., Dabir, B., Nazarbeygi, A. E., and Moeini, A. (2010). Rheological properties and storage stability of bitumen/SBS/montmorillonite composites. *Constr. Build. Mater.* 24 (3), 300–307. doi:10.1016/j.conbuildmat.2009.08.032

Glover, C. J., Davison, R. R., Bullin, J. A., Estakhri, C. K., Williamson, S. A., Billiter, T. C., et al. (2000). *A comprehensive laboratory and field study of high-cure crumb-rubber modified asphalt materials.*

Gong, F., Cheng, X., Chen, Y., Liu, Y., and You, Z. (2022). 3D printed rubber modified asphalt as sustainable material in pavement maintenance. *Constr. Build. Mater.* 354, 129160. doi:10.1016/j.conbuildmat.2022.129160

Gong, F., Cheng, X., Fang, B., Cheng, C., Liu, Y., and You, Z. (2023). Prospect of 3D printing technologies in maintenance of asphalt pavement cracks and potholes. *J. Clean. Prod.* 397, 136551. doi:10.1016/j.jclepro.2023.136551

Gong, F., Cheng, X., Wang, Q., Chen, Y., You, Z., and Liu, Y. (2023). A review on the application of 3D printing technology in pavement maintenance. *Sustainability* 15 (7), 6237. doi:10.3390/su15076237

Hallmark-Haack, B. L., Hernández, N. B., Williams, R. C., and Cochran, E. W. (2019). Ground tire rubber modification for improved asphalt storage stability. *Energy and Fuels* 33, 2659–2664. doi:10.1021/ACS.ENERGYFUELS.8B03558

Hosseinnezhad, S., Kabir, S. F., Oldham, D., Mousavi, M., and Fini, E. H. (2019). Surface functionalization of rubber particles to reduce phase separation in rubberized asphalt for sustainable construction. *J. Clean. Prod.* 225, 82–89. doi:10.1016/j.jclepro.2019.03.219

Hou, X., Lv, S., Chen, Z., and Xiao, F. (2018). Applications of Fourier transform infrared spectroscopy technologies on asphalt materials. *Measurement* 121, 304–316. doi:10.1016/j.measurement.2018.03.001

Jackson, R. J., Wojcik, A., and Miodownik, M. (2018). 3D printing of asphalt and its effect on mechanical properties. *Mater. and Des.* 160, 468–474. doi:10.1016/j.matdes.2018.09.030

Kabir, S. F., Mousavi, M., and Fini, E. H. (2020). Selective adsorption of bio-oils' molecules onto rubber surface and its effects on stability of rubberized asphalt. *J. Clean. Prod.* 252, 119856. doi:10.1016/j.jclepro.2019.119856

Kim, H. H., Mazumder, M., Lee, M.-S., and Lee, S.-J. (2020). Laboratory evaluation of SBS modified asphalt binder containing GTR, SIS, and PE. *Adv. Civ. Eng.* 2020, 8830622. doi:10.1155/2020/8830622

Leng, Z., Padhan, R. K., and Sreeram, A. (2018). Production of a sustainable paving material through chemical recycling of waste PET into crumb rubber modified asphalt. *J. Clean. Prod.* 180, 682–688. doi:10.1016/j.jclepro.2018.01.171

Li, Z., Nie, X., Yao, H., Zhou, H., and Li, C. (2019). Study on properties of C9 petroleum resin/SBS composite modified asphalt. *J. Build. Mater.* 22 (05), 764–770. doi:10.3969/j.issn.1007-9629.2019.05.014

Li, F., Zhou, S., Cai, W., Du, Y., and Li, L. (2017). Laboratory evaluation of short and long term performance of hot-poured sealants. *Constr. Build. Mater.* 148, 30–37. doi:10.1016/j.conbuildmat.2017.05.014

Li J., J., Xiao, F., and Amirkhanian, S. N. (2019). Storage, fatigue and low temperature characteristics of plasma treated rubberized binders. *Constr. Build. Mater.* 209, 454–462. doi:10.1016/j.conbuildmat.2019.03.136

Ma, G., Wang, L., and Ju, Y. (2017). State-of-the-art of 3D printing technology of cementitious material—an emerging technique for construction. *Sci. China Technol. Sci.* 61, 475–495. doi:10.1007/s11431-016-9077-7

Mturi, G. A. J., O'Connell, J., Zoorob, S. E., and De Beer, M. (2014). A study of crumb rubber modified bitumen used in South Africa. *Road Mater. Pavement Des.* 15 (4), 774–790. doi:10.1080/14680629.2014.910130

Nie, X., Hou, T., Yao, H., Li, Z., Zhou, X., and Li, C. (2019a). Effect of C 9 petroleum resins on improvement in compatibility and properties of SBS-modified asphalt. *Petroleum Sci. Technol.* 37, 1704–1712. doi:10.1080/10916466.2019.1602642

Nie, X., Yao, H., Li, C., Zhou, H., and Li, C. (2019b). Effect of C9 petroleum resins on the performance of high-viscosity asphalt. *Acta Pet. Sin. Process. Sect.* 35 (01), 176–182. doi:10.1080/10916466.2019.1602642

Park, S. W., Richard Kim, Y., and Schapery, R. A. (1996). A viscoelastic continuum damage model and its application to uniaxial behavior of asphalt concrete. *Mech. Mater.* 24 (4), 241–255. doi:10.1016/S0167-6636(96)00042-7

Presti, D. L. (2013). Recycled Tyre Rubber Modified Bitumens for road asphalt mixtures: a literature review. *Constr. Build. Mater.* 49, 863–881. doi:10.1016/j.conbuildmat.2013.09.007

Presti, D. L., Airey, G., and Partal, P. (2012). Manufacturing terminal and field bitumen-tyre rubber blends: the importance of processing conditions. *Procedia - Soc. Behav. Sci.* 53, 485–494. doi:10.1016/j.sbspro.2012.09.899

Qian, C., Fan, W., Liang, M., Nan, G., and Luo, H. (2018). Influence of compatibilizer composition on performance of SBS modified asphalt. *AIP Conf. Proc.* 1971 (1). doi:10.1063/1.5041202

Qian, C., Fan, W., Ren, F., Lv, X., and Xing, B. (2019). Influence of polyphosphoric acid (PPA) on properties of crumb rubber (CR) modified asphalt. *Constr. Build. Mater.* 227, 117094. doi:10.1016/j.conbuildmat.2019.117094

Rowe, G. M., and Sharrock, G. (2009). *Functional forms for master curve analysis of bituminous materials.*

Shatnawi, S. R., and President, E. (2010). *Comparisons of rubberized asphalt binders asphalt-rubber and terminal blend for the rubber.*

Wu, H., Chen, P., Chen, C., and Zhang, W. (2022). Effect of aromatic petroleum resin on microstructure of SBS modified asphalt. *Adv. Mater. Sci. Eng.* 2022, 1–11. doi:10.1155/2022/5136748

Wu, X. (2023). Preparation and performance study of modified polyurethane sealant based on 3D printing. doi:10.26976/d.cnki.gchau.2023.000208

Xu, O., Rangaraju, P. R., Wang, S., and Xiao, F. (2017). Comparison of rheological properties and hot storage characteristics of asphalt binders modified with devulcanized ground tire rubber and other modifiers. *Constr. Build. Mater.* 154, 841–848. doi:10.1016/j.conbuildmat.2017.07.221

Xue, Y. (2023). *Preparation and properties of SBS/LNBR/CR modified asphalt for 3D crack repairing.* doi:10.26976/d.cnki.gchau.2023.001645

Yang, H. (2023). *Preparation and performance of 3D printable TPSiV/SBS/CR composite modified asphalt sealant.* doi:10.26976/d.cnki.gchau.2023.001549

Yu, J., Ren, Z., Yu, H., Wang, D., Svetlana, S., Korolev, E., et al. (2018). Modification of asphalt rubber with nanoclay towards enhanced storage stability. *Materials* 11 (11), 2093. doi:10.3390/ma11112093

Yusoff, N. I. M., Chailleux, E., and Airey, G. (2011). A comparative study of the influence of shift factor equations on master curve construction. *Int. J. pavement Res. Technol.* 4, 324–336. doi:10.6135/IJPRT.ORG.TW/2011.4(6).324

Zhang, J., Huang, W., Zhang, Y., Yan, C., Lv, Q., and Guan, W. (2021). Evaluation of the terminal blend crumb rubber/SBS composite modified asphalt. *Constr. Build. Mater.* 278, 122377. doi:10.1016/j.conbuildmat.2021.122377

Zhang, L., Hoff, I., Zhang, X., Liu, J., Yang, C., and Wang, F. (2023). A methodological review on development of crack healing technologies of asphalt pavement. *Sustainability* 15 (12), 9659. doi:10.3390/su15129659

Zhang, W., Qiu, L., Liu, J., Hu, K., Zou, L., Chen, Y., et al. (2021). Modification mechanism of C9 petroleum resin and its influence on SBS modified asphalt. *Constr. Build. Mater.* 306, 124740. doi:10.1016/j.conbuildmat.2021.124740

Zhao, M., and Dong, R. (2021). Reaction mechanism and rheological properties of waste cooking oil pre-desulfurized crumb tire rubber/SBS composite modified asphalt. *Constr. Build. Mater.* 274, 122083. doi:10.1016/j.conbuildmat.2020.122083

Performance optimization of asphalt pavements using binder film thickness as a criterion in innovative mix design compared to Marshall and Superpave methods

Muhammad Adeel Khan[1], Muhammad Salman Khan[1]*,
Bilal Nasir[2], Asad Khan[1], Mohanad Muayad Sabri Sabri[3],
Mahmood Ahmad[4,5]*, Wajeeha Qamar[6] and
Roberto Alonso Gonzalez-Lezcano[7]

[1]Department of Bridge Engineering, College of Civil Engineering, Tongji University, Shanghai, China,
[2]Department of Transportation Engineering, H-12 Campus, NUST Islamabad, Islamabad, Pakistan,
[3]Peter the Great St. Petersburg Polytechnic University, St. Petersburg, Russia, [4]Institute of Energy
Infrastructure, Universiti Tenaga Nasional, Kajang, Malaysia, [5]Department of Civil Engineering,
University of Engineering and Technology Peshawar (Bannu Campus), Bannu, Pakistan, [6]Department
of Civil Engineering, Institute of Engineering and Fertilizer Research, Faisalabad, Pakistan, [7]Department
of Architecture and Design, Escuela Politécnica Superior, Montepríncipe Campus, Universidad San
Pablo-CEU, CEU Universities, Madrid, Spain

The performance of asphalt pavements is significantly influenced by the mix design and the binder film thickness (BFT) around aggregates. Adjusting the proportions of binders and aggregates modifies the properties of asphalt mixtures, with different mix designs substantially impacting these properties. This study evaluates the influence of two traditional mix designs (i.e., Marshall and Superpave Gyratory Compacted) and one innovative mix design (the one using BFT as a criterion) on asphalt pavement performance Two methods, which are modifications of the Hveem Surface Area Factor method, were used to calculate the optimum BFT. The mix with 3.5% asphalt content (AC) was selected for the innovative mix design as it showed the optimal BFT. For the Marshall and Superpave mix designs, the optimum binder content was determined using the respective Marshall and Superpave Gyratory Compacted methods, yielding values of 4.3% and 4.4%, respectively. Samples were prepared from each type of mix design and then tested using a Universal Testing Machine (UTM) and a Double Wheel Tracker (DWT). Performance tests showed that the innovative mix design samples had superior rutting resistance under DWT, the Marshall samples had the highest Resilient Modulus (Mr) and moisture resistance, and the Superpave samples exhibited the best fatigue resistance, enduring the most cycles until failure in the Indirect Tensile Fatigue Test (ITFT). These findings underscore the importance of considering BFT as a critical mix design criterion, demonstrating its significant

potential to enhance the overall performance and durability of asphalt pavements.

1 Introduction

Modern infrastructure relies heavily on asphalt concrete for road construction due to its durability and adaptability. Asphalt concrete properties can be tailored by adjusting the proportions of bitumen, aggregate, and other components to meet specific performance requirements (Dhir et al., 2018; Dhir, Ghataora, and Lynn, 2017). While traditional methods like the Marshall Mix design and advanced approaches like Superpave have contributed significantly to asphalt pavement design, there remains a need to address performance challenges under high-traffic and adverse environmental conditions. Recent research points to Binder Film Thickness (BFT) as a promising factor to enhance durability and moisture resistance, addressing these challenges.

The Marshall Mix design, initially developed for optimizing stability and flow, has been widely used but demonstrates limitations under heavy traffic and high temperatures, where it struggles to maintain durability. Studies indicate that while modifications improve stability, flow, and Indirect Tensile Strength (ITS), Marshall Mix still underperforms under intense loads, underscoring a need for methods that incorporate field density and traffic impact considerations (Azzam, Al-Ghazawi, and Al-Otoom, 2016; Lv et al., 2018). As an evolution of these designs, Superpave introduced performance-graded binder specifications and gyratory compaction to improve rutting and fatigue resistance in high-traffic scenarios (Ghuzlan, Al-Mistarehi, and Al-Momani, 2020; Gu et al., 2017). Originating from the Strategic Highway Research Program (SHRP), Superpave emphasizes compaction levels (N_{design}) and BFT for durability, though challenges in meeting minimum voids in mineral aggregates (VMA) remain (Martinez Soto, 2018; Souza et al., 2024). Research has recommended refinements such as using average asphalt binder film thickness (ABFT) over VMA to enhance performance (Pérez-Jiménez et al., 2014; Harvey et al., 2015; Al-Khateeb and Aroon, 2019; Al-Khateeb, 2018). This shift from Marshall to Superpave reflects the need for adaptable design methods to meet modern infrastructure demands.

Sustainability has guided recent research toward environmentally friendly materials for asphalt applications, emphasizing the use of alternative materials and innovative techniques (Gu et al., 2023; Rudenko et al., 2024; Sun et al., 2024). Meanwhile, BFT has emerged as an essential parameter in enhancing the durability and moisture resistance of asphalt mixtures. Originally proposed by Francis Hveem, BFT has been recognized as a crucial factor in mix design. Researchers have correlated BFT with pavement durability, suggesting its inclusion in mixed design criteria (Remišová, 2015; Kandhal and Sanjoy, 1996; Elseifi et al., 2008; Jiang et al., 2022) and identified the optimal BFT for Hot Mix Asphalt (HMA) using SGC specimens, finding an optimum BFT of 9–10 μm to minimize moisture susceptibility, emphasizing its importance in HMA durability (Karim, Hussain, and Hafeez, 2021; Wang et al., 2024). Further research has quantified aging and durability across various BFTs, concluding that aging is more likely when BFT falls below 9–10 μm (Lin et al., 2023). Analytical imagery techniques have revealed that bitumen films surrounding larger aggregates in mastic asphalt can reach thicknesses above 100 μm (Cavalli, Partl, and Poulikakos, 2017). Additionally, air voids and binder content were shown to be significant, with an average BFT of 8 μm recommended for improved durability (Miranda et al., 2021; Lu et al., 2019; Zhang et al., 2024). The Shell Bitumen Handbook highlighted the role of BFT in asphalt hardening, suggesting a minimum thickness of 6–8 μm for satisfactory performance (Sims, 2016). In summary, BFT emerges as a crucial parameter in asphalt mixture durability, with researchers advocating for its inclusion in mix design criteria to enhance pavement longevity and moisture resistance.

Despite research supporting BFT's role in durability, its application in mix design remains limited, particularly in performance-based specification systems. Departments of Transportation (DOTs) globally, including Pakistan, face challenges in adopting BFT criteria due to precise binder control requirements and a lack of standardized testing methodologies. Increased traffic volumes, environmental stressors, poor construction practices, and outdated mix designs contribute to premature pavement failures, primarily due to fatigue, rutting, and other distresses. Thus, a performance-based study is needed to evaluate various mixes designed with BFT, Marshall, and Superpave criteria under diverse loading and climate conditions. This study aims to validate BFT determination techniques and conduct a performance-based analysis comparing Marshall, Superpave, and BFT-based innovative mix design under various conditions, including rutting, resilience, fatigue, and moisture susceptibility. By examining BFT's impact across these mix designs, this research addresses the need for comprehensive testing through both analytical and experimental approaches, contributing to the development of more durable, cost-effective asphalt mixtures suited for modern traffic and environmental demands.

2 Experimental program/methodology

The experimental program and methodology outline the material acquisition, sample preparation, and testing procedures, adhering to National Highway Authority (NHA) B gradation standards. Performance assessments were carried out utilizing the Double Wheel Tracker (DWT) and Universal Testing Machine (UTM). Virgin aggregates from the Margalla quarry and grade 60/70 bitumen from PARCO Islamabad were used. This study encompasses several critical steps to ensure comprehensive evaluation and accurate results. Initially, volumetrics and the Optimal Binder Content (OBC) were determined for the Marshall and Superpave mix designs. This involves assessing the specific gravity, air voids, voids in mineral aggregates,
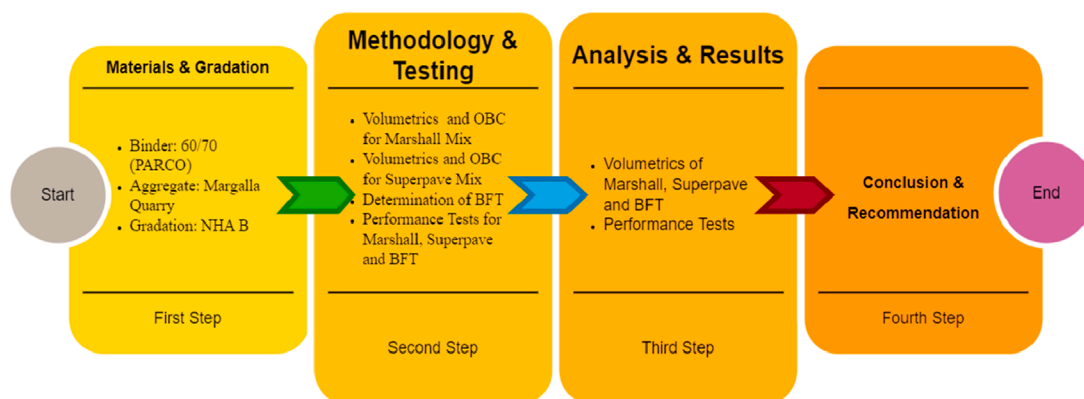
FIGURE 1
Flow chart for evaluating the influence of BFT on asphalt pavement performance.

and other relevant volumetric properties essential for defining the mix characteristics. Following this, the BFT was calculated using established analytical methods. BFT determination is crucial as it is a criterion for one of the mixes prepared in this study. Finally, performance tests were conducted to evaluate the efficacy of the mixes prepared under Marshall, Superpave, and BFT criteria. These tests included ITS, moisture susceptibility, rutting resistance using the DWT, fatigue life assessment using the Indirect Tensile Fatigue Test (ITFT), and Resilience Modulus (Mr) tests using a UTM. Each step in this methodology is designed to assess the properties and performance of the asphalt mixtures rigorously. This provides a comprehensive understanding of the impact of different mix designs and BFT on asphalt pavement performance. Figure 1 illustrates the research workflow chart for evaluating the influence of BFT on asphalt pavement performance.

2.1 Materials

In this study, fine and coarse aggregates were sourced from the Margalla quarry, while penetration grade 60/70 bitumen was obtained from PARCO Islamabad. Grade 60/70 was chosen due to its everyday use in Pakistan and suitability for colder to intermediate temperature regions. Aggregates primarily resist permanent deformation in the mix, with the asphalt binder contributing for the remaining 5%. Aggregates' gradation and surface texture significantly impact hot mix asphalt's properties and volumetrics, with rough-textured aggregates offering greater shear strength than smooth-surfaced ones. All necessary tests on the acquired aggregates and bitumen were conducted per standards and specifications.

2.2 Material testing

2.2.1 Aggregate testing

According to NHA specifications (1998), the aggregate selected for this research study adhered to NHA class B gradation, specifically designed for the wearing course. The Nominal Maximum Aggregate Size (NMAS) for NHA-B is 19mm, as per the Marshal Mix Design

FIGURE 2
NHA Class-B Gradation selected for Testing.
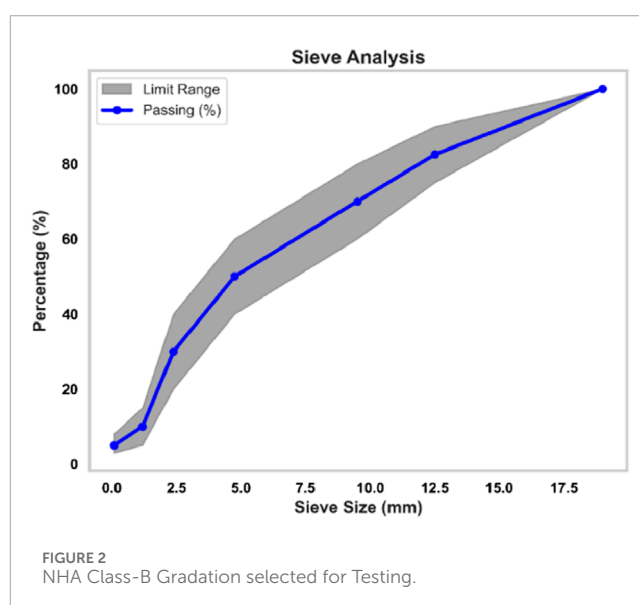
(MS2) (Asphalt Institute MS-2 1993). The specific gradation chosen for this research is outlined in Figure 2.

Several tests were performed to ensure the suitability of the aggregates for asphalt mix design, with each test conducted on three specimens and the average values used for analysis. Specific gravity tests for coarse and fine aggregates were performed according to ASTM C 127 and ASTM C 128, respectively (ASTM C 127-08 2008; ASTM C128/C128M 2001). Water absorption rates for both coarse and fine aggregates were also determined using these standards. The Los Angeles Abrasion test (ASTM C 131) was performed to evaluate the hardness and wear resistance of the aggregates (Monyakeng, 2022). The Shape Test (ASTM D 4791) assessed the quantity of elongated and flat particles (ASTM D4791-10 2010). The Impact Value Test was also performed following BS 812 to measure the aggregates' resistance to breaking (BS 812-112 1990). At the same time, the crushing Value Test was conducted to evaluate the aggregate strength under compressive loads (BS 812-110 1990). The results obtained from these tests are shown in Table 1.

TABLE 1 Properties of aggregates.

Test description	Specification reference	Result	Limits
Coarse Agg Specific Gravity	ASTM C 127	2.632	2.5–3
Fine Agg Specific Gravity	ASTM C 128	2.618	2.5–2.8
Coarse Agg Water Absorption	ASTM C 127	0.73%	≤3
Fine Agg Water Absorption	ASTM C 128	2.45%	≤3
Los Angles Abrasion	ASTM C 131	22	≤45
Elongation Index	ASTM D 4791	3.578%	≤15
Flakiness Index	ASTM D 4791	12.9%	≤15
Impact Value	ASTM C 131	17%	≤30

2.2.2 Asphalt binder testing

The binder's consistency, safety, and purity are crucial for construction and engineering applications. Since bituminous binder consistency varies with temperature, standard temperature testing is essential. To assess the performance and suitability of the asphalt binder (PARCO 60/70) for HMA mixtures, several tests were conducted; i.e., ductility, measured according to ASTM D 113-99 (ASTM D 113-99 2000), indicates the bitumen's elongation without breaking when pulled at a specified velocity at 25°C, with all specimens exceeding the 100 cm minimum criterion. The Rotational Viscosity (RV) test, conducted at 135°C and 160°C using the Brookfield RV apparatus, determines asphalt binder viscosity, following AASHTO T-316 (AASHTO T316 2019) and ASTM D4402 (ASTM D4402 2016). Heated bitumen is stirred, avoiding air bubbles, and poured into the sample chamber. The spindle rotates at 20 RPM, and three viscosity readings are averaged. The penetration test, conducted according to AASHTO T 49–03 standards (AASHTO T 49-15 2012), assesses the consistency of asphaltic materials, with softer binders exhibiting higher penetration values. This test is performed at 25°C with a 100-g load applied for 5 s. Five penetration values were recorded for each of the two Parco 60/70 specimens; all values met the required standards, confirming their appropriate consistency. According to ASTM D36-06 (ASTM D36-06 2008), the softening point is the temperature at which bitumen cannot support a 3.5 gm steel ball. The test performed for it involves heating bitumen disks until the steel balls drop one inch, using the standard ring and ball setup. Similarly, the flash and fire point test, conducted according to ASTM D3143/D3143M-13 standards (ASTM D3143/D3143M − 13 2013), assesses bitumen's suitability for mix preparation, ensuring safety and compliance with specifications. Table 2 provides a summary of the test outcomes.

2.3 Asphalt mixtures preparation

Laboratory samples were meticulously prepared for Marshall, SGC, and BFT methods. For both the Marshall Mix Design and the Superpave Gyratory Mix Design, five different bitumen content

TABLE 2 Physical properties of parco 60/70 binder.

Test description	Specification reference	Result
Penetration Test @ 25 (^{0}C)	AASHTO T 49-03	64
Flash Point (^{0}C)	ASTM D 3143/D 3143M-13	268
Fire Point (^{0}C)	ASTM D 3143/D 3143M-13	293
Specific Gravity	ASTM D 70	1.03
Softening Point (^{0}C)	ASTM D 36–06	48.2
Viscosity Test (Pa.sec)	ASTM D 4402	0.2625
Ductility Test (cm)	ASTM D 113–99	104

levels were tested: 3.5%, 4%, 4.5%, 5%, and 5.5%, with three samples prepared for each bitumen content level, totaling 15 samples per mix design. Subsequently, these samples underwent comprehensive testing and scrutiny to assess various volumetric properties and stability characteristics.

2.3.1 Preparation of bituminous mixes for marshall mix design

Bituminous mixes for the Marshall Mix Design were prepared using the Marshall Apparatus. Volumetric characteristics, including stability and flow, were determined to verify the criteria and establish the OBC. Aggregates were dried at 110°C after sieve analysis. For consistency, 1,200 g of aggregates were measured for each sample, following ASTM D6926 (ASTM D 6926 2014). The required asphalt cement for each sample was calculated as a percentage of the total mix weight from a predefined Equations 1, 2 (Roberts et al., 1996).

$$M_T = M_{Agg} + M_{Bin} \qquad (1)$$

$$M_{Bin} = \%X/100\,(M_T) \qquad (2)$$

FIGURE 3
Bituminous samples prepared using the marshall mix design method.

Where M_T stands for the total mass of the mix in kilograms (kg), M_{Agg} represents the aggregate's mass in kilograms (kg), M_{Bin} denotes the binder's mass in kilograms (kg), and %X indicates the binder's percentage. Following ASTM D6926 guidelines (ASTM D 6926 2014), a mechanical mixer thoroughly combined heated aggregates (160°C–165°C as per NHA specifications) and bitumen binder. The mix was then compacted with a Marshall Compactor, evenly distributed in the mold with a spatula, and filter paper applied to both ends. Each sample side received seventy-five (75) compaction blows to meet heavy traffic criteria. After compaction, specimens cooled before being ejected with an extraction jack and cooled to room temperature as shown in Figure 3.

2.3.2 Preparation of bituminous mixes for Superpave mix design

Achieving the required gradation is essential for the Superpave mix design. Following the Asphalt Institute's Mix Design Method for Superpave (SP-2) guidelines (Asphalt Institute MS-2 1993), aggregates were oven-dried at 105°C–110°C. A 19 mm NMAS was selected, using 4,500 g of aggregates for the 6-inch gyratory compacted specimen. The heated dry aggregates (Figure 4A) and bitumen (Figure 4B) were mixed using a mechanical mixer (Figure 5) at 160°C–165°C for 10–15 min.

According to SP-2 guidelines (Asphalt Institute MS-2 1993), specimens were compacted using the Superpave Gyratory Compactor (SGC) (Figure 6) at 135°C. The mold, preheated to 100°C for 30 min, had a 150 mm inner diameter and a base plate to ensure proper compaction. The SGC operated at a constant 30 rpm, with the mold at a 1.25-degree angle and 600 kPa pressure applied. The compaction process was carried out to meet heavy traffic design criteria until the desired compaction was achieved. After compaction, specimens were extracted from the mold for further testing as shown in Figure 7.

2.4 Determination of VFA (voids filled with asphalt), VMA, and OBC

Determining VFA, VMA, and OBC is crucial for Marshall and Superpave Mix Designs.

2.4.1 VFA, VMA, and OBC for Marshall mix design

For Marshall Mix Design, VMA, VFA, air voids (Va), and unit weight were calculated using Mix Theoretical Maximum Specific Gravity (G_{mm}) and Mix Bulk Specific Gravity (G_{mb}), determined according to ASTM D2041 (ASTM D2041 2018) and ASTM D2726 (ASTM D2726 2013), respectively. The mix characteristics are shown in Figure 2. After obtaining these values, specimens were conditioned in a water bath at 60°C for an hour and tested for stability and flow using Marshall testing equipment (Figure 8). A load was applied at a 5 mm/min deformation rate until failure. The maximum load (kN) was recorded as Marshall Stability, and the deformation at maximum load (mm) was noted as the flow number. Stability must be at least 8.006 kN for heavily trafficked-wearing courses, and the flow number should be between 2 and 3.5. The specimens were tested immediately after removal from the water bath. Following the Marshall mix design method guidelines, the OBC will be determined at 4% Va. This approach ensures durability and stability, as 4% air voids are optimal. Lower air voids may result in rutting and bleeding, while higher air voids can increase permeability and oxidation. This practice is recommended by the Asphalt Institute and various transportation agencies, as detailed in the Asphalt Institute's Manual Series No. 2 (MS-2) (Asphalt Institute MS-2 1993), which specifies that the air voids should be approximately 4%.

2.4.2 VFA, VMA, and OBC for super pave mix design

Samples for both 19mm and 25 mm gradations were prepared following the Superpave mix design manual (SP-2) to determine the optimal asphalt content (Asphalt Institute MS-2 1993). Binder content ranged from 3% to 4.5% in 0.5% increments. Two samples were prepared for each gradation for each binder content, resulting in eight samples for the 19 mm gradation and eight for the 25 mm gradation. Volumetric parameters, including theoretical maximum specific gravity (G_{mm}), effective specific gravity (G_{se}), bulk specific gravity (G_{mb}), and %G_{mm} of the prepared specimens, were measured and verified according to Superpave mix design criteria. Due to its weight, testing the entire Superpave sample was impractical, so 2000 g were used to determine the volumetrics. The same apparatus used for the Marshall test was employed. For a 19.0 NMAS, the minimum VMA is 13%; in this case, it was 15.71%. The VFA should be between 65% and 75%, calculated at 71.64%, meeting the criteria. The dust-to-binder ratio should be between 0.8 and 1.6; in this instance, it was 1.54. The OBC was then determined at the binder percentage, which achieved 96% G_{mm}. Based on the results, 19 mm NMAS was chosen as it effectively met all the Superpave mix design criteria.

2.5 Determination of BFT

Different researchers employed various equations to determine the BDT, many of which are modifications of the Hveem Surface Area Factor method. The following outlined methods were used for deciding BFT in this study.

2.5.1 The Shell Bitumen Handbook method

The Shell Bitumen Handbook uses the Hveem Surface Area Factor method to estimate the BFT (Sims, 2016). This method estimates the aggregate surface area by coating it with oil and measuring the required amount, accounting for absorbed asphalt. Alternatively, the Hveem (ASTM 1992) surface area factor can be

FIGURE 4
Pre-heating of **(A)** aggregate in oven, **(B)** bitumen in oven.

FIGURE 5
Mechanical mixer.

FIGURE 7
Bituminous samples prepared using superpave (grey) and marshall (black) mix design methods.

FIGURE 6
Superpave gyratory compactor.

used, assuming a spherical shape and a specific gravity of 2.65. Surface area factors are presented in Table 3:

To calculate the aggregate surface area, multiply the mass percentage passing each sieve by the corresponding surface area factor and sum the results. The BFT is then calculated using the following Equation 3:

$$ \text{BFT} = \left[\left(\frac{b\%}{100 - b\%} \right) * \left(\frac{1}{\rho b} \right) * \left(\frac{1}{\sum SAf} \right) \right] \tag{3} $$

Where ρb is the binder density (kg/m³), SAf is the surface area factor (m²/kg), and $b\%$ is the binder content (%). To obtain BFT in meters, all units must be in SI, which can then be converted to micrometers (μm).

2.5.2 The Hveem method in Zaniewski, Reyes, et al

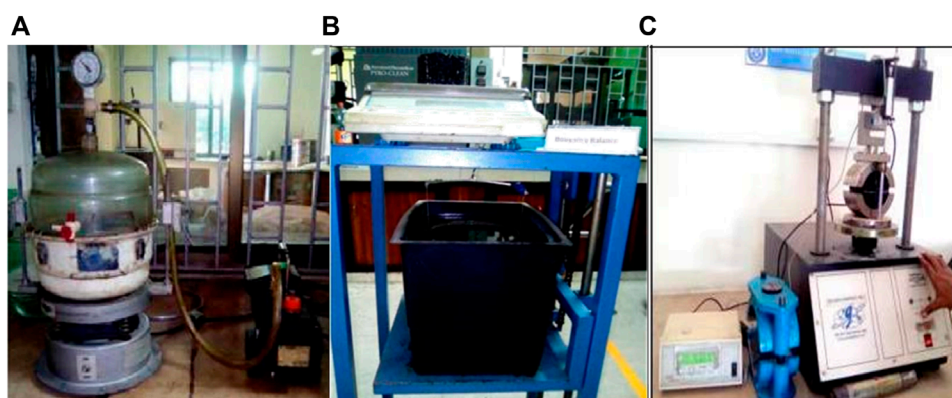Zaniewski, Reyes, et al. recommend Equation 4 for determining BFT (Sukkari et al., 2022):

FIGURE 8
Marshall Testing Equipment **(A, B)** Gmm, Gmb, determination apparatus **(C)** Stability and flow apparatus.

TABLE 3 Surface area factors for different sizes of aggregates.

Sieve size (mm)	Sieve size (inches)	Surface area factor (m2/Kg)
19	3/4	0.41
12.5	1/2	0.41
9.5	3/8	0.41
4.75	#4	0.41
2.36	#8	0.82
1.18	#16	1.64
0.075	#200	32.77

$$\text{BFT} = \left[\frac{W_b}{\left(\sum SAf * 1000\right)}\right] * G_b \qquad (4)$$

BFT is the average thickness of the binder film, measured in micrometers (µm). The term Wb represents the ratio of binder weight to aggregate weight, Gb is the specific gravity of the binder, and SAf denotes, the surface area factor of the aggregate, measured in square meters per kilogram (m^2/kg). This formula is advantageous due to its simplicity and the inclusion of binder percentage by the weight of the entire mix.

2.6 Performance comparison among mixes based on BFT, Marshall mix design, and SGC mix design

After determining the optimum criteria for all three mixes—Marshall, Superpave, and BFT—the mixes were subjected to a series of tests. Rutting was evaluated using the DWT. At the same time, the UTM was employed to assess the Mr, ITFT, ITS, and moisture susceptibility.

2.6.1 Performance comparison test using DWT

Performance tests for Marshall, Superpave, and BFT-designed mixes were conducted using the DWT to assess rutting. Samples, aged for 48 h, were prepared and cut to specified dimensions. As shown in Figure 9, the DWT operated at 25 cycles per minute for 5,000 cycles at room temperature. Despite initial weight differences, samples were uniformly cut for consistent testing.

2.6.2 Performance comparison tests using UTM

The Mr test was performed using the ASTM D7369-11 standard (ASTM D7369-11, 1860). It involves applying compressive loads in a haversine waveform to cylindrical specimens to record vertical and horizontal deformations. Resilient Poisson's ratio is calculated from these deformations, and two Mr values, instantaneous and total, are obtained based on recoverable deformations.

The ITS and Moisture Susceptibility tests were conducted using UTM, following ASTM D 6931-07 specifications (ASTM D6931-07 2022). Three unconditioned specimens per mix were tested, while another set of three conditioned specimens per mix underwent saturation and exposure to elevated temperatures before testing.
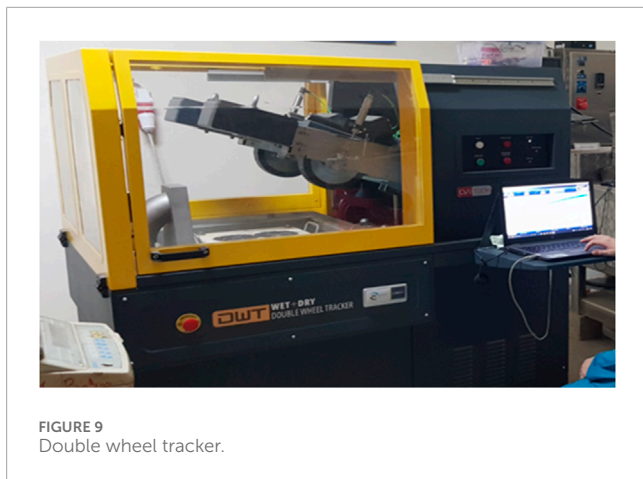
FIGURE 9
Double wheel tracker.

Conditioning was performed according to ALDOT-361 standards, involving saturation followed by immersion in a 60°C ± 1°C water bath for 24 h and subsequent immersion in a water bath at 25°C ± 1°C for 50 h as shown in Figure 10A (ALDOT-361-88 2005). Both unconditioned and conditioned specimens were loaded on their diametric plane at a 50 mm/min rate as shown in Figure 10B.

The tensile strength of each specimen was calculated based on its dimensions and failure load. The tensile strength ratio (TSR) was then determined by dividing the average tensile strength of conditioned specimens by the average tensile strength of unconditioned specimens, with an acceptable TSR value set at 80%. The resistance to moisture damage is then expressed as a ratio of the conditioned sample's tensile strength retained after the conditioning to the unconditional tensile strength. Tensile strength (St) was calculated using Equation 5:

$$St = \frac{2000P}{\pi D t} \qquad (5)$$

where St represents the tensile strength in kilopascals (KPa), P is the maximum load in newtons (N), t denotes the sample thickness in millimeters (mm), and D is the sample diameter in millimeters (mm).

The ITFT was conducted according to ASTM D7460–08 to assess fatigue cracking in asphalt pavements and primary distress caused by tensile and shear stresses from traffic loads (ASTM D7460-08 2010). Fatigue performance models, both empirical and mechanics-based, have been developed to characterize the behavior of HMA mixtures. The ITFT is conducted on cylindrical samples to characterize virgin and modified mixes under repeated vertical compression loads. This loading generates uniform tensile stress in the horizontal direction, perpendicular to the load. Figure 11 indicates failure by the sample splitting along the vertical plane. Vertical deformations calculate tensile stresses and strain at the specimen's center, assuming a Poisson's ratio. The number of cycles to failure determines the fatigue life.

3 Results and discussion

This section presents a detailed analysis of the results, beginning with volumetric calculations and the determination

of the OBC. Subsequently, it discusses the findings from various performance tests, including ITS and Moisture Susceptibility, rutting resistance using the DWT, and fatigue life assessment using the ITFT. Each test result is evaluated against relevant criteria to comprehensively understand the material's performance.

3.1 Volumetric analysis and OBC

The Volumetric Analysis included determining the VFA and VMA for Marshall Mix and Superpave mix Designs. Based on the calculated VMA and VFA, the OBC and BFT were determined for Marshall and Superpave mixes. The volumetric properties, stability, and flow of the Marshall mix are presented in Table 4.

To determine the Marshall mix's OBC, graphs were plotted in Figure 12 between asphalt content and volumetric properties, stability, and flow, as specified in the MS-2 manual (Asphalt Institute MS-2 1993).

The Marshall mix design results showed that the OBC was determined to be 4.30% at 4% air voids as shown in Figure 12A. This aligns with the typical practice of using 4% air voids to balance durability and stability in asphalt pavements. The VMA was calculated to be 13.23%, which exceeds the minimum requirement of 13%, indicating a sufficient void space within the aggregate structure to accommodate the asphalt binder. The VFA of 69% falls within the recommended range of 65%–75%, ensuring an adequate binder film around the aggregate particles, which is essential for long-term durability and resistance to moisture damage.

The stability and flow values at the OBC were also within acceptable ranges, with a stability of 12.5 kN (well above the minimum requirement of 8.006 kN) and a flow number of 2.7 mm (within the range of 2–3.5 mm). These results suggest that when properly optimized, the Marshall mix design method can produce asphalt mixtures that meet the required performance criteria for stability and durability.

For the Superpave mix design, the volumetric properties such as VMA and VFA were also within acceptable limits., as shown in Table 5. Figure 13 illustrates the relationship between the number of gyrations and the average %Gmm for various binder contents in the Superpave mix design. The vertical lines at N_ini = 8 and N_des = 125 represent the initial and design gyrations, respectively. The target %Gmm for optimal performance was 96% at 125 gyrations, consistent with the Superpave mix design criteria. The binder content that achieved this target was determined to be 4.4%, slightly higher than the Marshall mix design's OBC. This slight increase in binder content can be attributed to the more rigorous compaction process used in the Superpave method, which aims to simulate the long-term densification of the asphalt pavement under traffic loads.

The findings indicate that both mix design methods can produce high-quality asphalt mixtures. Still, the Superpave method provides a more comprehensive approach to optimizing the mix for long-term performance. Using gyrations to simulate compaction and the detailed analysis of volumetric properties ensure that the Superpave mix design can produce mixtures with improved resistance to rutting and fatigue cracking.
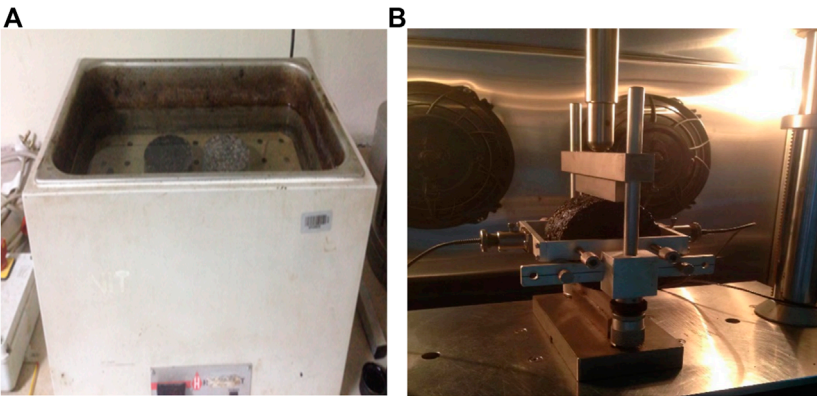
FIGURE 10
Sample placed in **(A)** Water bath **(B)** UTM machine.
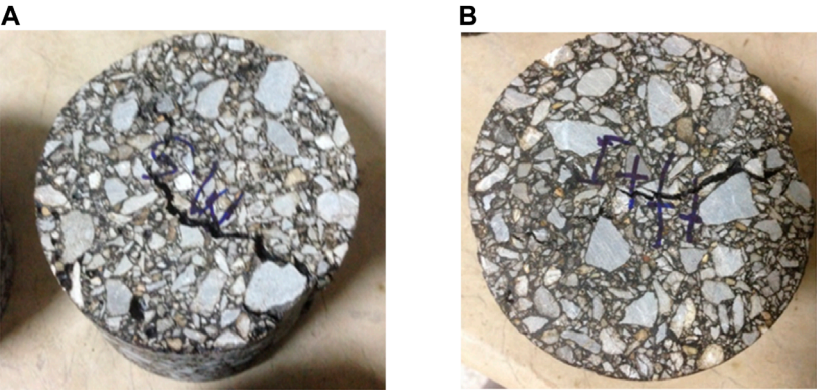
FIGURE 11
Damaged sample after **(A)** moisture testing **(B)** ITFT.

TABLE 4 Volumetric properties, stability, and flow correspond to the Marshall Mixes.

AC%	G_{mb}	G_{mm}	Unit Wt (mg/cm^3)	Va	VMA	VFA	Stability (KN)	Flow (mm)
3.5	2.32	2.49	2.32	6.83	14.2	50.9	10	2.5
4	2.35	2.47	2.35	4.86	13.5	63.3	11.9	2.7
4.5	2.37	2.46	2.37	3.66	12.95	71	12.7	3
5	2.38	2.45	2.38	2.86	13.2	78	11.9	3.4
5.5	2.39	2.42	2.39	2.59	13.6	82	9	4

3.2 Determination of BFT

This study determined the BFT using the Hveem surface area factor method, as detailed in the Shell Bitumen Handbook. The results, presented in Table 6 BFT for different, were calculated based on particle size distribution and specific surface area factors for each aggregate size, demonstrating the method's practical application in accurately determining the BFT for the asphalt mixtures analyzed. The binder content varies between 3.5% and 5%, and the BFT increases with higher binder content.

Similarly, BFT was also determined using the Hveem Method described by Zaniewski, Reyes, et al., which includes a formula for calculating BFT that uses the ratio of binder weight to aggregate weight, the surface area factor, and the specific gravity of the binder. The BFT values obtained using this method are presented in Table 7.

FIGURE 12
Relationship between **(A)** AC vs. Va **(B)** AC vs. VMA **(C)** AC vs. VFA **(D)** AC vs. Stability **(E)** AC vs. Flow.
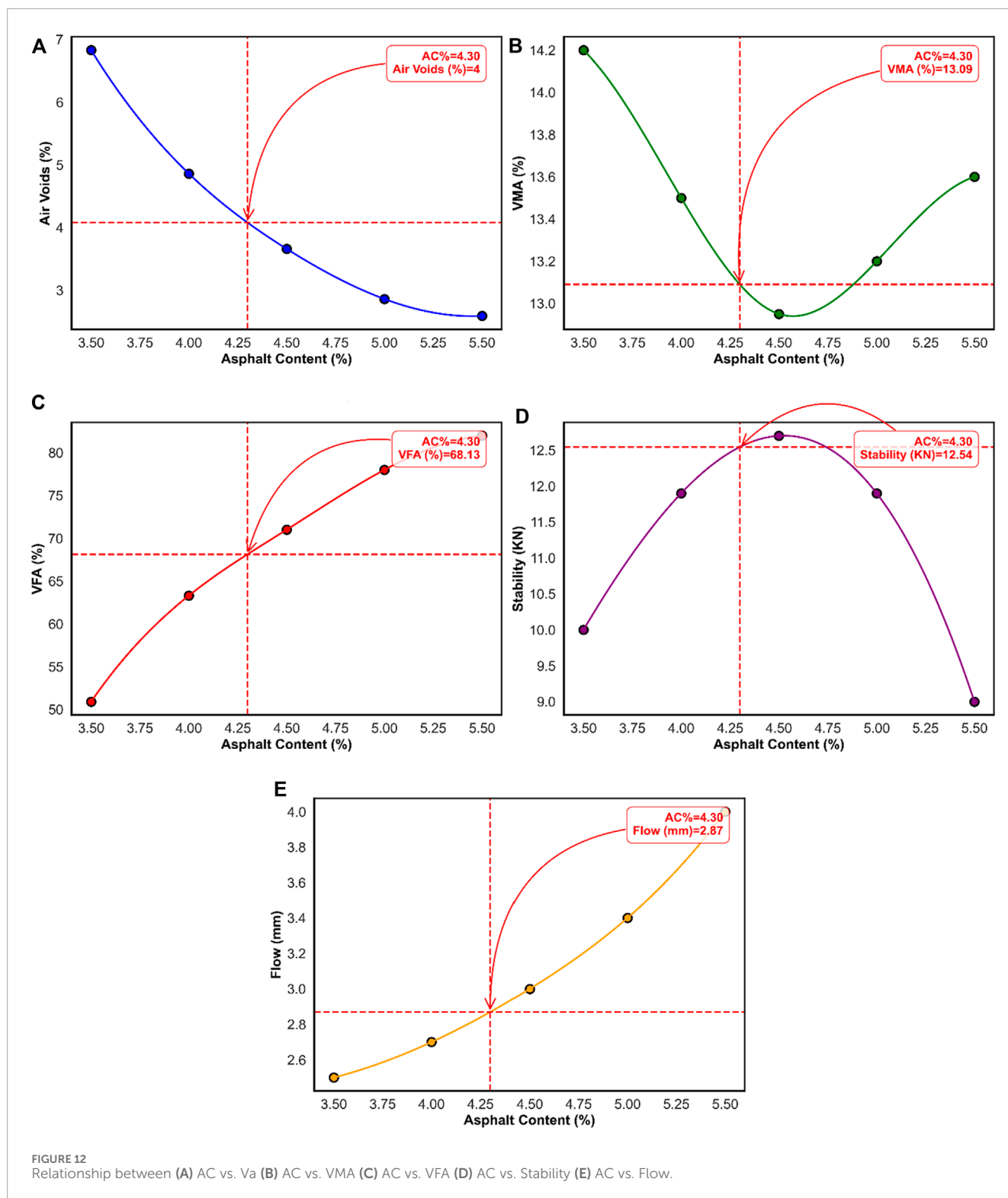
Both methods indicate that BFT increases with higher binder content, which aligns with expectations as more binder provides a thicker film around aggregates. However, the methods produce slightly different BFT values due to variations in calculation approaches:

Figure 14 shows a radar chart illustrating BFT across different binder content percentages obtained from both methods as explained earlier, and it also includes Marshall and Superpave OBC. This graph effectively demonstrates the importance of selecting an appropriate binder content to achieve optimal BFT. Higher binder content results in thicker binder films in both methods. This relationship is crucial for ensuring adequate binder coverage, impacting the durability and performance of asphalt mixtures. The Hveem surface area factor method provides a detailed calculation

TABLE 5 Volumetric properties for superpave mixes.

AC%	G_{mb}	G_{mm}	Va	VMA	VFA
3.5	2.31	2.52	8.04	14.13	43.13
4	2.32	2.46	5.92	14.44	59.01
4.5	2.34	2.45	3.88	13.88	72.02
5	2.40	2.44	1.94	12.07	83.93
5.5	2.41	2.44	1.10	12.08	90.90

based on specific aggregate sizes and their surface area factors. In contrast, the Zaniewski, Reyes et al. method uses a simplified approach based on the binder to aggregate weight ratio, which may lead to slightly higher BFT values. The comparison of the two methods highlights the significance of accurate BFT determination in asphalt pavement performance. Including BFT as a design criterion is essential for preventing moisture damage and enhancing the long-term durability of asphalt pavements. The study's results support the literature, emphasizing the importance of BFT in maintaining structural integrity under traffic loads (AASHTO, 2004).

3.3 Performance comparison test using DWT

The selection of the BFT criterion is essential for enhancing the durability and performance of asphalt mixtures, particularly under heavy traffic and adverse environmental conditions. BFT directly influences the binder distribution around aggregates, which is critical in reducing the risk of rutting, fatigue, and moisture damage, thereby potentially extending the pavement's service life as per previous studies. By calculating BFT values through two independent methods, a binder content of 3.5% was determined as optimal for achieving reduced BFT values. Consequently, three mix designs were prepared: a BFT-based design with 3.5% AC, a Marshall mix design with 4.3% OBC, and a Superpave mix design with 4.4% OBC.

The DWT test, set at 5,000 cycles or 10,000 wheel passes, was used to assess rutting resistance across the three mix designs. The BFT-based mix demonstrated superior rutting resistance, with a lower rut depth progression than both the Superpave and Marshall designs, as illustrated in Figure 15A. This improved performance suggests that the optimized BFT criterion at 3.5% binder content enhances the mix's ability to withstand high loads without significant deformation. The smaller BFT achieved at this binder content results in a more compact and stable mix structure, which distributes stress more evenly and minimizes rutting under repeated wheel loads.

In contrast, while effective in stability and ease of implementation, the Marshall mix design showed the highest rut depth, reaching an average of 3.645 mm, as depicted in Figure 15B. This value indicates that the Marshall design is more susceptible to

rutting, making it less suitable for high-stress conditions or heavy-traffic pavements. The Marshall design's performance aligns with its historical usage, where it has been effective in moderate traffic but may not offer the durability required for modern high-load applications.

3.4 Performance comparison test using UTM

A comprehensive performance comparison of the three asphalt mix designs, i.e., BFT, Marshall, and Superpave was carried out through several key mechanical tests. Each test provided insights into the distinct properties and advantages of the mix designs, including Resilience Modulus (Mr) to assess stiffness and load-bearing capacity, Indirect Tensile Strength (ITS) and Moisture Susceptibility to evaluate durability and resistance to moisture-induced damage, and Indirect Tensile Fatigue Test (ITFT) to determine fatigue life under repeated loading.

3.4.1 Resilience modulus test

The Mr is a critical parameter for evaluating the stiffness of asphalt mixtures and their capacity to recover after loading, directly affecting the pavement's ability to withstand repeated traffic loads. High Mr values indicate that a mix design can endure traffic stresses with minimal deformation, essential for maintaining pavement structure and longevity. The UTM was used to determine Mr for the BFT, Marshall, and Superpave mix designs, revealing distinctive performance characteristics that highlight the strengths and weaknesses of each approach.

Figure 16 illustrates the relationship between the OBC and the mean Mr for the three mix designs. In this graph, blue bars represent the OBC for each design, while the red line indicates mean Mr values. The Superpave mix design demonstrated the highest Mr value at 3,482 MPa, highlighting its suitability for heavy traffic loads and extreme conditions, where durability and resistance to deformation are essential. However, Superpave's required OBC of 4.4% may raise material costs, potentially impacting cost-effectiveness in budget-limited projects. Despite this, its high stiffness makes it an excellent choice when structural integrity is the priority.

In contrast, the Marshall mix design exhibited the lowest Mr at 3,443 MPa, even with a relatively high OBC of 4.3%. This more traditional mix design is well-suited to moderate traffic conditions, where stability rather than extreme load resistance is prioritized. Its ease of implementation and familiarity among engineers can make it an economical choice for less demanding environments, though its lower stiffness may lead to quicker deformation under heavy loads.

The BFT-based mix design, with a 3.5% binder content, achieved an Mr of 3,460 MPa, offering a balance between stiffness and flexibility. While slightly lower in stiffness than Superpave, the BFT mix's optimized binder distribution allows it to withstand load stresses efficiently, reducing the risk of cracking and deformation. This balance makes the BFT-based design a sustainable, cost-effective alternative for high-traffic applications, where comparable performance with reduced binder content is desired.
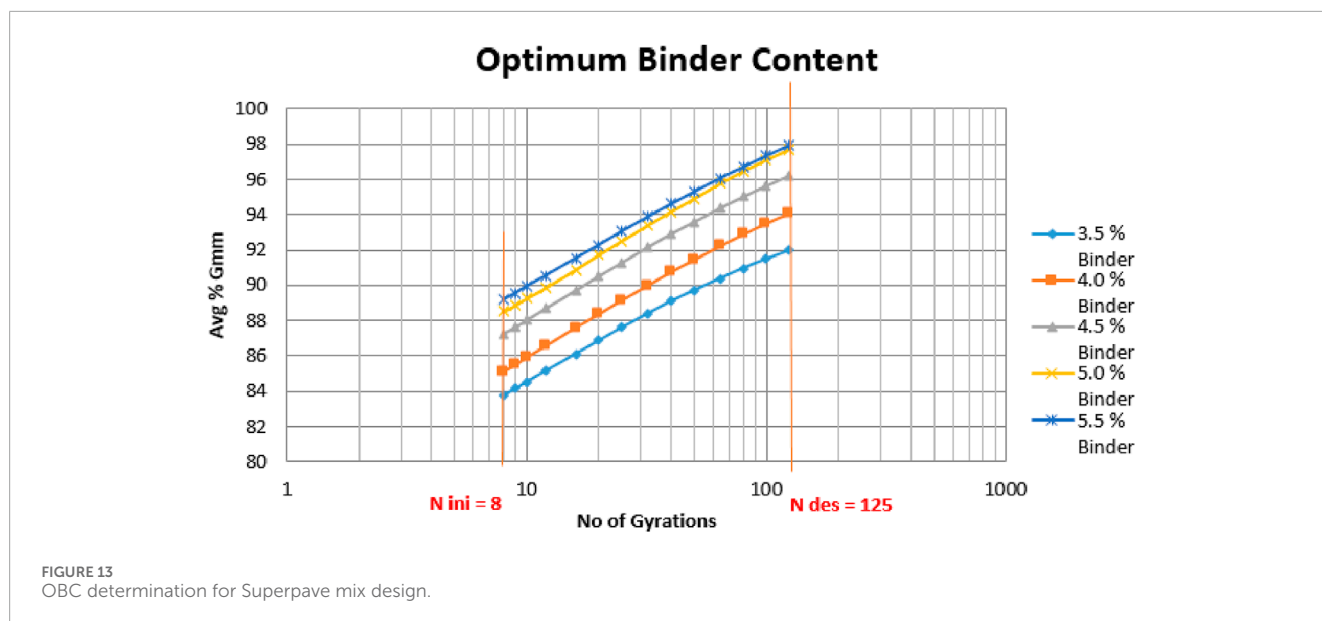
FIGURE 13
OBC determination for Superpave mix design.

TABLE 6 BFT for different AC using the Hveem surface area factor method.

Particle size (mm)	SAf	%Passing/100	%Passing*SAf	%binder	Gb	$\rho b = Gb*\rho w$	BFT (μm)
19	0.41	1	0.41	3.5	1.027	1,027	10.22878
12.5	0.41	0.825	0.33825	4	1.027	1,027	11.75092
9.5	0.41	0.7	0.287	4.5	1.027	1,027	13.28900
4.75	0.41	0.5	0.205	5	1.027	1,027	14.84327
2.36	0.82	0.3	0.246	4.3	1.027	1,027	12.67184
1.18	1.64	0.1	0.164	4.4	1.027	1,027	12.98010
0.075	32.77	0.055	1.80235				
			ΣSAf = 3.4526 (m^2/Kg)				

3.4.2 Indirect tensile strength and moisture susceptibility tests

The ITS and Moisture Susceptibility tests are essential for evaluating the durability and resistance of asphalt mixtures to moisture-induced damage, which is a critical factor in determining pavement longevity. These tests assess the TSR, a measure of a mixture's ability to retain tensile strength after moisture conditioning. Figure 17 provides a comparison of TSR values for the BFT, Marshall, and Superpave mix designs, along with their respective OBC.

The test results show that all three mix designs exhibit good moisture resistance, with varying levels of performance. The Superpave mix design achieved the highest TSR at 90.1%, which reflects excellent resistance to moisture-induced damage. This high TSR indicates that the Superpave mix retains a significant portion of its tensile strength after conditioning, making it highly suitable for regions with high moisture levels or frequent freeze-thaw cycles. However, this performance is achieved

with an OBC of 4.4%, leading to increased binder use, which may raise costs.

In comparison, the Marshall mix design achieved a TSR of 83.3% with an OBC of 4.3%. While this design demonstrates sufficient resistance to moisture, its lower TSR relative to Superpave indicates slightly reduced performance in moisture-prone environments. The Marshall mix remains suitable for moderate moisture conditions but may not offer the same durability under extreme environmental stress.

The BFT-based mix design, with a 3.5% binder content, achieved a TSR of 83.1%. This TSR indicates that the BFT mix retains 83.1% of its tensile strength after moisture conditioning, which is comparable to the Marshall mix despite the lower binder content. The BFT mix's ability to maintain strength with reduced binder content reflects a balanced approach to durability and cost-effectiveness, making it a practical choice for areas that require moderate moisture resistance without incurring high binder costs. The optimized binder distribution in the BFT design ensures that the mix retains

TABLE 7 BFT for different AC using the Hveem method described by Zaniewski, Reyes et al.

%binder	wt of agg (Kg)	wt of binder (Kg)	BFT (µm)
3.5	1.158	0.042	12.493
4	1.152	0.048	14.278
4.5	1.146	0.054	16.063
5	1.140	0.060	17.847
4.3	1.148	0.052	15.468
4.4	1.147	0.053	15.765

its integrity and strength even under wet conditions, supporting its long-term performance.

3.4.3 Indirect tensile fatigue test

The ITFT assesses the fatigue life of asphalt mixtures by applying repeated loading cycles until the material fails. Fatigue resistance is crucial for pavements subjected to heavy traffic, as it determines the material's ability to withstand cycles of stress without cracking. Figure 18 illustrates the mean cycles to failure for the BFT, Marshall, and Superpave mix designs, providing insights into their respective fatigue performance.

The ITFT results indicate that all three designs exhibit good fatigue resistance, with varying levels of performance. The Superpave mix design achieved the highest fatigue resistance, enduring 4,128 cycles to failure, indicating its suitability for high-stress applications and heavy traffic environments. This high cycle count demonstrates the Superpave mix's ability to resist cracking under repeated loading, which is particularly beneficial in regions with extreme traffic loads or environmental conditions.

In comparison, the Marshall mix design exhibited the lowest fatigue resistance, with an average of 3,129 cycles to failure. While this level of fatigue resistance may be adequate for moderate traffic conditions, the Marshall design's lower cycle count suggests it may be more susceptible to cracking and fatigue-related failure under heavy or frequent loading conditions. Consequently, the Marshall mix may be better suited for applications with lower traffic demands.

The BFT-based mix design, with an OBC of 3.5%, demonstrated a fatigue life of 3,297 cycles to failure. Although slightly lower than Superpave, this level of fatigue resistance indicates that the BFT-based design can effectively endure repeated loading cycles, making it a robust choice for high-traffic applications. The BFT mix's optimized binder content and balanced design allow it to withstand cyclic stress efficiently, reducing the risk of early fatigue failure. By achieving competitive fatigue resistance with a lower binder content, the BFT-based design supports cost-effective and durable pavement solutions.

The findings underscore the need for DOTs to adopt performance-based specifications, integrating BFT and advanced mix design methods to address the challenges posed by increased traffic and adverse conditions. The selection of BFT as a criterion in mix design is justified by its ability to improve rutting resistance, ensure balanced binder distribution, enhance durability, and provide comprehensive performance benefits. The results from the performance tests substantiate that BFT-based mix designs offer superior resilience and longevity, making it a critical parameter for optimizing asphalt pavement performance. This approach aligns with the need for high-performance pavements and supports sustainable and cost-effective construction practices.

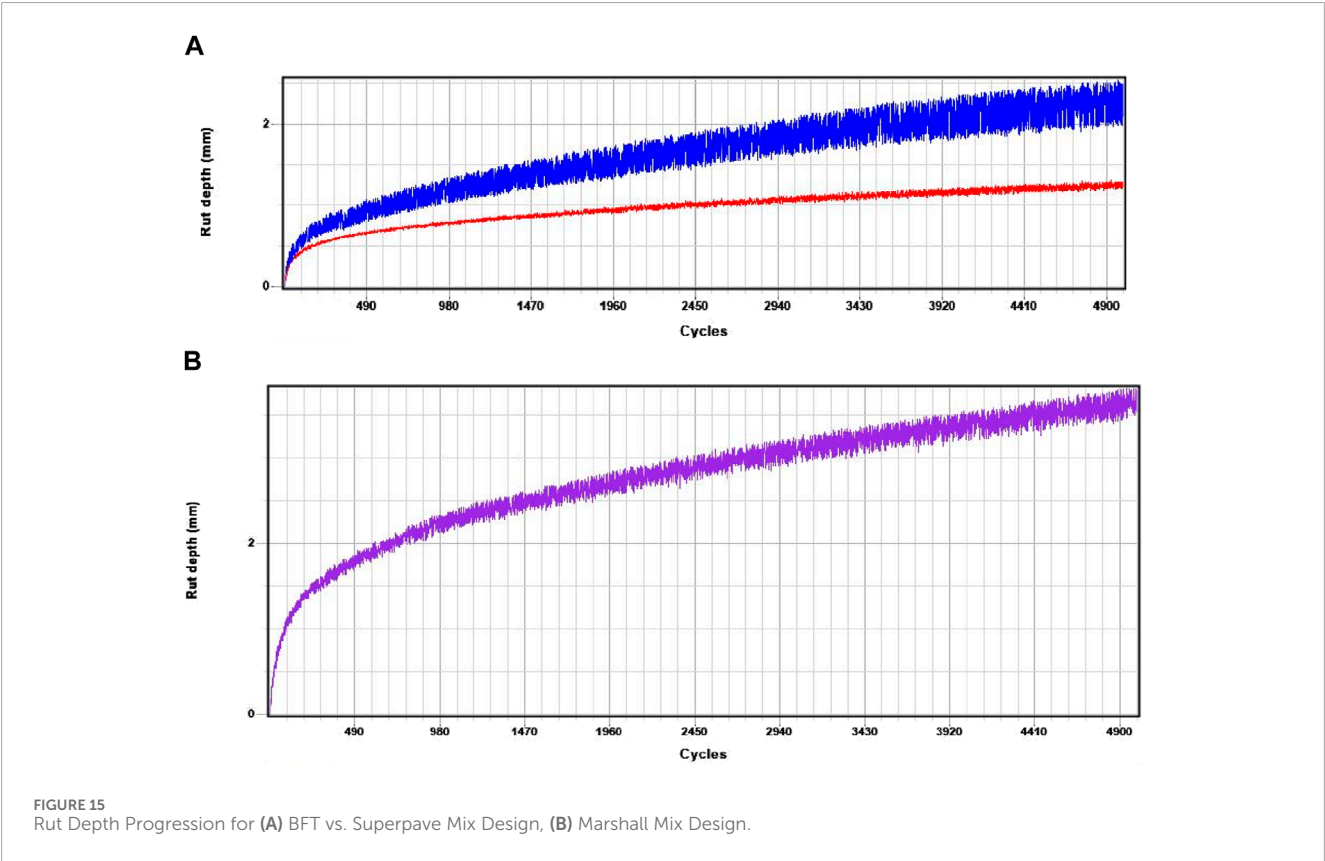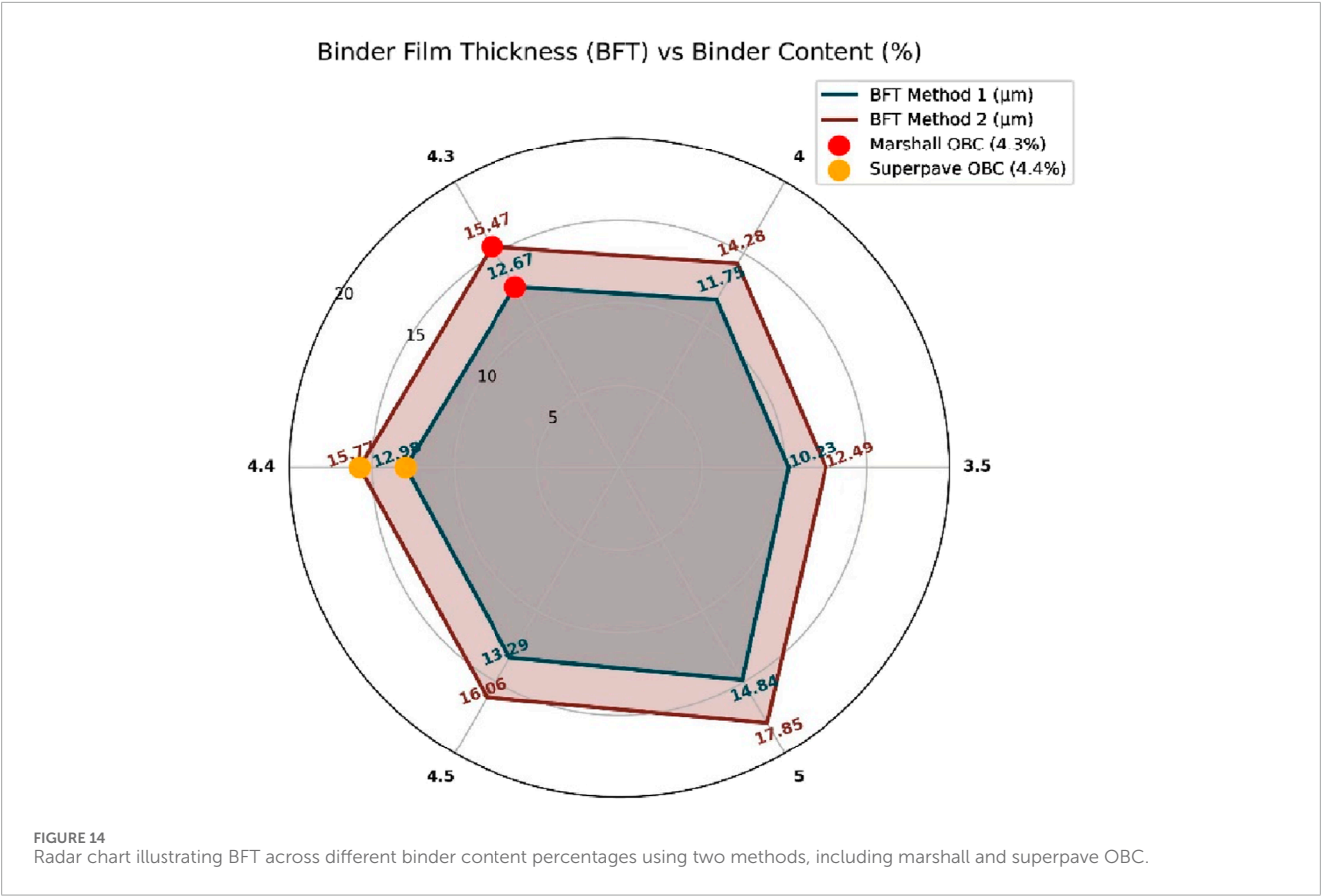## 3.5 Comparative analysis and limitations

The BFT-based mix design demonstrates several strategic advantages over both Superpave and Marshall designs across key performance metrics, offering a balanced approach that combines cost-efficiency with effective performance in stiffness, moisture resistance, and fatigue life.

In terms of Mr, the BFT mix achieves near-equivalent stiffness to Superpave but at a lower binder content (3.5% compared to Superpave's 4.4%), making it a more economical option. The balanced stiffness and flexibility of the BFT mix help reduce the risk of cracking and deformation over time, while Superpave's higher stiffness may lead to brittleness. Unlike the Marshall mix, which has the lowest Mr despite a higher binder content, the BFT mix optimizes binder distribution to provide efficient load-bearing capacity and durability.

For Moisture Susceptibility and ITS, the BFT mix achieves a comparable TSR to Marshall (83.1% vs. 83.3%) but with reduced binder usage, making it more cost-effective. Although Superpave provides the highest TSR, this performance comes at the expense of a higher binder content. The BFT mix, with its optimized binder usage, offers balanced moisture resistance, allowing it to retain strength under moderate moisture exposure without incurring high material costs.

In terms of Fatigue Resistance as measured by the ITFT, the BFT mix provides substantial fatigue life (3,297 cycles), closely approaching Superpave's performance at a lower binder cost. While Superpave demonstrates the highest fatigue life, its greater stiffness can increase susceptibility to cracking over time. The BFT design's flexibility helps mitigate fatigue cracking under repeated loads, making it a durable choice for variable loading conditions. Compared to Marshall, which has the lowest cycles to failure, the BFT design improves fatigue performance with a lower binder content, offering better durability without additional costs.

Despite its advantages, the BFT-based mix design has some limitations. The slightly lower stiffness compared to Superpave may make it less suitable for extreme, high-stress applications where maximum rigidity is essential. Additionally, while the BFT mix achieves good moisture resistance, it does not surpass Superpave in this aspect, which could be a consideration for regions with very high moisture levels or freeze-thaw cycles. Lastly, the BFT design requires precise control in binder distribution to optimize film thickness, which may introduce complexity in mix preparation and consistency, potentially limiting its application in areas where such control cannot be consistently maintained.

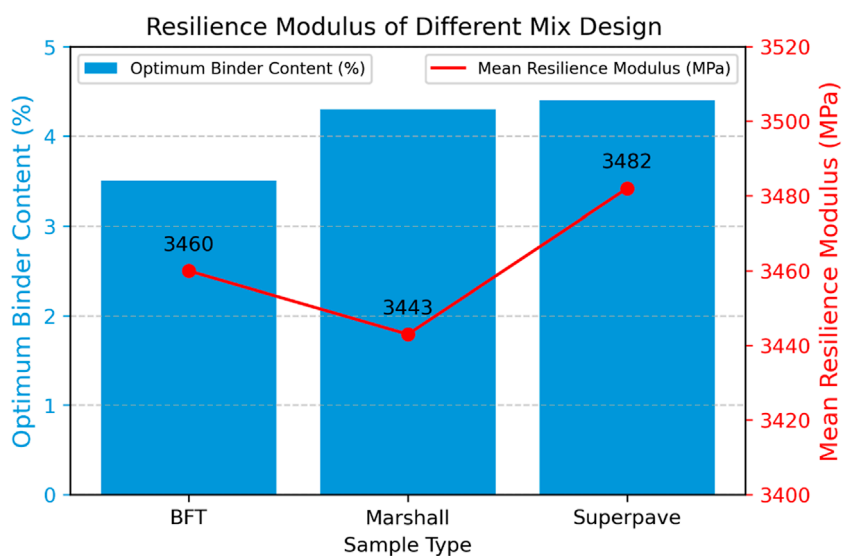**FIGURE 14**
Radar chart illustrating BFT across different binder content percentages using two methods, including marshall and superpave OBC.

FIGURE 15
Rut Depth Progression for **(A)** BFT vs. Superpave Mix Design, **(B)** Marshall Mix Design.

FIGURE 16
Comparison of Mr and OBC for BFT, marshall, and superpave mix designs.
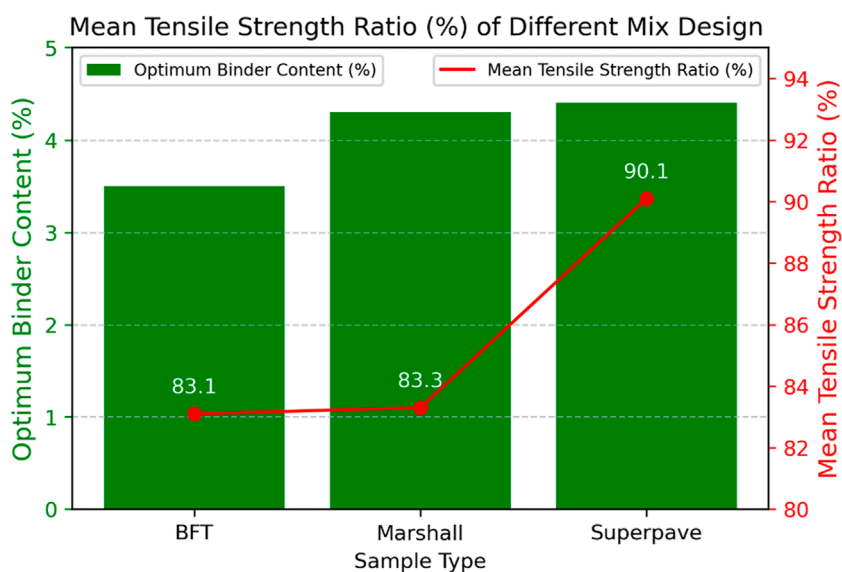
FIGURE 17
Comparison of mean tensile strength ratio and OBC for BFT, marshall, and superpave mix designs.

4 Conclusions and recommendations

This study aimed to test various design mixes and criteria, focusing on BFT. Detailed analysis of BFT was conducted using both analytical and experimental methods. The analytical calculation of BFT yielded an OBC of 3.5%. For Marshall Mix designs, samples with varying binder percentages determined an OBC of 4.3%. Similarly, samples were prepared with varying binder percentages for Superpave mix designs, resulting in an OBC of 4.4%, corresponding to 96% of Gmm. Once the OBC values were

established, samples were prepared for performance testing. These samples were subjected to rutting tests using a DWT and various UTM tests, including Mr, ITS, Moisture Susceptibility, and ITFT. The results of these tests led to the following conclusions and recommendations.

- By optimizing the BFT, the mix design ensures better distribution and adhesion of the binder around aggregates, enhancing the durability and performance of the asphalt pavement.
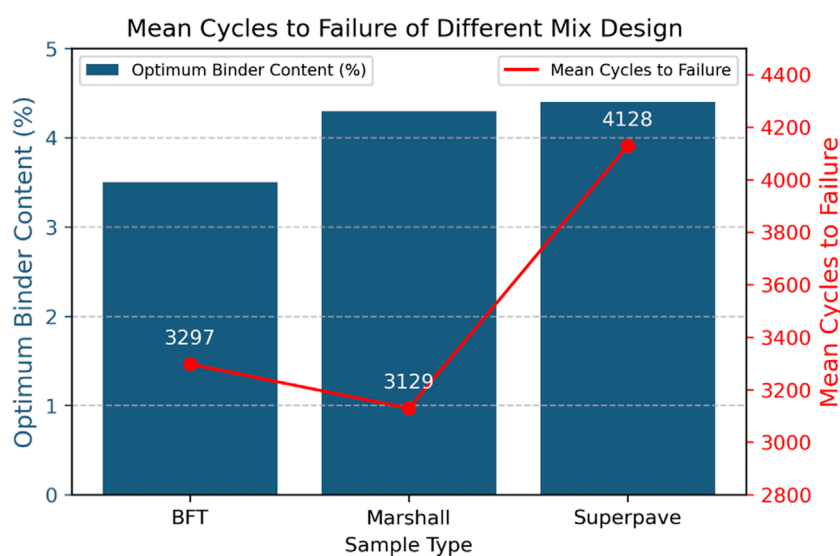
FIGURE 18
Comparison of mean cycles to failure and OBC for BFT, marshall, and superpave mix designs.

- The BFT criterion helps balance performance parameters, such as rutting resistance, stiffness, moisture susceptibility, and fatigue life.
- Incorporating BFT into the mix design allows for a comprehensive evaluation of asphalt mixtures under various performance conditions, leading to more resilient and long-lasting pavements.
- In rutting tests using the DWT, the BFT-based mix design with 3.5% binder content shows superior rutting resistance compared to Superpave and marshall mix design, which is crucial for pavements subjected to heavy traffic loads. The smaller BFT effectively minimizes rutting depth.
- Mr values indicate that all mix designs exhibit similar stiffness, indicating that the BFT criterion does not compromise the pavement's structural integrity.
- Superpave Mix showcased superior performance in ITS and Moisture Susceptibility Tests, with Marshall Mix and BFT Mix trailing behind. The BFT-based mix design shows good moisture resistance, ensuring durability in wet conditions.
- In the ITFT, the Superpave mix design shows the best fatigue performance, while the BFT mix design provides substantial fatigue resistance. This indicates that the BFT-based design can effectively withstand repeated loading cycles, reducing the risk of fatigue-related failures.
- Overall, BFT performed satisfactorily across most tests and excelled in the dry DWT test under room temperature conditions. Moreover, it is noteworthy that BFT mixes have the lowest OBC, implying a reduced need for binders.

Future research should validate BFT as a design criterion across various environmental conditions and traffic loads. Long-term performance studies under field conditions are essential to confirm the laboratory results. Additionally, optimizing BFT determination through advanced simulation models and exploring new materials or additives can lead to significant advancements in mix design. Addressing the limitations of this study, such as specific environmental conditions and the scale of the experimental setup, will be vital in refining the use of BFT in asphalt mix design. Interdisciplinary approaches, including collaboration with material scientists and incorporating nanomaterials, could further enhance binder properties and pavement performance, making BFT a robust criterion for future mix designs.

Data availability statement

The raw data supporting the conclusions of this article will be made available by the authors, without undue reservation.

Author contributions

MAK: Conceptualization, Data curation, Formal Analysis, Investigation, Methodology, Validation, Visualization, Writing–original draft, Writing–review and editing. MSK: Conceptualization, Formal Analysis, Software, Validation, Visualization, Writing–review and editing. BN: Conceptualization, Data curation, Formal Analysis, Investigation, Methodology, Software, Validation, Visualization, Writing–original draft, Writing–review and editing. AK: Data curation, Formal Analysis,

Investigation, Visualization, Writing–review and editing, Software. MMSS: Funding acquision, Validation, Project administration, Resources, Supervision, Writing–review and editing. MA: Formal Analysis, Validation, Resources, Writing–review and editing WQ: Formal Analysis, Project administration, Resources, Validation, Writing–review and editing. RAG-L: Formal Analysis, Validation, Writing–review and editing.

Funding

Conflict of interest

The authors declare that the research was conducted in the absence of any commercial or financial relationships that could be construed as a potential conflict of interest.

Publisher's note

All claims expressed in this article are solely those of the authors and do not necessarily represent those of their affiliated organizations, or those of the publisher, the editors and the reviewers. Any product that may be evaluated in this article, or claim that may be made by its manufacturer, is not guaranteed or endorsed by the publisher.

References

Aashto, M. P. 2 (2004). Standard specification for Superpave volumetric mix design. Available at: https://www.document-center.com/standards/show/AASHTO-MP2.1

AASHTO, T. 316. (2019). AASHTO t316-standard method of test for viscosity determination of asphalt binder using rotational viscometer. 1–5.

AASHTO, T. 49-15. (2012). Test method for penetration of bituminous materials. 15:1–5.

ALDOT-361-88 (2005). Resistance of compacted bituminous mixture," in *Testing manual bureau of materials and tests* (Montgomery, AL: Albama Dept. of transportation), 1–5.

Al-Khateeb, G. G. (2018). Conceptualizing the asphalt film thickness to investigate the Superpave VMA criteria. *Int. J. Pavement Eng.* 19 (11), 957–965. doi:10.1080/10298436.2016.1224414

Al-Khateeb, G. G., and Aroon, S. (2019). Mixture-property-independent asphalt film thickness model. *Mater. Today Commun.* 19 (November 2017), 482–486. doi:10.1016/j.mtcomm.2017.11.007

Asphalt Institute MS-2 (1993). *Asphalt mix design methods.* Lexington, KY: Asphalt Institute.

ASTM D7369-11. (1860). Standard test method for determining the resilient Modulus of bituminous mixtures by Indirect tension Test1. i:4–5. doi:10.1520/D7369-11.2

ASTM C 127-08 (2008). *Standard test method for density, relative density (specific gravity), and absorption of coarse aggregate,* 1–7.

ASTM C128/C128M (2001). "Standard test method for density, relative density (specific gravity), and absorption of fine aggregate," in *ASTM International.* West Conshohocken, PA: ASTM International, 1–6. Available at: www.astm.org,or.

ASTM D 113-99. (2000). Standard test method for ductility of bituminous materials. 08:13–4. doi:10.1520/C1709-18

ASTM D2041 (2018). "Standard test method for theoretical maximum specific gravity and density of bituminous paving mixtures," in *Designation* (West Conshohocken, PA: ASTM International), 778–87. *(Reapproved 2004), i:3–5.*

ASTM D2726. (2013). "Standard test method for bulk specific gravity and density of non-absorptive compacted asphalt mixtures, 1–3. doi:10.1520/D2726

ASTM D3143/D3143M – 13 (2013). Standard test method for flash point of cutback asphalt with tag open-cup. *Astm* 05, 1–6. doi:10.1520/D3143

ASTM D36-06 (2008). "Standard test method for softening point of bitumen (Ring-and-Ball apparatus)," in *ASTM International.* West Conshohocken, Pennsylvania: ASTM International, 50–54. doi:10.1520/mnl10830m

ASTM D4402 (2016). "Standard test method for viscosity determination of asphalt at elevated temperatures using a rotational viscometer," in *ASTM International.* West Conshohocken, Pennsylvania: ASTM International 14, 1–5.

ASTM D4791-10. (2010). "Standard test method for flat particles, elongated particles, or flat and elongated particles in coarse aggregate," 1–6. doi:10.1520/D4791-10.2

ASTM D 6926 (2014). Standard practice for preparation of bituminous specimens using marshall. *Annu. Book Am. Soc. Test. Materiasl ASTM Stand. i Sept.,* 1–6. doi:10.1520/D6926-10.2

ASTM D6931-07. (2022). "Standard test method for Indirect tensile (IDT) strength of bituminous mixtures. 1–4. doi:10.1520/D6931-07.2

ASTM D7460-08. (2010). "Standard test method for determining fatigue failure of compacted asphalt concrete subjected to repeated flexural bending, i:5–7. doi:10.1520/D7460-08.2

Azzam, M. O. J., Al-Ghazawi, Z., and Al-Otoom, A. (2016). Incorporation of Jordanian oil shale in hot mix asphalt. *J. Clean. Prod.* 112 (November), 2259–2277. doi:10.1016/j.jclepro.2015.10.128

BS 812-110 (1990). Methods of determination of aggregate crushing value (ACV). *Br. Stand.* 12.

BS 812-112 (1990). *Methods for determination of aggregate impact value (AIV),* 8. Available at: https://www.en-standard.eu/bs-812-112-1990-testing-aggregates-method-for-determination-of-aggregate-impact-value-aiv/.

Cavalli, M. C., Partl, M. N., and Poulikakos, L. D. (2017). Measuring the binder film residues on black rock in mixtures with high amounts of reclaimed asphalt. *J. Clean. Prod.* 149 (April), 665–672. doi:10.1016/j.jclepro.2017.02.055

Dhir, R. K., de Brito, J., Lynn, C. J., and Silva, R. V. (2018). "Geotechnics and road pavements," in *Sustainable construction materials,* 197–237. doi:10.1016/B978-0-08-100997-0.00006-3

Dhir, R. K., Ghataora, G. S., and Lynn, C. J. (2017). "Epilogue," in *Sustainable construction materials,* 261–263. doi:10.1016/B978-0-08-100987-1.00010-X

Elseifi, M. A., Al-Qadi, I. L., Yang, S.-H., and Carpenter, S. H. (2008). Validity of asphalt binder film thickness concept in hot-mix asphalt. *Transp. Res. Rec. J. Transp. Res. Board* 2057 (1), 37–45. doi:10.3141/2057-05

Ghuzlan, K. A., Al-Mistarehi, B. W., and Al-Momani, A. S. (2020). Rutting performance of asphalt mixtures with gradations designed using bailey and conventional Superpave methods. *Constr. Build. Mater.* 261, 119941. doi:10.1016/j.conbuildmat.2020.119941

Gu, F., Xie, J., Vuye, C., Wu, Ya, and Zhang, J. (2023). Synthesis of geopolymer using alkaline activation of building-related construction and demolition wastes. *J. Clean. Prod.* 420 (July), 138335. doi:10.1016/j.jclepro.2023.138335

Gu, F., Zhang, Y., Luo, X., Sahin, H., and Lytton, R. L. (2017). Characterization and prediction of permanent deformation properties of unbound granular materials for pavement ME design. *Constr. Build. Mater.* 155, 584–592. doi:10.1016/j.conbuildmat.2017.08.116

Harvey, J., Liu, A., Zhou, J., Signore, J. M., Coleri, E., and He, Y. (2015). Superpave implementation phase II: comparison of performance-related test results, no. July 2014.

Jiang, J., Ying, Li, Zhang, Y., and Bahia, H. U. (2022). Distribution of mortar film thickness and its relationship to mixture cracking resistance. *Int. J. Pavement Eng.* 23 (3), 824–833. doi:10.1080/10298436.2020.1774767

Kandhal, P. S., and Sanjoy, C. (1996). Effect of asphalt film thickness on short- and long-term aging of asphalt paving mixtures. *Transp. Res. Rec. J. Transp. Res. Board* 1535 (1), 83–90. doi:10.1177/0361198196153500111

Karim, F., Hussain, J., and Hafeez, I. (2021). Estimating the asphalt binder film thickness using scanning electron microscope and energy dispersive X-ray spectroscopy. *Adv. Mater. Sci. Eng.* 2021, 16. doi:10.1155/2021/8894970

Lin, P., Liu, X., Ren, S., Xu, J., Li, Yi, and Li, M. (2023). Effects of bitumen thickness on the aging behavior of high-content polymer-modified asphalt mixture. *Polymers* 15 (10), 2325. doi:10.3390/polym15102325

Lu, D., Liang, J., Du, X., Ma, C., and Gao, Z. (2019). Fractional elastoplastic constitutive model for soils based on a novel 3D fractional plastic flow rule. *Comput. Geotech.* 105, 277–290. doi:10.1016/j.compgeo.2018.10.004

Lv, J., Zhancheng, Xu, Yin, Y., Zhang, J., Sun, X., and Wu, C. (2018). Comparison of asphalt mixtures designed using the marshall and improved GTM methods. *Adv. Mater. Sci. Eng.* 2018, 1–7. doi:10.1155/2018/7328791

Martinez Soto, F. (2018). Volumetric mix-design optimization of bituminous rubber-mixtures in railway sub-ballast. *Int. J. Eng. Sci. and Res. Technol.* 7 (1), 483–507. doi:10.5281/ZENODO.1158653

Miranda, H. M. B., Batista, F. A., Neves, J., and Antunes, M. de L. (2021). Influence of the aggregate skeleton matrix and volumetric composition on the resistance of stone mastic asphalt to permanent deformation. *Road Mater. Pavement Des.* 22 (11), 2538–2551. doi:10.1080/14680629.2020.1773303

Monyakeng, G. M. (2022). "Los-angeles abrasion test, 0–12. doi:10.13140/RG.2.2.14470.04169

Pérez-Jiménez, F., Martínez, A. H., Miró, R., Hernández-Barrera, D., and Araya-Zamorano, L. (2014). Effect of compaction temperature and procedure on the design of asphalt mixtures using marshall and gyratory compactors. *Constr. Build. Mater.* 65 (August), 264–269. doi:10.1016/j.conbuildmat.2014.04.135

Remišová, E. (2015). Effect of film thickness on resistance to permanent deformation in asphalt mixtures. *Baltic J. Road Bridge Eng.* 10 (4), 333–339. doi:10.3846/bjrbe.2015.42

Roberts, F. L., Kandhal, P. S., Brown, E. R., Lee, D. Y., and Kennedy, T. W. (1996). *Hot mix asphalt materials, mixture design, and construction.* Lanham, MD: National Asphalt Pavement Association (NAPA).

Rudenko, O., Galkina, D., Sadenova, M., Beisekenov, N., Kulisz, M., and Begentayev, M. (2024). Modelling the properties of aerated concrete on the basis of raw materials and ash-and-slag wastes using machine learning paradigm. *Front. Mater.* 11 (October), 1–21. doi:10.3389/fmats.2024.1481871

Sims, I. (2016). The Shell bitumen Handbook. *Proc. Institution Civ. Eng. - Constr. Mater.* 169, 44. doi:10.1680/jcoma.15.00061

Souza, T. D. de, Enríquez-León, A. J., Mesquita, A. R., Gomes, O. da F. M., Ulsen, C., Underwood, B. S., et al. (2024). Characterization of binder, mastic, and FAM film thickness within asphalt concrete mixtures. *Constr. Build. Mater.* 421 (March), 135595. doi:10.1016/j.conbuildmat.2024.135595

Sukkari, A., Ghazi, Al K., Ziada, W., and Ezzat, H. (2022). Estimating asphalt film thickness in asphalt mixtures using microscopy to further enhance the performance of UAE roadways. In *Advances in road infrastructure and mobility*, 87–96. Springer, Cham. doi:10.1007/978-3-030-79801-7_7

Sun, Li, Wang, G., and Zhang, C. (2024). Experimental investigation of a novel high performance multi-walled carbon nano-polyvinylpyrrolidone/silicon-based shear thickening fluid damper. *J. Intelligent Material Syst. Struct.* 35 (6), 661–672. doi:10.1177/1045389X231222999

Wang, K., Cao, J., Ye, J., Qiu, Z., and Wang, X. (2024). Discrete element analysis of geosynthetic-reinforced pile-supported embankments. *Constr. Build. Mater.* 449 (April), 138448. doi:10.1016/j.conbuildmat.2024.138448

Zhang, S., Tan, D., Zhu, H., Pei, H., and Shi, B. (2024). Rheological behaviors of Na-montmorillonite considering particle interactions: A molecular dynamics study. *JRMGE.* doi:10.1016/j.jrmge.2024.07.003

frontiers | Frontiers in Materials

Check for updates

Corrigendum: Performance optimization of asphalt pavements using binder film thickness as a criterion in innovative mix design compared to Marshall and Superpave methods

Muhammad Adeel Khan[1], Muhammad Salman Khan[1]*,
Bilal Nasir[2], Asad Khan[1], Mohanad Muayad Sabri Sabri[3],
Mahmood Ahmad[4,5]*, Wajeeha Qamar[6] and
Roberto Alonso Gonzalez-Lezcano[7]

[1]Department of Bridge Engineering, College of Civil Engineering, Tongji University, Shanghai, China,
[2]Department of Transportation Engineering, H-12 Campus, NUST Islamabad, Islamabad, Pakistan,
[3]Peter the Great St. Petersburg Polytechnic University, St. Petersburg, Russia, [4]Institute of Energy
Infrastructure, Universiti Tenaga Nasional, Kajang, Malaysia, [5]Department of Civil Engineering,
University of Engineering and Technology Peshawar (Bannu Campus), Bannu, Pakistan, [6]Department
of Civil Engineering, Institute of Engineering and Fertilizer Research, Faisalabad, Pakistan, [7]Department
of Architecture and Design, Escuela Politécnica Superior, Montepríncipe Campus, Universidad San
Pablo-CEU, CEU Universities, Madrid, Spain

A Corrigendum on

Performance optimization of asphalt pavements using binder film
thickness as a criterion in innovative mix design compared to Marshall
and Superpave methods

by Khan MA, Khan MS, Nasir B, Khan A, Sabri MMS, Ahmad M, Qamar W and Gonzalez-Lezcano
RA (2025). Front. Mater. 11:1488310. doi: 10.3389/fmats.2024.1488310

In the published article, there was an error in the **Funding** statement. The correct
Funding statement appears below.

Funding

The authors apologize for this error and state that this does not change the scientific
conclusions of the article in any way. The original article has been updated.

Publisher's note

All claims expressed in this article are solely those of the authors and do not necessarily represent those of their affiliated organizations, or those of the publisher, the editors and the reviewers. Any product that may be evaluated in this article, or claim that may be made by its manufacturer, is not guaranteed or endorsed by the publisher.

frontiers | Frontiers in Materials

Research on the effect of lithology of fine aggregates on the performance of rubberized asphalt mixtures

Lihao Zeng[1]*, Honggang Zhang[1]*, Shuo Jiang[2]*, Hui Huang[1], Baolin Xiong[3] and Haitao Yuan[3]

[1]Guangxi Transportation Science and Technology Group Co., Ltd., Nanning, China, [2]School of Traffic and Transportation Engineering, Changsha University of Science and Technology, Changsha, China, [3]Guangxi Jiaoke New Materials Technology Co., Ltd., Nanning, China

This study aims to investigate the effect of fine aggregate lithology on the performance of rubberized asphalt mixtures. SEM, XRD, and contact angle tests were used to analyze the microscopic physical and chemical properties of 0−3-mm grain-size diabase and limestone. The performance characteristics of two types of ARAC-13 rubberized asphalt mixtures (with the diabase coarse aggregates and diabase fine aggregates, and diabase coarse aggregates and limestone fine aggregates, respectively) were then compared through conventional high-temperature water stability performance tests, uniaxial penetration tests, and accelerated loading abrasion tests. The results show that the surface roughness, chemical composition, and surface adhesion properties of limestone are better than those of diabase, and the surface roughness of limestone is 13.9% higher than that of diabase, and the surface adhesion energy is 6.4% higher. However, the results show relatively small differences between the asphalt mixtures with the diabase coarse aggregates and diabase fine aggregates and those with diabase coarse aggregates and limestone fine aggregates in the conventional water stability performance test and the high-temperature performance test. Furthermore, the strength reaches 90% when cured for 8 h for limestone and 12 h for diabase, with the curing rate being faster for limestone. The anti-abrasion performance of diabase specimens is superior to that of limestone specimens, but the anti-abrasion decay performance is the opposite. In summary, it can be observed that limestone fine aggregate shows better adhesion performance with asphalt than diabase fine aggregate, and it was recommended that diabase coarse aggregate and limestone fine aggregate be used to improve the asphalt−aggregate interface and enhance the road performance of the asphalt pavement.

1 Introduction

Rubber-modified asphalt is a mature, environmentally friendly pavement material in China, known for its good performance advantages in noise reduction, anti-skid properties, high- and low-temperature resistance, fatigue resistance, and other road performance aspects. Therefore, it has been widely used for decades (Xie et al., 2022; Zhao et al., 2023; Zhang et al., 2021; Peng et al., 2024). For example, rubberized asphalt pavement has been applied to more than 2000 km of highways, national and provincial trunk lines, and other projects in Guangxi from 2012 to 2023. Over this period, a mature construction technology system of Guangxi rubberized asphalt pavement was developed after more than 10 years of engineering practice. Aggregate is the most used material in road construction, and it can be classified into coarse and fine aggregates based on the particle size. Therefore, the properties and quantity of fine aggregate have different effects on the performance of asphalt mixtures. However, due to the different raw materials of the aggregates used in some new highways, the time of occurrence, type, and the evolution of damage during the service operation are significantly different (Huang et al., 2022; Li et al., 2020; Wang et al., 2022; Stukhlyak et al., 2015). Some rubberized asphalt pavement construction projects have faced technical problems, such as insufficient adhesion between the asphalt and aggregate and difficulties in compaction of the mixture, resulting in loose pavement, rutting, and other forms of damage shortly after opening to traffic, as shown in Figure 1. Therefore, it is essential to study the effect of fine aggregate on the performance of the rubberized asphalt mixtures to improve the mechanical properties of these mixtures and enhance the road performance of rubberized asphalt pavements.

Many studies show that aggregate affects the properties of asphalt mixtures in multiple dimensions. DelRio-Prat et al. (DelRio-Prat et al., 2010; Ingunza et al., 2013) investigated the effect of aggregate shape characteristics on the modulus of elasticity of asphalt mixtures, and the results showed that asphalt mixes with rounded aggregates are easy to compact, but it will result in a reduction of the modulus of elasticity of the mixture. Jamkar and Rao (Jamkar and Rao, 2004) suggested that the surface texture of the aggregates and the proportion of crushed gravel in the broken surface have a greater effect on the properties of the mixture. Prudêncio et al. (Prudêncio et al., 2013) investigated the correlation between this metric and asphalt mortar based on the metrics of fine aggregate shape characteristics obtained using a simple digital image analysis method and found that the measured metrics have a significant effect on the flowability of asphalt mortar. Ingunza et al. (2013) investigated the effect of aggregate shape characteristics on the modulus of elasticity of asphalt mixtures and found that needle-like particles are detrimental to the compaction of asphalt mixtures, and aggregates with rounded shapes are more conducive to compaction but reduce the modulus of elasticity values. Cheung and Dawson (2002) found that the angularity of the coarse aggregate is the main factor affecting the ultimate shear strength and permanent deformation. Mahboub et al. (2001) used Kentucky limestone with different contents of needle flake for asphalt mixture performance analysis and concluded that the asphalt mixture properties were significantly affected when the needle flake particle content exceeds 40%. Habal and Singh (2017) tested the water stability properties of three types of warm mix asphalt (WMA) using the surface free energy method test with two types of aggregates, namely, granite and limestone. The results showed a correlation between the elemental composition of the asphalt and the surface free energy parameter; the comparison revealed that limestone mixes had better resistance to water damage than granite aggregates. Wang et al. (2011) conducted abrasion tests on mixture specimens prepared from coarse and fine aggregates with different abrasion properties and tested the long-term skid resistance using the Prufstand Wehner/Schulze (PWS) dynamic coefficient of friction tester. It was found that the higher the abrasion value of the

FIGURE 1
Loose and rutted new asphalt pavement.

TABLE 1 Rubberized asphalt index test results.

Performance indicator	180°C Brinell viscosity/Pa-s	Softening point/°C	Elongation (5°C, 5 cm/min)/cm	Needle penetration at 25°C/0.1 mm	Elasticity recovery/%	Relative density
Test results	2.67	73.0	8.5	40	85	1.044

TABLE 2 Coarse aggregate performance index.

Mineral	Water absorption (%)	Apparent relative density	Gross volume relative density
1# Coarse aggregate (10–15) mm	0.27	3.040	3.016
2# Coarse aggregate (5–10) mm	0.31	3.054	3.025
Technical requirement	≤3.0	≥2.50	-

TABLE 3 Mineral screening test results.

Mineral	Percentage (%) of mass passing through the following sieve holes (mm)												
	31.5	26.5	19	16	13.2	9.5	4.75	2.36	1.18	0.6	0.3	0.15	0.075
Diabase 1[#] coarse aggregate (10–15) mm	100.0	100.0	100.0	99.8	80.3	14.9	0.2	0.2	0.2	0.2	0.2	0.2	0.2
Diabase 2[#] coarse aggregate (5–10) mm	100.0	100.0	100.0	100.0	100.0	95.5	2.9	1.2	1.2	1.2	1.2	1.2	1.2

TABLE 4 Fine aggregate properties.

Mineral	Water absorption (%)	Apparent relative density	Gross volume relative density
Diabase fine aggregate (geology) 3#(0~5)mm	—	3.012	2.971
Limestone mechanized sand 4#(0~5)mm	—	2.699	2.672
Mineral powder (0~0.6)mm	—	2.707	—
Technical requirement	—	≥2.50	—

Note: In this target proportion design, the gross bulk relative density of 3[#] and 4[#] fine aggregates is replaced by the gross bulk relative density of their sieved (2.36–4.75) mm portion.

TABLE 5 Fine aggregate sieve test results.

Mineral	Percentage (%) of mass passing through the following sieve holes (mm)												
	31.5	26.5	19	16	13.2	9.5	4.75	2.36	1.18	0.6	0.3	0.15	0.075
Diabase 3[#] fine aggregate (0–5) mm	100.0	100.0	100.0	100.0	100.0	100.0	100.0	80.9	53.9	36.3	22.7	16.3	11.2
Limestone 4[#] fine aggregate (0–5) mm	100.0	100.0	100.0	100.0	100.0	100.0	100.0	84.4	59.3	40.8	26.7	21.0	17.2
Mineral powder	100.0	100.0	100.0	100.0	100.0	100.0	100.0	100.0	100.0	100.0	100.0	100.0	98.0

TABLE 6 Mineral grade composition design table.

Material composition	Percentage (%) of mass passing through the following sieve holes (mm)												
	31.5	26.5	19	16	13.2	9.5	4.75	2.36	1.18	0.6	0.3	0.15	0.075
1# data: 2# data: 3# data/4# data: mineral powder	31.5	26.5	19	16	13.2	9.5	4.75	2.36	1.18	0.6	0.3	0.15	0.075
Synthetic grade	100	100	100	100	92.8	61.5	28.7	25.0	19.4	13.1	8.5	6.4	5.2

FIGURE 2
Image gray matrix processing based on "ImageJ" software. (A) SEM scanning of the diabase gray matrix. (B) SEM scanning of the limestone grayness matrix. (C) Diabase after ash treatment. (D) Limestone after ash treatment.
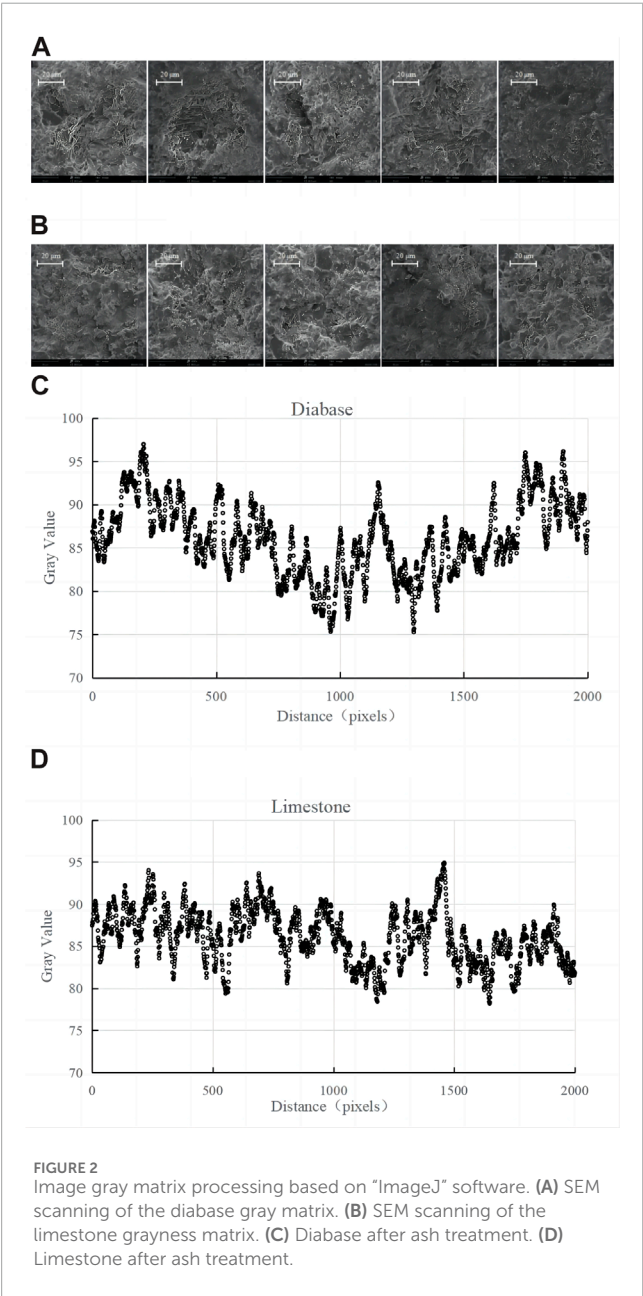
aggregate, the better the long-term skid resistance of the mixture and that the fine aggregate had a greater effect on the long-term skid resistance of the pavement compared to the coarse aggregate.

The abovementioned research shows that the various characteristics of the aggregate for asphalt mixture pavement performance need to be addressed. However, in recent construction projects, the traditional 0–5 mm limestone mechanized sand has been used instead of the 0–5-mm diabase mechanized sand. This paper investigates the effect of the different types of mechanized sand on adhesion and compaction properties. The study first focuses on two types of mechanism sand, analyzing their micro-physical properties, the chemical composition of the minerals, and surface adhesion energy. Microscopic adhesion properties are tested for comparison. Additionally, the pavement performance of the mixture is analyzed, including high temperature stability, water stability, strength, and skid resistance. The goal is to provide a theoretical reference basis for the selection of the appropriate sand type.

2 Material and methods

2.1 Materials

2.1.1 Mastic-modified asphalt

The pre-prepared finish rubberized asphalt was used in the validation test. The specific performance indicators are shown in Table 1.

2.1.2 Coarse aggregates

The coarse aggregates used to test the performance of this mixture were all taken from Nanzhan Expressway Division 1–1. The coarse aggregates are 1# (10–15) and 2# (5–10) mm diabase. The performance indexes and sieve test results are shown in Tables 2, 3.

2.1.3 Fine aggregates

The fine aggregates used in this mix performance test were taken from Nanzhan Expressway Division 1–1 and consisted of 3# (0–5) mm diabase mechanized sand and 4# (0–5) mm limestone mechanized sand. The performance indexes and the results of the sieve test are shown in Tables 4, 5.

2.1.4 Mineral gradation and oil/stone ratio

The synthetic grading of ARAC-13 was determined for this comparative validation based on the characteristics of the aggregate and the grading experience in projects under construction, as shown in Table 6. In this grading, 1# (10–15) mm and 2# (5–10) mm diabase were used as coarse aggregates, as shown in Table 2; and 3# (0–5) mm diabase mechanized sand and 4# (0–5) mm limestone mechanized sand were used as fine aggregates.

The bitumen-aggregate ratio of 5.7% was selected as the optimum asphalt content for all the tests based on engineering experience. Marshall specimens were prepared based on the optimum asphalt content, and volume indexes such as VV, VFA, and VMA were tested.
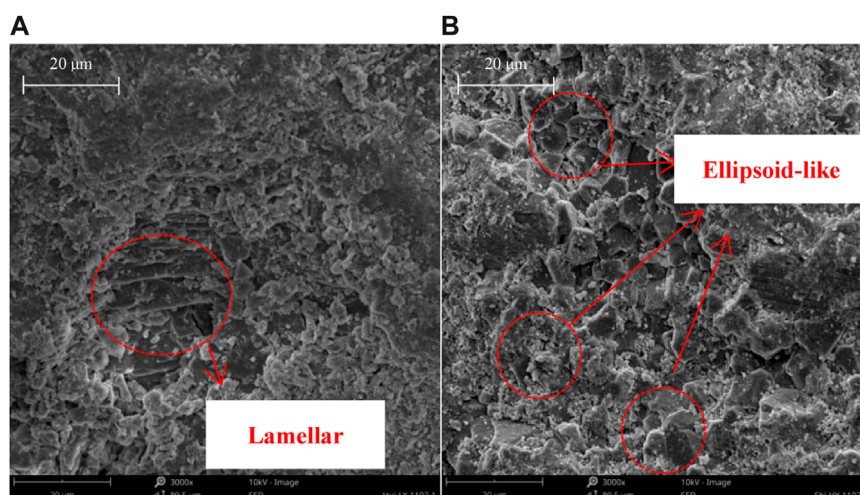
FIGURE 3
SEM scanning of glow aggregate microscopic properties (magnification 3,000). **(A)** Diabase. **(B)** Limestone.

2.2 Test methods

2.2.1 Fine aggregate adhesion microtest

The physical properties, chemical properties, and texture structure of the surface of fine aggregates were tested to investigate the micro-mechanism of the differences in the adhesion performance of different fine aggregates to asphalt. XRD was then used to determine the mineral composition of the fine aggregates and analyze their chemical composition to evaluate the adhesion performance between aggregates and asphalt. Finally, the surface energy of different aggregates with asphalt was tested using the seated drop method to compare and verify the adhesion properties of different fine aggregates with asphalt.

2.2.1.1 Surface microcharacterization test

The Phenom Pro SEM, manufactured by Phenom-World Company in the Netherlands, was used to scan the surface microscopic characteristics of diabase and limestone fine aggregates with a grain size of 2.36 mm after washing and drying. The SEM scanning magnification was chosen to be ×3,000, and the image unit size was 10 μm because the thickness of the asphalt film of intensively blended mixtures is generally 6~8 μm. Five parallel experimental specimens were selected and imaged for the quantitative analysis of the degree of roughness of the two types of aggregates. The images were then processed using ImageJ software, which first converted the images to the 8-bit format, calculated the gray value of the images, and then analyzed the variance of the gray value of the images, which was used to characterize the degree of surface roughness of the fine aggregates.

2.2.1.2 Mineral composition analysis test

A D8 advance X-ray diffractometer (Bruker, Germany) was used to analyze the mineral composition of the 2.36-mm grain-size diabase and limestone fine aggregates. The basic principle is that when X-rays are directed at the surface of a mineral crystal, they are scattered by the crystal's atoms, producing scattered

waves emanating from the center of each atom. Because of the periodic arrangement of the atoms within the crystal, a fixed-phase relationship exists between the scattered waves, where certain directions reinforce each other and others cancel out, resulting in diffraction. Given that the arrangement of the atoms within each crystal is unique, the resulting diffraction lines are distinctive in their spatial distribution and intensity. Therefore, the mineral composition of the aggregate can be determined by comparing the XRD results with the established card library.

2.2.1.3 Contact angle test

The SDC-200S Scientific Research Contact Angle Measuring Instrument (China) was used to test the surface energy of limestone, diabase, and rubberized asphalt. The rubber asphalt is first heated and allowed to flow to form a rubber asphalt sheet, which is then compacted with a thick rubber pad to complete the preparation of the asphalt sample. After washing and drying the aggregate, fine aggregates of limestone and diabase with a grain size of 9.5 mm were used to cut and prepare the aggregate specimens. The specimens are 1 cm × 1 cm × 0.5 cm in size, and different mesh coarse, medium, and fine sandpapers were used to polish them smoothly. The two types of test liquids, distilled water and anhydrous ethanol, were used for the seat-drop test to calculate the surface energy parameters of the specimens.

2.2.2 Comparative tests of mixture properties
2.2.2.1 Forming temperature test

The Marshall test is used to prepare specimens of asphalt mixture. The specimen size is Φ101.6 mm, and the diameter is 63.5 ± 1.3 mm. The mixed mixture specimens were placed in a constant-temperature oven set at different temperatures to keep them warm for 1 h. The actual temperature was measured using the inserted temperature sensor. The Marshall compactor was used to compact the mixture, and the void ratio indexes were tested for comparison to evaluate the effect of different fine aggregate lithologies on the mix-forming temperature.
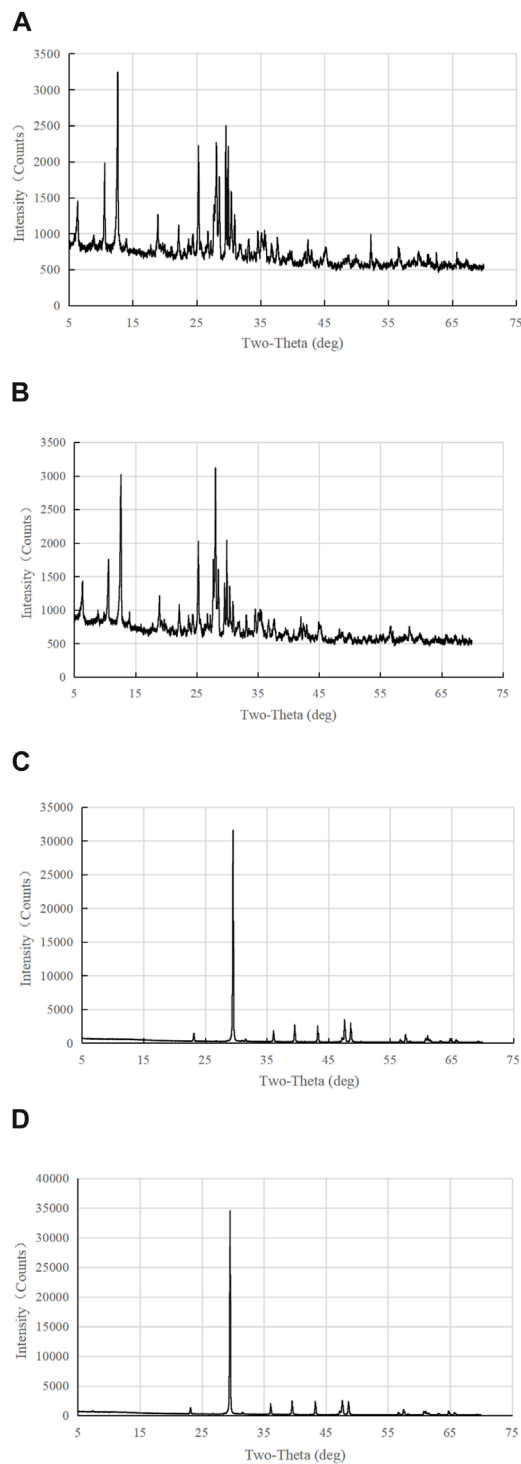
FIGURE 4
XRD-based mineral content analysis of whole rock of aggregates. **(A)** Diabase 1. **(B)** Diabase 2. **(C)** Limestone 1. **(D)** Limestone 2.

TABLE 7 Characterization of aggregate roughness based on image gray scale variance values.

Aggregate type	Image gray level variance value/%					
	1	2	3	4	5	Average value
2.36 mm diabase	14.7	24.2	24.9	18.1	13.4	19.06
2.36 mm limestone	14.1	18.6	40.1	10.0	25.7	21.72

aggregates was tested, and the effect of different fine aggregate lithologies on the water stability performance of the mixture was evaluated using the residual stability and the freezing–thawing cleavage tensile strength ratio.

2.2.2.3 High-temperature stability test

The rutting specimens were prepared using two types of fine aggregates, namely, diabase and limestone. The specimen size is 300 mm × 300 mm × 50 mm, and the high-temperature performance was tested using a conventional dynamic stability test. The test temperature was set at 60°C ± 1°C, and the ground pressure of the test wheels was set at 0.7 ± 0.05 MPa. Test durations of 45 min and 60 min were used to evaluate the stability of mixes and the effect of different fine aggregate lithologies on the high-temperature stability of the mixture.

2.2.2.4 Curing characteristic test

The diabase and limestone aggregates were used to prepare specimens using the SGC instrument in this paper. The specimens had a diameter of 100 mm ± 2.0 mm and a height of 100 mm ± 2.0 mm, making them cylindrical. The specimens were left at 20°C room temperature for 4 h, 8 h, 12 h, 18 h, and 24 h for asphalt mixture curing, according to the "Asphalt and Asphalt Mixture Test Procedures for Highway Engineering." The uniaxial penetration strength was tested on the SGC specimens using the MTS tester, and the penetration strength index was used to analyze the effect of different fine aggregate lithologies on the curing strength of the asphalt mixture.

2.2.2.5 Anti-slip decay performance test

Rutting specimens were prepared with two types of fine aggregates, diabase and limestone, and accelerated abrasion tests were conducted with the skid resistance decay simulation equipment for asphalt pavement studied by the research group, with the loading times of 0, 200, 500, 1,000, 2,000, 5,000, and 10,000 and a test temperature of 30°C. The ground pressure was 0.7 MPa, and the rotation speed was 60 r/min. At the end of each loading cycle, the depth of the structure of the specimen and the pendulum value were measured in the rutted plate track zone, with four measurement points uniformly taken to calculate the average value. Three parallel specimens of two types of fine aggregate were prepared. The depth of the structure and pendulum value index were used to analyze the effect of different fine aggregate lithologies on the skidding decay performance of the rubberized asphalt mixture.

2.2.2.2 Water stability test

The Marshall specimens were prepared using two types of fine aggregates, namely, diabase and limestone. The specimen size is Φ101.6 mm, and the diameter is 63.5 ± 1.3 mm. The water stability performance of the mixture specimens prepared with different fine

TABLE 8 Percentage of different mineral compositions of aggregates.

Material gathered together Typology	Whole rock mineral content/%										
	Sapphire	Potassium feldspar	Plagioclase (rock-forming mineral, type of feldspar)	Limonite	Dolomite	Dolomite	Calcite (CaCO$_3$ as rock-forming mineral)	Pyrite	Loam	Amphibole (silicate rock-forming mineral)	Diabase (family of rock-forming minerals)
	Qtz	Kfs	Ab	Sid	Ank	Dol	Cal	Py	Clays	Tm	Px
Diabase 1	1.5	0.0	18.9	0.0	0.0	3.8	7.0	2.0	39.1	11.1	16.5
Diabase 2	0.7	0.0	25.9	0.0	0.0	2.5	3.5	1.7	39.9	11.0	14.8
Limestone 1	0.2	0.0	0.0	0.0	0.0	0.5	99.3	0.0	0.0	0.0	0.0
Limestone 2	0.2	0.0	0.0	0.0	0.0	0.0	99.8	0.0	0.0	0.0	0.0

3 Test results and analysis

3.1 Fine aggregate adhesion microtest results and analysis

The asphalt/aggregate interface is the main determinant of the adhesion properties between asphalt and aggregate. When the same type of asphalt is used as a binder, the surface microstructure of individual aggregate at the physical level determines the total adhesion area of the asphalt–aggregate interface, while the mineral composition of the aggregates at the chemical level determines the strength of asphalt–aggregate adhesion. Therefore, the physical and chemical characteristics of the aggregate play a key role in the adhesion performance of the asphalt, which directly affects the high-temperature mechanical properties of the mixture.

3.1.1 Fine aggregate surface microcharacterization

The images of the different aggregates after SEM scanning are shown in Figure 4. It can be observed that the microstructure of the 2.36-mm-sized pyrodiabase is mainly in the form of lamellae, with fewer overlying fine particles. The microstructure of 2.36-mm limestone is mainly ellipsoidal, with more overlying fine particles, and the overall intuitive feeling of the roughness of the two aggregates is relatively low. To quantitatively analyze the degree of roughness of the two types of aggregates, each parallel test group was photographed and grayscale-processed, as shown in Figure 2. ImageJ was used to analyze the grayscale matrix value of the image and then seek its variance value; the results are shown in Table 7. From Table 7, the gray scale variance of the limestone image at 2.36-mm particle size is 13.9% higher than that of the diabase image; the reason for this is the larger specific surface area of the ellipsoid-like structure than that of the laminar lamellar structure at the same volume, and it can be intuitively observed in Figure 3 that there are more fine particles in the upper layers of limestone than in the diabase. Therefore, the total adhesion area at the asphalt aggregate interface is greater in limestone than in the diabase. The microstructural roughness of limestone is better than that of diabase, and its overall adhesion area at the asphalt–aggregate interface is greater than that of diabase.

3.1.2 Fine aggregate mineral composition

The XRD test results of the two groups of materials are shown in Figure 4; it can be observed that the shape of the diffraction pattern remains the same for the same type of aggregate. In contrast, the intensity of the diffraction peaks is slightly different, indicating that the constituent minerals are similar within the same aggregate lithology. However, their proportions are slightly different because the sources are different. In addition, there is a large difference between the two when the aggregate lithologies are different. For further quantitative analysis, the mineral composition of the aggregates can be obtained by analyzing Figure 4, as shown in Table 8.

1) Diabase is mainly composed of eight mineral components, including clay, plagioclase, and diabase; among these,

TABLE 9 Surface energy parameters of different specimens.

Type of substance	Surface energy/(mJ/m2)	Dispersive component/(mJ/m2)	Polar component/(mJ/m2)	Adhesion ΔGsb/(mJ/m2)
Rubberized asphalt	17.27	9.98	7.29	—
Diabase	117.06	7.23	109.83	−163.5
Limestone	115.62	30.26	85.36	−174.0

TABLE 10 Specimens' void ratio at different compaction temperatures.

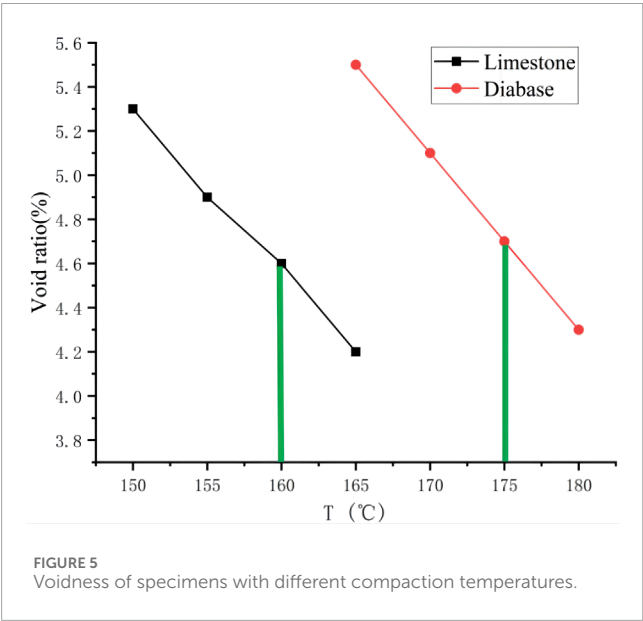| Fine aggregate Typology	Void ratio/%						
	150°C	155°C	160°C	165°C	170°C	175°C	180°C
Limestone	5.3	4.9	4.6	4.2	—	—	—
Diabase	—	—	—	5.5	5.1	4.7	4.3

FIGURE 5
Voidness of specimens with different compaction temperatures.

the clay component accounts for the highest proportion of approximately 40%, followed by plagioclase, diabase, amphibole, calcite, dolomite, pyrite, and quartz, accounting for a total of approximately 60%.

2) The main mineral composition of limestone is calcite, accounting for more than 99%, with trace amounts of other components such as dolomite and quartz.

3) According to the existing literature, it is confirmed that the oxides that affect the adhesion between aggregate and asphalt mainly include four types, namely, SiO_2, Al_2O_3, MgO, and CaO. Among these, CaO and MgO exhibit stronger adhesion to asphalt, whereas SiO_2 and Al_2O_3 show weaker adhesion. Although the main chemical composition of calcite is CaO, the main chemical

compositions of clay and plagioclase are SiO_2 and Al_2O_3, respectively, and the main chemical composition of diabase is SiO_2. Therefore, the XRD test results confirm that the adhesion of limestone to asphalt, analyzed in terms of its chemical composition, is significantly better than that of diabase.

3.1.3 Fine aggregate surface energy properties

Adhesion of asphalt–aggregate refers to the process of solid and liquid surfaces being replaced by solid–liquid interfaces, and the change in Gibbs free energy of the system before and after the process can characterize the tendency of the system state change. Equations 1, 2 were used to calculate the adhesion energy.

$$\Delta Gsb = \gamma_{sb} - \gamma_s - \gamma_b, \qquad (1)$$

$$\Delta Gsb = -2\left(\sqrt{\gamma_s^{LW}\gamma_b^{LW}} + \sqrt{\gamma_s^+\gamma_b^-} + \sqrt{\gamma_b^+\gamma_s^-}\right), \qquad (2)$$

where ΔGsb is the adhesion free energy; γsb is the solid–liquid substance interfacial energy; γs is the solid substance surface energy; γb is the liquid substance surface energy; γ_s^{LW} is the solid matter dispersion component; γ_b^{LW} is the liquid substance dispersion component; $\gamma_s^+\gamma_s^-$ is the solid matter polar force component; and $\gamma_b^+\gamma_b^-$ is the liquid substance polar force component.

The various aggregate and asphalt surface energy parameters were calculated, as shown in Table 9.

1) The adhesion of limestone rubberized asphalt is better than that of diabase-rubberized asphalt. As shown in Table 9, the adhesion energy of limestone and rubberized asphalt is −174.0 mJ/m^2. It is 6.4% lower than that of diabase and rubberized asphalt (−163.2 mJ/m^2), which means that the adhesion between the limestone and rubberized asphalt releases more energy, the whole solid–liquid interface is more stable, and the adhesion is better.

2) The polarity component of diabase is significantly higher than that of limestone. From Table 9, the difference in

TABLE 11 Results of immersion Marshall residual stability tests.

Gradation type	Unconditional		Prerequisite		Residual stability MS0 /%
	Marshall stability MS /kN	Void ratio /%	Immersion Marshall stability MS1 /kN	Void ratio /%	
Diabase ARAC-13	11.72	4.5	11.18	4.6	95.39
Limestone ARAC-13	11.41	4.5	11.09	4.5	97.20
Technical requirement	≥8	3 to 6	—	3 to 6	≥85

TABLE 12 Freeze−thaw splitting test results.

Gradation type	Unconditional		Prerequisite		Freeze−thaw split tensile strength ratio /%
	RT1 without freeze−thaw cycles /MPa	Void ratio /%	Freeze−thaw cycle RT2 /MPa	Void ratio /%	
Diabase ARAC-13	1.133	5.5	1.014	5.5	89.50
Limestone ARAC-13	1.108	5.4	1.006	5.5	90.79
Technical requirement	—	—	—	—	≥80

TABLE 13 60°C rutting test results.

Gradation type	Test piece Serial number	Deformation/mm		DS/(times/mm)	
		45 min	60 min	Single-valued (math.)	Average value
Diabase ARAC-13	1	0.863	0.927	9,844	10,120
	2	0.908	0.983	8,400	
	3	1.163	1.215	12,115	
Limestone ARAC-13	1	1.588	1.667	7,975	10,047
	2	1.088	1.148	10,500	
	3	1.065	1.119	11,667	
Technical requirement					≥3,000

surface energy between diabase and limestone is relatively small. However, the polarity component of diabase is 109.83 mJ/m^2, which is 28.7% higher than that of limestone (85.36 mJ/m^2), indicating that diabase is more hydrophilic than limestone. It shows that when diabase is used as a fine aggregate in an asphalt mixture, it is more susceptible to water-induced damage; capillary water can more easily penetrate the interface between asphalt and aggregate, leading to asphalt film detachment, reduced adhesion, and early-stage deterioration.

3.2 Comparative test results and analysis of mix performance

3.2.1 Comparison of molding temperatures

After comparing the test results of the previous trial compaction, it was found that for the same grading and bitumen–aggregate ratio, it is difficult to achieve the same mixture filling state under the same compaction conditions when molding the mixture. This is due to the differences in the surface microstructure and lithology of diabase and limestone fine aggregates. To investigate

TABLE 14 Uniaxial penetration strength of specimens with different curing times.

Curing time/h	Specimen number	Uniaxial penetration strength/Mpa	
		Diabase	Limestone
4	1	1.478	1.86
	2	1.605	1.924
	3	1.608	1.923
	Average value	1.564	1.902
8	1	2.052	2.994
	2	1.872	2.544
	3	1.89	2.854
	Average value	1.938	2.797
12	1	2.771	2.904
	2	2.343	2.688
	3	2.331	2.629
	Average value	2.482	2.740
18	1	2.662	3.094
	2	2.726	2.911
	3	2.337	2.934
	Average value	2.575	2.980
24	1	2.624	2.892
	2	2.675	2.955
	3	2.535	2.986
	Average value	2.611	2.944

FIGURE 6
Trend of specimens' penetration strength and degree of curing at different curing times.

the compaction conditions of different specimens, specimens were prepared at different compaction temperatures. Specific results are shown in Table 10.

From Figure 5, it can be observed that the compaction temperature required for the diabase specimens is approximately 15°C higher than that for the limestone specimen when the same compaction effort is proposed to achieve the target void ratio. To comparatively analyze the pavement performance of the mix specimens prepared with different fine aggregates, two types of ARAC-13 mixes were prepared for the water immersion Marshall test, the freeze-thaw splitting test, and the rutting test based on the selected gradation, bitumen-aggregate ratio, and molding temperature (160°C for limestone and 175°C for diabase), using the same gradation of SGC to prepare the specimens. The uniaxial penetration method was used to compare the cure time-strength,
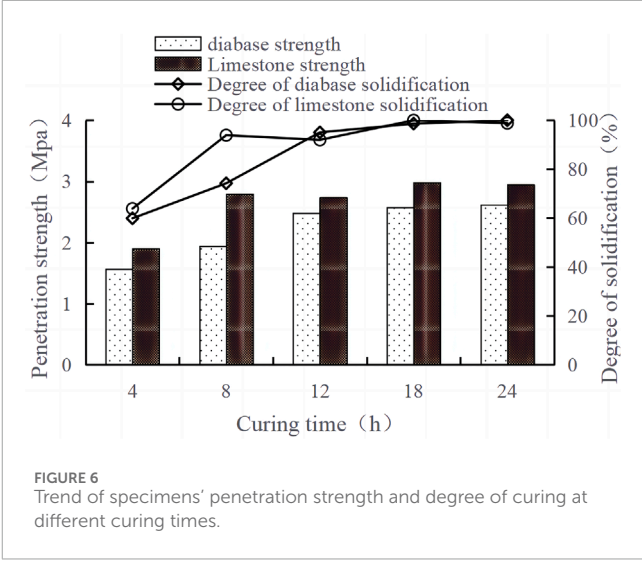
and finally, the accelerated loading abrasion test was used to compare the skidding decay resistance.

3.2.2 Comparison of water and high-temperature stability

The results of water stability tests are shown in Tables 11, 12, and the results of high-temperature stability tests are shown in Table 13. From Tables 11–13, the water stability performance and high-temperature stability performance of the mix specimens prepared at different molding temperatures (160°C for limestone and 175°C for diabase) are much higher than the specification requirements, and there is no significant difference between them.

3.2.3 Effect of curing time on strength

The results of uniaxial penetration tests at different curing times are shown in Table 14; Figure 6.

1) The cured strength of the limestone specimens is significantly higher than that of diabase specimens, and the penetration strength is 10%–20% higher under different curing times. The cured strength of the two types of rubberized asphalt mixtures under curing for 4 h is 1.563 MPa and 1.902 MPa, respectively. The limestone specimens are 21.7% higher than the diabase specimen, and its cured strength under a curing time of 24 h is elevated to 2.944 MPa and 2.611 MPa. The limestone specimens are still 12.7% higher than the diabase specimen.

2) The curing rate of limestone specimens is significantly higher than that of diabase specimens, and the curing time is more than 4 h faster than that of diabase specimens. Figure 6 illustrates that the degree of curing of the two rubberized asphalt mixtures is approximately 60% when the curing time is 4 h. The degree of curing of the limestone asphalt mixture curing strength has reached 90% when the curing time is 8 h. At the same time, the curing strength of the diabase asphalt mixture is only 74% when the curing time is extended to 12 h,
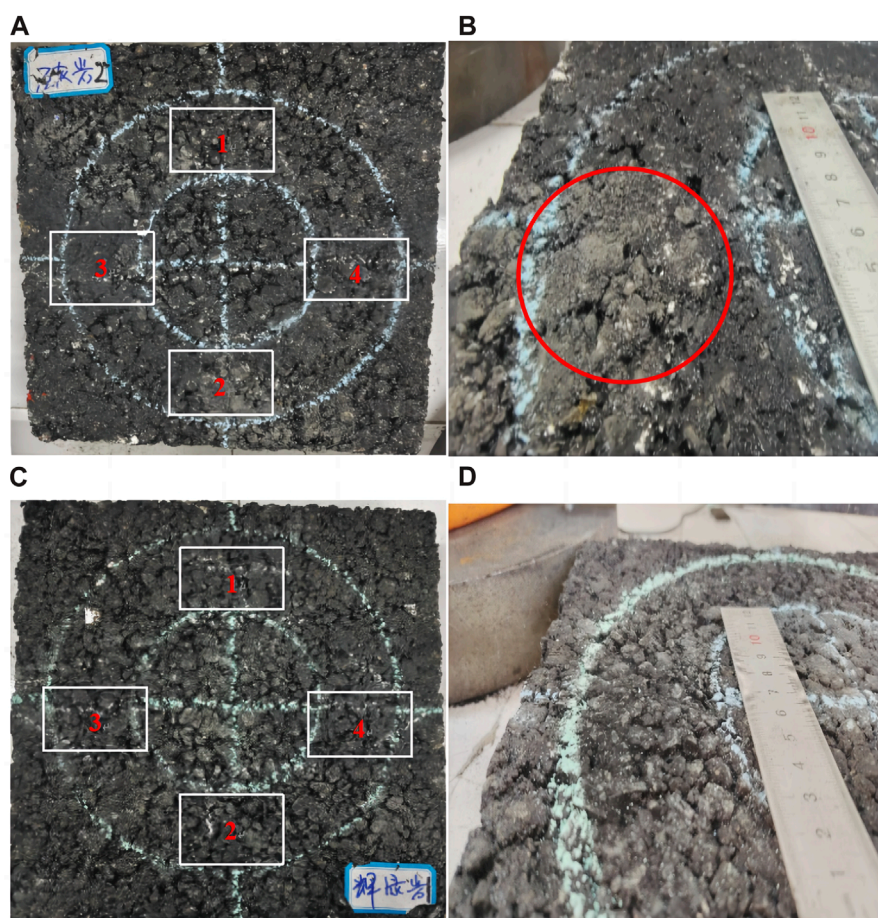
FIGURE 7
Different specimens' measuring point positions and the effect after abrasion. **(A)** Measurement points of limestone specimens. **(B)** Surface structure of limestone specimens after 10,000 cycles of abrasion. **(C)** Measurement points of diabase specimens. **(D)** Surface structure of diabase specimens after 10,000 cycles of abrasion.

but the curing strength of the limestone asphalt mixture is more than 90%.

3.2.4 Anti-slip decay properties

The location of the two specimens' measuring points and the effects after abrasion are shown in Figure 7. The test data, after taking the mean values, are shown in Table 15. When plotted, these data (provided in Table 15) reveal the trend shown in Figure 8.

1) As the number of abrasions increases, the anti-skid performance of two types of specimens gradually decreases. However, the declining trend gradually tends to level off, as shown in Figure 8. After 10,000 cycles of abrasion, the anti-skid performance index tends to stabilize for all six specimens. This phenomenon is primarily attributed to the abrasion wheel aggregating the surface of the asphalt, leading to significant initial decreases in anti-skid performance. Over time, the abrasion mainly relies on wear resistance, hardness, and other properties of the aggregate, resulting in a slower rate of decrease in anti-skid performance.

2) Limestone and diabase specimens have advantages and disadvantages with respect to abrasion slip resistance performance indexes. The pendulum values of the limestone and diabase specimens were 67.5 BPN and 62.3 BPN, respectively, with the limestone specimens slightly higher by 8.34%. The structural depths were 1.125 mm and 1.568 mm, with the diabase specimens displaying a 39.3% greater depth.

3) The anti-abrasion performance of the limestone specimen is slightly worse than that of the diabase specimen. As shown in Table 14, the BPN value is 47.3 and 50.1, and tectonic depth is 0.68 mm and 0.87 mm for limestone specimens and diabase specimens, respectively, after 10,000 cycles of abrasion.

4) Limestone specimens have slightly better anti-slip properties than diabase. From Table 14, it is observed that the initial pendulum value and the average value of the tectonic depth of the limestone specimens are 67.5 BPN and 1.125 mm, respectively. With the number of abrasions increasing from 0 to 200 cycles, these values decreased by 9.48% and 23.55%,

TABLE 15 Specimens' pendulum value and construction depth data under different abrasion times.

(Of cargo, etc.) load ordinal number	Pendulum value/BPN								Depth of construction/mm							
	Limestone-1	Limestone-2	Limestone-3	Average value	Diabase-1	Diabase-2	Diabase-3	Average value	Limestone-1	Limestone-2	Limestone-3	Average value	Diabase-1	Diabase-2	Diabase-3	Average value
0	70.6	66.0	65.9	67.5	63.1	62.6	61.4	62.3	1.244	1.056	1.077	1.125	1.694	1.579	1.431	1.568
200	62.2	61.7	59.4	61.1	60.5	59.1	58.5	59.3	0.979	0.735	0.866	0.86	1.290	1.272	1.128	1.23
500	57.7	56.7	56.0	56.8	57.1	56.6	55.3	56.3	0.957	0.739	0.906	0.867	1.256	1.159	1.056	1.157
1,000	54.8	54.5	54.5	54.6	53.1	55.1	53.4	53.8	0.879	0.726	0.819	0.808	1.188	1.044	0.946	1.059
3,000	52.3	50.3	52.5	51.7	53.7	54.3	50.8	52.9	0.881	0.623	0.674	0.726	0.926	0.995	1.049	0.99
5,000	51.3	49.5	50.5	50.4	51.8	54.5	49.4	51.9	0.759	0.644	0.693	0.698	0.877	0.855	0.915	0.882
7,000	48.8	48.1	48.4	48.4	51.6	52.5	50.0	51.3	0.770	0.590	0.691	0.683	0.855	0.914	0.953	0.907
10,000	47.5	46.7	47.7	47.3	49.9	51.0	49.3	50.1	0.809	0.629	0.602	0.68	0.880	0.843	0.887	0.87

respectively. However, between 7,000 and 10,000 cycles, the values decreased by 2.27% and 0.44%, respectively. In contrast, the initial pendulum value and tectonic depth of the diabase specimens are 62.3 BPN and 1.568 mm, respectively. As the number of abrasion cycles increased from 0 to 200, these values decreased by 4.81% and 21.55%, respectively. Between 7,000 and 10,000 cycles, the values decreased by 2.53% and 4.07%, respectively. These results indicate that limestone specimens exhibit better resistance to abrasion decay compared to diabase specimens, and the anti-slip properties of both may converge as the number of abrasion cycles continues to increase.

4 Conclusion

This paper presents comparative tests on the microphysical characteristics, mineral chemical composition, and surface adhesion energy of two types of manufactured sands (diabase and limestone). It then compares and analyzes the compaction characteristics, high temperature, water stability, strength, skid resistance, and other road properties of the two types of mixtures. The conclusions obtained are as follows.

1) Based on the microscopic test results, it is shown that the adhesion of limestone to asphalt is significantly better than that of diabase. SEM image analysis shows that the surface roughness of limestone is 13.9% higher than that of diabase. XRD analysis reveals that the mineral composition of the limestone, consisting of 99% CaO system alkaline components, exhibits excellent adhesion to asphalt. In contrast, the chemical composition of diabase, which comprises 60% SiO_2 and an Al_2O_3-based acidic and neutral system, shows poor adhesion to asphalt. According to surface energy theory, the adhesion energy at the limestone–asphalt interface is 6.4% higher than that at the diabase–asphalt interface.

2) Based on the test of compaction characteristics of the mixture, it is shown that the compaction performance of the limestone sand specimens is significantly better than that of the diabase specimens. To achieve the target void ratio under the same compaction work, the compaction temperature of the diabase specimens needs to be approximately 15°C higher than that of the limestone specimens.

3) Based on the mixture curing characteristics, the test shows that the curing rate and strength of limestone specimens are significantly better than those of the diabase specimens. Under the same conditions, the curing strength of limestone specimens reaches more than 90% in just 8 h, whereas diabase specimens need 12 h. Additionally, the final curing strength of limestone specimens is 7.8% higher compared to diabase specimens.

4) The anti-abrasion performance of limestone specimens is slightly inferior to that of diabase specimens. After 10,000 cycles of abrasion, the BPN values for limestone and diabase specimens were 47.3 and 50.1,
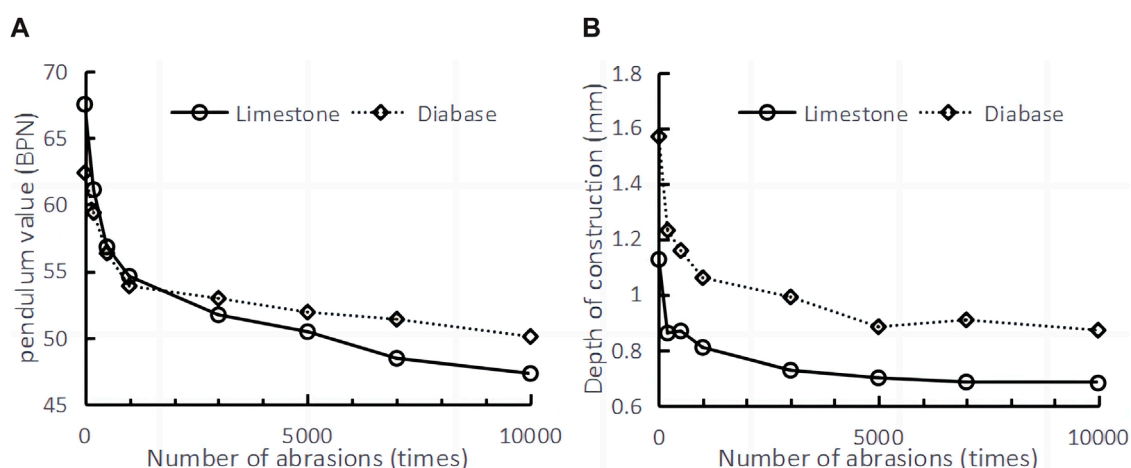
FIGURE 8
Trend of skidding decay of specimens with a different number of abrasions. **(A)** Pendulum value. **(B)** Depth of construction.

respectively, with structural depths of 0.68 mm and 0.87 mm. The decrease in the anti-slip index for diabase specimens is smaller than that of the limestone specimens.

5) The limestone specimens are slightly better than the diabase specimens in wear decay resistance. When the number of abrasions increased from 7,000 to 10,000 cycles, the BPN and tectonic depth of the limestone specimens decreased by 2.27% and 0.44%, respectively, whereas the BPN and tectonic depth of the diabase specimens decreased by 2.53% and 4.07%, respectively. As the number of abrasions continues to increase, the slip resistance properties of the two materials may gradually converge.

In summary, for asphalt pavement construction, limestone sand should be used as a fine aggregate due to its superior asphalt adhesion and strength characteristics. If diabase sand is utilized as a fine aggregate, the open traffic time must be strictly controlled. It is recommended that traffic be opened after 5 days of traffic restriction, especially during high summer temperatures, following milling.

Data availability statement

The original contributions presented in the study are included in the article/supplementary material; further inquiries can be directed to the corresponding authors.

Author contributions

LZ: conceptualization, data curation, formal analysis, funding acquisition, investigation, methodology, project administration, resources, software, supervision, validation, visualization, writing–original draft, and writing–review and editing. HZ: writing–original draft and writing–review and editing. SJ: writing–original draft and writing–review and editing. HH: data curation and writing–review and editing. BX: writing–review and editing. HY: writing–original draft.

Funding

Conflict of interest

Authors LZ, HZ, and HH were employed by Guangxi Transportation Science and Technology Group Co., Ltd. Authors BX and HY were employed by Guangxi Jiaoke New Materials Technology Co., Ltd.

The remaining author declares that the research was conducted in the absence of any commercial or financial relationships that could be construed as a potential conflict of interest.

Publisher's note

References

Cheung, L. W., and Dawson, A. R. (2002). Effects of particle and mix characteristics on performance of some granular materials. *Transp. Res. Rec. J. Transp. Res. Board* 1787, 90–98. doi:10.3141/1787-10

Delrio-Prat, M., Vega-Zamanillo, A., Castro-Fresno, D., and Calzada-Pérez, M. Á. (2010). Energy consumption during compaction with a gyratory intensive compactor tester. Estimation models. *Constr. Build. Mater.* 25, 979–986. doi:10.1016/j.conbuildmat.2010.06.083

Habal, A., and Singh, D. (2017). Moisture damage resistance of gtr-modified asphalt binders containing wma additives using the surface free energy approach. *J. Perform. Constr. Facil.* 31. doi:10.1061/(asce)cf.1943-5509.0000995

Huang, Z. G., Liu, B. Q., and Gong, W. J. (2022). Discussion on the quality engineering construction mode of wide highway pavement under the hot and humid mountain environment in Guangxi Province. *West. China Commun. Sci. and Technol.*, 16–18. doi:10.13282/j.cnki.wccst.2022.10.005

Ingunza, M. D. P. D., Júnior, O. F. D. S., and Medeiros, S. A. (2013). Sewage sludge as raw-material in asphalt mixtures. *Adv. Mater. Res.* 664, 638–643. doi:10.4028/www.scientific.net/AMR.664.638

Jamkar, S. S., and Rao, C. B. K. (2004). Index of aggregate particle shape and texture of coarse aggregate as a parameter for concrete mix proportioning. *Cem. Concr. Res.* 34, 2021–2027. doi:10.1016/j.cemconres.2004.03.010

Li, S. C., Bai, W., and Chen, N. (2020). Comparative study on performance of rubber asphalt pavement and SBS modified asphalt pavement of yihe Expressway in Guangxi. *Subgr. Eng.*, 89–93. doi:10.13379/j.issn.1003-8825.201911001

Mahboub, K. C., Oduroh, P. K., and Anderson, R. M. (2001). Hot mix asphalt with flat and elongated aggregates. *Constr. Mater. Issues* 2001, 183–192. doi:10.1061/40591(269)19

Peng, W., Li, P., Gao, J., Liu, Z., Wang, X., Wang, S., et al. (2024). Long-term skid resistance evolution and influence mechanism of asphalt pavement based on self-developed wear equipment. *Constr. Build. Mater.* 453, 139085. doi:10.1016/j.conbuildmat.2024.139085

Prudêncio, L. R., Weidmann, D. F., de Oliveira, A. L., and Damo, G. F. (2013). Particle shape analysis of fine aggregate using a simplified digital image processing method. *Mag. Concr. Res.* 65, 27–36. doi:10.1680/macr.11.00199

Stukhlyak, P. D., Buketov, A. V., Panin, S. V., Maruschak, P. O., Moroz, K. M., Poltaranin, M. A., et al. (2015). Structural fracture scales in shock-loaded epoxy composites. *Phys. Mesomech.* 18, 58–74. doi:10.1134/S1029959915010075

Wang, D., Steinauer, B., and Yin, C. (2011). "Optimization of long-term skid resistance on asphalt concrete pavement," in Paper presented at 2011 International Conference on Remote Sensing, Environment and Transportation Engineering, Nanjing, 24-26 June 2011, 4246–4248. doi:10.1109/rsete.2011.5965267

Wang, Y., Yan, J. C., and Yuan, H. T. (2022). Study on the high temperature storage performance of rubber composite modified asphalt on wulong Expressway. *West. China Commun. Sci. and Technol.*, 96–98. doi:10.13282/j.cnki.wccst.2022.05.030

Xie, C., Luo, J., Zeng, L., Ren, T., Liu, H., and Chen, J. (2022). Research on evaluation index of high temperature performance of rubberized asphalt binder. *Front. Mater.* 9. doi:10.3389/fmats.2022.904087

Zhang, H. G., Tan, H., Wang, B., Xiong, J. P., Kuang, D. L., and Liu, W. C. (2021). Performance evaluation, modification mechanism and application research progress of rubber asphalt. *Appl. Chem. Ind.* 50, 299–303. doi:10.16581/j.cnki.issn1671-3206.2021.s2.059

Zhao, Z., Wu, S., Xie, J., Yang, C., Yang, X., Chen, S., et al. (2023). Recycle of waste tire rubber powder in a novel asphalt rubber pellets for asphalt performance enhancement. *Constr. Build. Mater.* 399, 132572. doi:10.1016/j.conbuildmat.2023.132572

Effect of recycled aggregate and freeze-thaw cycles on fatigue performance of asphalt concrete

Yihong Yan[1], Wenbo Li[1] and Lei Wang[2]*

[1]School of Transportation, Changsha University of Science and Technology, Changsha, China,
[2]College of Traffic and Transportation, Chongqing Jiaotong University, Chongqing, China

Fatigue damage is a primary mode of failure in asphalt pavements under repeated traffic loading. The incorporation of recycled concrete aggregate (RCA) in asphalt mixtures addresses issues of construction waste landfilling while enhancing sustainability. This study investigated the influence of RCA sizes and freeze-thaw (F-T) cycles on fatigue lives of recycled aggregate asphalt concrete (RAAC) through laboratory tests. Three RCA size fractions (4.75–9.5 mm, 9.5–13.2 mm, and 13.2–16 mm) underwent Los Angeles abrasion tests to quantify morphological changes, including convexity, axiality coefficient (AC), and roundness. After 800 abrasion rotations, fine RCA showed minimal convexity reduction of approximately 0.4%, whereas coarse RCA exhibited a greater reduction exceeding 1.0%. Semi-circular bend (SCB) fatigue tests revealed that RAAC specimens with finer RCA consistently exhibited better fatigue resistance and higher stiffness modulus retention compared to medium and coarse gradations. Grey correlation analysis indicated a strong correlation between RCA size and fatigue life, with AC identified as the most influential morphological index. Fatigue life predictions using Basquin model demonstrated high accuracy ($R^2 > 0.90$). Furthermore, F-T cycles accelerated damage accumulation and stiffness reduction in RAAC over fatigue loading repetitions. These findings underscore the critical role of RCA particle morphology in enhancing RAAC durability under coupled environmental and mechanical loading conditions.

1 Introduction

The volume of construction and demolition waste (CDW) is increasing rapidly, driven by global urbanization and infrastructure development. The effective utilization of CDW has become a critical issue for environmental sustainability. Recycled concrete aggregate (RCA) produced from CDW provides a viable solution for waste management by being beneficially reused in recycled aggregate asphalt concrete (RAAC). However, the mechanical performance and durability of RAAC remain concerns due to the inherent deficiencies of RCA.

RCA exhibits inherent defects such as high porosity, irregular shape and angular texture inherited from the original concrete (Aboutalebi Esfahani, 2020; Zhang et al., 2019). These defects compromise the strength and deformation resistance of RAAC. In particular, the porosity of RCA results in higher water absorption and susceptibility to moisture damage

GRAPHICAL ABSTRACT
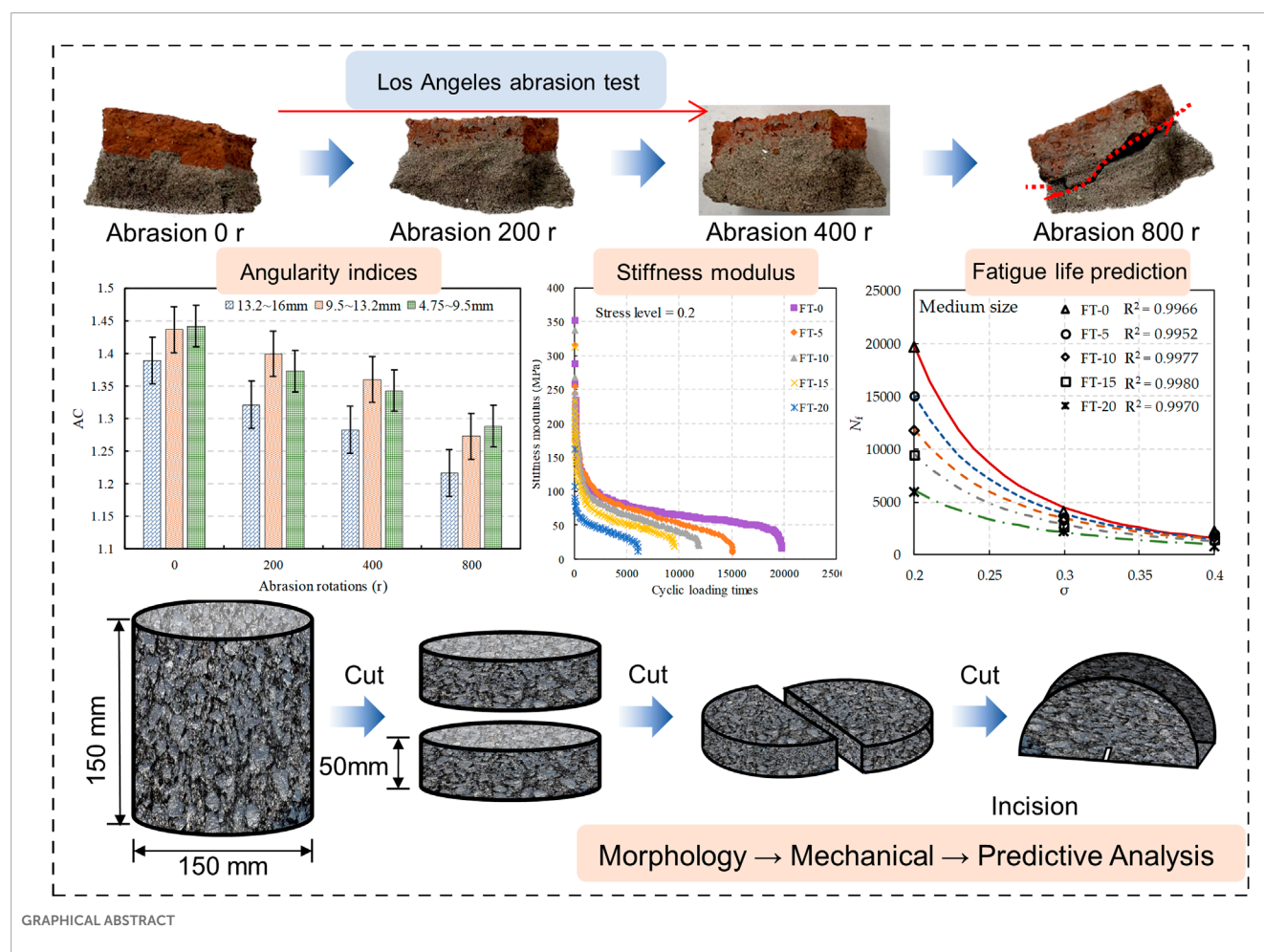
(Silva et al., 2019; Vieira and Pereira, 2015). Additionally, microcracks formed at the asphalt-aggregate interface during the service life of RAAC weaken its resistance to cracking and fatigue failure under repetitive traffic and environmental loads (Wang R. et al., 2020; Zheng et al., 2021). Previous studies have reported reductions in the resilient modulus, fatigue life and resistance to moisture-induced damage of RAAC compared to conventional asphalt concrete (Sahebzamani et al., 2022; Wang B. et al., 2021; Zieliński, 2024). Therefore, improving the mechanical and durability performance of RAAC requires a more detailed understanding of the physical and morphological characteristics of RCA. These attributes critically influence the long-term behavior and structural integrity of the asphalt mixture.

Fatigue failure stands out as a primary factor contributing to asphalt pavement distress, exerting a significant impact on the long-term performance of asphalt pavements (Li N. et al., 2025; Yao and Xu, 2023; Zhao et al., 2025). Subjected to the combined effects of traffic loading and environmental influences, asphalt pavements experience prolonged periods of stress and strain overlap (Liu et al., 2024; Yang et al., 2024; Zhang et al., 2025). This continuous exposure leads to progressive internal damage and deterioration within the asphalt concrete structure, ultimately compromising its overall integrity (Bazoobandi et al., 2023; Sreedhar and Coleri, 2022; Yousefi et al., 2021). Wang S. et al. (2021) investigated the

resistance to fatigue of semi-flexible based pavement across varying temperatures and stress levels, with an in-depth analysis of the fatigue cracking mechanisms in the asphalt surface. Another critical issue is the freeze-thaw (F-T) durability of asphalt pavements in cold regions. The composition of RAAC plays a crucial role in determining the performance of asphalt concrete, with a notable discrepancy in the susceptibility of asphalt mixtures containing different recycled aggregates to F-T cycles (Hosseini et al., 2023; Xiao et al., 2023). Notably, the response of coarse and fine recycled aggregates to F-T induced damage in asphalt concrete varies. Yang et al. (2016) conducted experiments to evaluate the impact of F-T cycles on the fracture energy of asphalt mixtures, revealing the damage behavior of recycled asphalt pavement. During F-T cycles, ingress of moisture into the air voids of RAAC generates development and propagation of internal microcracks (Hao et al., 2018; Xia et al., 2024). The repeated expansion and contraction caused by phase changes of water induce damage accumulation and deterioration of the asphalt-aggregate bond (Feng et al., 2010; Kakar et al., 2015). It has been suggested that the higher porosity and heterogeneity of RCA lead to greater F-T susceptibility compared to natural aggregate asphalt concrete (Akbas et al., 2023; Li et al., 2024b; Upshaw and Cai, 2020). However, limited research has systematically evaluated the effects of combined F-T conditioning and fatigue loading representative of field conditions.

The morphological characteristics of aggregates play a crucial role in determining the mechanical properties and stability of asphalt concrete, encompassing factors such as shape, angularity, and surface texture (Arasan et al., 2011; Cui et al., 2018; Wang et al., 2022). Angularity refers to the extent of protrusions on the surface of aggregate particles. Coarse aggregates with pronounced angularity create a dense interlocking structure, enhancing their strength and stability through an increase in the internal friction angle of RAAC (Ding et al., 2017). Aggregate particles with sharp edges facilitate improved surface texture by interlocking, whereas horizontally oriented flat and elongated particles exhibit shallower interlocking depths (Kogbara et al., 2016). Bessa et al. (2015) demonstrated that increased roughness on the aggregate surface enhances particle-to-particle interface bonding within the asphalt mixture, thereby enhancing the fatigue resistance of the asphalt mixture. In the context of coarse aggregates in asphalt concrete, a preference is given to angular and rough shape characteristics to promote stronger mechanical properties (Olard and Perraton, 2010; Radević et al., 2020). The angular nature of aggregates fosters enhanced interlocking among particles, leading to superior mechanical strength (Wang H. et al., 2020). Conversely, flat and elongated aggregates are prone to breakage, weakening the inter-particle bonding and significantly impacting the mechanical properties of asphalt concrete (Gong et al., 2021; Kong et al., 2019). Studies by Liu et al. (2017) evaluated the fatigue resistance of asphalt mixtures with varying coarse aggregate morphologies, revealing that a higher proportion of spherical aggregates and fewer flake-like aggregates effectively mitigated stiffness degradation. These morphological distinctions directly influence the engineering performance of RCA, with the structural and morphological disparities of RCA rendering it more susceptible to breakage under loading conditions compared to natural aggregates (Li et al., 2024a), consequently affecting the fatigue life of RAAC (Li et al., 2023). Although previous studies have investigated the fatigue performance and F-T durability of recycled asphalt mixtures. Nevertheless, existing research predominantly focused on external factors such as moisture, temperature, and loading conditions. Limited attention has been given to the effects of particle wear, size gradation, and F-T cycles on the fatigue behavior of RAAC, particularly in relation to RCA's evolving morphology during service.

This study contributes a novel perspective to the durability assessment of RAAC by integrating the morphological evolution of RCA with the coupled effects of mechanical fatigue and F-T environmental loading. While earlier research has indicated that finer RCA may enhance asphalt mixture performance, the present work moves beyond this general observation by systematically quantifying RCA morphology changes caused by abrasion. More importantly, it establishes a direct relationship between RCA morphological characteristics and the fatigue life of asphalt concrete under F-T conditions. In addition, a fatigue life prediction model that considers both RCA size and F-T effects is proposed. This approach provides a mechanistic understanding of how geometric properties and environmental stressors jointly influence the long-term structural behavior of asphalt pavements. This study considered RCA size and particle morphology to improve fatigue resistance under combined mechanical and F-T environmental loading. The findings of this research offer critical insights to guide the design and application of recycled materials in sustainable pavement engineering.

2 Materials and methods

2.1 Materials

2.1.1 Asphalt binder

A 70# penetration grade asphalt binder was used in this study. The basic performance tests of the asphalt binder were conducted according to JTG E20-2019 "Standard Test Method of Bitumen and Bituminous Mixtures for Highway Engineering". Table 1 summarizes the test results and specification limits of the asphalt binder.

2.1.2 Recycled concrete aggregate

The recycled concrete aggregates (RCA) used in this study were obtained from construction and demolition waste (CDW) processed at a construction site in Changsha, China. The production process of RCA involved primary crushing of CDW, secondary crushing and screening to separate aggregate fractions. The recovered aggregates were then cleaned to produce new RCA.

Figure 1 illustrates the RCA production process from CDW. The CDW was first subjected to primary crushing. It was further crushed and screened into different fractions, followed by washing to obtain the final RCA products.

The gradation curve of the produced RCA is shown in Figure 2. The RCA with different particle sizes were designed to replace natural coarse aggregates in asphalt mixtures. The size ranges of the three replacing RCA were 4.75–9.5 mm, 9.5–13.2 mm and 13.2–16 mm, respectively.

Table 2 summarizes the basic physical properties of the RCA, including apparent density, crushing value, water absorption, Los Angeles abrasion loss and needle flake content. All properties met the specification limits.

The apparent density of RCA was relatively low compared to natural aggregates, which was attributed to the high porosity resulting from cement mortar attaching on aggregate surfaces. The crushing value (representing aggregate crushing resistance) exceeded the maximum limit of 30% specified in some regions such as Europe, suggesting the aggregates were susceptible to crushing under repeated loading. The water absorption of RCA was about 5–7 times that of natural aggregates due to the porous cement paste on the aggregate surface. Both the crushing value and water absorption could deteriorate the volumetric and mechanical properties of asphalt mixtures.

The high Los Angeles abrasion loss indicated that the aggregates were vulnerable to fragmentation and polished surfaces when subjected to vehicle traffic and environmental conditions. The needle flake content of below 10% met the specification limit. Overall, the test results showed the need to improve the moisture resistance and fracture resistance of RCA through rational particle size selection and mixing process optimization when incorporated in asphalt mixtures.

TABLE 1 Properties of 70# asphalt binder.

Test items	Unit	Results	Requirements	Test method
25°C Needle penetration	0.1 mm	60.5	60–80	JTG E20 T 0604
Penetration index (PI)	—	−0.64	—	JTG E20 T 0604
Softening point	°C	49.0	≥44.0	JTG E20 T 0606
10°C ductility	cm	93.0	≥25.0	JTG E20 T 0605
15°C density	g/cm³	1.032	—	JTG E20 T 0603

2.1.3 Mix design of RAAC

By replacing the coarse aggregate with RCA in asphalt concrete, the mix proportions for three RCA components were designed using the Marshall mix design method. For each of the three mixtures, the natural coarse aggregate within the specified size range was fully replaced by 100% RCA. The optimal asphalt content was determined through iterative designs to achieve targets of air voids, voids in mineral aggregate (VMA) and voids filled with asphalt (VFA). Compared to conventional asphalt concrete with natural aggregates, higher asphalt content was required in RAAC to compensate for the higher water absorption and surface flaws of RCA. The high absorption resulted in asphalt coating deficiency on RCA surfaces during the mixing and compaction process. Additional asphalt was thus needed to achieve satisfactory mix workability and volumetrics.

As the RCA size increased from fine to coarse particles, the corresponding optimal asphalt content slightly decreased. This was because the larger RCA particles had lower surface area to volume ratio and were less porous compared to the smaller ones, leading to reduced asphalt demand. Specifically, the determined optimal asphalt binder content was 5.2% for the fine RAAC mixture (4.75–9.5 mm), 5.0% for the medium RAAC mixture (9.5–13.2 mm), and 4.8% for the coarse RAAC mixture (13.2–16 mm). However, all three RAAC mixtures met the specified design criteria. Semi-circular bend (SCB) beam specimens with a diameter of 150 mm and thickness of 50 mm were then prepared from the compacted mixtures for fatigue testing.

2.2 Test design

2.2.1 Los Angeles abrasion test

The Los Angeles abrasion test was conducted to evaluate the change in angularity of RCA from different size fractions under the action of abrasion. RCA of sizes 4.75–9.5 mm, 9.5–13.2 mm, and 13.2–16 mm were subjected to 0, 200, 400, and 800 rotations in the Los Angeles abrasion machine as shown in Figure 3 to generate RCA materials with different levels of angularity.

Figure 4 displays the morphological characteristics of RCA particles from different size fractions after various rotations. Initially at 0 rotations, RCA surfaces were intact with distinct edges and irregular rough textures resulting from the original composite material. With increasing rotations to 200 and 400, surface abrasion occurred as sharp corners gradually smoothed out and particle shapes became more rounded and regular. Significant fragmentation and surface polishing were observed after 800

rotations, exhibiting the transformation of RCA morphology under prolonged abrasional forces.

After abrasion, the RCA materials were sieved to obtain single-sized fractions within the given size ranges for further testing. Convexity, axiality coefficient (AC) and roundness were selected as angularity indices to quantify the changes in RCA morphology. Each test was conducted in triplicate to ensure repeatability. For each condition, the average value was calculated from three replicates, and the corresponding standard deviation was used to represent data variability.

Convexity is an important indicator for evaluating the complexity of the RCA surface, as shown in Equation 1. The convexity value reflects the regularity of the RCA particle shape. The closer the convexity value is to 1, the more elliptical the shape. Higher convexity values indicate a more irregular aggregate particle surface with more protrusions.

$$Convexity = \frac{C_{convex}}{C_{ellipse}} \tag{1}$$

where C_{convex} is the convex perimeter of the RCA, and $C_{ellipse}$ is the equivalent elliptical perimeter of the RCA.

The AC reflects the elongation of aggregate particles, defined as the ratio of the lengths of the major axis to the minor axis of the equivalent ellipse, as shown in Equation 2. A higher AC may indicate poorer workability and higher internal friction in the RCA, thereby affecting the performance of asphalt concrete.

$$AC = \frac{D_{max}}{D_{min}} \tag{2}$$

where D_{max} and D_{min} are the lengths of the major and minor axes of the equivalent ellipse of the aggregate, respectively.

Roundness is a parameter used to measure the degree to which the shape of RCA particles approximates a circle, as shown in Equation 3.

$$Roundness = \frac{4\pi A}{C^2} \tag{3}$$

where A and C are the projected area and perimeter of the aggregate, respectively.

2.2.2 Semi-circular bend (SCB) test

The SCB test was performed to evaluate the fatigue resistance of RAAC. Figure 5 illustrates the fabrication of SCB specimens with a diameter of 150 mm and thickness of 50 mm. A Universal Testing Machine (UTM-100) was employed to load

FIGURE 1
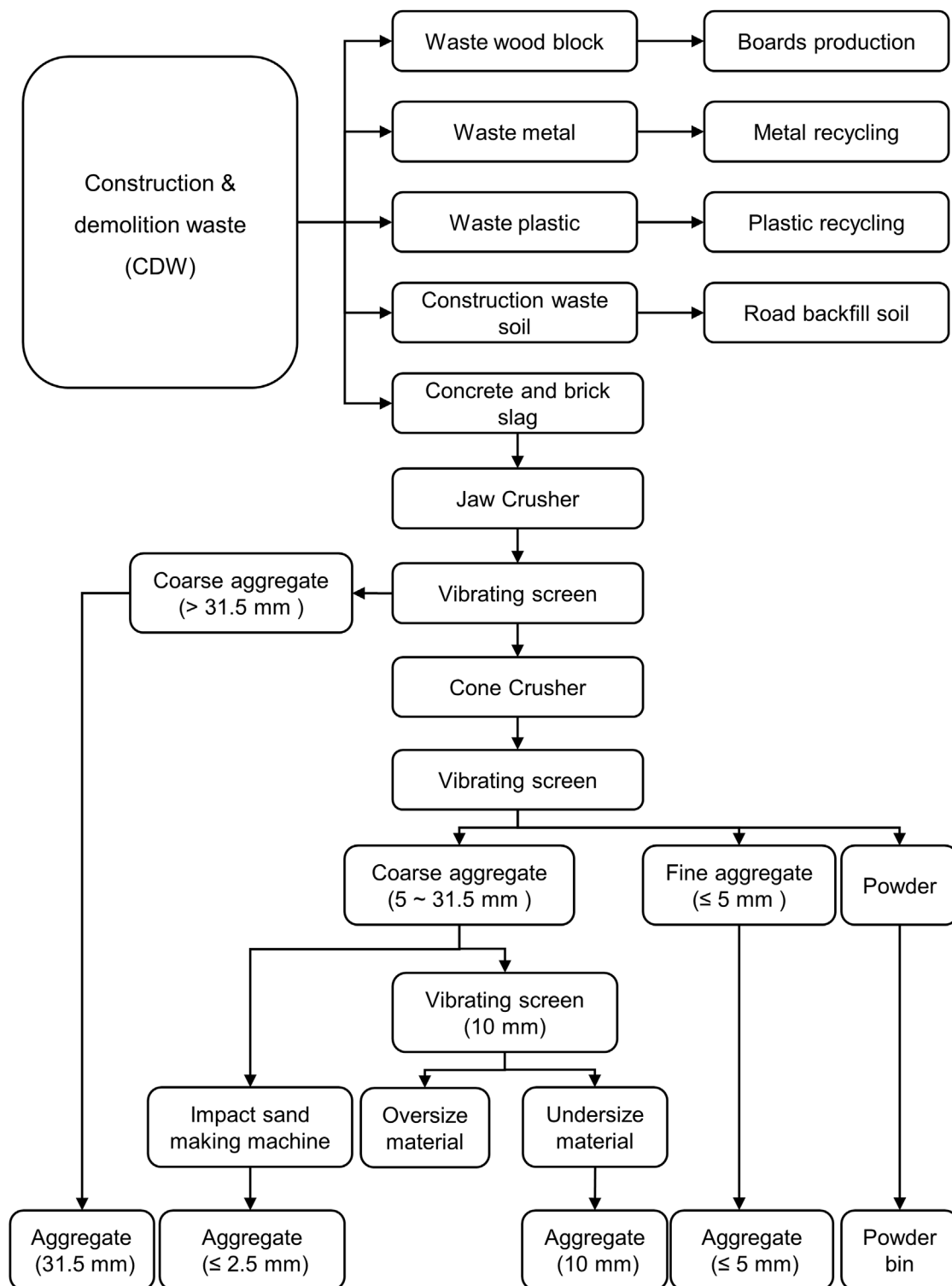Recovery of CDW and production process of RCA.

the SCB specimens in a three-point bending mode with a loading roller diameter of 1 mm and support roller span of 0.8 times the beam diameter.

The stress level, defined as the ratio of applied stress to the maximum tensile stress in the test, is typically employed to simulate the stress state of materials under various loading conditions. In

FIGURE 2
The gradation curve of the produced RCA.
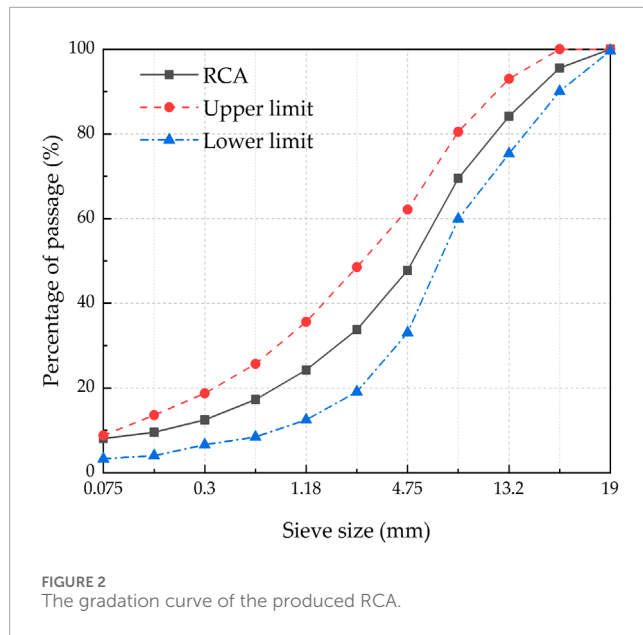
cyclic SCB fatigue testing, three loading levels were established based on the maximum tensile stress (σ_t): 20%, 30%, and 40% of σ_t, corresponding to distinct stress levels of 0.2, 0.3, and 0.4 respectively. The maximum tensile stress at the bottom of an SCB specimen was determined using Equation 4. In accordance with the recommended specifications outlined in NCHRP 09–46, the loading rate for fracture tests was set at 50 mm/min. The cyclic SCB fatigue tests employed a half-sine wave loading configuration with a period of 0.1 s per cycle. The loading frequency was maintained at 10 Hz, determined based on typical vehicle speeds ranging from 60 to 120 km/h.

$$\sigma_t = \frac{4.976P}{TD} \tag{4}$$

where P is the vertical load, T is the beam thickness and D is the beam diameter.

Stiffness modulus (S_t) defined as the slope of the tensile stress-strain curve was used to characterize the damage development in SCB specimens, as shown in Equation 5. Assuming a plane section assumption, the tensile strain (ε) at the beam bottom center was calculated using Equation 6,

$$S_t = \frac{\sigma_t}{\varepsilon} \tag{5}$$

$$\varepsilon = \frac{6Ld}{1.14D^2\left(5.578\frac{L}{d} - 1.3697\right)} \tag{6}$$

where L is the distance between two fixed supports and d is the beam deflection at center.

2.2.3 Freeze-thaw test

A F-T test protocol was designed to simulate severe environmental conditioning and accelerate damage accumulation in recycled asphalt concrete. Vacuum-saturated SCB specimens were subjected to freezing at −20°C for 12 h, followed by thawing in a 60°C water bath for 12 h to complete one F-T cycle (JTG E20 2011). The number of cycles applied was 0, 5, 10, 15, and 20 (He and Lu, 2024).

3 Results

3.1 Effect of abrasion rotations on RCA angularity

The evolution of angularity indices for RCA across various size ranges was quantified as a function of abrasion rotations. As shown in Figure 6a, the initial convexity values around 0.99 reflected the irregularity of RCA particle surfaces across all size fractions. With abrasion, the convexity decreased to around 0.98, suggesting a more uniform distribution of surface asperities due to the porous internal structure of RCA. This transformation is primarily driven by surface polishing, edge chipping, and local fragmentation caused by repeated particle-particle and particle-wall impacts within the Los Angeles abrasion drum. Furthermore, larger RCA particles showed greater fragmentation during abrasion, leading to more pronounced changes in convexity. This is attributed to the higher internal porosity and residual cement mortar in coarse RCA, which make them structurally weaker under impact and frictional forces. Conversely, finer RCA particles generally possess higher surface area-to-volume ratios, facilitating more uniform wear distribution.

It is noteworthy that in Figure 6a, coarse RCA particles exhibit temporary fluctuations in convexity at 200 and 400 revolutions. Convexity is defined as the ratio of the convex perimeter (C_{convex}) to the equivalent ellipse perimeter ($C_{ellipse}$), reflecting the boundary irregularity of particles. At intermediate abrasion stages, partial detachment of residual mortar and localized edge fracture may expose new angular features, increasing C_{convex} while $C_{ellipse}$ remains relatively stable. This transient rise or fluctuation in convexity reflects the inherent instability of RCA materials during the abrasion process.

As the rotations number increased to 800, the convexity values tended to stabilize, indicating that RCA particles had reached a relatively stable rounded state. The small RCA size fraction exhibited minimal shape alteration during abrasion, reflected by a limited change in convexity values. The cumulative friction and micro-fracturing removed sharp projections and smoothed the surface features, leading to a reduction in angularity.

In terms of AC (Figure 6b), higher initial values were found for larger RCA sizes suggesting an elongated particle geometry. The AC decreased with increasing rotations as edges smoothed out and shapes became rounder. The reduction was more pronounced for coarse RCA that fragmented and deformed to a larger extent under abrasional forces. This evolution suggests that abrasion not only removes surface asperities but also causes larger structural reshaping, especially in coarse RCA. In contrast, the AC of small RCA remained relatively stable as a result of its integrity against abrasion owing to the finer particle scale. Figure 6c presents the variations of roundness with abrasion rotations. Initially, minor discrepancies in roundness existed among different RCA size ranges. After abrasion treatment, the roundness approached 1, indicating well-rounded particle shapes.

Overall, the abrasion mechanism in RCA is governed by a combination of surface polishing, corner breakage, and internal cracking, especially in porous zones, which reduces angularity and enhances shape regularity. The results confirm that abrasion reduces particle angularity, but angular indices eventually stabilize as

TABLE 2 Basic physical properties of the RCA.

Items	Tested values			Requirements	Specification
	4.75–9.5 mm	9.5–13.2 mm	13.2–16 mm		
Apparent density (g/cm^3)	2.55	2.6	2.66	≥2.25%	JTG E20 T 0328
Crushing value (%)	16.9	14.8	19.2	≤30.0%	JTG E20 T 0316
Water absorption (%)	6.2	6.8	4.7	≤8.0%	JTG E20 T 0307
Los Angeles attrition loss (%)	24.0	24.2	27.7	≤28.0%	JTG E20 T 0317
Needle flake content (%)	8.8	6.0	8.8	≤10.0%	JTG E20 T 0312

FIGURE 3
Los Angeles abrasion machine.
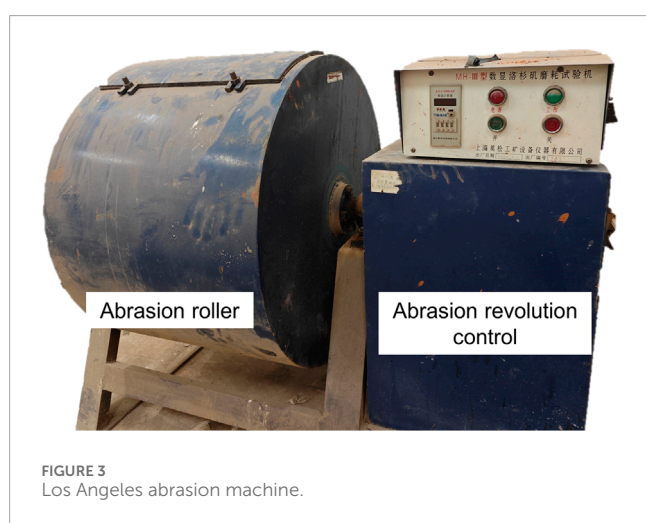
particles transition to a more equilibrium geometry. In conclusion, fine RCA showed the least shape degradation under abrasion and preserved stable angularity, which is advantageous for asphalt mixture performance. Favorable angularity enhances internal friction and interlocking, ultimately improving structural integrity and load-bearing capacity.

3.2 Fatigue life of RAAC with different RCA sizes and F-T cycles

Figure 7 illustrates the fatigue life of RAAC mixtures containing coarse, medium and fine RCA size, subjected to 0, 5, 10, 15 and 20 F-T cycles under stress levels of 0.2, 0.3 and 0.4. The data points in each bar graph represent the mean fatigue life obtained from three replicates, with error bars indicating one standard deviation. The standard deviations were calculated for each test condition to ensure statistical rigor. In general, the fatigue life decreased with increasing F-T cycles regardless of stress level applied.

At a stress level of 0.2 (Figure 7a), F-T cycling significantly affected the fatigue resistance as failures occurred in a linear manner. The internal damages in RAAC propagated and cracks extended more readily when subjected to alternating environmental and mechanical loadings. The phase change of water to ice in pores during freezing generated substantial expansion pressures, severely damaging the aggregate-binder interfaces.

In addition, increment of freeze depth with successive cycles further accumulated ice in pores, worsening the microcracking state. Thawing induced extra pore expansion/contraction and rearranged pore structure, weakening the samples. It was also observed that at a given stress level and F-T condition, different RCA sizes led to distinct fatigue lives. Specifically, the trend was: Coarse size < Medium size < Fine size.

Fine RCA size RAAC mixture exhibited the highest fatigue resistance attributed to its denser microstructure and strong interlocking between filler and coarse aggregates, effectively mitigating the expansion stresses during freezing. Medium RCA size provided moderate particle sizes and structural integrity, while large RCA particles in the coarse mixture lowered the resistance against F-T damages likely due to higher porosity and weaker bonding.
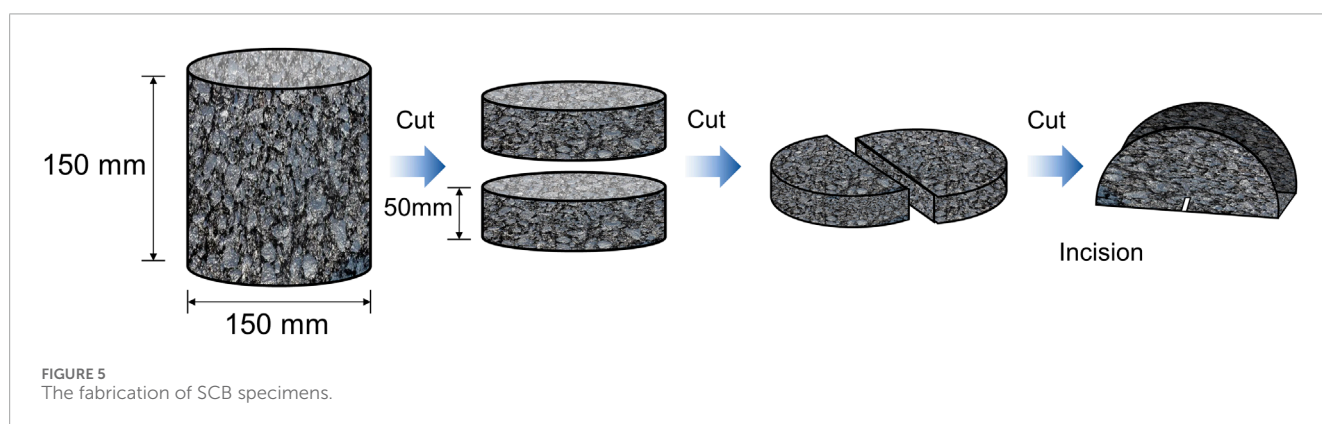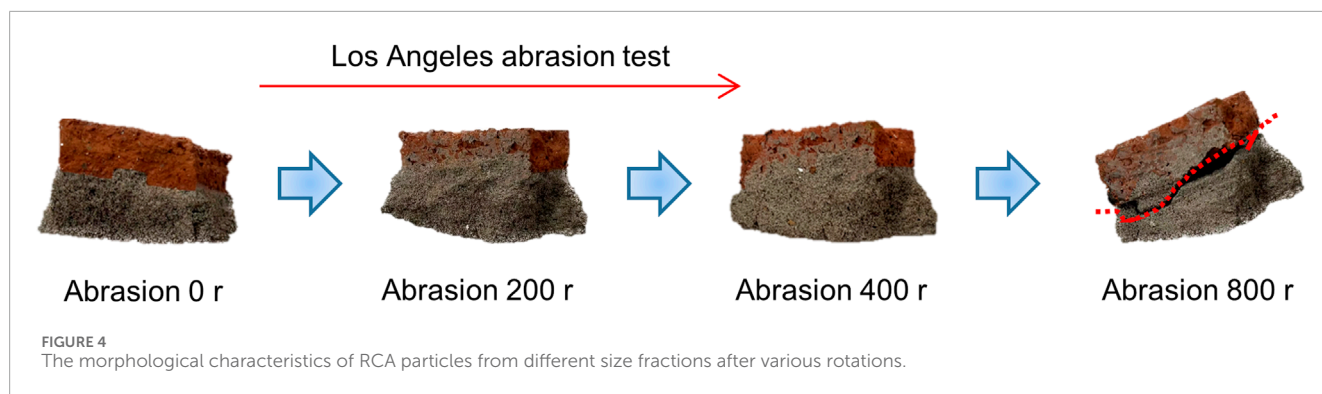
Furthermore, Figure 7 indicates that F-T cycling gradually flattened the slope of S-N curves, especially for coarse RAAC as its sensitivity to stress levels reduced substantially with F-T deterioration. This phenomenon could be explained by the fact that F-T accelerated fatigue damage accumulation so that applied stresses had limited additional effect on the weakened mixtures.

In summary, RCA size and F-T cycles played a vital role in governing the fatigue life of RAAC. Fine RCA size demonstrated optimal resistance against F-T hazards and fatigue failures compared to other sizes.

3.3 Stiffness modulus of RAAC under F-T cycles

Figure 8 illustrates the change of RAAC stiffness modulus with the increase of fatigue load cycles under different F-T conditions. Regardless of stress level, RCA size or F-T cycle times, the stiffness modulus steadily decreased as cracking and damage developed within RAAC beams. A three-stage evolution pattern was exhibited, including abrupt change, balance and failure stages.

In the initial stage, fatigue loading rapidly reduced the stiffness due to the formation and propagation of critical cracks. This

FIGURE 4
The morphological characteristics of RCA particles from different size fractions after various rotations.

FIGURE 5
The fabrication of SCB specimens.

was attributed to stress concentration at flaws and openings in RAAC. As cracking stabilized through stress redistribution in the samples, the modulus dropped at a steady slow pace during the balance period.

When internal damages accumulated to a critical level, a second sharp decrease occurred until complete failure. As shown in Figure 8a, coarse RCA size mixture presented the most precipitous stiffness loss compared to the medium (Figure 8b) and fine mixtures (Figure 8c). Its higher porosity facilitated moisture ingress and exacerbated expansion stresses during F-T, leading to faster cracking propagation and structural deterioration.

F-T cycles accelerated the reduction of stiffness modulus for all RAAC mixtures. Exposure to alternating freezing and thawing induced cumulative microcrack growth inside the samples by pore pressure effects. Moreover, F-T exacerbated fatigue damage development under cyclic loading, shortening the lifespan before structural instability.

Among the different RCA sizes at equivalent stress levels and F-T conditions, fine RCA size mixture exhibited the highest modulus retention capacity, followed by medium then coarse size. The trend could be attributed to the more compact microstructure and improved interfacial bonding achievable with decreasing particle sizes. In particular, smaller RCA enabled better pore amelioration and reduced damage sensitivity against environmental conditioning.

In summary, RAAC stiffness drastically reduced as a function of both fatigue cycles and F-T exposures. However, rational RCA size

for replacement could enhance the resistance of recycled mixtures against coupled fatigue-environmental damages.

4 Discussion

4.1 Evaluation of angularity indices response to fatigue life

To further assess the relative importance of morphological and environmental parameters on fatigue performance, a gray correlation analysis (GCA) was performed on our test results. The influencing factors include RCA size (coarse, medium and fine), convexity, *AC*, roundness and number of F-T cycles. Fatigue life was considered as a reference sequence. A gray correlation coefficient of more than 0.6 was defined as a strong correlation, while between 0.4 and 0.6 was a moderate correlation. Table 3 summarizes the results of the correlation analysis between the influencing factors and fatigue life.

The correlation results showed that RCA sizes exhibited a strong correlation, and angularity indices and the number of F-T cycles exhibited a moderate correlation. The effect of roundness is the least among them. RCA sizes inherently affect multiple aspects of the asphalt concrete's internal structure, including aggregate packing density, void content, and interfacial bonding area. Finer RCA promotes a denser microstructure and better filler-binder integration, reducing crack initiation points and enhancing fatigue resistance. Conversely, coarse RCA often leads to weaker
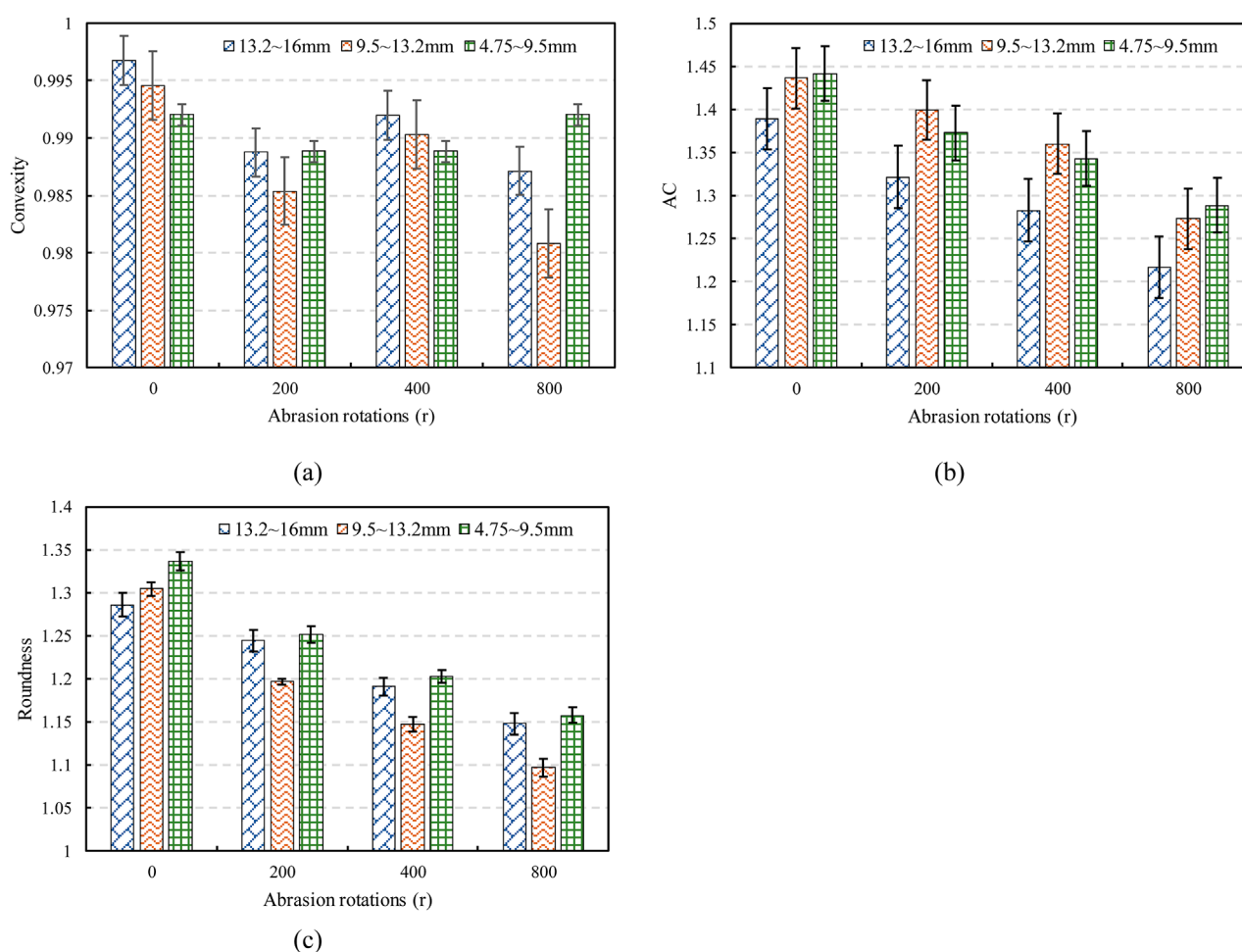
FIGURE 6
The changes in angularity indices of RCA from different size fractions with increasing abrasion rotations: **(a)** Convexity, **(b)** AC and **(c)** Roundness.

interfacial zones and higher porosity, increasing susceptibility to environmental and mechanical deterioration.

Among the three angularity indices, AC demonstrated the highest grey relational grade. This is reasonable because AC reflects particle elongation or anisotropy, which plays a crucial role in load transfer and inter-particle interlock. Elongated particles may enhance frictional contact, limit relative movement, and improve resistance to fatigue crack propagation. Moreover, the beneficial effect of high AC may be more pronounced under F-T cycle damage conditions, where interfacial degradation reduces chemical bonding and mechanical interlock becomes a more dominant factor in maintaining structural integrity.

4.2 Fatigue life prediction of RAAC

The fatigue life of RAAC was greatly influenced by RCA size and F-T cycles. Three fatigue life prediction models, namely, the Basquin model, the S-logN model, and the Exponential model, were used for comparative analysis. The results are shown in Table 4 and Figure 9. The Basquin model showed high fitting accuracy under all conditions, with most R^2 values exceeding 0.99.

This indicates strong predictive performance. Although the S-logN and Exponential models also performed well in some cases, their overall R^2 values were lower, especially at early F-T cycles. As the number of F–T cycles increased, the differences among the models became smaller. However, the Basquin model still maintained a clear advantage.

Therefore, the effects of the parameters are discussed further for the Basquin model. Figure 10 shows the fitting curves of fatigue life versus stress level for various RCA size gradations under different F-T conditions, based on the experimental data.

Consistently across gradations, RAAC fatigue life decreased with increasing stress levels, consistent with Basquin's equation. Higher stress levels accelerated crack initiation and propagation, thereby shortening fatigue life. Moreover, F-T cycling contributed to progressive degradation, as evidenced by the general downward shift of fitting curves. Contrary to initial expectations, the fitted Basquin parameter n tended to increase with the number of F-T cycles, indicating that fatigue life became more sensitive to stress levels as the material accumulated microstructural damage. This increasing sensitivity was especially noticeable in coarse RAAC mixture.
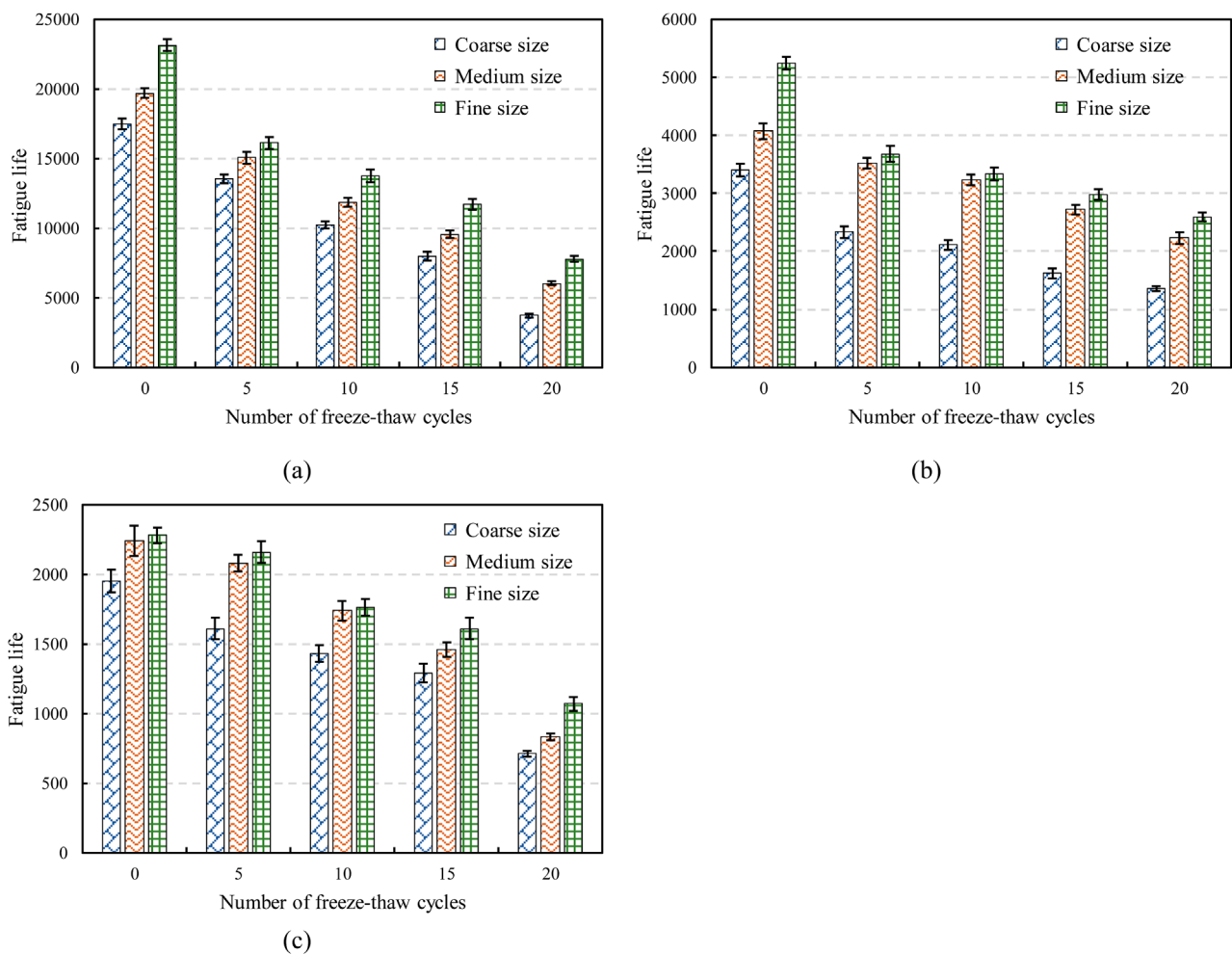
FIGURE 7
The effect of different F-T cycles on the fatigue life of RAAC mixtures with coarse, medium, and fine RCA sizes at stress levels of **(a)** 0.2, **(b)** 0.3, and **(c)** 0.4.

The fatigue parameters k and n were estimated through nonlinear regression and summarized in Table 5, where the associated root mean square error (RMSE) and mean absolute error (MAE) values are also reported to quantify the accuracy of the fitted models. To evaluate the generalization capability of the fatigue life prediction model, both leave-one-out cross-validation (LOOCV) and five-fold cross-validation were performed based on the log–log regression between stress ratio and fatigue life. The average relative prediction error was 4.13% and 4.14%, respectively, indicating high model robustness and predictive reliability across all RCA gradations and F-T conditions.

Parameter k represents the inherent fatigue resistance (higher k values indicate longer fatigue life), whereas n reflects the sensitivity of fatigue life to stress variation (a higher n value signifies stronger stress dependency). As the number of F-T cycles increased, $\lg k$ generally decreased, reflecting the material's weakening resistance to repeated loading. Simultaneously, n values increased, demonstrating that stress effects became more dominant in governing fatigue performance under deteriorated conditions. It is evident that both k and n were affected significantly by F-T cycling. For all RCA

sizes, the k value generally decreased with increasing F-T cycles from 0 to 20, indicating fatigue resistance reduction. Meanwhile, the n value exhibited an increasing trend, suggesting higher stress responsiveness of RAAC weakened by cyclic environmental damage. This was in line with the flattened S-N curves under more extensive F-T conditioning shown in Figure 9a. Furthermore, at equivalent F-T conditions, fine RCA size mixture achieved the highest k and lowest n amongst the three sizes, inferring its superior resistance against coupled fatigue-environmental effects compared to other sizes. In summary, the fatigue model reasonably characterized the influence of RCA properties and F-T cycles on RAAC durability. Rational size governed the changes of predictive parameters and material performance.

4.3 Fracture mechanics perspective on SCB fatigue performance

F-T cycling accelerates fatigue damage in RAAC by promoting early crack development and reducing the mixture's ability to resist
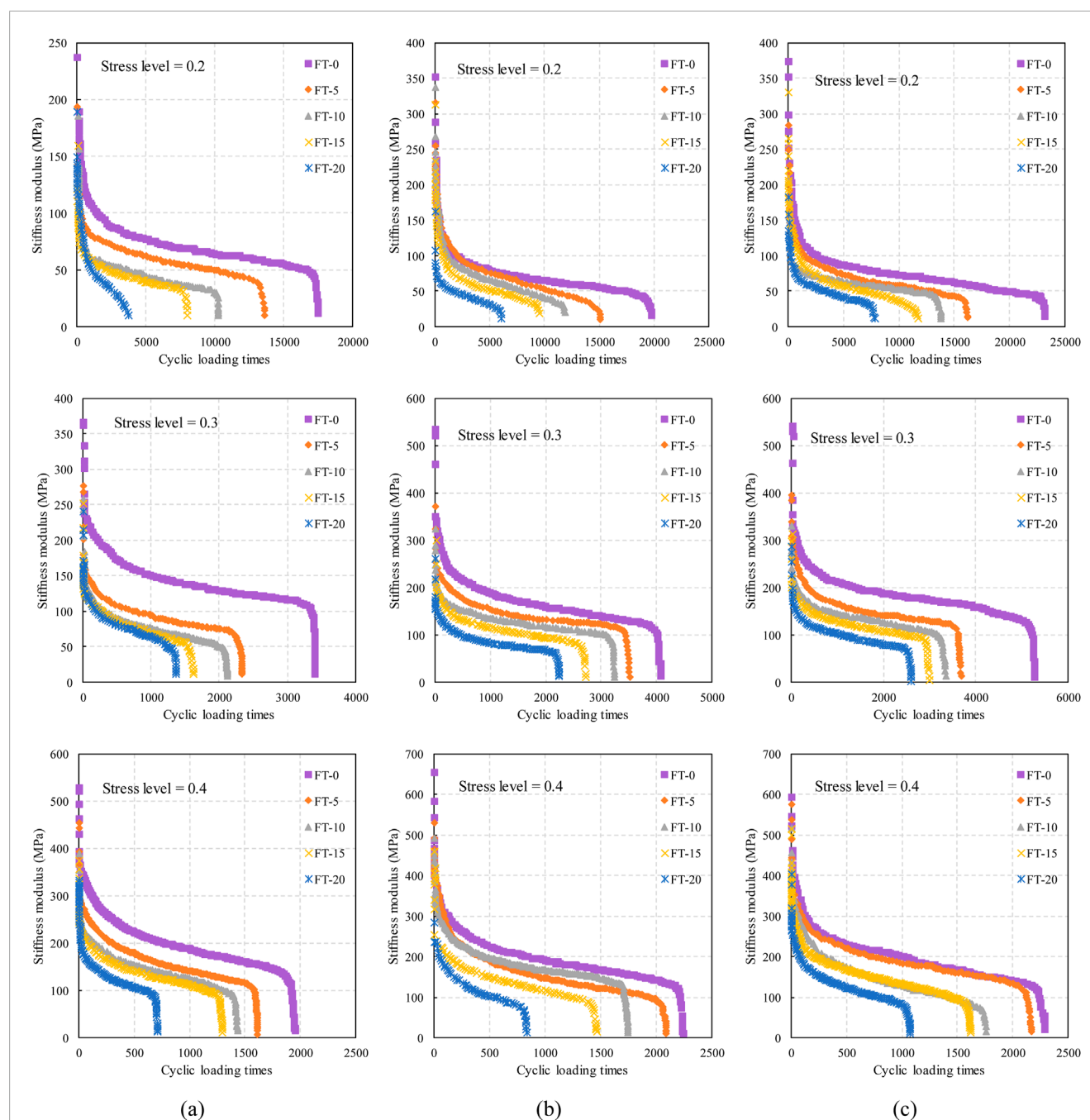
FIGURE 8
Variation of the stiffness modulus of RAAC with coarse **(a)**, medium **(b)**, and fine **(c)** RCA sizes under different F-T cycles as a function of fatigue loading cycles.

fracture. Each F-T cycle introduces micro-cracks and weakens the asphalt–aggregate bond, so less energy is required for a crack to initiate and grow under repeated loading. From a fracture mechanics standpoint, this manifests as a reduction in fracture toughness or fracture energy after conditioning – the material cannot absorb as much strain energy before crack propagation occurs (Launey and Ritchie, 2009). F-T damage causes earlier micro-crack formation, faster macro-crack growth, and premature asphalt–aggregate debonding in asphalt mixtures (Haghighatpour

and Aliha, 2023). In terms of energy dissipation, a damaged RAAC specimen will dissipate energy more rapidly through crack extension rather than elastic deformation, which means the critical strain energy release rate is reached in fewer cycles (Li X. et al., 2024). Consequently, the SCB fatigue performance of RAAC drops after F-T exposure because the material's fracture energy threshold has been lowered by internal damage.

The inclusion of recycled concrete aggregates intensifies these fracture effects due to the distinct morphology and interfacial

TABLE 3 Grey correlation analysis results between influence factors and fatigue life.

Influence factor	Grey correlation coefficient	Degree of correlation
RCA sizes	0.604	Strong correlation
Convexity	0.571	Moderate correlation
AC	0.574	Moderate correlation
Roundness	0.526	Moderate correlation
Number of F-T cycles	0.566	Moderate correlation

TABLE 4 Comparison of R^2 values for three fatigue life prediction models.

Number of F-T cycles	RCA sizes	R^2		
		Basquin	S-logN	Exponential
0	Coarse	0.9959	0.9679	0.9904
	Medium	0.9966	0.9699	0.9911
	Fine	0.9994	0.9815	0.9962
5	Coarse	0.9922	0.9638	0.9857
	Medium	0.9952	0.9682	0.9876
	Fine	0.9954	0.9683	0.9881
10	Coarse	0.9915	0.9624	0.9829
	Medium	0.9977	0.9759	0.9908
	Fine	0.9976	0.9743	0.9917
15	Coarse	0.9847	0.9560	0.9730
	Medium	0.9980	0.9773	0.9910
	Fine	0.9973	0.9741	0.9907
20	Coarse	0.9998	0.9879	0.9944
	Medium	0.9970	0.9999	0.9999
	Fine	0.9997	0.9960	0.9988

structure of RCA (Zhang et al., 2023). RCA particles are more porous and often carry residual cement mortar, which creates a weaker interfacial transition zone with the asphalt mastic (Huang et al., 2021; Li M. et al., 2025). Cracks tend to initiate at these flawed interfaces or within the porous RCA itself, rather than through intact binder or strong natural aggregates. This means that less external energy is needed to drive crack growth in RAAC – a significant portion of the fracture process is accommodated by debonding at the RCA mastic interface (Kazemian et al., 2019; Xiao et al., 2022). Recent fracture tests confirm that cracks in RAAC preferentially follow the asphalt-RCA interface, indicating that this is the path of least resistance (Hu et al., 2024). As RCA content

increases, the total fracture energy of the mix declines markedly because more crack-prone zones are introduced. In fact, high RCA mixtures (e.g., >50% replacement) exhibit significantly lower SCB fracture resistance, reflecting the dominance of weak RCA interfaces in energy absorption and crack propagation (Hu et al., 2024; Kou et al., 2025). These weaknesses are further exacerbated under F-T conditions. This is mainly due to the fact that water can infiltrate the porous RCA and expand during freezing, widening interfacial transition zone (ITZ) micro-cracks and eroding the asphalt-RCA bond (Ren et al., 2022). The result is a compounding effect in which RAAC after F-T has both a inherently weaker crack-resistant skeleton (due to RCA) and additional micro-fractures from
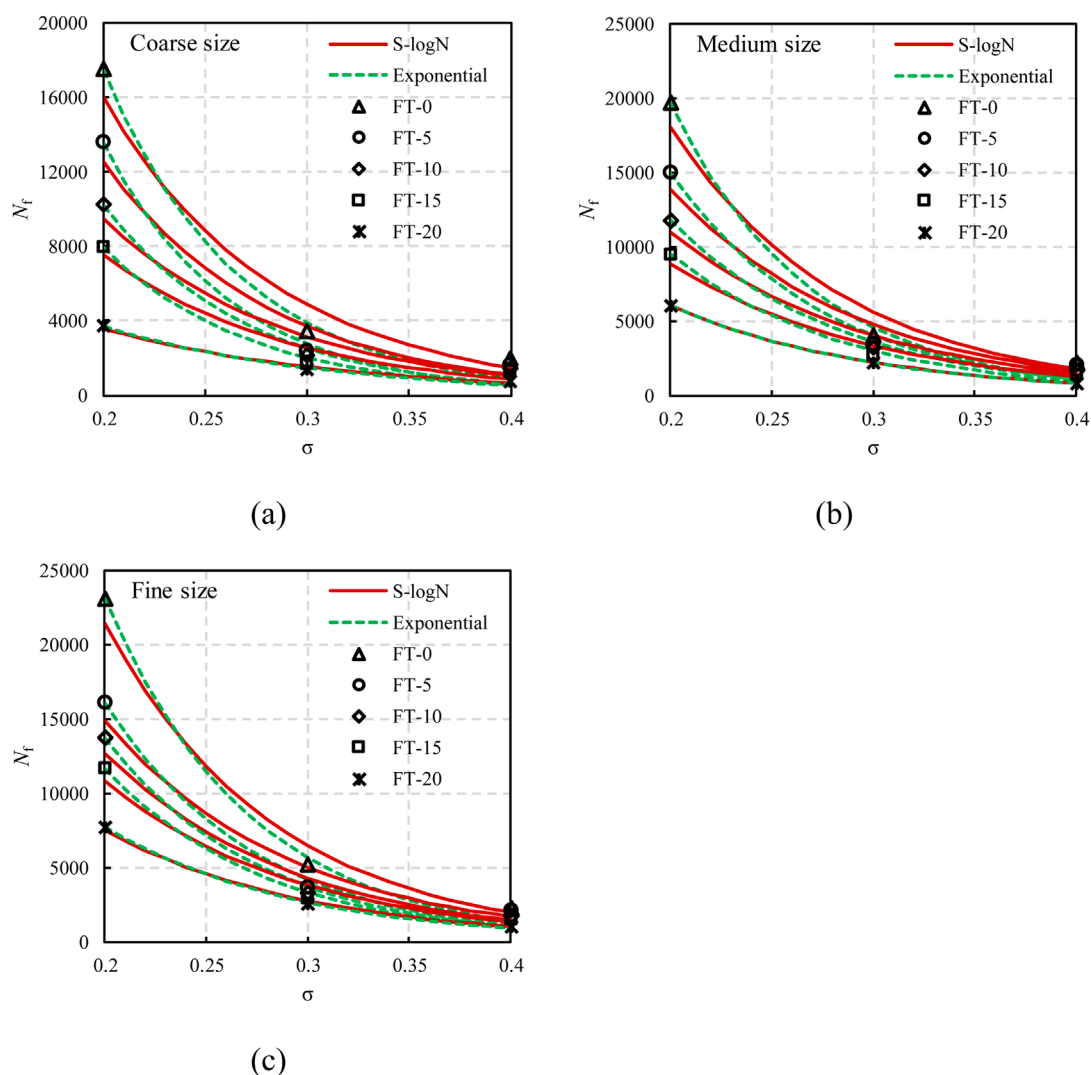
FIGURE 9
Fitted curves of fatigue life and stress level based on S-logN model and exponential model under different F-T cycles: **(a)** coarse size; **(b)** medium size, and **(c)** fine size.

thermal cycling. Thus, when subjected to cyclic bending loads, a F-T damaged RAAC specimen dissipates energy quickly through interfacial cracking and shows accelerated fatigue failure.

In summary, the SCB fatigue life of RAAC is governed by its fracture mechanics–lower fracture toughness in the RCA-modified, F-T leads to easier crack initiation and faster crack growth, explaining the observed reduction in fatigue performance from an energy-based perspective.

5 Conclusion

This study investigated the influence of recycled concrete aggregate and freeze-thaw (F-T) cycles on the fatigue performance of recycled asphalt concrete. The following conclusions can be drawn:

(a) Los Angeles abrasion tests revealed that finer RCA fractions underwent less morphological transformation and maintained

relatively stable angularity during abrasion. Convexity decreased gradually with increasing abrasion rotations, while axiality coefficient (AC) and roundness stabilized for all RCA size fractions, indicating a balanced morphological evolution.

(b) Semi-circular bend (SCB) tests showed that RCA size and the number of F-T cycles significantly affected RAAC mixtures' fatigue performance. Under equivalent stress levels and environmental conditions, the trend of fatigue followed the order of coarse size replacement < medium size replacement < fine size replacement.

(c) F-T cycling accelerated damage accumulation in RAAC, demonstrated by reductions in fatigue life and stiffness modulus with increasing cycle numbers. Mixtures incorporating fine RCA exhibited the greatest resistance to F-T-induced deterioration, followed by medium and coarse RCA mixtures, respectively. Grey correlation analysis further indicated a strong correlation between RCA size and
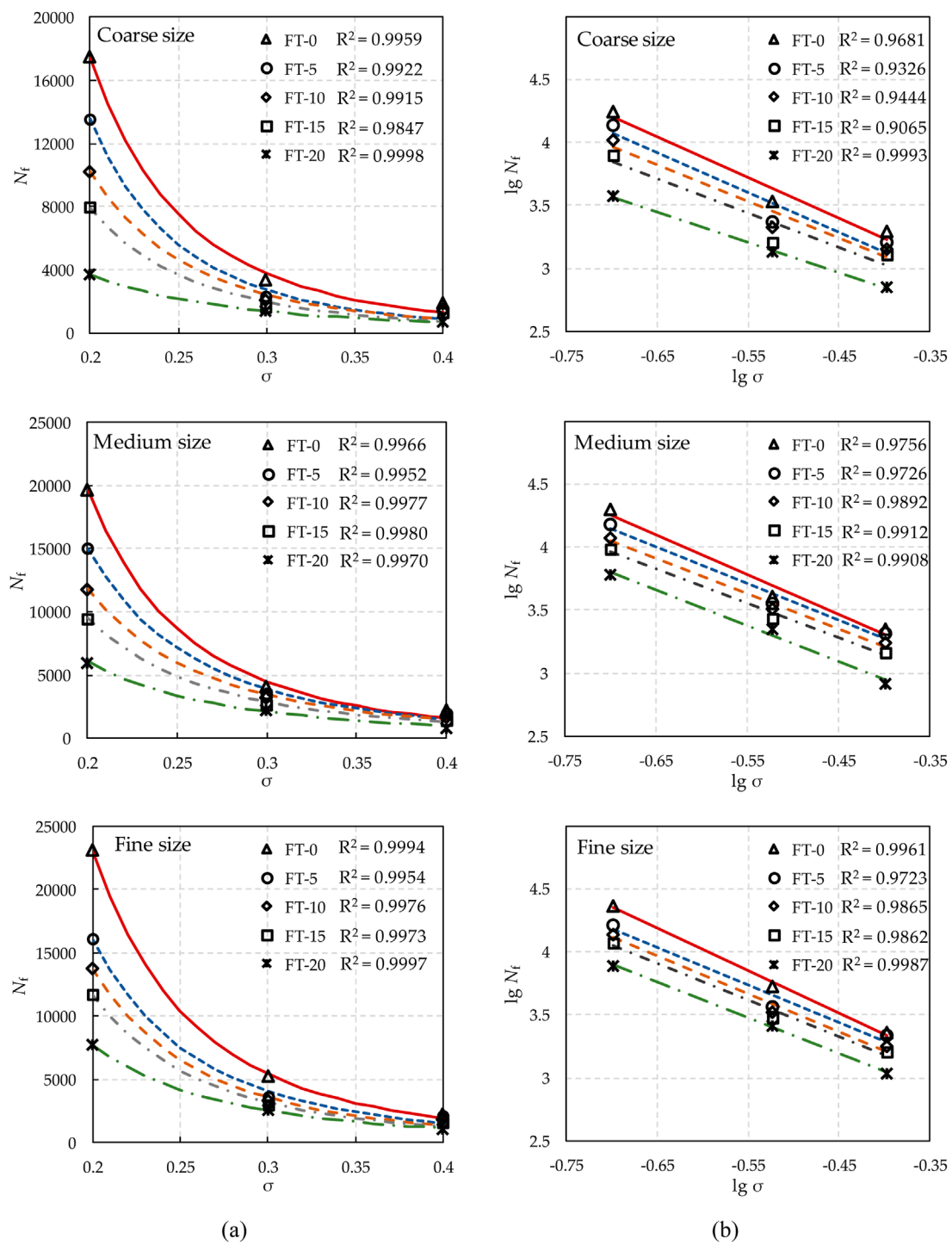
FIGURE 10
Fitted curves of fatigue life and stress levels for mixtures with different RCA sizes under different F–T cycles: **(a)** nonlinear curves; **(b)** linear curves.

fatigue life, while the AC exhibited a moderate correlation, being the more influential morphological index among those analyzed.

(d) A three-stage evolution pattern of stiffness change with fatigue loading comprised an initial abrupt drop, subsequent balanced decline and final failure phase. The presence of F-T cycles

significantly exacerbated stiffness degradation. Rational RCA size effectively improved resistance against F-T impacts and retarded structural deterioration.

(e) The fatigue model reasonably predicted the performance through fitting parameters ($R^2 > 0.90$). Both k and n were sensitive to F-T conditioning, while fine size

TABLE 5 Fitted parameters and evaluation metrics for the fatigue life prediction model.

Number of F-T cycles	RCA sizes	The fatigue parameters		R^2	RMSE	MAE
		Lg k	n			
0	Coarse	1.949	2.395	0.9681	0.0722	0.0677
	Medium	2.113	2.732	0.9756	0.0622	0.0583
	Fine	2.110	2.850	0.9961	0.0260	0.2044
5	Coarse	1.943	2.711	0.9326	0.1048	0.0983
	Medium	2.099	2.793	0.9726	0.0602	0.0565
	Fine	2.021	2.894	0.9723	0.0616	0.0578
10	Coarse	1.926	2.909	0.9444	0.0872	0.0818
	Medium	2.051	2.834	0.9892	0.0360	0.0337
	Fine	2.015	2.950	0.9865	0.0434	0.0407
15	Coarse	1.892	3.156	0.9065	0.1075	0.1009
	Medium	2.031	2.904	0.9912	0.0319	0.0299
	Fine	1.998	3.001	0.9862	0.0422	0.0396
20	Coarse	1.865	3.222	0.9993	0.0076	0.0072
	Medium	1.819	3.186	0.9908	0.0337	0.0316
	Fine	1.905	3.365	0.9987	0.0125	0.0117

RCA mixture achieved the highest k and lowest n, suggesting optimal fatigue-environmental resistance amongst the sizes.

In summary, this study established that RCA size selection and F-T cycling significantly influence RAAC fatigue performance. Optimal RCA morphological properties can enhance RAAC durability under combined environmental and mechanical stresses. These findings provide critical insights and guidance for the design and structural evaluation of sustainable asphalt mixtures containing recycled aggregates.

Data availability statement

The original contributions presented in the study are included in the article/supplementary material, further inquiries can be directed to the corresponding author.

Author contributions

YY: Software, Writing – original draft, Data curation, Formal Analysis, Investigation, Validation. WL: Conceptualization, Supervision, Project administration, Writing – original draft, Investigation, Methodology. LW: Writing – original draft, Methodology, Conceptualization, Investigation, Formal Analysis, Writing – review and editing.

Conflict of interest

The authors declare that the research was conducted in the absence of any commercial or financial relationships that could be construed as a potential conflict of interest.

Generative AI statement

The author(s) declare that no Generative AI was used in the creation of this manuscript.

Publisher's note

References

Aboutalebi Esfahani, M. (2020). Evaluating the feasibility, usability, and strength of recycled construction and demolition waste in base and subbase courses. *Road. Mater. Pavement Des.* 21, 156–178. doi:10.1080/14680629.2018.1483259

Akbas, M., Ozaslan, B., and Iyisan, R. (2023). Utilization of recycled concrete aggregates for developing high-performance and durable flexible pavements. *Constr. Build. Mater.* 407, 133479. doi:10.1016/j.conbuildmat.2023.133479

Arasan, S., Yenera, E., Hattatoglu, F., Hinislioglua, S., and Akbuluta, S. (2011). Correlation between shape of aggregate and mechanical properties of asphalt concrete: digital image processing approach. *Road. Mater. Pavement Des.* 12, 239–262. doi:10.1080/14680629.2011.9695245

Bazoobandi, P., Karimi, H. R., Mousavi, S. R., Karimi, F., and Aliha, M. (2023). Full range of mode I and ii cracking performance of asphalt mixtures containing low to high reclaimed asphalt pavement (rap) contents; modified by recycling agent and substituting of a softer binder. *Case Stud. Constr. Mater.* 19, e02487. doi:10.1016/j.cscm.2023.e02487

Bessa, I. S., Branco, V. T. C., Soares, J. B., and Neto, J. A. N. (2015). Aggregate shape properties and their influence on the behavior of hot-mix asphalt. *J. Mater. Civ. Eng.* 27, 04014212. doi:10.1061/(asce)mt.1943-5533.0001181

Cui, P., Xiao, Y., Yan, B., Li, M., and Wu, S. (2018). Morphological characteristics of aggregates and their influence on the performance of asphalt mixture. *Constr. Build. Mater.* 186, 303–312. doi:10.1016/j.conbuildmat.2018.07.124

Ding, X., Ma, T., and Gao, W. (2017). Morphological characterization and mechanical analysis for coarse aggregate skeleton of asphalt mixture based on discrete-element modeling. *Constr. Build. Mater.* 154, 1048–1061. doi:10.1016/j.conbuildmat.2017.08.008

Feng, D., Yi, J., Wang, D., and Chen, L. (2010). Impact of salt and freeze–thaw cycles on performance of asphalt mixtures in coastal frozen region of China. *Cold Regions Sci. Technol.* 62, 34–41. doi:10.1016/j.coldregions.2010.02.002

Gong, F., Liu, Y., You, Z., and Zhou, X. (2021). Characterization and evaluation of morphological features for aggregate in asphalt mixture: a review. *Constr. Build. Mater.* 273, 121989. doi:10.1016/j.conbuildmat.2020.121989

Haghighatpour, P. J., and Aliha, M. (2023). The influence of recycled asphalt pavement materials on low and intermediate fracture behavior of asphalt concrete (Ac) after exposing to different thawing and freezing periods. *Eng. Fract. Mech.* 293, 109715. doi:10.1016/j.engfracmech.2023.109715

Hao, L., Liu, Y., Wang, W., Zhang, J., and Zhang, Y. (2018). Effect of salty freeze-thaw cycles on durability of thermal insulation concrete with recycled aggregates. *Constr. Build. Mater.* 189, 478–486. doi:10.1016/j.conbuildmat.2018.09.033

He, R., and Lu, N. (2024). Hydration, fresh, mechanical, and freeze-thaw properties of cement mortar incorporated with polymeric microspheres. *Adv. Compos. Hybrid Mater.* 7, 92. doi:10.1007/s42114-024-00899-2

Hosseini, S. G., Kordani, A. A., and Zarei, M. (2023). Effect of recycled additives on pure mode I fracture resistance and moisture susceptibility of hot mix asphalt (hma): an experimental study using semicircular bending (scb) and indirect tensile strength (its) tests. *Theor. Appl. Fract. Mech.* 128, 104168. doi:10.1016/j.tafmec.2023.104168

Hu, J., Zhao, W., Liu, P., Huang, Q., and Luo, S. (2024). Study on fracture characteristics of recycled aggregates asphalt concrete. *Constr. Build. Mater.* 419, 135431. doi:10.1016/j.conbuildmat.2024.135431

Huang, Q., Qian, Z., Hu, J., Zheng, D., Chen, L., Zhang, M., et al. (2021). Investigation on the properties of aggregate-mastic interfacial transition zones (itzs) in asphalt mixture containing recycled concrete aggregate. *Constr. Build. Mater.* 269, 121257. doi:10.1016/j.conbuildmat.2020.121257

JTG E20 (2011). *Standard test methods of bitumen and bituminous mixtures for Highway engineering*. Beijing, China: JTG E20; Ministry of Transport of the People's Republic of China.

Kakar, M. R., Hamzah, M. O., and Valentin, J. (2015). A review on moisture damages of hot and warm mix asphalt and related investigations. *J. Clean. Prod.* 99, 39–58. doi:10.1016/j.jclepro.2015.03.028

Kazemian, F., Rooholamini, H., and Hassani, A. (2019). Mechanical and fracture properties of concrete containing treated and untreated recycled concrete aggregates. *Constr. Build. Mater.* 209, 690–700. doi:10.1016/j.conbuildmat.2019.03.179

Kogbara, R. B., Masad, E. A., Kassem, E., Scarpas, A. T., and Anupam, K. (2016). A state-of-the-art review of parameters influencing measurement and modeling of skid resistance of asphalt pavements. *Constr. Build. Mater.* 114, 602–617. doi:10.1016/j.conbuildmat.2016.04.002

Kong, D., Chen, M., Xie, J., Zhao, M., and Yang, C. (2019). Geometric characteristics of bof slag coarse aggregate and its influence on asphalt concrete. *Materials* 12, 741. doi:10.3390/ma12050741

Kou, C., Fan, R., Zhang, M., Zhu, Z., Kang, A., and Baaj, H. (2025). Investigation into the crack propagation behaviors of asphalt mixture containing recycled concrete aggregates using digital image correlation. *Constr. Build. Mater.* 470, 140636. doi:10.1016/j.conbuildmat.2025.140636

Launey, M. E., and Ritchie, R. O. (2009). On the fracture toughness of advanced materials. *Adv. Mater.* 21, 2103–2110. doi:10.1002/adma.200803322

Li, J., Qin, Y., Zhang, J., Zhang, A., and Zhang, X. (2024a). Compaction and shear characteristics of recycled construction and demolition aggregates in subgrade: exploring particle breakage and shape effects. *J. Clean. Prod.*, 142776. doi:10.1016/j.jclepro.2024.142776

Li, J., Qin, Y., Zhang, X., Shan, B., and Liu, C. (2024b). Emission characteristics, environmental impacts, and health risks of volatile organic compounds from asphalt materials: a state-of-the-art review. *Energy and Fuels* 38, 4787–4802. doi:10.1021/acs.energyfuels.3c04438

Li, J., Zhang, J., Yang, X., Zhang, A., and Yu, M. (2023). Monte Carlo simulations of deformation behaviour of unbound granular materials based on a real aggregate library. *Int. J. Pavement Eng.* 24, 2165650. doi:10.1080/10298436.2023.2165650

Li M., M., Xie, J., Zhang, L., Wu, S., Li, C., Sun, Q., et al. (2025). Investigation of a novel method to improve the physical properties of recycled concrete aggregate for asphalt mixtures: laboratory characterization and mechanisms. *J. Mater. Civ. Eng.* 37, 04025074. doi:10.1061/jmcee7.mteng-19114

Li N., N., Morozov, I. B., Fu, L. Y., and Deng, W. (2025). Unified nonlinear elasto-visco-plastic rheology for bituminous rocks at variable pressure and temperature. *J. Geophys. Res. Solid Earth* 130, e2024JB029295. doi:10.1029/2024jb029295

Li, X., An, H., Chen, Y., Qin, Y., Li, Y., and Zhou, Y. (2024). Mechanical properties of recycled aggregate concrete under cyclic loading and unloading in alpine areas. *J. Build. Eng.* 85, 108759. doi:10.1016/j.jobe.2024.108759

Liu, X., Liu, X., Zhang, Z., and Ai, X. (2024). Effect of carbonation curing on the characterization and properties of steel slag-based cementitious materials. *Cem. Concr. Compos.* 154, 105769. doi:10.1016/j.cemconcomp.2024.105769

Liu, Y., Huang, Y., Sun, W., Nair, H., Lane, D. S., and Wang, L. (2017). Effect of coarse aggregate morphology on the mechanical properties of stone matrix asphalt. *Constr. Build. Mater.* 152, 48–56. doi:10.1016/j.conbuildmat.2017.06.062

Olard, F., and Perraton, D. (2010). On the optimization of the aggregate packing characteristics for the design of high-performance asphalt concretes. *Road. Mater. Pavement Des.* 11, 145–169. doi:10.1080/14680629.2010.9690330

Radević, A., Isailović, I., Wistuba, M. P., Zakić, D., Orešković, M., and Mladenović, G. (2020). The impact of recycled concrete aggregate on the stiffness, fatigue, and low-temperature performance of asphalt mixtures for road construction. *Sustainability* 12, 3949. doi:10.3390/su12103949

Ren, H., Qian, Z., Lin, B., Huang, Q., Crispino, M., and Ketabdari, M. (2022). Effect of recycled concrete aggregate features on adhesion properties of asphalt mortar-aggregate interface. *Constr. Build. Mater.* 353, 129097. doi:10.1016/j.conbuildmat.2022.129097

Sahebzamani, H., Alavi, M. Z., Farzaneh, O., and Moniri, A. (2022). Laboratory and field investigation of the effect of polymerized pellets on the fatigue and low-temperature performance of asphalt mixtures. *Constr. Build. Mater.* 323, 126527. doi:10.1016/j.conbuildmat.2022.126527

Silva, R., De Brito, J., and Dhir, R. (2019). Use of recycled aggregates arising from construction and demolition waste in new construction applications. *J. Clean. Prod.* 236, 117629. doi:10.1016/j.jclepro.2019.117629

Sreedhar, S., and Coleri, E. (2022). The effect of long-term aging on fatigue cracking resistance of asphalt mixtures. *Int. J. Pavement Eng.* 23, 308–320. doi:10.1080/10298436.2020.1745206

Upshaw, M., and Cai, C. (2020). Critical review of recycled aggregate concrete properties, improvements, and numerical models. *J. Mater. Civ. Eng.* 32, 03120005. doi:10.1061/(asce)mt.1943-5533.0003394

Vieira, C. S., and Pereira, P. M. (2015). Use of recycled construction and demolition materials in geotechnical applications: a review. *Resour. Conserv. Recycl.* 103, 192–204. doi:10.1016/j.resconrec.2015.07.023

Wang, B., Yan, L., Fu, Q., and Kasal, B. (2021). A comprehensive review on recycled aggregate and recycled aggregate concrete. *Resour. Conserv. Recycl.* 171, 105565. doi:10.1016/j.resconrec.2021.105565

Wang, H., Wang, C., Bu, Y., You, Z., Yang, X., and Oeser, M. (2020). Correlate aggregate angularity characteristics to the skid resistance of asphalt pavement based on image analysis Technology. *Constr. Build. Mater.* 242, 118150. doi:10.1016/j.conbuildmat.2020.118150

Wang, L., Yao, Y., Li, J., Tao, Y., and Liu, K. (2022). Review of visualization technique and its application of road aggregates based on morphological features. *Appl. Sci.* 12, 10571. doi:10.3390/app122010571

Wang, R., Yu, N., and Li, Y. (2020). Methods for improving the microstructure of recycled concrete aggregate: a review. *Constr. Build. Mater.* 242, 118164. doi:10.1016/j.conbuildmat.2020.118164

Wang, S., Zhou, H., Chen, X., Gong, M., Hong, J., and Shi, X. (2021). Fatigue resistance and cracking mechanism of semi-flexible pavement mixture. *Materials* 14, 5277. doi:10.3390/ma14185277

Xia, P., Khan, S., Tahir, M., Hassam, M., Gong, F., and Zhao, Y. (2024). Characterizations and quantification of freeze-thaw behaviors of recycled brick aggregate concrete. *J. Build. Eng.* 86, 108821. doi:10.1016/j.jobe.2024.108821

Xiao, J., Tang, Y., Chen, H., Zhang, H., and Xia, B. (2022). Effects of recycled aggregate combinations and recycled powder contents on fracture behavior of fully recycled aggregate concrete. *J. Clean. Prod.* 366, 132895. doi:10.1016/j.jclepro.2022.132895

Xiao, X., Li, J., Cai, D., Lou, L., Shi, Y., and Xiao, F. (2023). Low-temperature cracking resistance of asphalt concretes for railway substructure exposed to repeated freeze-thaw cycles. *Cold Regions Sci. Technol.* 206, 103721. doi:10.1016/j.coldregions.2022.103721

Yang, L., Gao, Y., Chen, H., Jiao, H., Dong, M., Bier, T. A., et al. (2024). Three-dimensional concrete printing Technology from a rheology perspective: a review. *Adv. Cem. Res.* 36, 567–586. doi:10.1680/jadcr.23.00205

Yang, S., Braham, A., Wang, L., and Wang, Q. (2016). Influence of aging and moisture on laboratory performance of asphalt concrete. *Constr. Build. Mater.* 115, 527–535. doi:10.1016/j.conbuildmat.2016.04.063

Yao, X., and Xu, T. (2023). Fatigue fracture and self-healing behaviors of cold recycled emulsified asphalt mixture containing microcapsules based on semicircular bending test. *J. Clean. Prod.* 410, 137171. doi:10.1016/j.jclepro.2023.137171

Yousefi, A. A., Sobhi, S., Aliha, M. M., Pirmohammad, S., and Haghshenas, H. (2021). Cracking properties of warm mix asphalts containing reclaimed asphalt pavement and recycling agents under different loading modes. *Constr. Build. Mater.* 300, 124130. doi:10.1016/j.conbuildmat.2021.124130

Zhang, H., Liu, H., Deng, Y., Cao, Y., He, Y., Liu, Y., et al. (2025). Fatigue behavior of high-strength steel wires considering coupled effect of multiple corrosion-pitting. *Corros. Sci.* 244, 112633. doi:10.1016/j.corsci.2024.112633

Zhang, L., Sojobi, A., Kodur, V., and Liew, K. (2019). Effective utilization and recycling of mixed recycled aggregates for a greener environment. *J. Clean. Prod.* 236, 117600. doi:10.1016/j.jclepro.2019.07.075

Zhang, T., Chen, M., Wang, Y., and Zhang, M. (2023). Roles of carbonated recycled fines and aggregates in hydration, microstructure and mechanical properties of concrete: a critical review. *Cem. Concr. Compos.* 138, 104994. doi:10.1016/j.cemconcomp.2023.104994

Zhao, Y., Lu, Z., Gedela, R., Tang, C., Feng, Y., Liu, J., et al. (2025). Performance and geocell-soil interaction of sand subgrade reinforced with high-density polyethylene, polyester, and polymer-blend geocells: 3d numerical studies. *Comput. Geotechnics* 178, 106949. doi:10.1016/j.compgeo.2024.106949

Zheng, Y., Zhang, Y., and Zhang, P. (2021). Methods for improving the durability of recycled aggregate concrete: a review. *J. Mater. Res. Technol.* 15, 6367–6386. doi:10.1016/j.jmrt.2021.11.085

Zieliński, P. (2024). The use of the semi-circular bending method to assess the intermediate-temperature fracture toughness of asphalt concrete mixes with reclaimed asphalt shingles. *Road. Mater. Pavement Des.* 25, 81–98. doi:10.1080/14680629.2023.2194432

Frontiers in
Materials

Investigates the discovery and design of materials for future application

A multidisciplinary journal that explores the breadth of materials science, engineering and mechanics - from carbon-based materials to smart materials.

Discover the latest Research Topics

See more →

Frontiers in
Materials

frontiers | Research Topics